Multiscale Structural and Mechanical Design of Mineralized Biocomposites

by

Benjamin J.F. Bruet

Diplôme d'Ingénieur
Ecole Centrale Paris, France, December 2003

M.S., Materials Science and Engineering
Massachusetts Institute of Technology, June 2004

Submitted to the Department of Materials Science and Engineering
in partial fulfillment of the requirements for the degree of

Doctor of Philosophy in Materials Science and Engineering

at the

MASSACHUSETTS INSTITUTE OF TECHNOLOGY

February 2008

Author……..……...
Department of Materials Science and Engineering

Certified by……...……....
Christine Ortiz
Associate Professor of Materials Science and Engineering
Thesis Supervisor

Accepted by……...…
Samuel M. Allen
POSCO Professor of Physical Metallurgy
Chair, Departmental Committee on Graduate Students

Multiscale Structural and Mechanical Design of Mineralized Biocomposites

by Benjamin J.F. Bruet

Submitted to the Department of Materials Science and Engineering
On February, 2008 in partial fulfillment of the
requirements for the degree of
Doctor of Philosophy in Materials Science and Engineering

ABSTRACT

Gastropod mollusk nacre tablets and *Polypterus senegalus* armored scales share common features such as a very complex and changing structure spanning several length scales. The smallest building blocks are single crystals, have dimensions of a from tens of nanometers to several microns and are intimately blended with an organic glue present within pores or between the crystallites. In particular, our results strongly suggest that nacre tablets possess nanoscale porosity in the form of elongated tubules that may contain the intratablet macromolecules. Their unique structure allows these materials deform in a ductile way at the nanoscale, with no cracks observed, and to confine deformation at the microscale so as to impede crack propagation.

Gradient in the mechanical properties are ubiquitous at both the microscale (scales) and the nanoscale (nacre tablets), preventing stress concentration and enhancing strain distribution. The armored scales thus exhibit a unique spatial functional form of mechanical properties with regions of differing levels of gradation within and between material layers, as well as layer with an undetectable gradation

Though highly mineralized, these biomaterials also exhibit greater local heterogeneity in their mechanical properties compared to pure minerals. Materials layers have distinct morphology and mechanical properties depending on their role (resistance to abrasion for harder outer layers, resistance to fracture for tougher inner layers) and their interface are reinforced (by anchored organic fiber ligaments and corrugated interfaces that maximize contact surface., preventing propagation of cracks both through and along the interfaces. The heterogeneity in size and shape of the crystallites and the pores, as well as the variation in the composition (mineral / organic, crystalline /

amorphous) are likely responsible for the desirable variations of mechanical properties as observed in these biocomposites at the smallest length scales, resulting in more spatially distributed strains and greater energy dissipation.

Thesis Supervisor: Christine Ortiz
Title: Associate Professor of Materials Science and Engineering

ACKNOWLEDGMENTS

A very intense period of my life is about to come to a close, and while it might be too early to reflect on all the changes I have lived since I first set foot at MIT, it is clear that these have been some of the richest years of my life.

I express my deepest gratitude to Professor Christine Ortiz for her great enthusiasm and invaluable guidance during my PhD. She gave me the opportunity to discover a world that was unbeknownst to me only a few years ago, and to conduct research in an intensely challenging but likewise intensely rewarding environment. I am particularly grateful that she encouraged me to try a wealth of new ideas, as well as helped me set up fruitful collaborations with other researchers.

I would like to thank my thesis committee members, Professor Mary Boyce and Professor Angela Belcher for providing me with the right balance between support and intellectual challenge. This has been crucial to my scientific maturation.

I also would like to thank all my collaborators, Professor Alain Baronnet for his great patience, knowledge and his infectious passion for science. Many thanks to Juha, Cathal, Daniel and Haimin for it has truly been a pleasure to work you. My UROP students, Lauren, Connie, Bob, Terianne, Julian and Elaine were also a very important part of my life in the lab, and in the end they probably taught me much more than I taught them. Thanks to all the Ortiz group members, Kuangshin, Miao, Lin, Jae, BoBae, Hsu-Yi, for providing an atmosphere close to that of a family. I gratefully acknowledge Alan Schwartzman and the MIT NanoLab, Scott Speakman at the CMSE X-Ray facility and MIT Institute for Soldier Nanotechnologies staff for being so friendly and helpful no matter what the circumstances were.

This unique MIT life would never have been so fulfilling if it weren't for all my all friends, in France, in the US and all over the world, who have been the true mainstay of my life, managing to bring a smile to my face by simply being their very unique selves. Forgive me if I do not detail all your names here. Just be sure that they inhabit my heart.

Finally, I would like to thank my family, which I have been missing dearly and am so much looking forward to spending more time with again. I thank my mother, Aleth, who supported me with all her love, her simplicity and wisdom, and my father, Bernard, for his soul is still very much present in my life and continues to guide me over the years. I thank my dear Fenia for never failing to fill my life with laugh, surprise, joy and happiness, making it very much the life of my dreams.

This project was funded by the Institute for Soldier Nanotechnologies (Contract #DAAD-19-02-D0002).

« Et tout ca pour du Schnapps !?? »

Monsieur Manatane

TABLE OF CONTENTS

LIST OF FIGURES

Fig. 3-9 Contact mode deflection atomic force microscopy (AFM) image of top down view of inner laminate columnar nacre of *T. niloticus* nacreous layer fractured in uniaxial compression 30 μm scan.

Fig. 3-10 Optical images under cross polarized light of a thin section (ion milled) of *T. niloticus* nacre layer. *Image by A. Baronnet*.

Fig. 3-11 SEM images of the fractured cross-section of the nacre layer of **(a,b)** *T. niloticus*, **(c)** fresh *H. rufescens*.

Fig. 3-12 TEM image of the ion polished cross-section of the nacre layer of *T. niloticus*. *Image by A. Baronnet*.

Fig. 3-13 SEM image of the etched cross-section of the nacre layer of *T. niloticus* (EDTA 0.5 M, 1 min sonication).

Fig. 3-14 SEM image of the etched cleaved surface of the nacre layer of *T. niloticus* (EDTA 0.5 M, 1 min soaking).

Fig. 3-15 SEM image of the etched cleaved surface of the nacre layer of **(a)** *T. niloticus* (DI water, 30 min soaking).

Fig. 3-16 AFM images of top down view of inner laminate columnar nacre of *T. niloticus* nacreous layer fractured in uniaxial compression **(a)** Contact mode deflection 10 m scan, **(b)** Tapping mode amplitude image of nanoasperities and organic matrix on the top of an individual nacre tablet of *T. niloticus,* 500 nm scan **(c)** 200 nm scan, and **(d)** 100 nm scan.

Fig. 3-17 Tapping mode phase atomic force microscopy images of nanoasperities and organic matrix on the top of an individual nacre tablet of *Trochus niloticus* that was freshly cleaved in uniaxial compression; **(a)** 1 μm scan, phase shift from -124º (darker) to +28º (lighter) **(b)** 200 nm scan, phase shift from -105º (darker) to +64º (lighter).

Fig. 3-18 Histograms of various features observed by SEM **(a,b)** and AFM **(c to h)**; the inset of numerical values indicates mean ± standard deviation for each dataset, *w* is the bin width (chosen based on Sturges' and Scott's rules), and the number of data points for each histogram > 20.

Fig. 3-19 TEM image of an ion-thinned tablet piece from *H. rufescens* (top view, parallel to c-axis) showing planar lattice defects and twinned nano-lamellae (white lines). *Image by A. Baronnet*.

Fig. 3-20 SEM image of the fractured cross-section of the nacre layer of *T. niloticus*. **(a) to (c)** cryofractured surface. **(d)** sonicated in EDTA 0.5 M for 2 min **(e,f)** sonicated in DI water for 5 min.

Fig. 3-21 SEM image of the cryofractured cross-section of the nacre layer of *T. niloticus*.

Fig. 4-5 Height profiles for 1000 uN and 5000 μN maximum load indents taken from tapping mode atomic force microscopy (AFM) images on freshly cleaved individual *Trochus Niloticus* nacre tablets. The inset is an AFM image of the residual indent for the 1000 μN maximum load.

Fig. 4-6 Mechanical properties derived from nanoindentation curves on freshly cleaved and artificial seawater-soaked individual *Trochus Niloticus* nacre tablets as a function of maximum load; average elastic moduli, E, using both Oliver-Pharr analysis and FEA simulations

Fig. 4-7 Average hardness, H, derived using the Oliver-Pharr analysis.

Fig. 4-8 H/E plot. The vertical error bars represent the standard deviation for that particular dataset and the * datasets indicate statistically significant differences ($p<0.05$) between the freshly cleaved and artificial seawater-soaked samples.

Fig. 4-9. Isotropic elastic-plastic finite element analysis (FEA) nanoindentation simulations; **(a)** schematic of model, **(b)** boundary conditions to ensure one sixth symmetry (top view), **(c)** simulations fit to average nanoindentation data on loading and unloading for 1000 μN maximum load. Input parameters were as follows; freshly cleaved nacre (E = 90 GPa, σ_Y = 11GPa) and artificial seawater soaked nacre (E = 76 GPa, σ_Y = 8.4 GPa) and **(d)** simulations for both nacre samples for maximum loads of 500 μN and 1000 μN.

Fig. 4-10 The top view (plane perpendicular to nacre tablet *c*-axis) of the contour for the maximum principal stress **(a)** at a maximum load of 1000 μN, and **(b)** after unloading from 1000 μN and height contours **(c)** at a maximum load of 1000 μN and **(b)** after unloading from 1000 μN. Since only one sixth of the material is modeled, the plot here consists of six identical images from numerical simulations (E = 90 GPa, σ_Y = 11 GPa).

Fig. 5-0 Schematic of the mapping indentation experiments and relative shape of indenter probes.

Fig. 5-1 100 μN indentation mapping of the polished surface of T. niloticus **(a)** TMAFM height image of the indented region. **(b)** corresponding Indentation modulus map and **(c)** hardness map.

Fig. 5-2 Correlation between mechanical properties and probed location **(a)** Indentation modulus versus distance to tablet boundary **(b)** hardness versus distance to tablet boundary **(c)** modulus versus RMS roughness and **(d)** hardness versus RMS roughness.

Fig. 5-3 30 μN indentation mapping of the polished surface of H. rufescens **(a)** TMAFM height image of the indented region. **(b)** corresponding Indentation modulus map and **(c)** hardness map.

Fig. 6-8 **(a)** SEM image of the ganoin and dentin underneath after 20 seconds etching with H_3PO_4 **(b)** High resolution SEM image of the thin elongated nanocrystals (in a fractured area) constituting the ganoine layer after 5 minutes of etching with NaOCl **(c)** High resolution SEM image of the nanocrystals after 2 minutes of etching with EDTA 0.5M. **(d)** High resolution SEM image of ganoine surface cross-section after 5 minutes of etching with NaOCl. Axis 1 is parallel to the long axis of a scale, axis 2 is parallel to short axis of a scale, and axis 3 is perpendicular to the ganoine layer surface. The raised topographical feature observed of one of the array of surface "tubercles."

Fig. 6-9 **(a)** BSEM image of the polished dentin-ganoin junction **(b)** BSEM image of the dentin-ganoin junction after 10 minutes etching with EDTA 0.5M **(c)** SEM image of the dentin-ganoin junction after 10 seconds etching with H_3PO_4 **(d)** BSEM image of the cross-section of dentin and underlying isopedine after 10 minutes EDTA 0.5M etching.

Fig. 6-10 **(a)** SEM image of the ganoine and dentin layers after 10 seconds etching with H_3PO_4 **(b)** BSEM image of the same area.

Fig. 6-11 **(a)** SEM image of the isopedine layer cross-section after 10 seconds etching with H_3PO_4 **(b)** High resolution SEM image of one of the isopedine sub-layers.

Fig. 6-12 **(a)** Tapping Mode Atomic Force Microscope (TM-AFM) height image of the polished cross-section of the bony plate. **(b)** TMAFM amplitude image of the same area.

Fig. 6-13 1 μm scan size Tapping Mode Atomic Force Microscope (TM-AFM) images of the polished cross-section of an individual scale. Leftmost are height images, middle are amplitude images and rightmost are phase images. From top row to bottom, images were taken in ganoine, dentin, isopedine and bone respectively.

Fig. 7-1 Mechanical properties derived from nanoindentation experiments across the cross-section of the different material layers of an individual *Polypterus senegalus* scale. Indentations were conducted across the scale cross-section with the loading axis parallel to axis 1. All data represents an average of three parallel columns of 125 indents each. 500 μN maximum load; average indentation moduli, $E_{O\text{-}P}$, and hardness, $H_{O\text{-}P}$, both reduced from Oliver–Pharr analysis as a function of distance across the scale cross-section. The vertical error bars represent one standard deviation. "Epo." is the epoxy used for embedding.

Fig. 7-2 Average $E_{O\text{-}P}$ and $H_{O\text{-}P}$ for each of the different layers derived from 500 μN maximum load nanoindentation curves using Oliver–Pharr analysis. The vertical error bars represent one standard deviation for that particular dataset (n = number of individual nanoindentation experiments: ganoine, n=6; dentin, n=24, isopedine, n=32, bone, n=336).

Fig. 7-3 **(a)** Average nanoindentation load-depth curves for all four layers. Solid lines are the experimental data averages, dashed lines are elastic-perfectly plastic finite element analysis (FEA) predictions. Horizontal error bars represent one experimental standard deviation. **(b)** FEA predictions of von Mises stress field for the indentation of the cross-section of ganoine at a maximum depth of 62 nm correspondingly to a maximum load of 500 μN. **(c)** FEA predictions of plastic equivalent strain (PEEQ) for indentation of the cross-section of ganoine at a maximum depth of 62 nm corresponding to a maximum load of 500 N.

Fig. 7-4 Tapping mode atomic force microscopy (TMAFM) amplitude images of the residual indents (500 μN maximum load) on the cross-section of each of the four material layers. From top left to bottom right: **(a)** ganoine, **(b)** dentin, **(c)** isopedine, and **(d)** bone. **(e)** TMAFM phase image of the residual indentation (500 μN maximum load) on the cross-section of isopedine.

Fig. 7-5 Predictions of effective microindentation mechanical properties of *P. senegalus* scale via multilayered finite element analysis (FEA) simulations. a, Multilayered structures of discrete layers (left) and gradient layer and junctions (right) with their corresponding elastic modulus and yield stress distributions (center). *Figure by J. Song*.

Fig. 7-6 **(a)**, Simulated microindentation load versus depth curves showing loading and unloading maximum loads of 0.25 and 0.5 N comparing the discrete and gradient multilayer systems to all-ganoine, all-dentin, and all-bone. **(b)**, Simulated effective indentation modulus as a function of maximum indentation load for the five material systems revealing the load dependent effective modulus of the multilayered structures. *Figure by J. Song*.

Fig. 7-7 Predictions of effective microindentation mechanical properties of *P. senegalus* scale via multilayered finite element analysis (FEA) simulations. **(a)** Simulated effective microhardness as a function of the maximum indentation load for the five material systems and the experimentally measured values. **(b)** Simulated effective energy dissipation as a function of the maximum indentation load for the five material systems. *Figure by J. Song*.

Fig. 7-8 Simulation contours of stress, plastic strain, and pressure fields of *P. senegalus* scale via multilayered finite element analysis (FEA) simulations. FEA predictions of von Mises stress field, S11 (normal stress on the plane perpendicular to the 1 axis), S33 (normal stress on the plane perpendicular to the 3 axis), and pressure at a maximum depth when fully loaded, and S12 (shear stress on the plane perpendicular to 2 axis acting in the 1 direction), S22 (normal stress on the plane perpendicular to the 2 axis) and plastic equivalent strain after fully unloaded for three models: **(a)** all ganoine, **(b)** discrete and **(c)** gradient FEA models for 1 N maximum load indentation. *Figure by J. Song*.

Fig. 7-9 Topographic profiles, residual impressions of microindentation, and fracture of the outer ganoine surface of an individual *P. senegalus* scale. **(a)**, Tapping mode atomic force microscopy (TMAFM) amplitude image of a 1 N maximum load microindentation. **(b)** Optical micrograph of a 1 N maximum load microindentation **(c)** Finite element analysis prediction of the residual depth topography obtained from the gradient multilayer simulation and experimental height profiles from TMAFM images (from Fig. 7-9 a) for 1 N maximum load microindentation **(d)** Optical micrograph of a 2 N maximum load microindentation.

Fig. 7-10 TMAFM amplitude image of the residual imprint of a 10 mN Berkovich indent in fused silica. The black arrows indicate radial cracks emanating from the indent apexes.

Fig. 7-11 Scanning electron micrograph (SEM) of cross-section of isopedine layers showing orthogonal cracks in sublayers.

Fig. 7-12 Back-scattered SEM of cross-section of ganoine and dentin layers (etched with phosphoric acid for 20 seconds) showing cracks arrested at ganoine-dentin interface as well as pieces of ganoine cracked off from outer surface.

Fig A1 FTIR spectra of fresh and EDTA-demineralized nacre from *Trochus Niloticus*.

Fig. B-1 Finite element analysis model using two-dimensional axisymmetric indenter. Sample mesh and indenter tip surface profile.

Fig. B-2 Three-dimensional Berkovich indenter FEA model. **(a)**, Rounded Berkovich indenter tip mesh. The entire tip is shown in the inset. **(b)**, Schematic of the indenter tip end showing how the end radius, R_{tip}, and truncate height, *h,* are defined.

Fig. C-1 FEA simulation of a series of nine nanoindentations in a bone sample positioned on a 3 × 3 square grid spaced 3 um apart. **(a)**, The residual von Mises stress field. For illustration, the uppermost residual indentation is covered by the Berkovich indenter tip. **(b)**, Simulated load-depth nanoindentation curves corresponding to all nine grid indentation virtual experiments from a.

Fig. D-1 Nanoindentation data for loading axis normal to the outer *Polypterus senegalus* ganoine scale surface at two different locations (center of scale and anterior process) on loading and unloading for different maximum loads. Average force versus depth data for **(a)** 100, 500 and 1000 μN maximum loads and **(b)** 5000 and 10,000 μN maximum loads. The horizontal error bars represent the standard deviation for that particular dataset (n=25). Mechanical properties reduced from the data shown in parts **(a)** and **(b)**; **(c)** average indentation moduli, E, calculated via the Oliver–Pharr analysis **(b)** average hardness, H, derived using

Oliver–Pharr analysis. The vertical error bars represent the standard deviation for that particular dataset (n=25)

Fig. D-2. TMAFM images of the residual indentation at the ganoine surface(height, amplitude and phase) **(a)** 10 mN indent **(b)** 1mN indent.

LIST OF TABLES

CHAPTER 1 INTRODUCTION

1.1 MOTIVATION

Many soft-bodied animals have developed exceedingly tough natural body armor (e.g. mollusk and turtle shells, arthropod exoskeleton, hoof, antler, tusks, dinosaur and certain fish scales) over millions of years of evolution for protection and survivability from predators, the environment, and sometimes even their own biological processes. All of these materials exhibit *mechanical property amplification,* i.e. they are composed of constituents that are readily available in the environment which exhibit poor macroscale properties (e.g. brittle bioceramics such as calcium carbonate or hydroxyapatite and flexible biomacromolecules such as proteins) and yet are able to achieve huge increases in toughness and strength (Fig. 1-1). Amazingly, the key to this accomplishment is nanotechnology. Natural materials have varied, complex, hierarchical and heterogeneous nanostructures that undergo a wide variety of deformation mechanisms at many length scales. Many of these energy- dissipating mechanisms are barely, if at all, being exploited in currently used synthetic body armor systems. Natural materials are a great untapped resource for providing new engineering designs for synthetic, biologically inspired soldier protection and survivability materials technologies. Hence, the overall goal of this project is not to use natural materials directly for soldier body armor applications, but to

learn the nanostructured design principles responsible for mechanical property amplification. In this way, we can then create biomimetic armor materials with the same

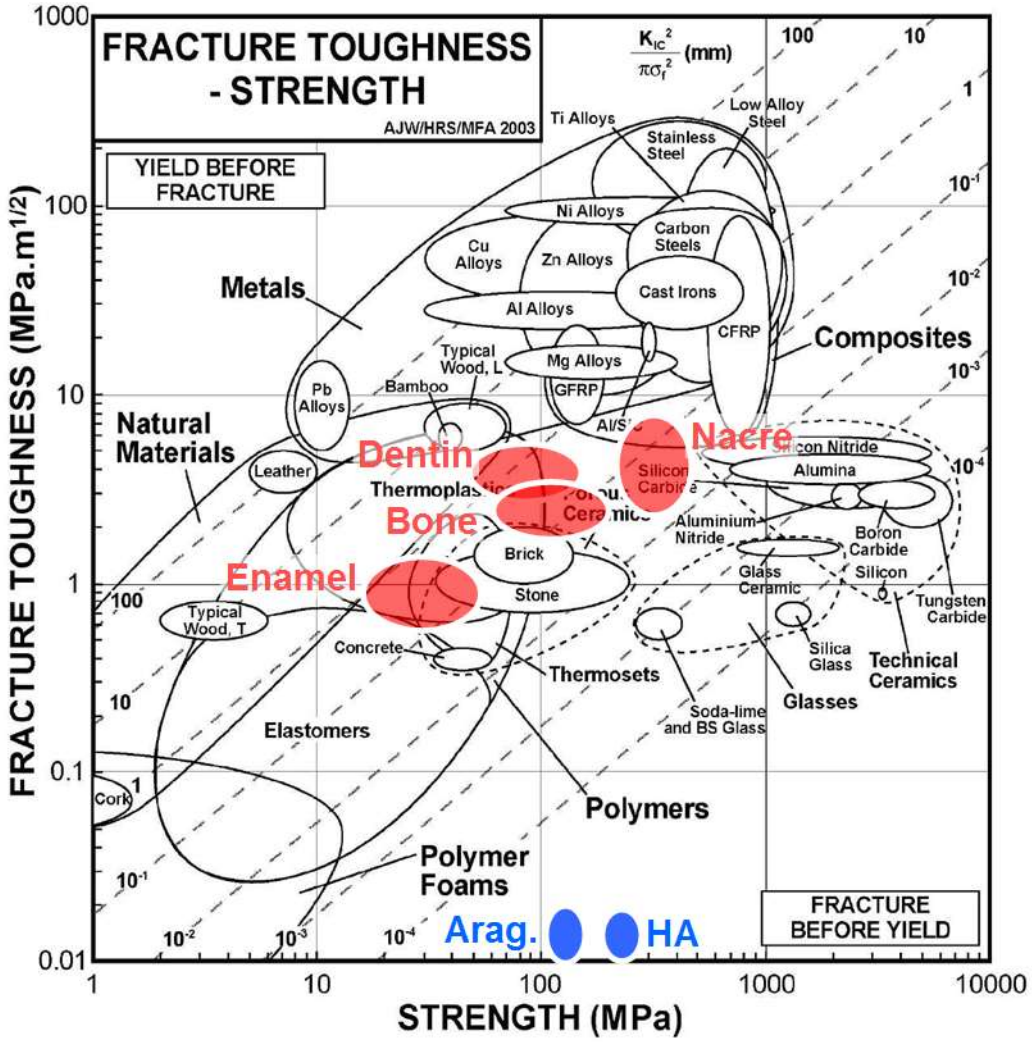

Fig. 1-1 Comparison of the mechanical properties of certain mineralized biocomposites (red areas) to pure minerals (blue circles, Arag. = Aragonite and HA = Hydroxyapatite) and a variety of other types of materials (from *Ashby, 1999*)

type of structures as natural systems, but with advanced nanomaterials (e.g. carbon nanotubes, ceramic and metal nanoparticles, etc.) replacing the basic constituents, thereby amplifying mechanical properties even further.

1.2 OBJECTIVES

The overall goal of this project is to establish the nanostructured design principles responsible for mechanical property amplification in nacre, i.e. to understand how biological systems utilize constituent materials available in the environment which possess relatively poor macroscale properties (e.g. brittle bioceramics such as calcium carbonate and flexible biomacromolecules such as proteins) and yet are able to achieve huge increases in energy dissipation, toughness, and strength. Model systems studied in this thesis are the tough, inner aragonite-rich nacreous layer of the gastropod mollusks *Trochus niloticus* and *Haliotis rufescens* as well as their outer calcite-rich layer (the first line of defense against penetrating impacts by predators), single crystal aragonite (which forms the basis for many natural materials), and finally the multilayered, hydroxyapatite based ganoid scales of a rare breed of armored fish, *Polypterus senegalus*. The specific aims of this thesis are as follows:

1) To comprehensively characterize the multiscale hierarchical structure of the aforementioned biomaterials.

2) To quantify and understand the micro/nanomechanical heterogeneity in these natural materials and understand its relationship to mechanical property amplification.

3) To establish how natural microscale layered systems (where each layer is nanostructured) are utilized to create an effective armor and to determine the mechanical role of each layer

1.3 OVERVIEW

This thesis begins with a summary of the current state of knowledge regarding the structure and mechanical properties of nacre in Chapter 2. Chapter 3, a portion of which is published in Journal of Materials Research in 2005, reports a comprehensive study of the hierarchical structure of gastropod mollusk nacre, from the nano- to the macroscale. Chapter 4, which was in part published in the Journal of Materials Research in 2005, describes the deformation behavior and mechanical properties at the micro and nanoscale in nacre. Chapter 5 studies the nanoscale mechanical heterogeneity in nacre and links it to ultrastructural features. Chapter 6, which is currently submitted for publication, describes the ultrastructure of the armored scales of *Polypterus senegalus*. Chapter 7, also submitted for publication, contains a multiscale study of the mechanical properties of these scales and presents a detailed model of its resistance to penetration.

CHAPTER 2 NACRE: A REVIEW OF THE CURRENT STATE OF KNOWLEDGE

2.1 INTRODUCTION

Mollusks are a very large phylum of invertebrates, which appeared in the Early Cambrian, about 600 million years ago.[1] Among the classes still extant nowadays, we can cite the Gastropods (snails, slugs), the Bivalves (clams, scallops, oysters, mussels) and the Cephalopods (ammonites, nautiluses, octopuses, squids, cuttlefish etc, which appeared in the late Cambrian). At the early stage of their development, the majority of these animals had an external protective shell, and many still retain this characteristic nowadays. While cephalopods are exclusively marine, bivalves live in rivers and lakes as well, while gastropods can be found in many different environments, either aquatic or terrestrial.

Nacre, commonly called mother-of-pearl, is the iridescent internal layer that can be found in many mollusk shells.[2] Its smooth, shiny appearance and superior mechanical properties are among the reasons for its century-long use for jewelry creation. For several decades, scientists have expressed an ever growing interest in studying the microstructure and mechanical properties of this amazing material, in particular to achieve a better understanding of the mechanisms participating to its outstanding toughness, strength and

stiffness. As a matter of fact, even though mostly composed of calcium carbonate, a common mineral with mediocre mechanical characteristics, nacre's unique and highly organized design at multiple length scales enables outstanding mechanical performance including an excellent combination of stiffness, strength, impact resistance, and toughness.[3-7]

2.2 NACRE STRUCTURE

2.2.1 OVERVIEW

The types of shell exhibited by many mollusks are in their majority composed of several microscopic layers, including (principal component in parenthesis):

- outermost: periostracum (thin organic layer composed mainly of sclerotized protein)
- prismatic (calcite)
- laminar nacreous (aragonite or calcite)
- innermost : irregular crossed-lamellar (calcite)

The thickness and microstructure of these shells vary with the species, the age of the animal as well as the environmental conditions.[8]

The prismatic layer is generally recognized as the hardest one, while the nacreous layer is the toughest. The former is thus thought to prevent the initiation of cracks while the latter will impede crack propagation. Being primarily interested in impact resistance and enhancement of fracture toughness, we will now focus on the study of the nacreous layer.

Nacre is a complex, multilayered biocomposite the structural elements of which span hierarchically over 9 orders of magnitude in size. The mineral phase is Aragonite, a metastable form of $CaCO_3$ at normal conditions of temperature and pressure. This mineral phase amounts to ~ 95 % of the weight while an organic glue composes the remaining ~ 5 % wt. The structure of nacre well described down to the micron[9, 10], while at smaller length scales some interrogations remain. Different microstructures have been observed, from the simplest, “sheet” nacre to the more complex “crossed lamellar” nacres. In this thesis I will focus on “columnar” nacre, which belongs to the nacreous microstructures commonly denominated by the term "brick-and-mortar" (Fig. 1a) and that consist of successive layers of mineral tablets separated by thin layers of a biomacromolecular "glue." Within each tablet layer, neighboring tablets are also separated from each other by thin walls of this organic matrix.

2.2.2 MINERAL POLYMORPHS IN NACRE

The only mineral present in mollusk shells is calcium carbonate[2, 8, 11, 12]. Three distinct polymorphs are encountered, namely calcite (rhombohedral, present in particular in the outer prismatic layer of bivalvae[13] and gastropods[14]), aragonite (orthorhombic, *Pnma,*[15] present in all nacre types[10, 16-18]) and amorphous calcium carbonate or ACC (as a crystal precursor [19, 20] as well as a minor constituent of the tablets[21]).

Interestingly, contrary to calcite, aragonite is not thermodynamically stable at the normal conditions of pressure and temperature. Due to its atomic configuration, pure crystalline aragonite has a better packing in the c-direction and thus tends to form spherulitic clusters of small needles. Calcite grows as a rhombohedra and can form large

crystals. However, it fractures readily along its faces. Aragonite on the other hand doesn't have cleavage planes and hence is more resistant to fracture. ACC is always hydrated and is described as $CaCO_3$-$(H_2O)_{1.5}$. It is very unstable and rapidly crystallizes. It can be stabilized when contained inside a vesicle.

2.2.3 MICROSTRUCTURAL CHARACTERISTICS

According to Carter and Clarke II,[12] nacreous microstructures are "aragonitic laminar structures consisting of polygonal to rounded tablets arranged in broad, regularly formed, parallel sheets." Columnar nacre consists of stacks of interdigitating uniform tablets with their center approximately coinciding, and polygonal to rounded shapes. Sheet nacre is composed of superimposed layers of uniform, often hexagonal tablets. In both type, the polished cross-section resembles a brick wall structure. Cross-lamellar types of nacre are much more complex and have been less studied. They will not be treated here.

Bivalve tablets have a very regular hexagonal appearance, while cephalopod and gastropod tablets exhibit a much greater variety of polygonal shapes[22] Depending on the species, tablets have dimensions of ~ 5-20 μm (parallel to the crystallographic *ab* [010] and [100] face) and ~ 0.3-1.5 μm in thickness (vertically parallel to the *c*-axis [001] face)[9, 10] The surface of nacre tablets (Fig. 1d) from *California red abalone* (*Haliotis rufescens*) exhibits a dense population of nanoasperities (~ 30-100 nm diameter and ~ 10 nm in height)[3, 23] and mineral "bridges" between sheets and through continuous organic intertablet layers (~ 25-34 nm in size, ~ 91-116 μm^{-2} surface density).[24-28] Additionally,

even smaller vertical crystalline elements have been described within the nacre tablet lamellae.[29]

Even though calcified (and even monocrystalline[30]), the center is rich in organic material[31] for gastropods (faster dissolution rate) but this does not seem to be true for bivalves.[32] For gastropod nacre, each aragonitic tablet contains an radial organic membranes that subdivide it into a varying number (2-50) of mineral sectors (Fig. 1c) which have been interpreted as polysynthetically twinned crystalline lamellae,[31] though this hypothesis as been infirmed by X-Ray diffraction studies[17, 18] No sectors can be found in bivalve nacre.[31]

So-called mineral bridges[27, 33, 34] protruding through the pores of the chitin sheets and connecting adjacent tablets have been often observed. However, in spite of many SEM, AFM and TEM studies, doubts subsist whether these bridges are true mineral connection or mere contacting nanoasperities[35]. The associated pores observed in the interlamellar organic layer could also be due to some extent to dehydration artifacts[36]

2.2.4 CRYSTALLINE CHARACTERISTICS

In all nacre types, the c axis is strongly oriented toward the interior of the shell, i.e. orthogonal to the local shell curvature.[18] In bivalve nacre the a axis is often parallel to the margin and the consequently the b-axis to the growth direction. In gastropod nacre with columnar structure the a and b axes appear to have a fairly random orientation. For cephalopods, the b axis is either parallel to the growth direction or oriented at 60 deg, (twinning on (201) which is the common twin law in aragonite). These result show that

nacre differs widely between mollusk classes but little within classes, with the exception of the gastropod class which show a large variety of nacres, from columnar to cross-lamellar.

Sarikaya and Aksay show that certain *H. rufescens* (Red Abalone) nacre tablets are twins-related with a twin plane o f {110} type.[37, 38] They found two more levels of similar twining, namely the sectors of individual tablets as well a small scale between sectors to account for the fact that the angle between {110} planes is not an exact multiple of 60 (and hence tablets cannot be simply hexagonal with 6-fold twins). They emit the hypothesis that nacre tablet sectors always have a twin relation, however the observation of odd numbers of sectors within tablets seem to contradict this view.[31]

2.2.5 ORGANIC TEMPLATE

In nacre, the selection of the calcium carbonate polymorph, the control of its crystalline orientation, shape and size is determined by the proteins that constitute the organic phase, as is universally observed in the formation of mineralized biocomposites[39]. Through several strategies such as space confining, ion input controlling, organic matrix framework and nucleation sites building, crystal orientation and growth controlling. Basically, certain proteins assemble into a structural core while some other are either adsorbed on the surface of this template or dissolved in the liquid that soaks it. Furthermore, the proteins present in this organic matrix are generally categorized as either water-insoluble structural proteins or water-soluble control macromolecules, though this classification has been recently questioned.[40] It might be more accurate to distinguish between EDTA (ethylenediaminetetraacetic acid) soluble

and EDTA insoluble proteins. I will now describe the current state of knowledge regarding the location of these proteins within the nacre tablet, their arrangement and their putative functions.

The framework proteins form a relatively rigid continuous membrane[33, 41], delineating confined spaces in which the mineralization will occur. The thickness of this organic delimiting sheet is 10-50 nm.[33, 37] The polysaccharide chitin forms the structural backbone.[42-45] It is present in a well ordered β-sheet conformation that exhibits a preferred orientation over several microns. Relatively hydrophobic silk fibroin-like proteins constitute the major protein fraction.[46] They were originally described as a ordered and intimately associated with the chitin sheets,[47] but recent results have shown that they might rather constitute a gel that fills the structural organic compartments before becoming pushed toward the organic compartment boundaries during mineralization or occluded within the crystallites.[36, 48] Silk proteins are thought to act as an initial substrate for the adsorption of soluble macromolecules as well as to keep a uniform spacing between the successive interlamellar sheets and prevent their collapsing. It has also been proposed that the two surfaces of an individual matrix sheet should be different, one promoting nucleation and the opposite one inhibiting it, so as to stop the growth of the underlying tablet.[11]

It has also been claimed that collagen is also present in the interlamellar matrix[45]. TEM[49, 50] and AFM[51] studies have shown that the chitin framework is might be porous, thus facilitating the diffusion of ions and macromolecules into the structure The density of these pores is about 100 μm^{-1} with a spacing between 20 and 100 nm.[27] In addition to acting as a relatively rigid template, this structural core might have additional roles, such

as defining the tablet thicknesses[52] or even controlling certain aspects of the nucleation[51, 53]. However, some recent studies suggest that the pores could merely be artifacts due to the stretching of the interlamellar organic layer during dehydration[36, 48]

This complex organic phase is soaked in the extrapallial fluid (secreted by the mantle epithelium of the animal) with contains ions with a defined concentration,[54] as well as mainly acidic macromolecules.[33, 55] This microenvironment also has a strong influence on the biomineralization.[51]

2.2.6 FUNCTIONALIZING PROTEINS

Hydrophilic control proteins functionalize the organic structural template further. In nacre, they will favor the growth of aragonite over calcite,[56-58] select the crystalline orientation where the c-axis is roughly normal to the tablet surface[52], and likely plays a role in the size and shape of the nanograins[51, 52]. Thus they can usually be found embedded within the mineral crystallites or adsorbed on the interlamellar organic sheets. They are often strongly acidic[33, 59, 60], rich in aspartic acid[55] and glutamic acid.[51] Acidic sulfated polysaccharide have also been detected.[61] They usually display anionic groups that can interact with cations in solution such as Ca^{2+} or with surface of crystals. The aspartic acid-rich proteins have been shown to adopt a β-sheet conformation upon binding of Ca^{2+} ions to their carboxylate groups,[62] while others adopt a random coil conformation in solution.[63]

One of the proteins present in Haliotis rufescens (Red abalone), AP8, has been shown to significantly accelerate the kinetics of calcite formation in one orientation while modifying the shape of the growing crystal through step-specific interactions.[64] Another

closely related family, AP7, also present in Haliotis rufescens (Red abalone) can interrupt the aragonite crystal growth as well as promote the smoothening of step edges, depending on its concentration.[65] It also form complexes with another family (AP24)[66], which stresses the complexity of interactions between these different molecules, and a potential altering of their function through mutual interaction.

The lustrin superfamily is a group of proteins that exhibit elastomeric and adhesive behavior. High Resolution Force Spectroscopy (HRFS) experiments conducted on Lustrin showed that is possesses folded domains that break during stretching of the molecules, effectively giving it a hidden length allowing enhanced energy dissipation[67]. The sacrificial bonds reform upon release of the tensile force. Proteins from the lustrin family have been sequenced and were shown to have modular domains which might perform separate functions such has force unfolding, intermolecular or mineral binding.[68]

Many other nacre proteins have been studied[69] and it appears that they often have multipurpose functions. It has even been suggested that they change role depending on their location, from being crystallization inhibitors when dissolved in the silk gel to nucleators when adsorbed onto the chitin framework due to conformational changes.[70]

A clear separation of roles for the different types of proteins (insoluble structural vs. soluble controlling the mineralization) is still under discussion. For instance it has been claimed that the presence of acidic macromolecules were necessary to the nucleation of crystallites[51], while in another study the water-insoluble ("structural") matrix alone was enough to grow densely packed aragonite tablets.[53]

2.2.7 LOCATION OF PROTEINS

The actual location of the acidic proteins within the mineralized structure can be linked to their roles they play during nacre formation as well as in the mechanical properties of the mature composite. To date, two histochemical studies have been conducted on cephalopod (columnar nacre) and bivalve (sheet nacre) specimens.[71, 72]

For cephalopod nacre it was shown that the nucleation center within each tablet comprises a core of carboxylate groups surrounded by a ring of sulfate groups. Aragonite nucleating proteins were also detected in this tablet central region. They were also detected at the outer boundaries of the tablet, as well as carboxylate and sulfate groups. On the other hand, the region in between the center and the boundaries yielded only scarce quantity of either species. These proteins could be either adsorbed proteins onto the chitin, or intracrystalline proteins that became bound to the matrix after being released during decalcification. The lower yield of proteins in this region could also be due to the fact that part of them was washed away with the calcium carbonate during decalcification and subsequent washings. Carboxylate groups have been linked to aspartate side-chains and sulfate groups to sulfated polysaccharide side chains. The later are known to be involved in the nucleation of crystallites,[8] and there are indications that both might actually cooperate in order to generate oriented calcite nucleation.[73]

For bivalve nacre, only the aragonite nucleating proteins (present both at the nucleation site and tablet boundaries) could be detected. This difference could simply be due to the fact that sheet nacre exhibits much smaller stack order and hence the boundaries of the tablet become all blurred when successive organic layers collapse into each other after demineralization.

As a word of caution, it should be noted that the difficulty to fix intracrystalline proteins and the extensive washing during the sample preparation might have induced some proteins to be dispersed and possibly adsorbed on secondary locations.

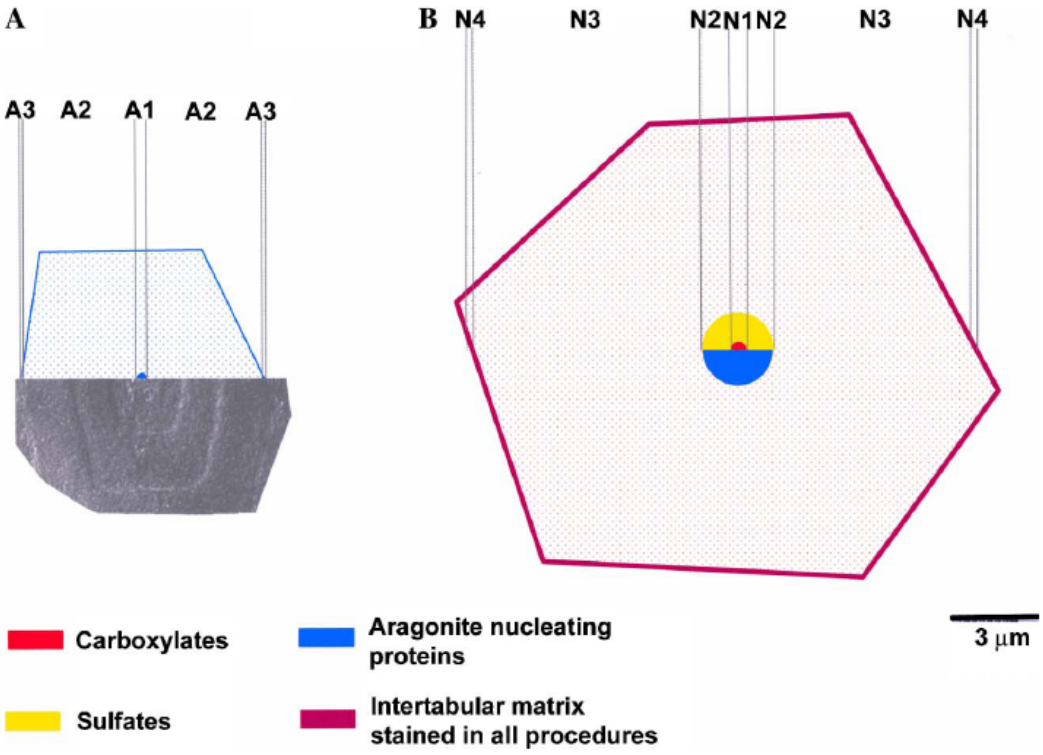

Fig. 2-1: Mapping the distribution of organic matrix components underlying a single aragonitic tablet in nacre[72]

2.3 NACRE FORMATION

Mineralized biomaterials can take on extremely complex shapes, drawing on a hierarchical organization that can span as much as 10 orders of magnitude from the smallest length scale (Angstroms) to the macroscopic world, and exhibits several distinct levels of structure depending on the scale considered. They typically are composite

materials, with one or several mineral phases intimately associated with organic macromolecules. These materials have typically skeletal or exoskeletal functions, and hence their mechanical properties have particularly been optimized to meet these. Among the roles other than mechanical fulfilled by biocomposites we can cite permanent dipole moment[74] that allow bacteria to move along geomagnetic fields, or near-perfect optical lenses[75] allowing certain types of starfish to capture light more efficiently in order to lure food to them.

The formation of such materials, through what is called biomineralization, is very complex and the subject of intense scientific scrutiny[11, 76-80]. Indeed, mineralized biocomposites are usually grown at ambient temperature and pressure conditions through a bottom-up fashion where the material's structure is controlled from the very atomic scale to the macroscale.

2.3.1 NUCLEATION OF THE TABLETS

Several models have been proposed to explain the nucleation and growth of the tablets. The major issues that these models have to address are:

- The supply of calcium carbonate
- The different characteristics of the ultrastructure of the tablets (nucleation site, location of the organic components, nanograins and nanoasperities…)
- The nucleation and growth mechanisms of the crystalline component
- The crystalline characteristics of the tablets (crystalline orientation of the tablets as well as crystalline domains of the order of several tablets

depending on the species - tens of tablets (for gastropods and cephalopods) to virtually all of them (bivalvae).

In the early seventies, it was suggested that tablet mineralization initiated on the open surfaces of the organic matrix, in a fashion similar to epitaxy.[81] Another competing model hypothesized that the nucleation and growth occurred and were controlled by preexisting compartments of organic matrix.[82] Nakahara showed that the tablets grow in between two organic layers that have been pre-deposited prior the start of crystallization.[83]

Further studies seemed to show that the epitaxial model was more accurate[84], and in 1984 Weiner and Traub[47] refined it based on TEM[85] and X-Ray diffraction[43, 44] data. They described the structural component of the matrix as a sandwich of a thin ordered layer of β-chitin surrounded by silk fibroin-like proteins in a β-sheet conformation orthogonal with that of chitin, and with control acidic macromolecules adsorbed onto them and in direct contact with the nucleating aragonite crystallites. The orientation of the crystallites would come from the binding of the Ca^{2+} cations with the oriented proteins, forcing it to nucleate from the ab face. Indeed, a well-defined spatial relationship was shown to exist between the orientation of the chitin and the a and b crystallographic axes of the aragonite crystals. The authors suggested that nucleation site is composed of acidic proteins in β-sheet conformation that, in addition to inducing the nucleation of the first crystallite, are also responsible for its initial orientation.

Some experimental incertitude subsisted in the fact that observations were made on EDTA-decalcified samples, and thus prone to some extent to artifacts. Furthermore,

the authors noted that the electron diffraction study conducted simultaneously with the TEM observation show a much better order of the mineral than the organic structures over regions as small as 6 μm^2, with the protein diffraction axis ranging as mush as ±30° around the mean direction while the mineral appears essentially as a single crystal.[44]

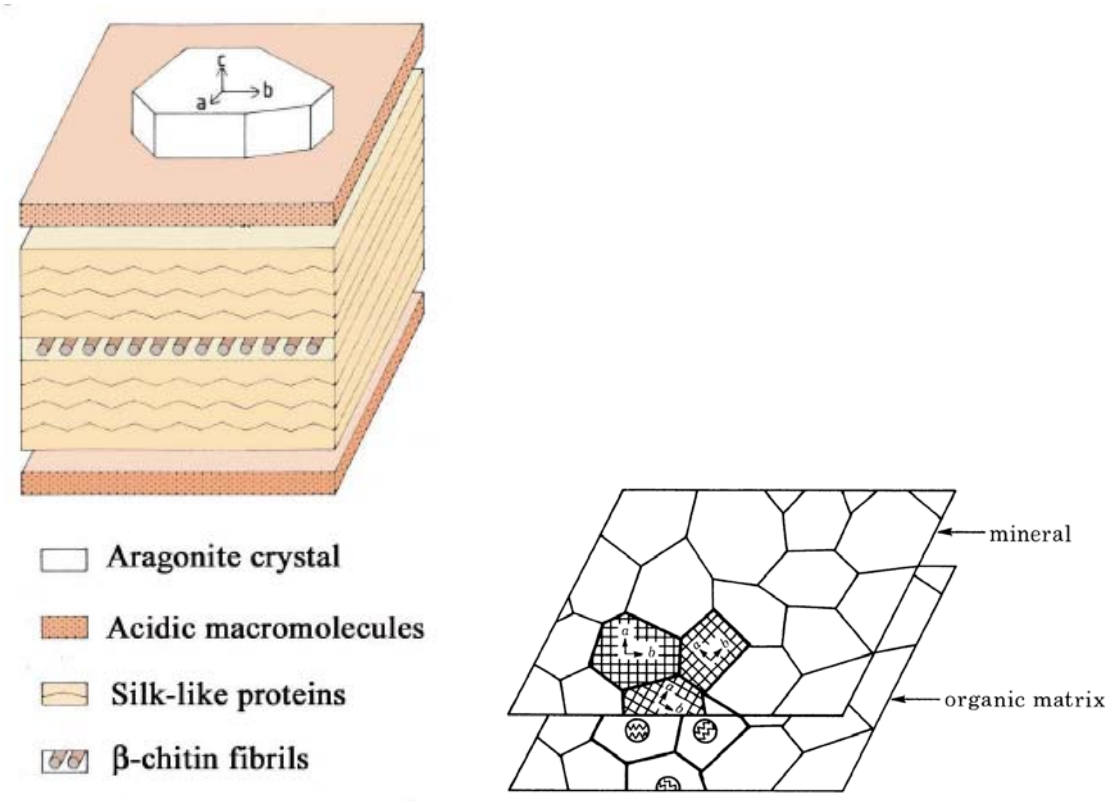

Fig. 2-2: Early model of epitaxial growth for nacre[11, 36, 47]

A refined model was recently suggested, based on cryo-TEM observations of the mature nacre of bivalve mollusk *Atrina*.[69, 86] It hypothesizes that prior to mineralization the silk may be in the form of a hydrated swollen gel located between the chitin sheets, rather than within them. The acidic macromolecules would then be adsorbed directly onto the chitin fibers, or be floating within the silk gel. This model calls into question the

notion of purely epitaxial growth that was a corollary of the previous model, based on a putative order of the silk proteins atop the chitin framework.

Rather than epitaxial matching between the organic sheet and the ion arrangement in the nucleated crystal, the nucleation of a certain polymorph with a certain crystalline orientation could still be controlled by the surface charge density at the surface of the organic network.[51, 59] Indeed, macromolecules promoting either aragonite or calcite nucleation are known to be strongly polyanionic, with the calcite-inducing one being more strongly acidic than the aragonite specific ones.[43, 44] Patches of them were observed on the chitin layer, implying that they could still take on a β-sheet configuration and account for the relationship in the chitin fibers alignment and the crystallographic orientation to the aragonite crystals observed by Weiner, et al.[8, 73] Nevertheless it must be noted that this new model is based on observations made on mature organic matrix, which can have undergo major changes compared to its prior mineralization stage. Also, the presence of silk protein under a gel-like state was inferred from the absence of a structured silk layer lining the chitin framework, rather than direct observation.

Nudelman, et al. also described how oriented crystalline growth could take place at the nucleation site. Based on their findings related to the potential location of various organic components within a tablet compartment (see previous section), the aspartate side chains and polysaccharide side chains found in the nucleation center could cooperate to generate oriented crystalline nucleation.[87] More precisely, the surrounding unstructured sulfates may induce a ionotropic effect[48] and the resulting supersaturation might in turn lead to oriented nucleation on the ordered carboxylate-rich aspartate acid proteins at the center.

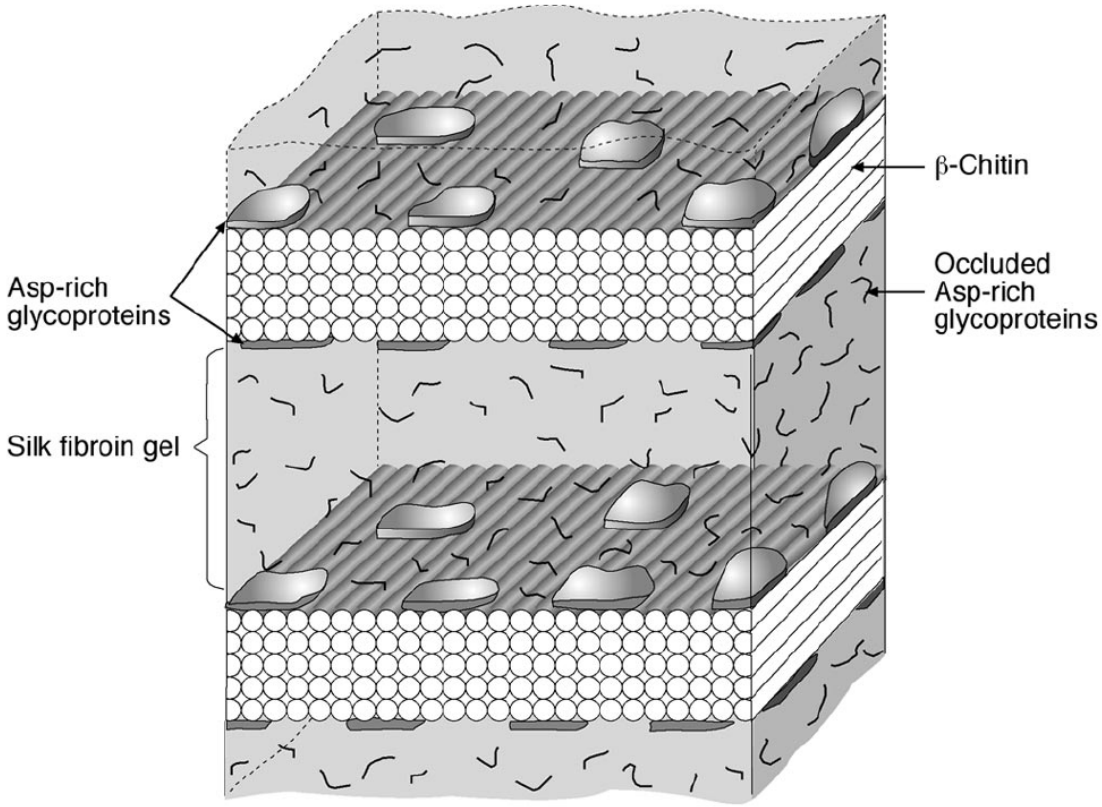

Fig. 2-2: 2006 model of the organization of the organic template in nacre[36]

This model was further refined in Addadi, et al.[88, 89] to incorporate the theory that the mineral material is provided through transient colloidal amorphous calcium carbonate (ACC). Nucleation still occurs on the matrix, with the crystalline orientation being dictated by the chitin fibers alignment. The crystal then grows at the expense of the ACC phase, occluding some of the acidic proteins, and pushing the silk gel-phase toward the boundaries away, eventually trapping it at the tablets boundaries, both horizontal (top and bottom) and vertical (tablet walls).

Other factors can account for the shift of balance between the two $CaCO_3$ polymorphs as well as some aspects of the crystalline orientation of the aragonite phase.

For instance, the concentration in Mg^{2+} ions in the fluid soaking the organic template[52], or the polymorph-specific acidic macromolecules interacting with certain faces of the nucleating crystal (as discussed above) could fulfill this role. For instance, Belcher et al. showed that the presence of a nucleating protein sheet and soluble proteins from *Haliotis rufescens* (Red Abalone) was sufficient to grow flat polycrystalline aragonitic plates with the c-axis perpendicular to the nucleating sheet.[53] A recent study also showed that the insoluble matrix alone might be able to generate the growth of oriented aragonite crystals.[38]

Sarikaya, et al.[47] emit the hypothesis that the organic template actually is a single crystals, in order to account for the twinned appearance of nacre layer they observe in their TEM and electron diffraction study. As they note, six-fold twin structures can readily be found in geological aragonite, where twin domains grow side by side. However, the fact that tablets grow from distant nucleation centers seems to call for a more complex growth mechanism

2.3.2 DISCUSSION

The models discussed above are all based on the organic phase controlling the local crystalline orientation of the mineral part. One of the major problems is that because the organic phase is likely less ordered than the mineral part,[21] such mechanism cannot convincingly explain why domains of even a few tablets appear as a perfect single crystal under X-Ray or electron diffraction. If an organic template with short distance order (i.e. a few microns) is responsible for the local crystalline orientation, how could it be propagated from one tablet to another, as is observed on virtually all types of nacre?

Casting more doubt on the possibility of crystalline control by the organic phase is a 2006 High Resolution Transmission Electron Microscopy (HRTEM) study on *Haliotis laevigata* which showed that crystalline aragonite tablets might be surrounded by a 3 to 5 nm thick coating of amorphous Calcium Carbonate (ACC).[90, 91] This amorphous layer seems to not interact with proteins. However this result could still be compatible with the theory that non-specific electrostatic interactions govern the nucleation of a specific polymorph and crystalline orientation, as the authors calculated that the highly polar aragonite (001) face could still interact with charged organic molecules throughout this ACC layer.

It was also shown by AFM imaging that when single tablets embedded in epoxy are soaked in conditions similar to the extrapallial fluid they can grow further even after having been bleached while preserving their crystalline orientation.[27, 34, 35] These results hint that the role of proteins could be limited to initiating growth or controlling the shape and size of the tablets.

Given the current state of knowledge regarding in-situ order of the organic components of nacre, it seems more likely that the propagation of the crystalline orientation of the mineral part is controlled by the mineral part itself. The still debated existence of mineral bridges[48] protruding through the pores of the chitin sheets and connecting adjacent tablets could serve as another means of control to the characteristics of the tablet nucleation. Over the past decades, the actual existence of pores and mineral bridges, as well as the role they might play has been controversial (see previous sections). Addadi, et al.[18]note that both mineral bridges and structured nucleation sites could very well exist side by side, simply creating a built-in redundancy in the formation process.

Indeed it could be that mineral bridges are responsible for the transmission of crystalline order over tablet domains of various sizes depending on the mollusk species, with the larger scale disorder created by the organic phase being responsible for the loss of coherence the local crystalline order over greater length scales.

2.3.3 CONCLUSIONS

In summary, the most current models seem to agree on the following characteristics regarding the formation of nacre:

- Chitin fibers are assembled into a rigid organic layers by the epithelium cells
- The nucleation site is constituted of several type of proteins facilitating the nucleation of a certain CaCO3 polymorph and maybe its crystalline orientation as well
- A hydrated gel of silk fibroin-like proteins with dissolved acidic proteins fills the rest of the compartment and keep the spacing between two successive chitin layers uniform
- Amorphous calcium carbonate (ACC) is brought on-site encapsulated in small vesicles that stabilize it
- nucleation is originated at the nucleation site by calcium binding acidic proteins
- crystalline growth occurs by fusion of the transient ACC and rapid crystallization into a specific CaCO3 polymorph. Acidic proteins probably control the shape and possibly the size of this fused grains.

- the crystal grows vertically along its fast-growing c-axis until it reaches the above chitin layer, and then starts expanding laterally
- as it grows certain acidic proteins (and more doubtfully some of the hydrophobic silk phase) become occluded, while other are pushed ahead of the growth front
- when the growing mineral phase encounters neighboring tablets, it stops, entrapping some of the silk and acidic protein mixture at the intertablet/interlamellar boundary

-

More controversial topics include:

- local crystalline orientation could be controlled either by oriented acidic polysaccharides or mineral bridges from the underlying tablet, or even both
- what happens to the vesicles containing the ACC?
- Are the nanograins separated or fused together?
- Are there actual pores in the chitin? Are there true mineral bridges?
- Does a silk gel indeed fill up the organic template prior to mineralization?

Note that the mechanisms could be different between different mollusk group, since it is known that the tablets have different morphologies and crystalline texture from one groups to another.

As a conclusion, though many different roles have been demonstrated for both fractions of the organic matrix (structural insoluble and adsorbed/dissolved soluble),

many aspects of the nucleation and growth of the nacre tablets remain unclear. In particular, the composition of the soluble component, its localization and organization within the insoluble structural framework, as well as the clear attribution of the roles mentioned above to either fraction still pose many interrogations. The scarce quantity of organic component that can be extracted from natural nacre, the difficulty to selectively isolate the proteins from the mix, the complex interactions between different proteins and with their in-vivo context all still pose major challenges to reproducing and understanding all the biomineralization processes involved in nacre growth. The variety of nacre types within the mollusk phylum[6, 7] also adds further complexity.

2.4 NACRE MECHANICAL PROPERTIES

Micro- and macroscopic mechanical testing on nacre has been performed in tension,[3, 6] three-point bend,[3] four-point bend,[92] and indentation.[93] Recurrent features in these tests show that nacre is anisotropic,[7] exhibits hysteresis on unloading, and plastically deforms up to fracture strains of ~0.018 in tension.[3, 6] Nacre mechanical property values have been reported as follows: elastic moduli (60-80 GPa[6, 7]), tensile, compressive, and three-point bend strengths (130-168,[4] 235-540,[3] and 194-248[3, 6] MPa, respectively). Its work of fracture has been shown to be ~3000 times higher than the one of pure aragonite ceramic[94]. Nacre having soaked in water for several weeks is also known to show larger plasticity than fresh nacre.[1] Many studies have been conducted in order to assess what are the mechanisms that contribute to this dramatic enhancement of toughness in nacre. The ones reported so far: rupture of "sacrificial" weaker bonds in the

organic component,[6] extension, pull-out, and/or ligament formation of a organic component bridging the tablet interfaces,[3, 94] interacting nanoasperities and mechanical interlocking providing slip resistance and leading to inelastic strain, formation of periodic dilatation bands between plate edges,[95] debonding of mineral-organic interfaces, tortuous crack propagation due to the microlaminate "tablet and mortar" structure, crack tip blunting due to plasticizing of the organic matrix. However it has been shown that these mechanisms as they are understood today can only account for part of the energy absorption skills of nacre. The difficulty to accurately characterize their origins at the nanoscale and quantify their contributions is the main reasons for this situation.

More theoretical approaches have been developed in the recent years in order to provide a different insight on these issues. Two and three-dimensional finite element analysis (FEA) models based on continuum mechanics have been elaborated to investigate the role of some of these mechanisms such as nanoasperities, mineral bridge contacts, inelastic deformation, and strain hardening.[96] The effectiveness of the organic matrix to shield cracks and influence the toughness of nacre has been studied via a virtual internal bond (VIB) model.[97, 98] Micromechanical models are also starting to be developed which take into account both the spatial organization of the organic and inorganic components as well as sequential force-induced unfolding of the individual compacted domains in the organic matrix.[99]

CHAPTER 3 ULTRASTRUCTURAL STUDY OF GASTROPOD MOLLUSK NACRE

3.1 INTRODUCTION

Nacre is a complex, multilayered biocomposite and the toughest constitutive layer of seashells. While composed of 95% of calcium carbonate, its work of fracture is an amazing 3000 times greater than the one of pure crystalline calcium carbonate (aragonite form). This characteristic has sparked considerable interest for nacre from researchers in the past decades, nevertheless many structural aspects of this material remain unclear owing to its complexity. Indeed, the structure of nacre consists in several hierarchical levels, spanning at least seven orders of magnitude in length. Here we focus on nacre from Gastropod Mollusk *Trochus niloticus* and *Haliotis rufescens* (commonly referred as Red Abalone) to try and unravel its intimate organization, with particular attention to the sub-micron scale.

Through the joint use of a variety of observations technique, we aim at gaining an overall understanding of how nacre's different components (mineral, organic and water) are organized together. Scanning Electron Microscopy (SEM) is a very suitable technique for the observation of the microstructure of nacre down to a few hundreds of nanometers. Tablet shape, dimensions and organization can be conveniently investigated, as well as microcracks in fractured samples and other phenomena occurring at this scale. For higher

resolutions we will resort to Atomic Force Microscopy (AFM), which can be conducted in nearly physiological condition. This technique not only yields qualitative information on the surface topography (Amplitude Tapping mode) and mechanical properties (Phase mode) but also quantitative data on the surface component dimensions (Deflection Tapping mode). It will enable accurate imaging of nanoasperities and nanograins or distinguish between softer/stickier zones (covered with the organic matrix) and harder (mineral) ones. Combined with nanoindentation, we will for instance be able to monitor the plastic response of specific submicron features. Transmission Electron Microscopy (TEM) is a powerful imaging technique with atomic resolution and will be used in association with electron diffraction to determine the crystalline characteristics of nanosized elements such as nanograins.

Chemical and physical characterization techniques such as porosimetry, density measurement, ash weighing, X-Ray and electron diffraction, Fourier Transform Infrared Spectroscopy (FTIR) and Raman spectroscopy complete this study and allow us to further develop our structural observations.

3.2 MATERIALS AND METHODS

3.2.1 SAMPLE PREPARATION

A structural and mechanical study of nacre imposes a few requirements on the choice of the shell specimen. Having chosen to study laminate columnar gastropod mollusk nacre for its – relative – simplicity, we then had to choose from the large pool of specimens featuring this type of nacre. Dimensions, availability and traceability led us to

pick Gastropod Mollusks *Trochus niloticus* and *Haliotis rufescens*, both large (< 4 in) seashells with thick prismatic and nacreous layers. *T. niloticus* is commonly found on the coasts of the Indian Ocean while *H. rufescens* is a common species on the US West Coast.

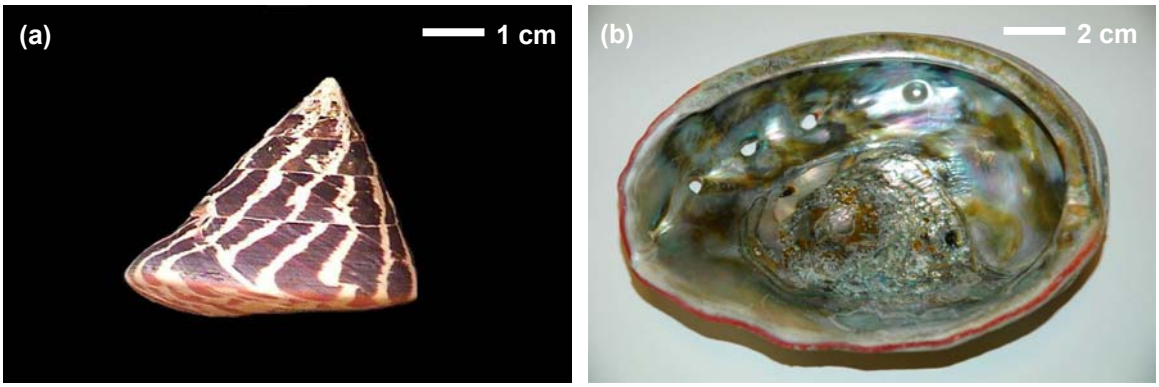

Fig. 3.1 Seashell specimens **(a)** *Trochus niloticus* **(b)** *Haliotis rufescens*.

Dry *T. niloticus* shell specimens were purchased from *Shell Horizons* (Clearwater, FL) and fresh *H. rufescens* specimens from *The Abalone Farm* (Cayucos, CA). The least destructive, minimum sample preparation procedures possible were employed including no alcohol dehydration, thermal or chemical treatment, embedding, or polishing. First, nacre from the inner layers shells was sectioned into parallelepipedal samples using a diamond impregnated annular wafering saw (*Buehler* Isomet 5000) running at 1000 rpm with constant phosphate buffered saline (PBS, pH8.0) irrigation. The samples of each series were cut from the same area of the same shell, to minimize variations due to age, history of the shell, etc. Care was taken to obtain parallel sides, plane layers by cutting where the curvature of the shell is minimal. The samples were then cleaned in reverse osmosis filtrated water for 10 seconds using an *Ultramet* ultrasonic cleaner.

The samples were then further processed according to three different protocols: “Cleaved” samples were observed within less than one hour after cleaving via uniaxial compression. “Hydrated” samples were immersed for several months in reverse osmosis filtrated water with 0.4221 mol/L NaCl, 0.011 mol/L KCl, pH = 7.1 in a hermetically sealed container at 20ºC, then uniaxially compressed and observed within less than one hour after cleaving. Desiccated samples were stored in an open container and were in contact with room air in 20ºC for several months.

Samples for nacre layer surface observation (view parallel to the aragonite c-axis) were produced by uniaxial compression (Fig. 3.2-a) using a Zwick mechanical tester (Model BTC-FR010TH.A50, 10 kN maximum load cell, 0.01 mm/min, ambient conditions). The externally applied load was oriented perpendicular to the aragonite c-axis, producing a clean intertablet cleavage (Fig. 3c). Samples for cross-sectional SEM imaging (perpendicular to the aragonite c-axis) were produced by 3-point bend (Fig. 3.2-b) using the same Zwick mechanical tester (0.1 mm/min, ambient conditions) where the

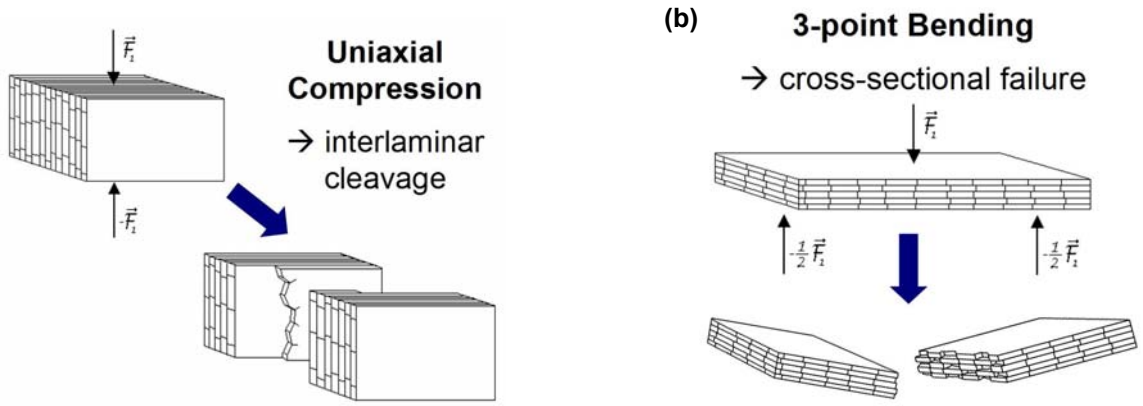

Fig. 3.2 Sample preparation protocols **(a)** interlaminar cleavage **(b)** cross-section fracture.

externally applied load was oriented parallel to the aragonite c-axis.

Cross-sectional samples that underwent etching were polished beforehand using a metallographic polishing wheel (*Buehler,* at ~100 rpm), a polishing cloth (*Buehler* Microcloth) and a water-based polishing suspension (*Buehler* Mastermet, colloidal silica, particle mean diameter ~60 nm). The RMS roughness of polished nacre sample was measured with an AFM and found to be consistently lower than 1 nm. Upon polishing samples were rinsed copiously with DI water and ultrasonicated in DI water for 10 s.

Ethylenediaminetetraacetic acid (EDTA, 0.5 M) etching removes the soluble part of the organic matrix as well as calcium carbonates crystallites and was applied for times ranging from 10 seconds to 1 hour. Cryofractured samples were plunged into liquid nitrogen and broken in several pieces using tweezers immediately upon withdrawal.

3.2.2 HIGH RESOLUTION IMAGING TECHNIQUES

Scanning Electron Microscopy. Samples were coated with 10 nm of Au-Pd and imaged using a *JEOL* SEM 6060 and a *JEOL* SEM 6320F. The working distance was 6-9 mm (SEM 6060) and 12-15 mm (SEM 6320F) and the sample plane was oriented perpendicular to the electron beam incidence. A 10-20 kV accelerating voltage was employed. Desiccated top view *T. niloticus* SEM samples were dried in ambient conditions 12 weeks prior to imaging. An environmental SEM (*Philips/FEI* XL30 FEG SEM) that allows for low vacuum electron detection in a water vapor environment using uncoated samples (electron acceleration ~ 15 kV, operating current ~ 42 μA, working distance ~ 11 mm, water vapor pressure ~ 0.4 Torr) was also employed to produce back-scattered electron microscope (BSE) images of cleaved samples.

Transmission Electron Microscopy. Certain samples were polished down to 100 um thickness, then slowly thinned using a ion polisher (Precision ion polishing system – PIPS 691, *Gatan Inc,* Pleasanton CA, 2.5 keV and angles 4° and 9°*),* while other were prepared using a focused ion beam system (*JEOL)*. They were imaged using a *JEOL* 2011 (at 200 keV) for general purpose and a *JEOL* 3010 (at 300 keV) for high resolution imaging.

Atomic Force Microscopy. Contact and tapping mode atomic force microscope (CMAFM and TMAFM, respectively) imaging in ambient conditions were employed to produce surface topographical images of freshly cleaved nacre samples. In ambient humidity, a thin layer of water (2 –10 Å thick) exists on the surface[99] yielding closer to physiological images than completely dried samples. A *Digital Instruments* (*DI*, Santa Barbara, CA) Multimode SPM IIIA was used with AS-130 "JV" or "EV" piezoelectric scanners. Contact mode scans were conducted with *Veeco* Si_3N_4 cantilevers (V-shaped with approximately square pyramidal probe tip geometry, tip half angle of ~35^o, cantilever length, l ~ 200 μm, nominal spring constant, k ~ 0.32 N/m, and nominal probe tip radius of curvature, R_{TIP} ~ 40 nm) and tapping mode scans with *Veeco* Si cantilevers (V-shaped with approximately square pyramidal probe tip geometry, tip half angle of ~17.5^o, l ~ 125 μm, k ~ 0.40 N/m, and R_{TIP} ~ 10 nm). A scan rate of 0.25-2 Hz using a maximum sample size of 512 x 512 pixels was employed at gains between 0.1-0.3. The drive amplitude and amplitude set-point were optimized upon tuning. The x- and y- scan directions were calibrated with a 10 x 10 μm^2 grid and the z-direction was calibrated with 5 nm diameter beads on a cleaved mica surface. The images to be shown report amplitude (i.e. cantilever oscillation amplitude) and phase (i.e. cantilever phase lag) for tapping

mode or deflection for contact mode (i.e. cantilever deflection). Amplitude and deflection both reflect of surface topography while phase mode is sensitive to many properties such as friction, adhesion, (visco)elasticity, and composition.

3.3 RESULTS

In the figures of this section, ⊙ indicates aragonite *c*-axis direction is approximately out of the page, ↑ indicates it is approximately parallel to the long side of the page.

3.3.1 PRISMATIC LAYER

While the prismatic layer is not the focus of this thesis, it is interesting to note certain characteristics of the prismatic layer, as it shares certain common aspects with the nacreous layer. For both seashells, the appearance of the cryofractured prismatic layer was very diverse (Fig. 3.3). In *H. rufescens* the cracks sometimes ran nearly straight, creating local planar cleavage (Fig. 3.3 a, b) and delimiting large faceted blocks of often larger than a hundred microns. In other places the crack path was more tortuous,

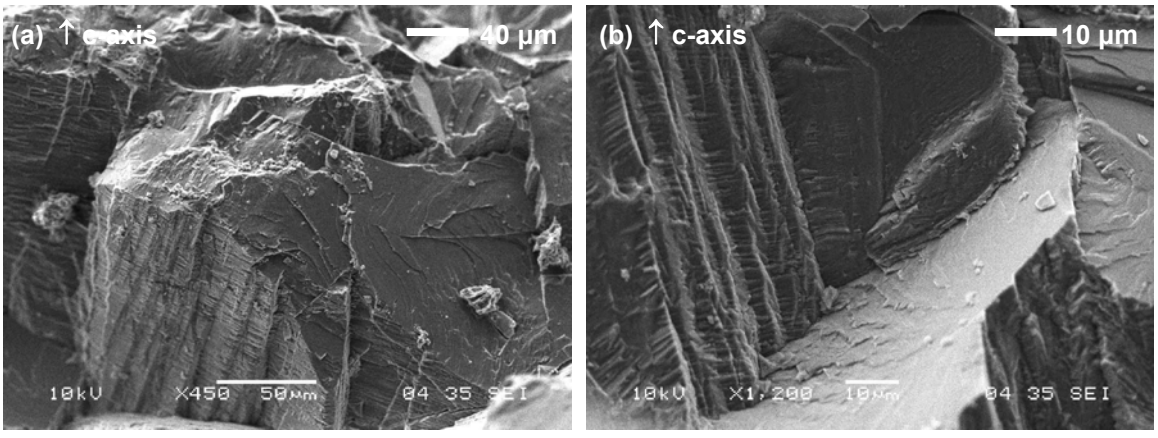

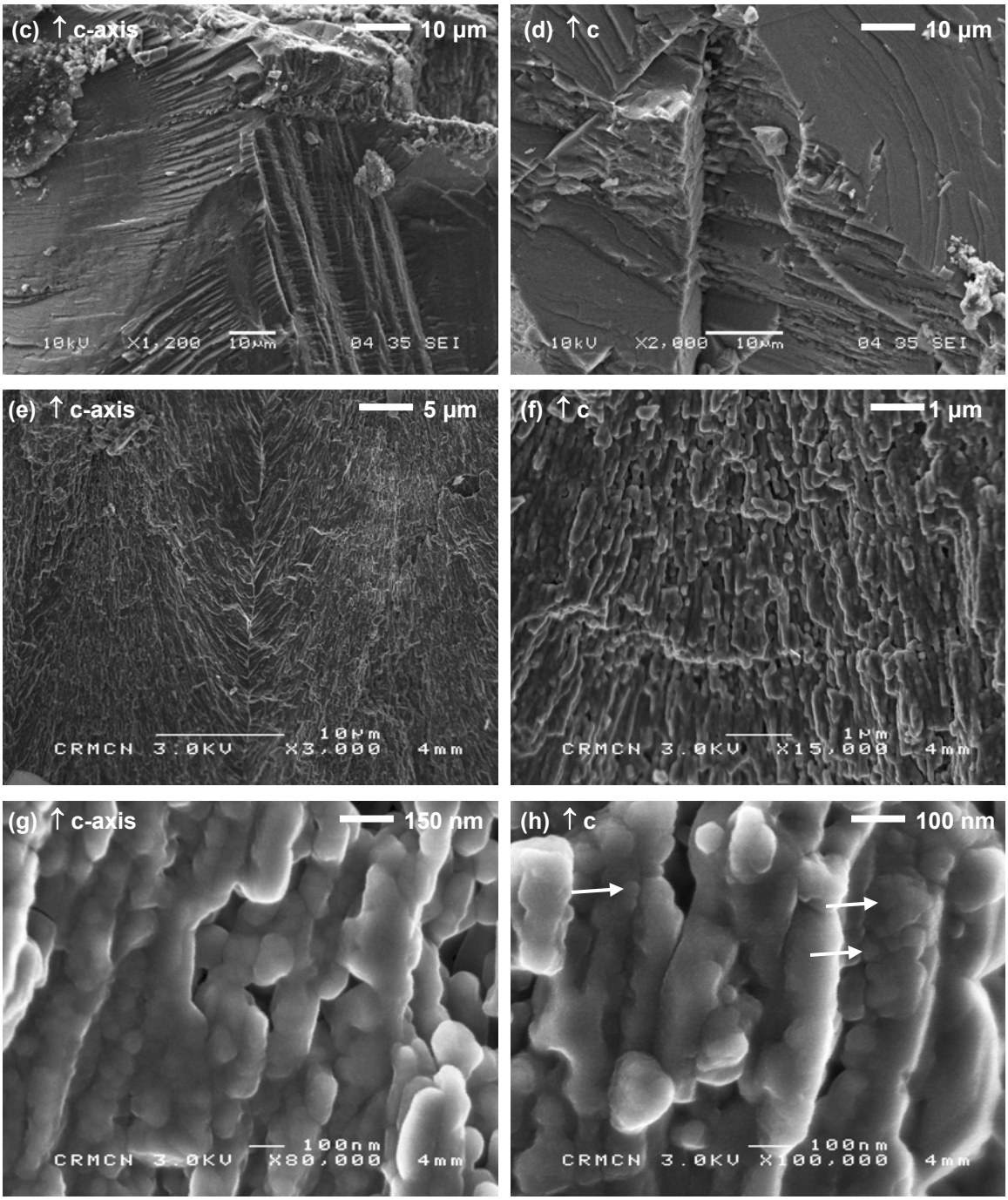

Fig. 3.3 SEM images of the cross-sectional surface of the prismatic layer of: **(a) to (d)** *H. rufescens*, fractured fresh **(e) to (g)** *T. niloticus*, cryofractured.

revealing substructures within the large calcite prisms (Fig. 3.3 c, d). In *T. niloticus*, the fracture surfaces were generally less jagged (Fig. 3.3 e), possibly because it was fractured

after cooling in liquid nitrogen, which render the fracture very brittle. Nevertheless, at higher magnification, the presence of additional levels of structure hierarchy was obvious (Fig. 3.3 f). The calcite prisms appear made of elongated rods (~ 1 μm long, 100 nm in diameter) of small rounded crystallites blended with organic material (Fig. 3.3 g), which give them a smooth appearance. The crystallites themselves appear to have a mean radius of 100 nm, but at certain locations it is clear that these nanograins might be subdivided further, with the smaller units having a diameter around 30 nm (arrows, Fig. 3.3 g).

3.3.2 PRISMATIC-NACREOUS TRANSITION

3.3.2.1 Optical Microscope

In cross-sectional view, optical microscopy can barely resolve (especially in reflection) the tablets because their thickness it about the value of visible light wavelength. On the other hand, calcite prisms are readily visible, in particular in cross polarized light, due to their varying crystalline orientation from one prism to another. Thus it can be seen that their width is of the order of a few microns to about hundred and their height ranges from about a hundred microns to several hundreds (Fig. 3.4 a).

The transition between prismatic and nacreous layer is rather abrupt and consists in a layer of aggregated crystallites with a ~ 5 μm diameter (Fig. 3.4 b, highlighted area). Interestingly, there is a ~ 30° angle between the calcite prisms and the aragonite columns long axes.

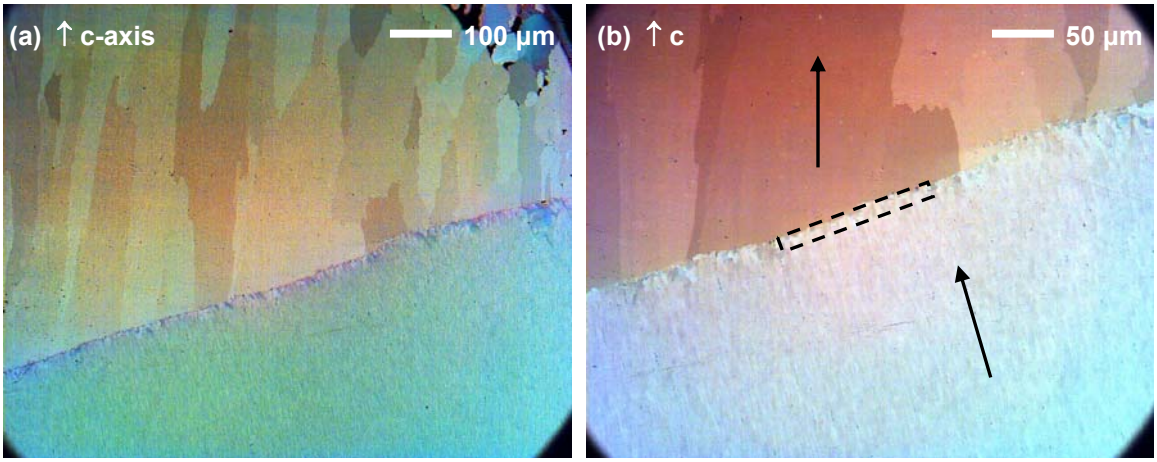

Fig. 3.4 Reflection optical images of the cross-sectional cryofractured surface of the prismatic layer of *T. niloticus*.

3.3.2.2 Scanning Electron Microscope

Differences between fracture surfaces of prismatic and nacreous layers are obvious on micrographs of the interface (Fig. 3.5). In *H. rufescens*, the calcite prism shape is distinguishable due to the crack often either running around or cutting through in a straight fashion (Fig. 3.5 a and b), creating a chaotic appearance at the length scale of a millimeter. Nacre seems somewhat smoother at this length scale, but at higher magnification the opposite becomes true (Fig. 3.5 c and d). At the length scale of a few microns, it is obvious that nacre locally deflects the crack path more efficiently than the prismatic layer. Based on Fig. 3.5 c, a quick calculation shows that approximately 5 times more surface is needed in *H. rufescens* nacre for the crack front to progress than in the prismatic layer. One can also notice the ~ 5 µm thick transition layer between the two, consistent with optical microscope observations (Fig. 3.4 b). The crystallites at this interface have also a distinct morphology from both prismatic and nacreous ones.

The picture is somewhat different in *T. niloticus* since the prismatic layer has a rougher appearance the microscale than in *H. rufescens*. However nacre still exhibits a more tortuous fracture surface (Fig. 3.5 e and f).

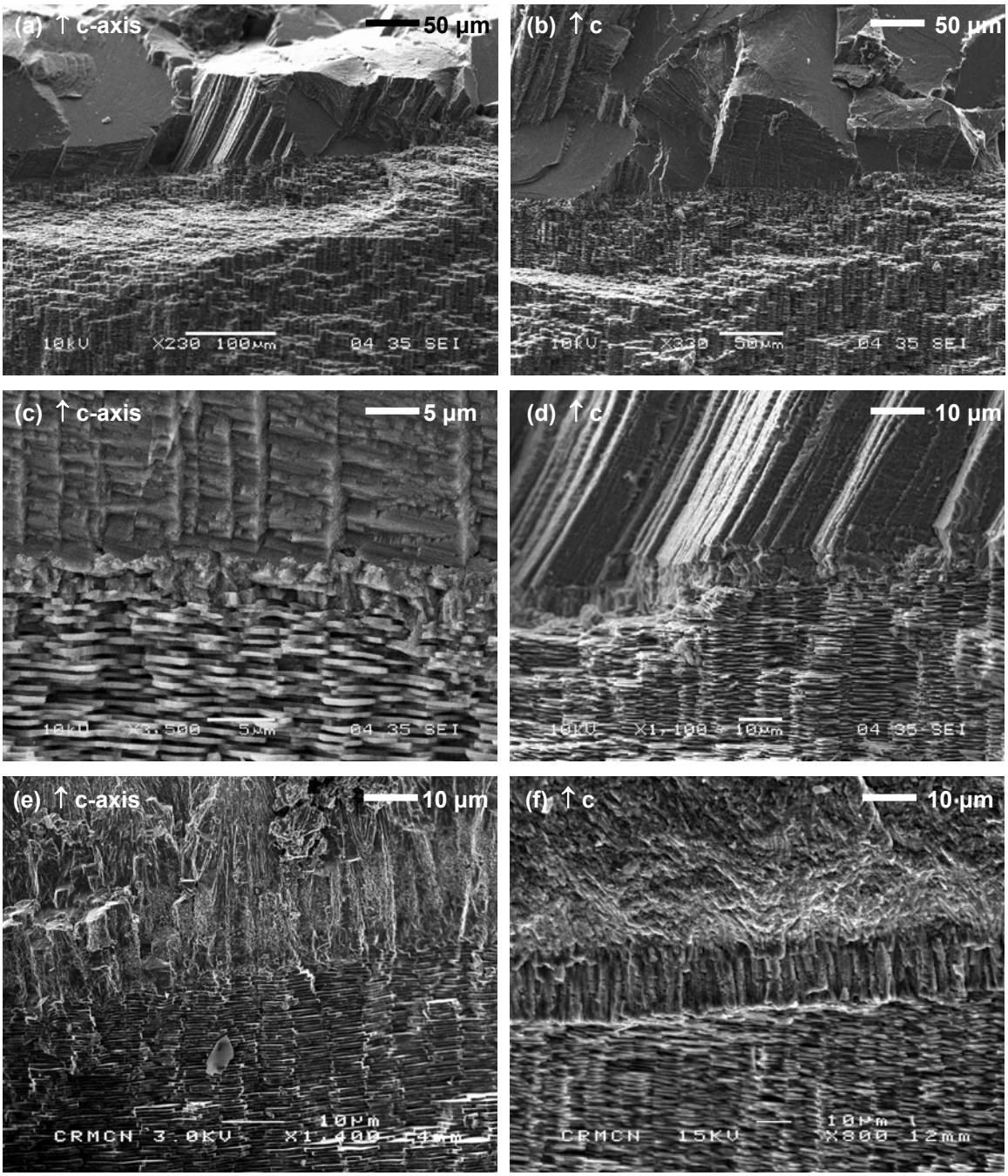

Fig. 3.5 SEM images of the cross-sectional fractured interface between the prismatic and nacreous layers of: **(a) to (d)** *H. rufescens*, **(e) to (f)** *T. niloticus*.

consistent with optical microscope observations (Fig. 3.4 b). The crystallites at this interface have also a distinct morphology from both prismatic and nacreous ones.

The picture is somewhat different in *T. niloticus* since the prismatic layer has a rougher appearance the microscale than in *H. rufescens*. However nacre still exhibits a more tortuous fracture surface (Fig. 3.5 e and f).

3.3.3 TABLET LAYERS SURFACE

This section presents the main features of tablet layers in-plane. Samples were prepared by uniaxiale compression fracturing, followed in certain case by polishing, etching or air drying.

3.3.3.1 Optical microscope

Nacre is well known for its beautiful iridescence, which in addition to its unique mechanical properties makes it a sought-after material for jewelry creation. It arises from the diffraction of light due to the periodic planar arrangement of the tablets, which as a fine grating.[100, 101] Optical microscopy is obviously a privileged means to observe these colorful patterns. Fig. 3.6 shows images of the top view of the plane perpendicular to the aragonite *c*-axis for a sample fractured in uniaxial compression). One can note the somewhat regular appearance of the cleaved surface in dry *T. niloticus* (Fig. 3.6 a), where gently descending and ascending stairs of plane tablet layers account for most of the morphology. Rehydrated samples surprisingly exhibit a much rougher surface, even though nacre's structural design (planar layers of flat tiles) does not seem to be able to

prevent crack propagation along the plane of the tablet. This is a hint at how well calibrated the interaction between the interlamellar organic glue and the tablet is when nacre is in its normal hydrated state, still promoting crack deflection in a structurally less

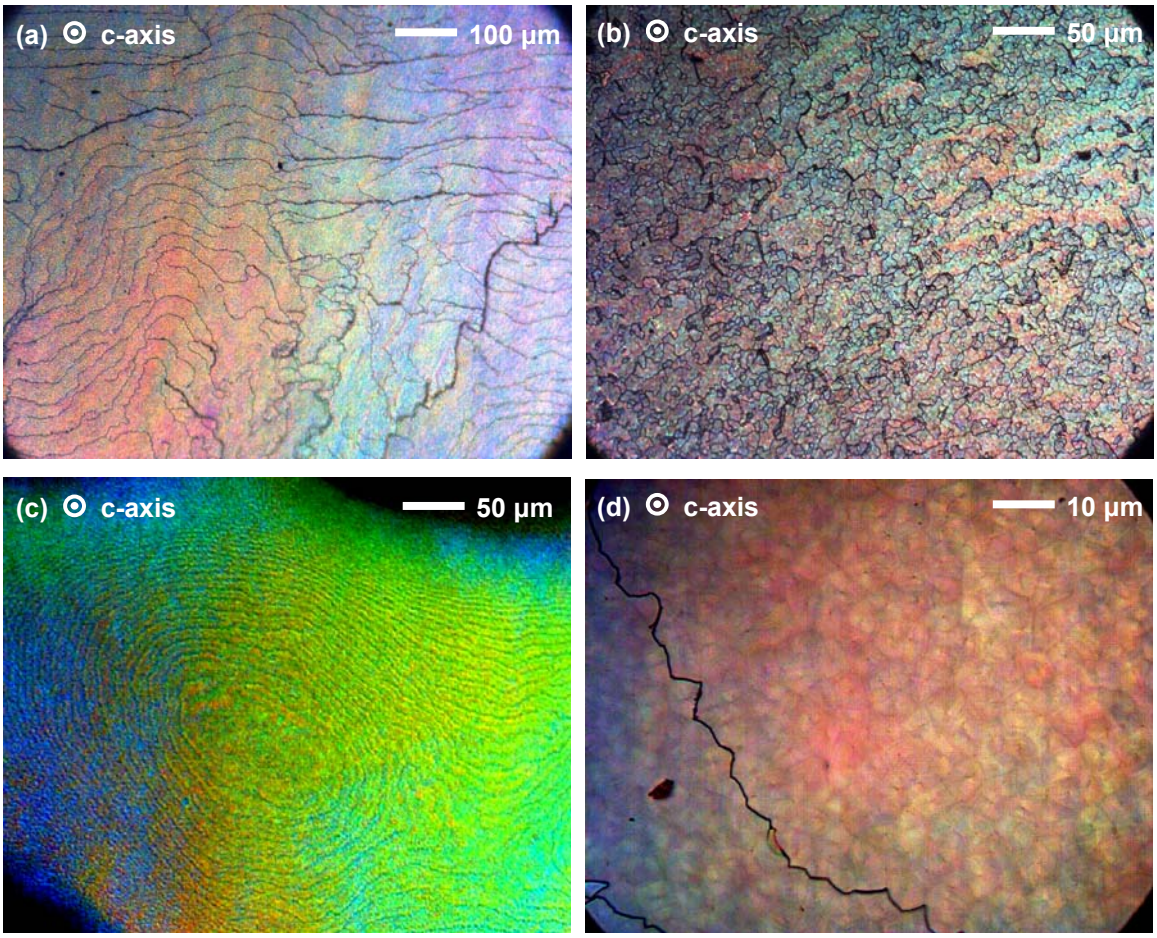

Fig. 3.6 Optical microscope images under cross polarized light of the cleaved surface of the nacre layer of **(a)** dry *T. niloticus* shell, **(b)** rehydrated *T. niloticus* shell, **(c)** polished *H. rufescens* **(d)** dry *T. niloticus* with tablets apparent.

advantageous configuration with regard to fracture resistance. Fig. 3.6 c shows that the tablet layers are still distinguishable after careful polishing, even though the actual steps are smaller than 50 nm (measured by AFM).

Even at smaller length scale, the somewhat changing planar thickness of individual tablets (see Fig. 3.11) is responsible for a locally varying light retardation

which leads to interesting color effects, allowing one to distinguish the outline of single tablets (Fig. 3.6 c).

3.3.3.2 Scanning Electron Microscope

Owing to their remarkable smoothness (local RMS roughness of the order of 6 nm as measured by AFM) and unique interfacial cohesion, little can be distinguished on simply cleaved nacre surfaces besides the ledge of tablet layers (Fig. 3.7 a and b). Letting the sample desiccate in air for several months enables clear visualization of the tablet boundaries, center biomineralization nucleation sites, and fracture within individual tablets (presumably along the intratablet crystalline sector boundaries[31]) most likely due to macromolecular shrinkage upon dehydration (Fig. 3.7 c and d). Image analysis yielded a maximum lateral tablet dimension (perpendicular to the aragonite *c*-axis) of 7.9 ± 1.7 μm for *T. niloticus* and 6.4 ± 1.5 μm for *H. rufescens*. The "±" symbol here and henceforth refers to one standard deviation.

In Fig. 3.7 e and f, the samples were soaked upon cleavage in EDTA 0.5 M for 20 min. Such a treatment induces partial decalcification of the upper layers (along with dissolution of certain components of the organic phase), resulting in thinned tablets. Prolonging the treatment over several days eventually leads to complete demineralization

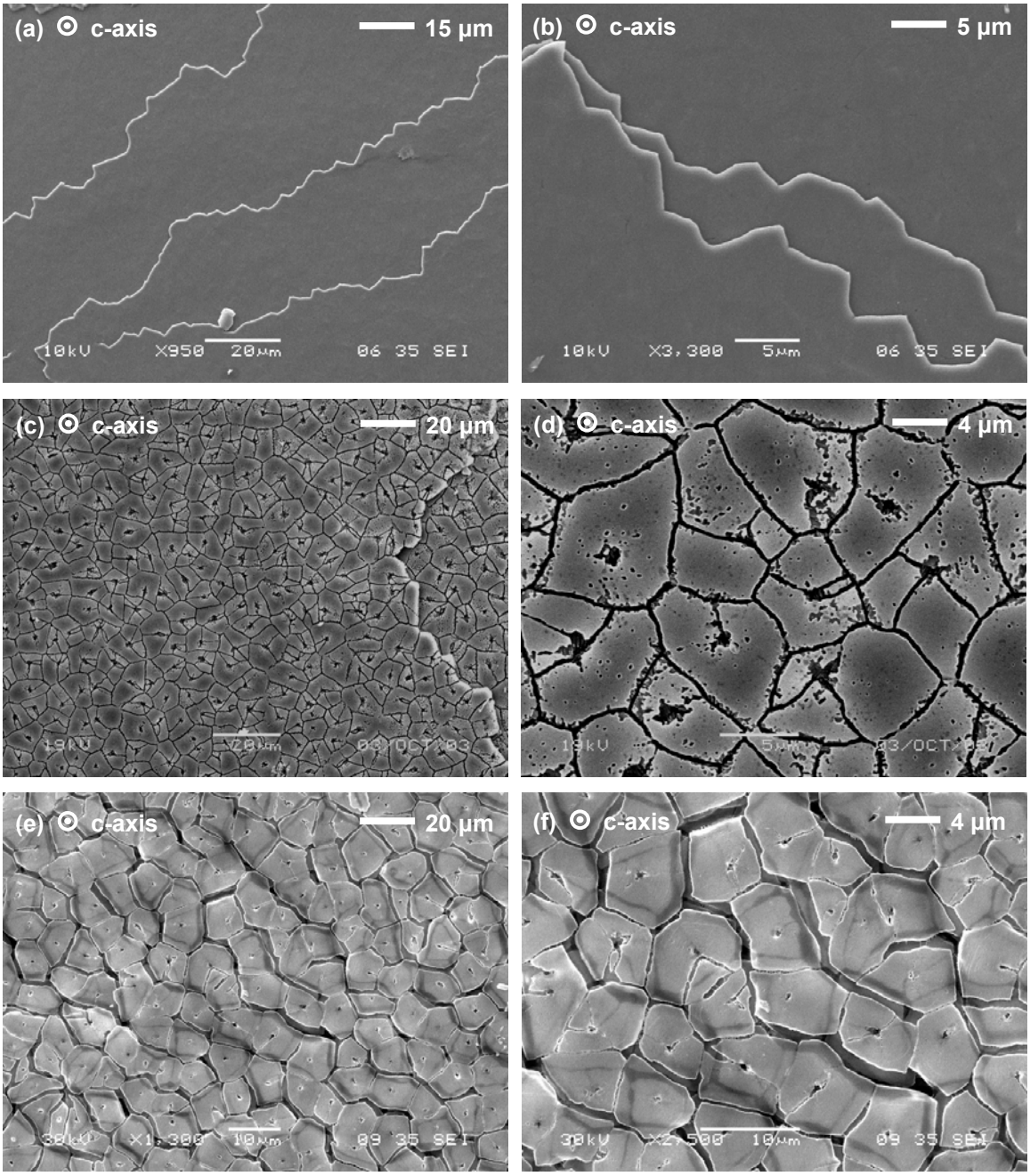

Fig. 3.7 SEM images of the cleaved surface of the nacre layer of **(a,b)** fresh *H. rufescens*, **(c,d)** desiccated *T. niloticus*, **(e,f)** *T. niloticus* immersed in EDTA 0.5 M for 20 min, allowing to distinguish both the top layer and the one underneath.

of the sample. By using a high electron acceleration voltage (30 kV), one can readily see through the semi-transparent top tablet layer and distinguish the underlying layer.

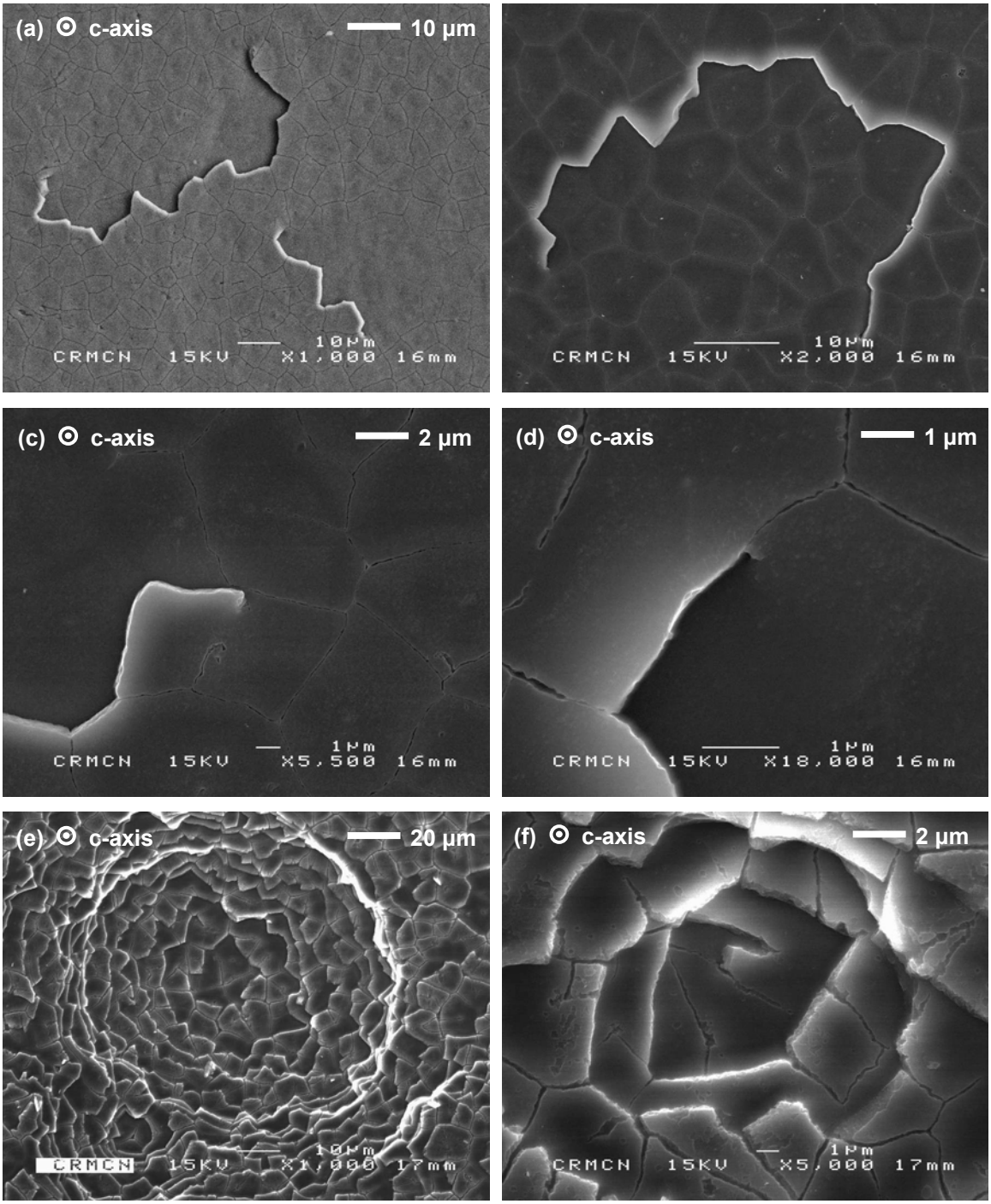

Fig. 3.8 SEM images tablet spirals on the cleaved surface of the nacre layer of *T. niloticus*. **(a)** after sonication in sodium hydroxide for 5 min **(b) to (d)** after sonication in DI water. **(e,f)** Spiral patterns apparent on the surface after sonication of the samples in EDTA 0.5 M.

Notably, it appears that the nucleation centers accurately overlap between the two layers, and that while directly superimposed tablets exhibit some similarities in shape and area, their boundaries are also rather consistently offset.

Among the noteworthy features of nacre layers is the presence of “screw dislocations” interconnecting successive tablet layers (Fig. 3.8 a and b), which occur when layers on top of each other share the same bridging tablet (Fig. 3.8 c and d). Their planar density was calculated to be about 44 per square millimeter, or 1 every ~ 800 tablets. Sonication in ethylenediaminetetraacetic acid revealed 3D spirals composed of these continuous tablet "screw dislocations" (Fig. 3.8 e and f).

3.3.3.3 Atomic Force Microscope

Fig. 3.9 shows a top view (plane perpendicular to the aragonite *c*-axis) contact mode AFM deflection image of the surface of tablets produced by cleavage in uniaxial

Fig. 3.9. Contact mode deflection atomic force microscopy (AFM) image of top down view of inner laminate columnar nacre of *T. niloticus* nacreous layer fractured in uniaxial compression 30 μm scan.

compression. The nucleation site is well apparent at the center of most tablets. Boundaries can be distinguished by the vertical topographical shift that occurs at their level. Thanks to the very high z-resolution of AFM, it can be seen that the tablets do have uneven surfaces, with the center of tablets often appearing slightly lower than their more outer parts.

3.3.4 TABLET COLUMN CROSS-SECTION

3.3.4.1 Optical Microscope

Another interesting characteristic of nacre is its birefringence at the microscale. This property arises from the anisotropic nature of single aragonite crystals, which are the main constituents of the nacreous tablets. Light will travel at different speeds depending on the orientation of its polarization with regard to the different crystalline axes of the material. Use of a retardation plate in a microscope allows one to observe the relative delay in polarized light before and after traversing the sample by comparison with a color scale. Here, since the c-axis is aligned with the polarization plane, slight change in c orientation causes a local change of color. It should be noted that varying thickness also creates a delay in the light path and hence a color change.

In the nacre beveled thin section shown in Fig. 3.10, the main color fringes parallel to the sample edge are the result of the regularly increasing thickness from the edge inward. Within the fringes however, and particularly along the edge, the lateral variations of color are related to local changes of the c-axis orientation of the tablets. Hence it can be seen that certain columns possibly exhibit vertical domains of 5 to 20 tablets with a common crystalline orientation (white arrow), while on the contrary other

have succession of tablet with alternating orientation (black arrow). Neighboring tablets often have different crystalline orientations. Columns appear as having a spindle shape when their axes are not exactly parallel to the surface of the sample or change slightly along the column (for instance if the nucleation sites are offset little by little).

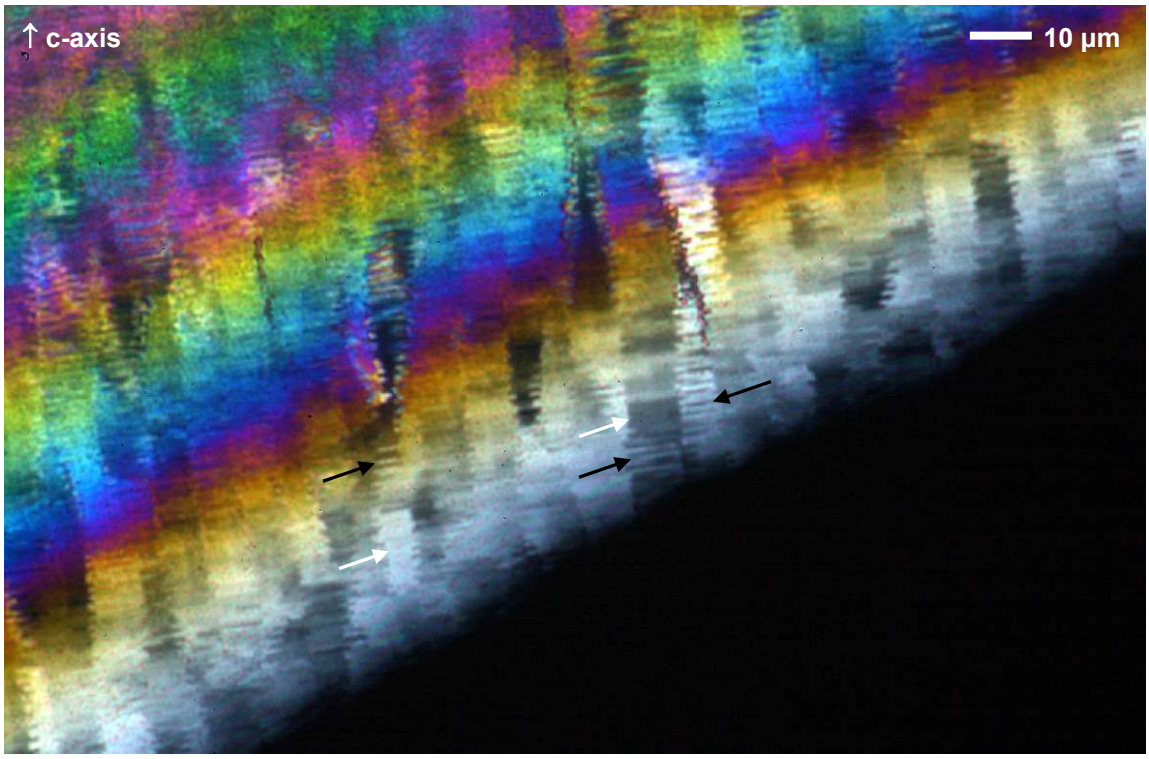

Fig. 3.10 Optical images under cross polarized light of a thin section (ion milled) of *T. niloticus* nacre layer. *Image by A. Baronnet*.

3.3.4.2 Scanning Electron Microscope

Fig. 3.11 shows SEM images of nacre samples fractured in 3-point bending (aragonite *c*-axis orientation is vertical) and reveals a regular microstructure consisting of planes of tablets stacked in the aragonite *c*-axis direction where the tablets are staggered with respect to one another from plane to plane. Image analysis yielded a tablet thickness (parallel to the aragonite *c*-axis) of 0.92 ± 0.21 µm for *T. niloticus*, 0.42 ± 0.11 µm for *H.*

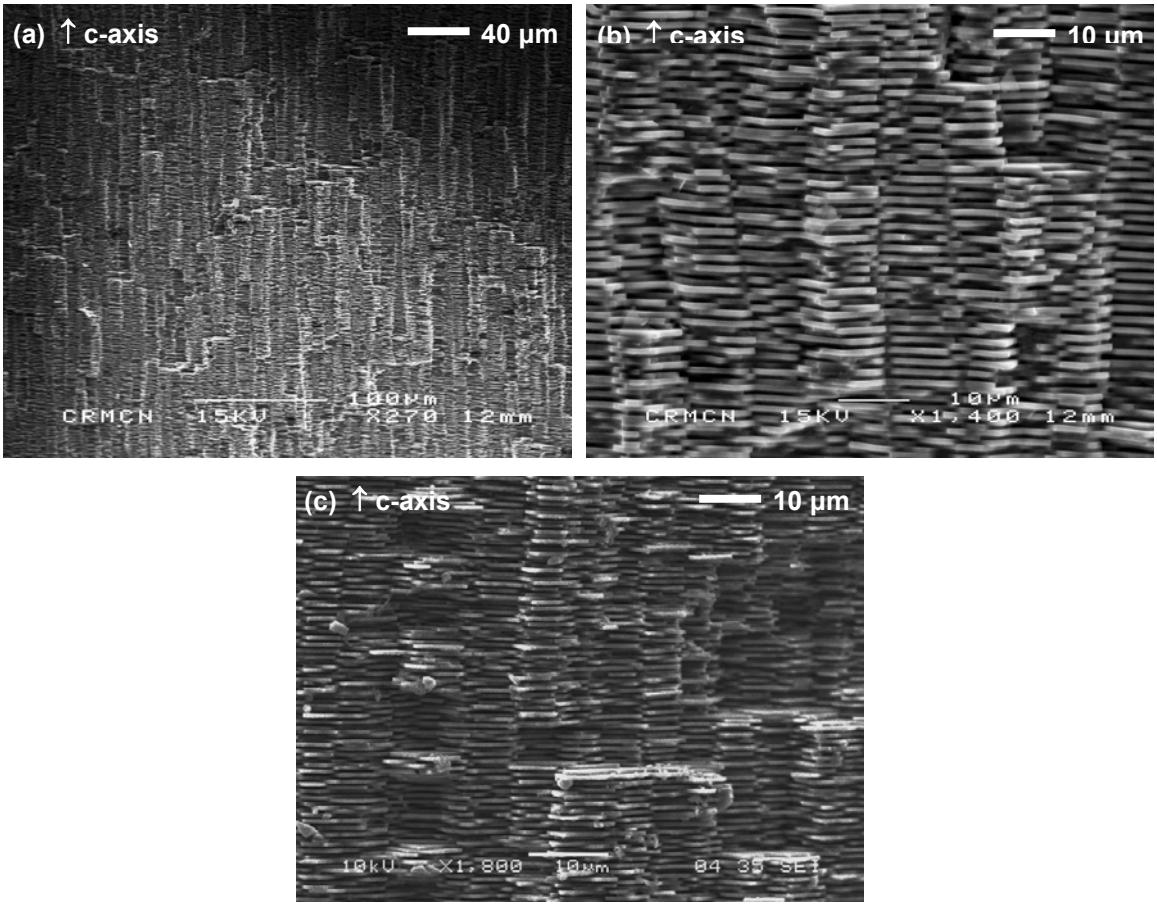

Fig. 3.11 SEM images of the fractured cross-section of the nacre layer of **(a,b)** *T. niloticus*, **(c)** fresh *H. rufescens*.

rufescens. In both seashells, the crack morphology reveals a very regular vertical stacking of the tablets as well as a quasi-periodic interdigitation of adjacent columns. This is particularly striking in Fig. 3.11 b, where the alternation of grey bands (tablet edge) and black bands (empty space left by the extraction of adjacent tablets) is binary in most locations. One can also recognize the bulkier format of tablets from *T. niloticus* (Fig. 3.11 b) compared with *H. rufescens* (Fig. 3.11 c).

3.3.4.3 Transmission Electron Microscope

TEM is ideal for a precise evaluation of local variation of the tablet thickness. In Fig. 3.12, a nacre sample has been polished along its cross-section using mechanical grinding followed by ion milling (is responsible for the faint diagonal grooves). While the average thickness is rather constant from one tablet to another, a local waviness (white arrows) can be observed.

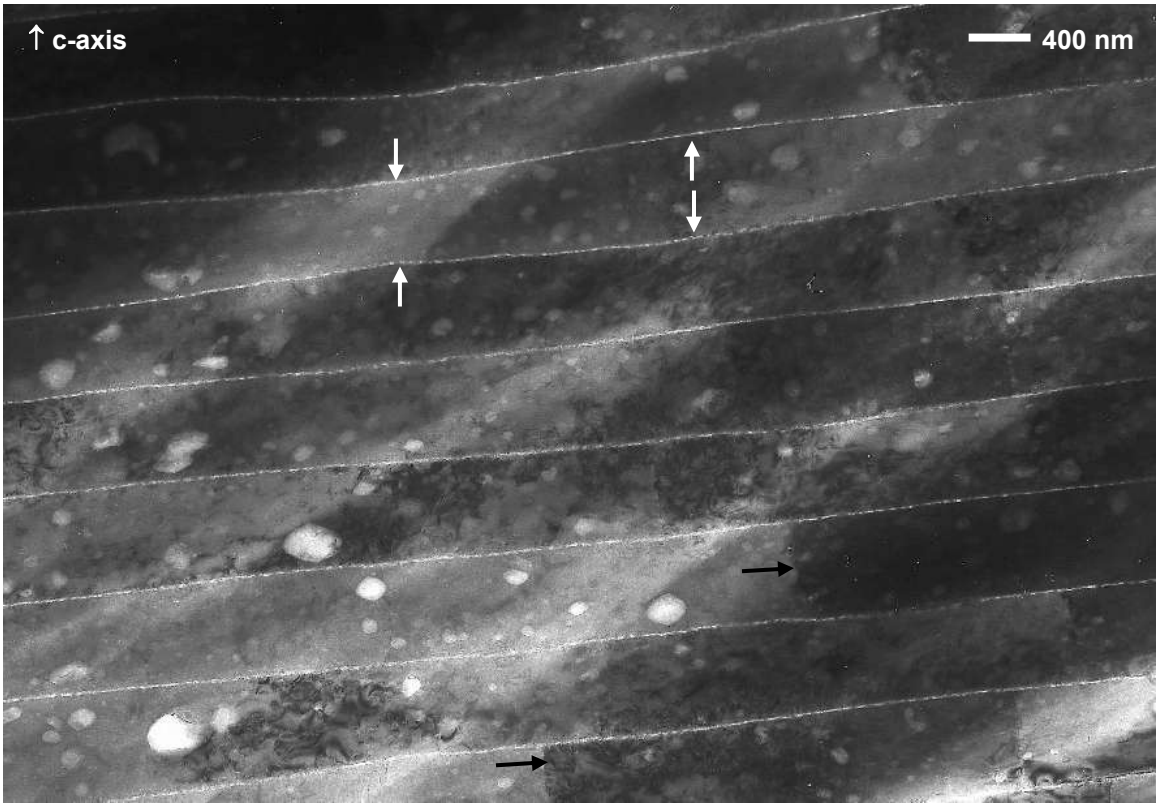

Fig. 3.12 TEM image of the ion polished cross-section of the nacre layer of *T. niloticus*. *Image by A. Baronnet*.

The many rounded vacuoles are believed to be etch pits possibly caused by reactivity of this extremely thin area (around a few nanometers) and the ambient moisture when the sample is transported from the ion milling instrument to the TEM chamber.

3.3.5 INTERLAMELLAR ORGANIC MATRIX

3.3.5.1 Scanning Electron Microscope

As can be seen on previous SEM images of the untreated nacre structure, the intimate blending of mineral and organic phase and the scarcity of the latter in nacre makes it difficult to directly image the organic matrix. EDTA etching for 20 min locally disrupts the planar arrangement of the tablets (by possibly releasing residual stresses in the

structure) and allows the observation of stretched filaments of insoluble organic matrix

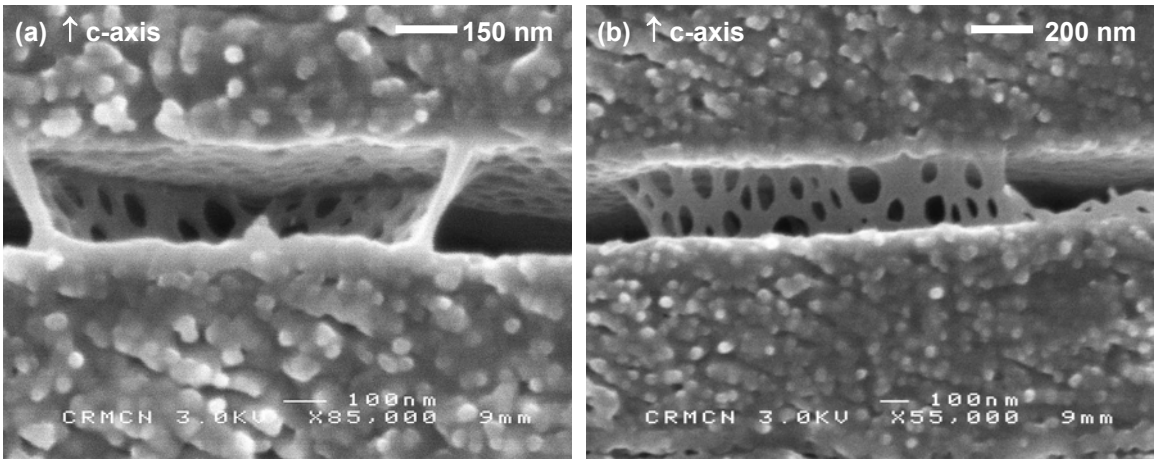

Fig. 3.13 SEM image of the etched cross-section of the nacre layer of *T. niloticus* (EDTA 0.5 M, 1 min sonication).

bridging vertically adjacent tablets (Fig. 3.13). It is also interesting to note the nanoscale texture of the tablet cross-section, though some of it is likely due to local recrystallization of the aragonite upon removal of the sample from the EDTA solution.

3.3.6 INTERTABLET ORGANIC MATRIX

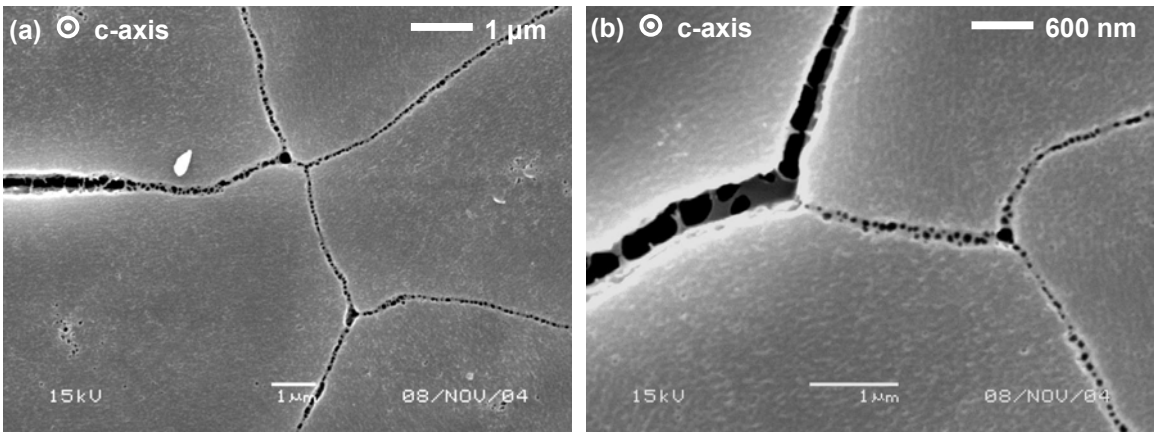

Fig. 3.14 SEM image of the etched cleaved surface of the nacre layer of *T. niloticus* (EDTA 0.5 M, 1 min soaking).

The intertablet organic matrix can also be observed when the cleaved surface is subjected to a quick EDTA etching (Fig. 3.14). As is the case for interlamellar matrix, thin stretched ligaments appear to bridge neighboring tablets.

3.3.7 SINGLE TABLET SURFACE

3.3.7.1 Scanning Electron Microscope

Fig. 3.15 reveals the nanoscale roughness of the tablet surface after quick sonication of the cleaved surface in DI water. Preferential decalcification at the tablet interfaces reveals the presence of intertablet organic material, while the tablet tops exhibit a rather regular roughness constituted of a small rounded asperities.

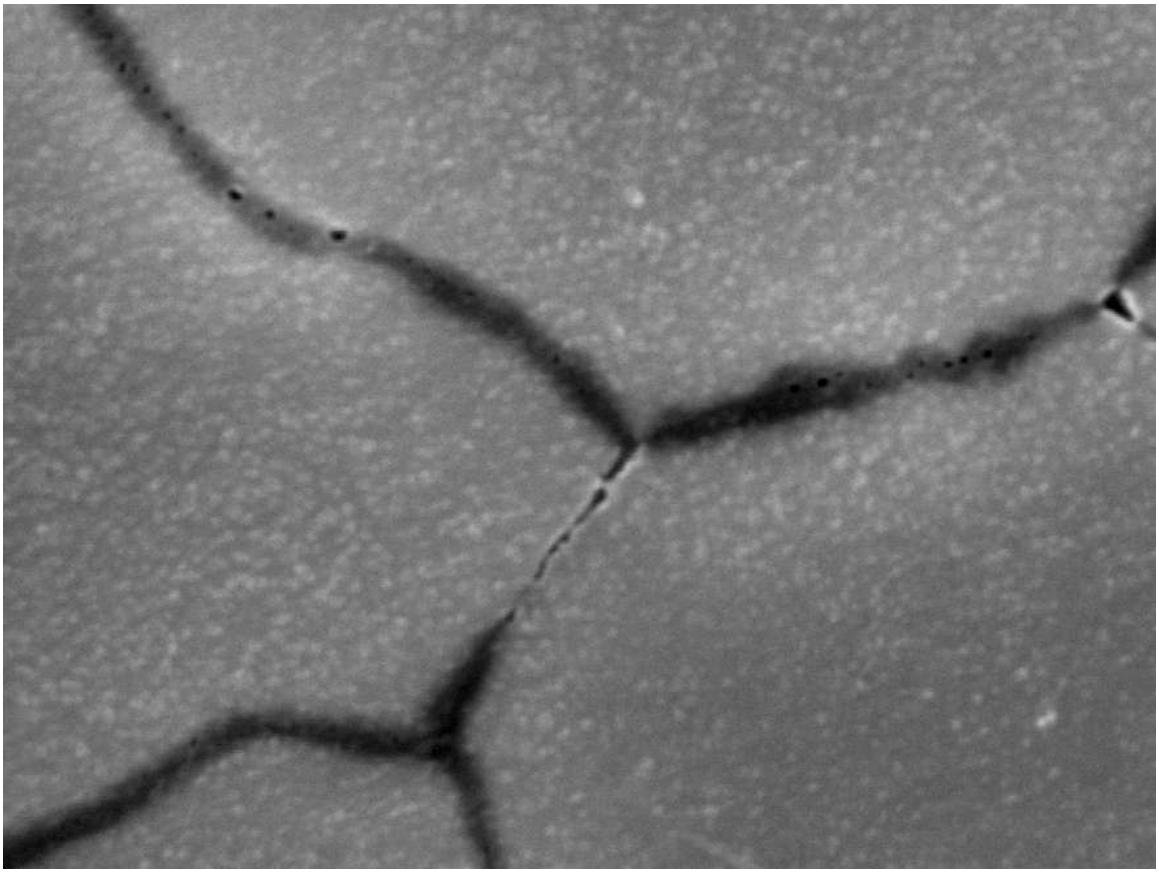

Fig. 3.15 SEM image of the etched cleaved surface of the nacre layer of **(a)** *T. niloticus* (DI water, 30 min soaking).

3.3.7.2 Atomic Force Microscope

Fig. 3.16 a shows a top view (plane perpendicular to the aragonite *c*-axis) contact mode AFM deflection image of the surface of an individual nacre layer produced by recent cleavage in uniaxial compression. Confirming the observation from Fig. 3.16, the surface of individual tablets possesses surface roughness due to topographical features

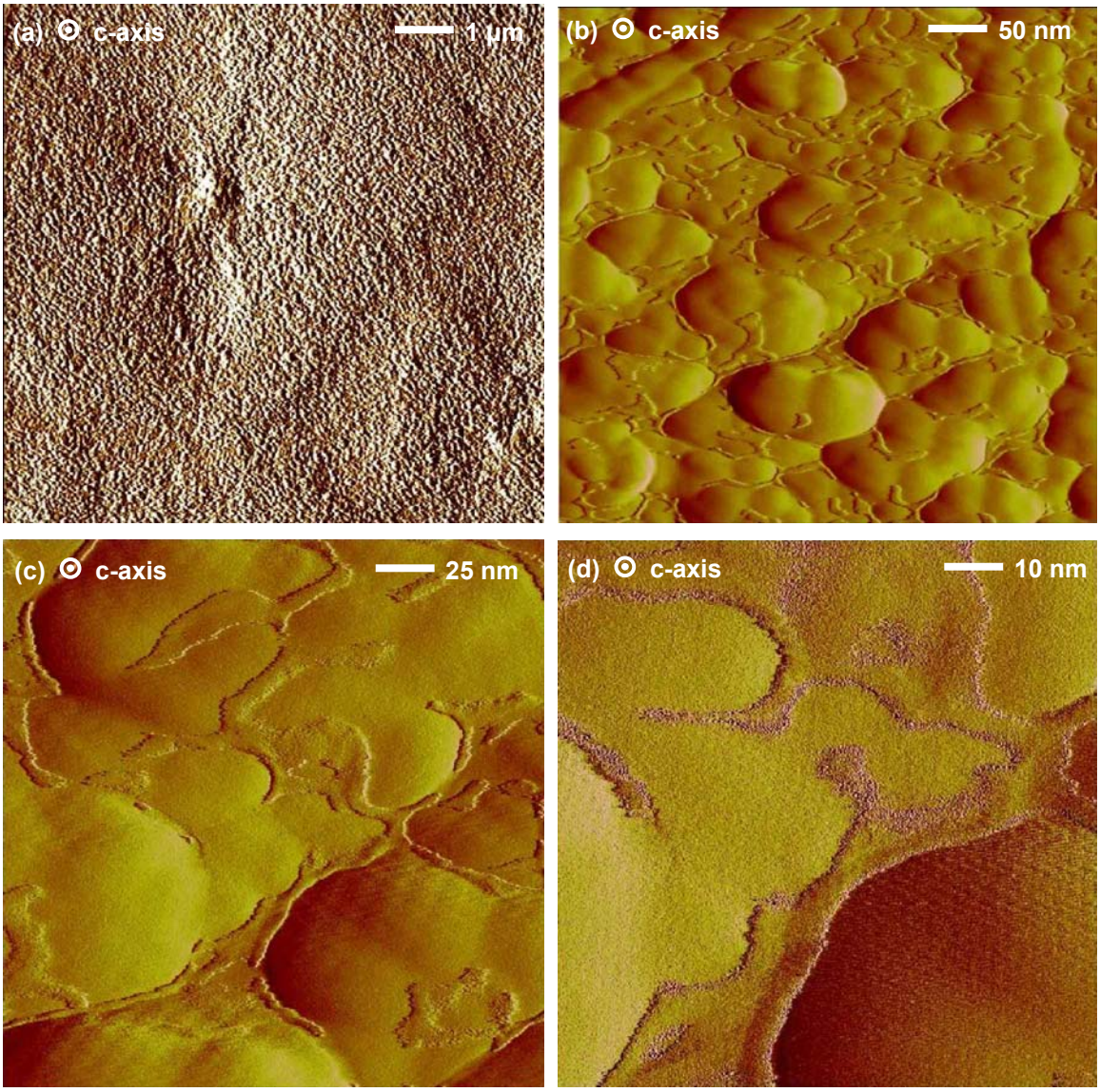

Fig. 3.16 AFM images of top down view of inner laminate columnar nacre of *T. niloticus* nacreous layer fractured in uniaxial compression **(a)** Contact mode deflection 10 μm scan, **(b)** Tapping mode amplitude image of nanoasperities and organic matrix on the top of an individual nacre tablet of *T. niloticus,* 500 nm scan **(c)** 200 nm scan, and **(d)** 100 nm scan.

(which we identify as "nanoasperities") and a central nucleation site which is ~ 500 nm large and ~ 40 nm high. The tablet boundaries are less distinguishable than those observed by SEM for the air-dried samples (Fig. 3.7 c and d), most likely due to the more hydrated organic component keeping the tablets in closer contact. A higher resolution

tapping mode AFM amplitude image (Fig. 3.16 b) enables direct visualization of the fine details of the nanoasperities on an individual nacre tablet and corresponding height images yield values of 109.9 ± 37.4 nm in maximum lateral dimension perpendicular to the aragonite *c*-axis and 7.4 ± 3.2 nm in peak-to-valley height parallel to the aragonite *c*-axis. Each nanoasperity is observed to actually be composed of an assembly of smaller nanoasperities (previously referred to as nanograins[23]) that are 28.0 ± 11.9 nm in maximum lateral dimension. Fig. 3.16 c and d show further magnified TMAFM amplitude images perpendicular to the aragonite *c*-axis, capturing the resolution of the individual smaller nanoasperities. Here, organic coils are directly visualized on top of

Technique	Feature	Mean ± Standard Deviation
SEM	nacre table thickness (// to *c*-axis)	0.9 ± 0.2 μm
SEM	nacre tablet maximum dimension (⊥ to *c*-axis)	7.9 ± 1.7 μm
TMAFM	maximum dimension of small nanoasperities (⊥ to *c*-axis)	28.0 ± 11.9 nm
TMAFM	maximum dimension of larger clusters of nanoasperities (⊥ to *c*-axis)	109.9 ± 37.4 nm
TMAFM	nanoasperity assembly height (// to *c*-axis)	7.4 ± 3.2
TMAFM	polymer width (⊥ to *c*-axis)	8.8 ± 5.6 nm
TMAFM	polymer end-to-end length (⊥ to *c*-axis)	52.1 ± 37.5 nm
TMAFM	polymer height (// to *c*-axis)	0.96 ± 0.25 nm

Table 1. Features observed in SEM and AFM images (number of data points for each feature, $n > 20$)

the nacre tablets and are measured to have a mean width of 8.8 ± 5.6 nm, end-to-end length of 52.1 ± 37.5 nm, and height of 0.96 ± 0.25 nm. The organic component appears to be primarily localized within the valleys of the nanoasperities. Table 1 summarizes the

means and standard deviations corresponding to morphological features discussed measured using SEM and AFM for *T. niloticus*.

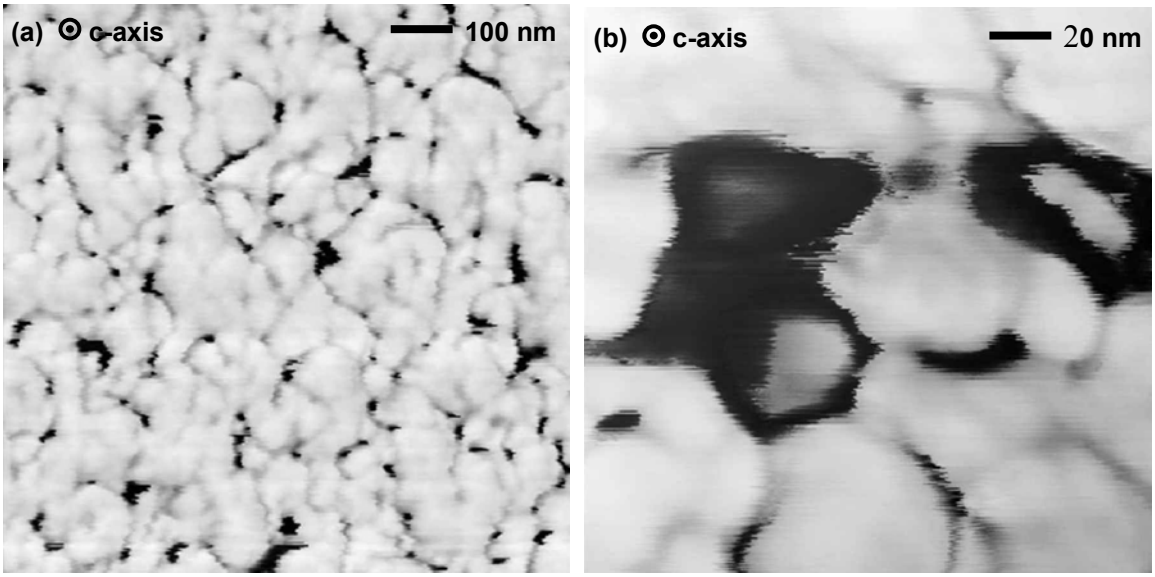

Fig. 3.17 Tapping mode phase atomic force microscopy images of nanoasperities and organic matrix on the top of an individual nacre tablet of *Trochus niloticus* that was freshly cleaved in uniaxial compression; **(a)** 1 μm scan, phase shift from -124º (darker) to +28º (lighter) **(b)** 200 nm scan, phase shift from -105º (darker) to +64º (lighter).

Fig. 3.17 shows TMAFM phase images of similar regions as that shown in Fig. 3.17 c and d. Contrast in these images is sensitive to variations in surface properties such as friction, adhesion, (visco)elasticity, and composition. Fig. 3.17 clearly demonstrates the presence of two different types of materials. Darker areas correspond to a greater cantilever lag and larger energy dissipation and hence, support the previous identification (via height images) of the organic component (dark areas) and the nanoasperities (lighter areas).

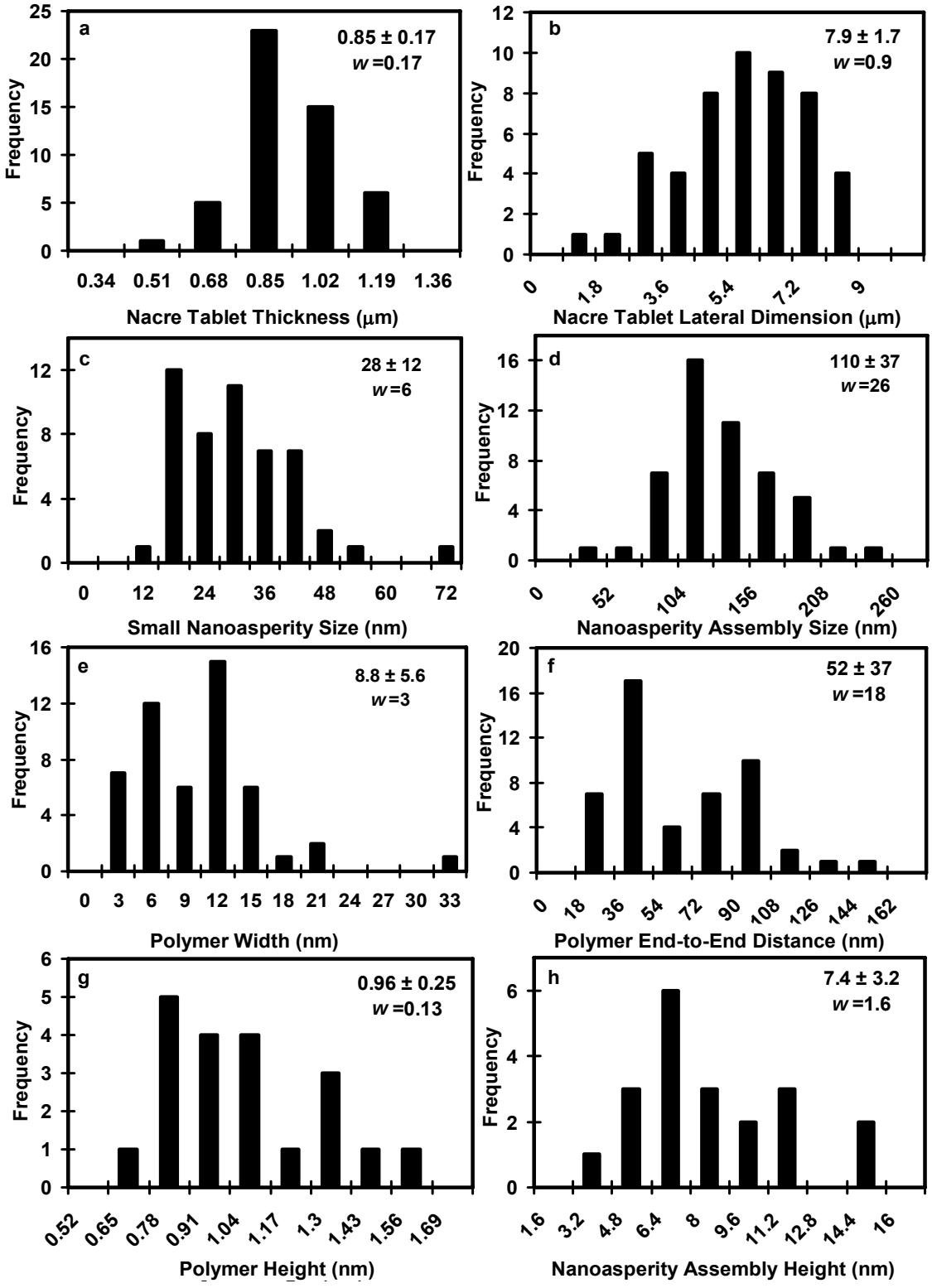

FIG. 3.18. Histograms of various features observed by SEM (a,b) and AFM (c-h); the inset of numerical values indicates mean ± standard deviation for each dataset, *w* is the

bin width (chosen based on Sturges' and Scott's rules[102, 103]), and the number of data points for each histogram > 20.

3.3.7.3 Transmission Electron Microscope

High resolution TEM allows the direct visualization of the crystalline lattice. In Fig. 3.19, the small black dots thus are the lattice nodes. This top view of an ion-thinned tabled from *H. rufescens* contains a lot of information. First, planar defects (oriented

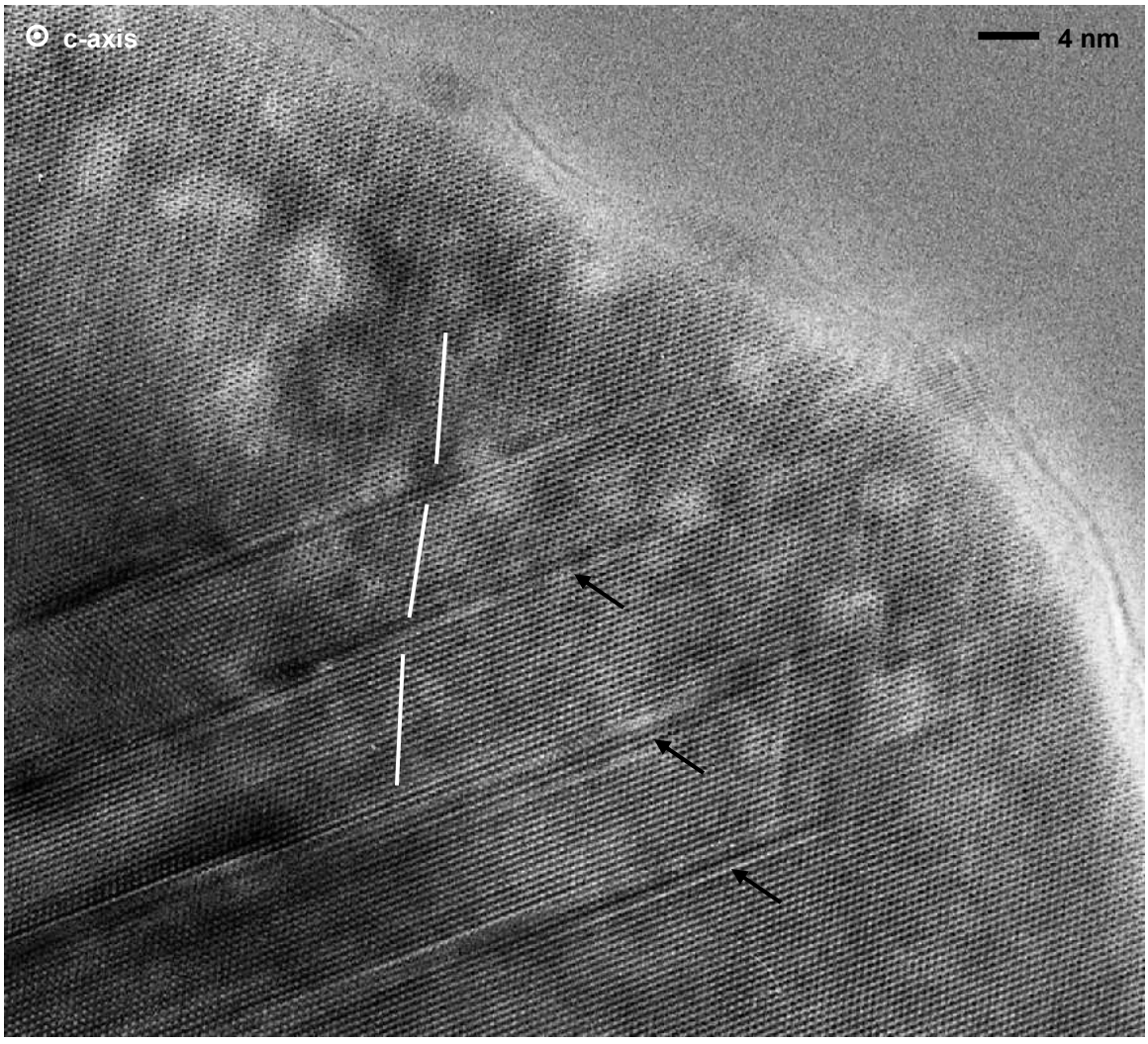

Fig. 3.19 TEM image of an ion-thinned tablet piece from *H. rufescens* (top view, parallel to c-axis) showing planar lattice defects and twinned nano-lamellae (white lines). *Image by A. Baronnet*.

perpendicularly to the page) can be seen running from the bottom left of the image toward its center (black arrows). They sometimes encompass twinned lamellae (the white lines show the slight deviation of the lattice rows crossing the twinning plane). The fact that the planar defects run without interruption implies that no grain boundary is present, an observation that was consistent in all the TEM micrographs. This tends to show that the crystalline lattice is continuous through the tablet, rather than discretized by nanograin boundaries.

3.3.8 SINGLE TABLET CROSS-SECTION

3.3.8.1 Scanning Electron Microscope

While etching of samples before observation is a common technique to reveal substructures, it also creates artifacts such as partial recrystallization on the surfaces exposed to the chemicals. Cryofracturation allows very brittle fracture to occur in materials, thus inducing minimum deformation to the surface. As can be seen in Fig. 3.20, both techniques produce surfaces with rather different aspects. Cryofractured nacre tablets (Fig. 3.20 a to c) exhibit a wide variety of morphologies even in adjacent tablets, from smooth cleavages (Fig. 3.20 a, white arrow) to much rougher textures (black arrow). Fig. 3.20 b offers a more faceted appearance, while Fig. 3.20 c shows a roughness of the order of 20-100 nm. In Fig. 3.20 d, the nacre cross-section has been sonicated in EDTA (0.5 M) for 2 min. It exhibits tiny globules with sizes again ranging from 20 to 100 nm. Image 2.20 e features what is probably a large defect in the nacreous structure, where a hole with dimensions of a few tens of microns has not been mineralized. It is interesting the compare the surface of the polished then sonicated in DI water main surface with the

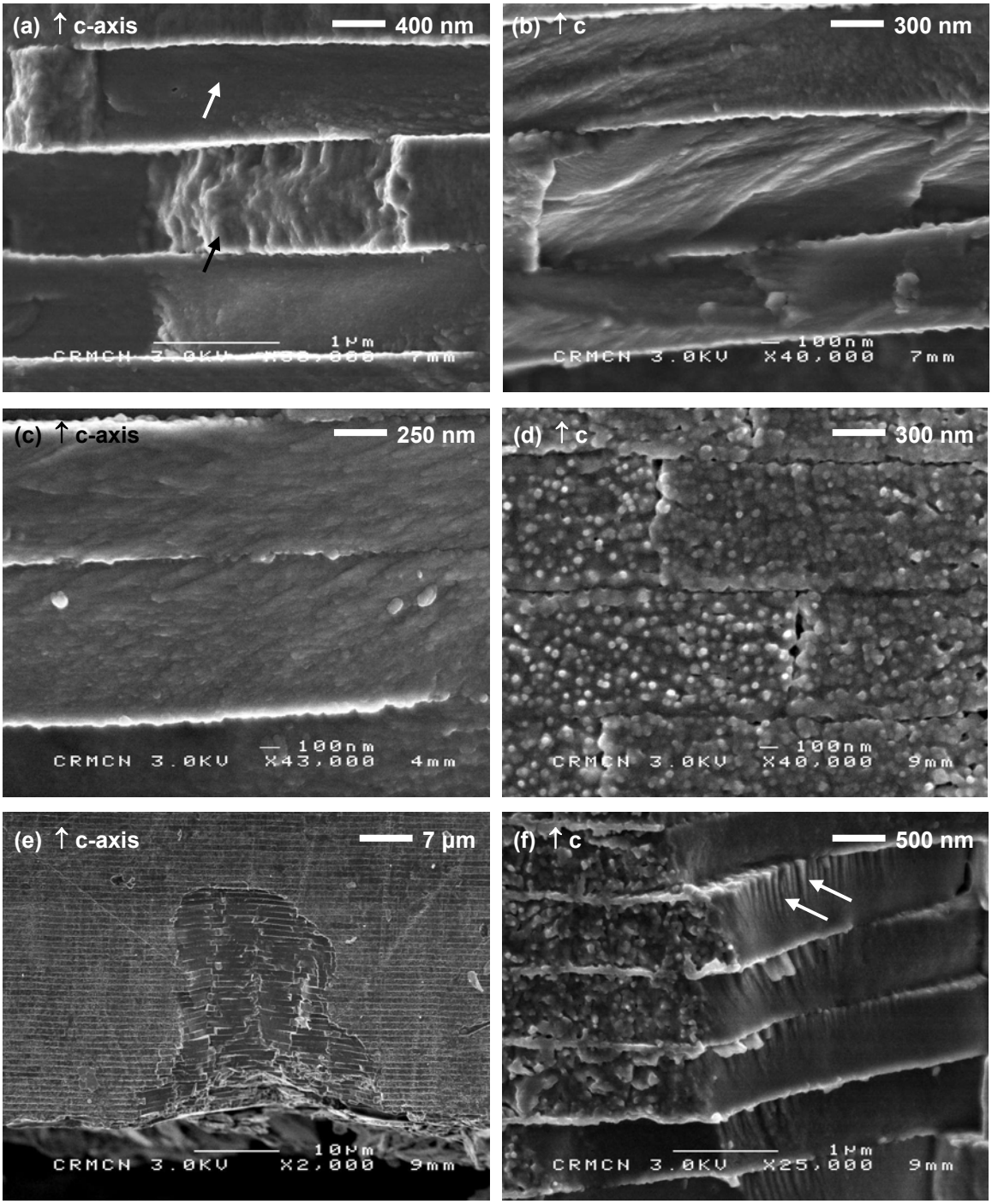

Fig. 3.20 SEM image of the fractured cross-section of the nacre layer of *T. niloticus*. **(a) to (c)** cryofractured surface. **(d)** sonicated in EDTA 0.5 M for 2 min **(e,f)** sonicated in DI water for 5 min.

inner face of the hole. Tablets carpeting the hole have a very rough surface on the polished side and a very smooth one inside the hole (Fig. 3.20 f). This suggests that the hole prevented wetting of the tablets within its enclosure to some extent, however one can notice small stalactites coming down from surface nanoasperities on the side of certain tablets close to the border (white arrows), possibly due to tiny aragonite crystal growth along the c-axis.

Micron-sized holes resulting in local absence of mineralization are useful to observe tablets cross-section not modified either by fracturing, polishing or etching. All tablets in the area are characterized by a rough appearance, be it the top surface or the

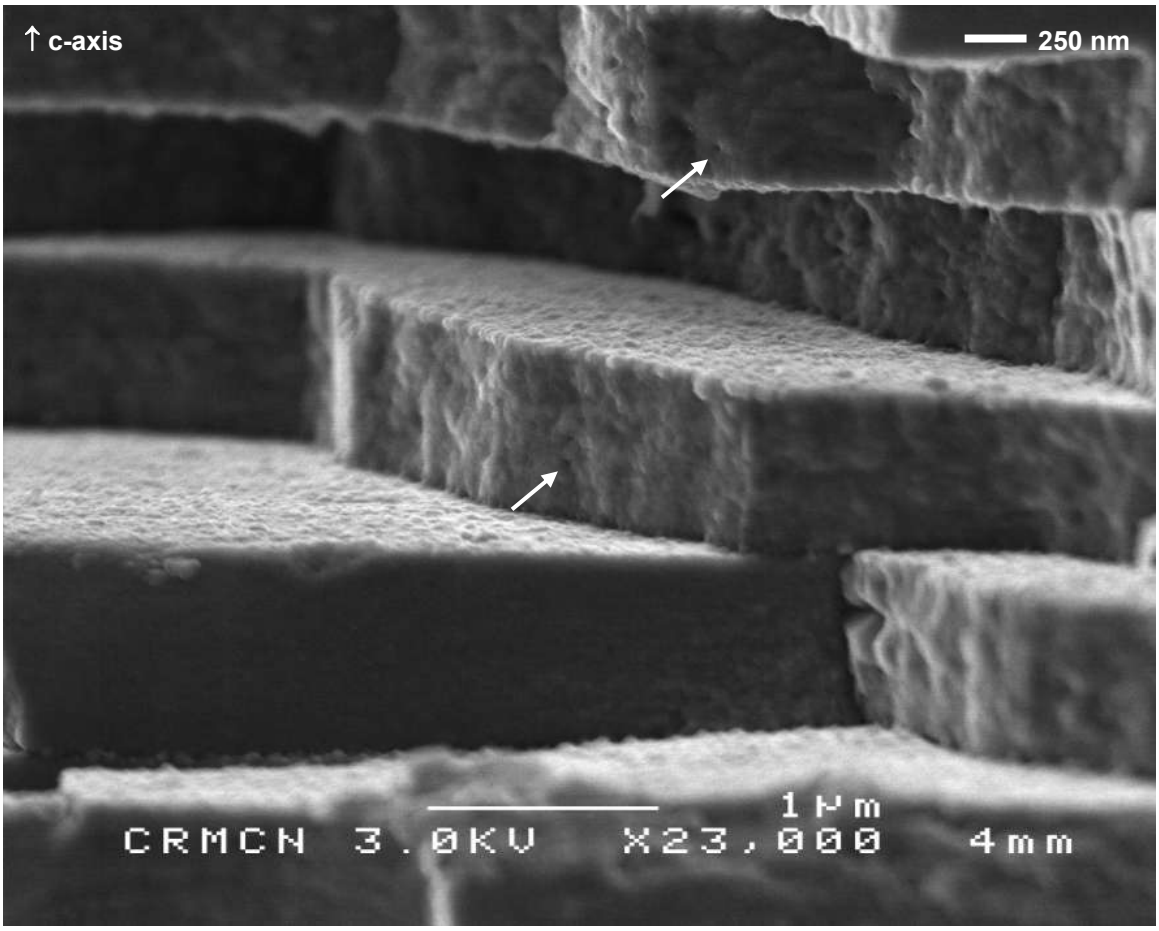

Fig. 3.21 SEM image of the cryofractured cross-section of the nacre layer of *T. niloticus*.

vertical walls. Again the roughness is of the order of a few tens of nanometers. The surface has a somewhat more regular appearance. White arrows indicate possible nanopores in-between the grains.

3.3.8.2 Transmission Electron Microscope

It is difficult to directly visualize the inner structure of single tablets. SEM and AFM imaging are limited to observation of surfaces, which are prone to artifacts such as local recrystallization. Additionally, SEM is still limited in resolution at the nanoscale, and AFM produces additional artifacts due to the convolution of the probe tip with the sample surface features. The strengths of TEM reside in its extremely high resolution (of the order of the Angstrom) as well as the ability to see through the bulk of the sample, though this causes a perpendicular averaging of the features along the thickness of the sample. However, inherent artifacts due to the sample preparation (mechanical grinding, ion thinning) require a cautious interpretation of the TEM images. Due to their extreme thinness, TEM nacre sections are also very reactive with the moisture in the air.

In Fig. 3.22 and 3.23 we see a FIB-prepared (typical out of plane thickness of ~ 100 nm) section from the nacre layer of *H. rufescens*. The typical spacing between the mineral tablets is 40-50 nm between layers and less than 10 nm between vertical walls of the tablets. Individual tablets diffract as single crystals under electron diffraction. Several features can be observed in the bulk of the tablets. First, diamond to rounded-shaped etch pits with typical diameters of 10 to 40 nm (black arrows) are artifacts likely due the FIB thinning (Ar ions ingrained into the surface during the thinning and creating bubbles) or

recrystallization of CaCO3 into calcite favored by the ambient moisture at the surface of the sample. They do not grow under the TEM beam. Also visible are tiny elongated

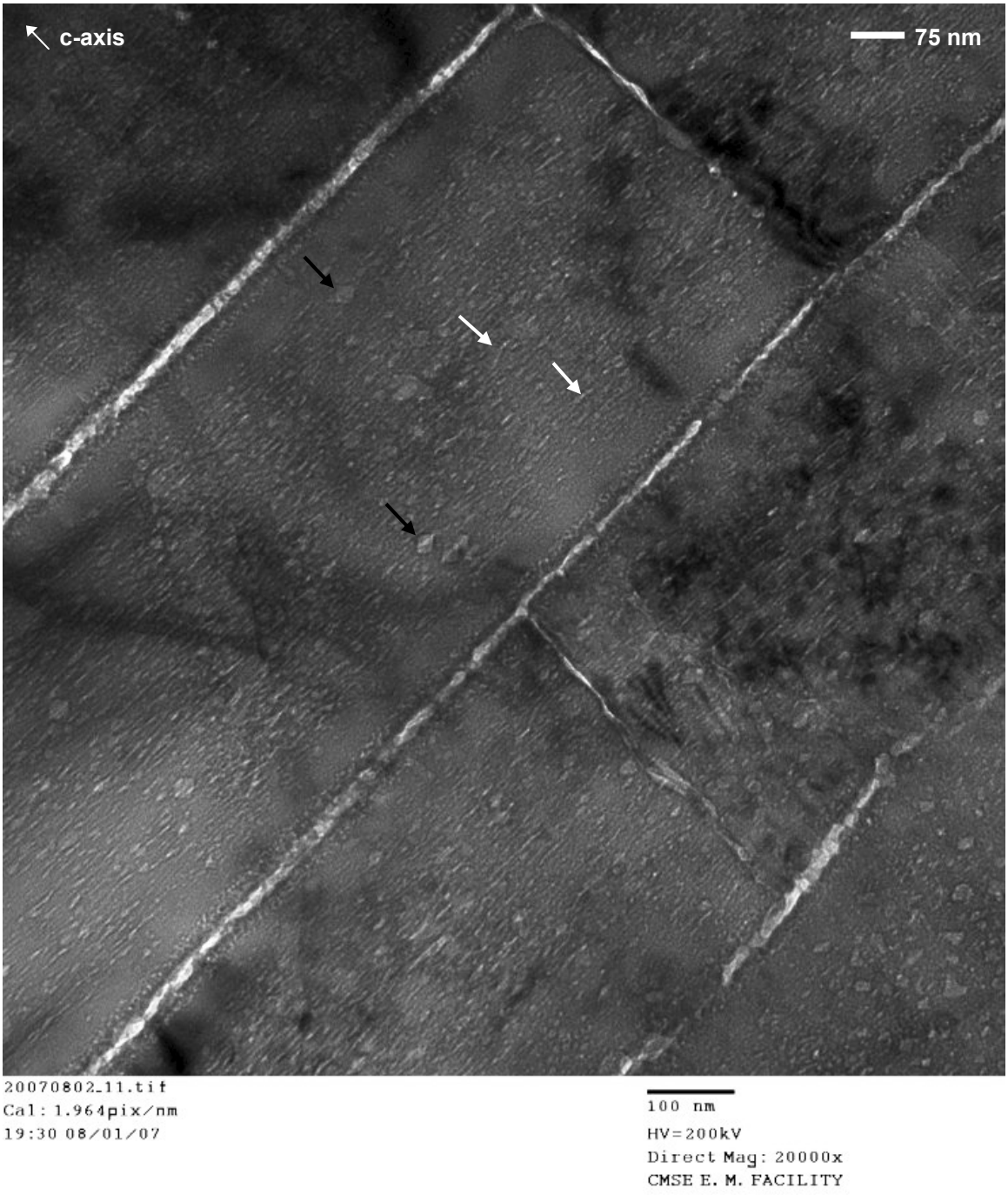

Fig. 3.22 TEM image of a FIB-prepared section from the cross-section of the nacre layer of fresh *H. rufescens*. *Image by D. Alcazar*.

Fig. 3.23 TEM image of a FIB-prepared section from the cross-section of a nacreous tablet from fresh *H. rufescens*. *Image by D. Alcazar*.

tubules (white arrows)with diameters between 5 and 10 nm and lengths from 30 to 60 nm that run approximately parallel to the tablet top and bottom surfaces. The fact that they

are absent from the border zone of the tablet (highlighted area in Fig. 3.23, within 50 to 100 nm from the tablet surface) indicates that they are not mere FIB artifacts, but are related to the tablet inner structure. One can hypothesize that they indicate a potential tubular nanostructure inside the tablet. A sample of single crystal aragonite prepared in the same way (thin FIB slice with c-axis in-plane) has a perfectly smooth surface under TEM imaging (data not shown), and neither etch pits or elongated features can be observed. This further suggests that the apparent porosity on nacre FIB slices is more than an artifact.

Fig. 3.24 presents TEM images of tiny pieces of tablets gently removed from the nacre layer of *H. rufescens* by means of mineralogist knife so as to avoid the artifacts

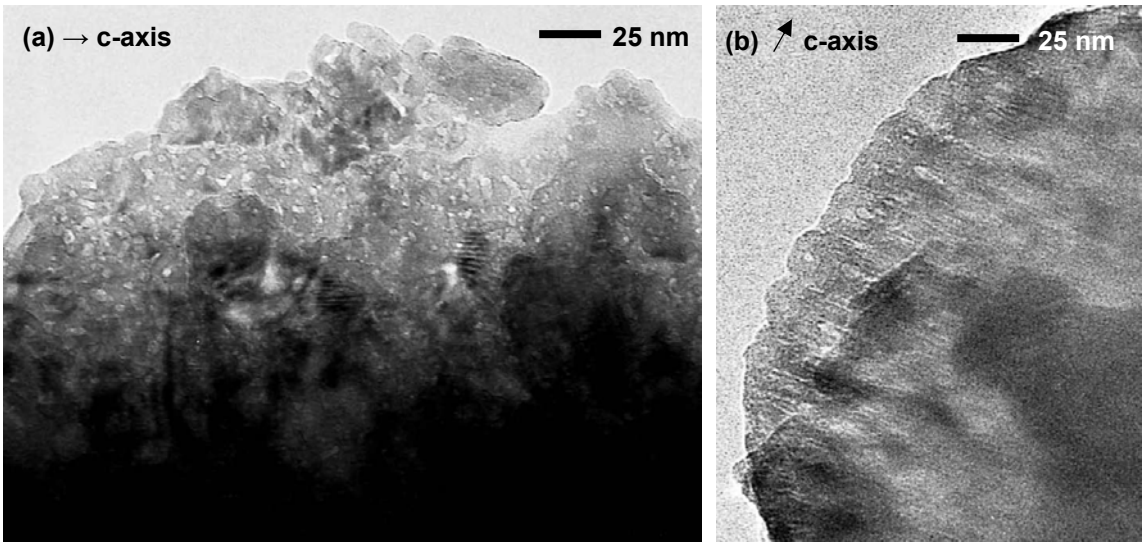

Fig. 3.24 TEM image of a detail of the side of small pieces of *H. rufescens* tablet, showing: **(a)** nanopores inside the mineral and **(b)** parallel tubule-like hollow features. *Images by A. Baronnet.*

a diameter of 3 to 4 nm (Fig. 3.24 a). They appear as parallel tubules in Fig. 3.24 b, possessing a hollow core with a mean diameter of 2 to 5 nm and again running in a parallel fashion with regard to the basal plane of the tablet.

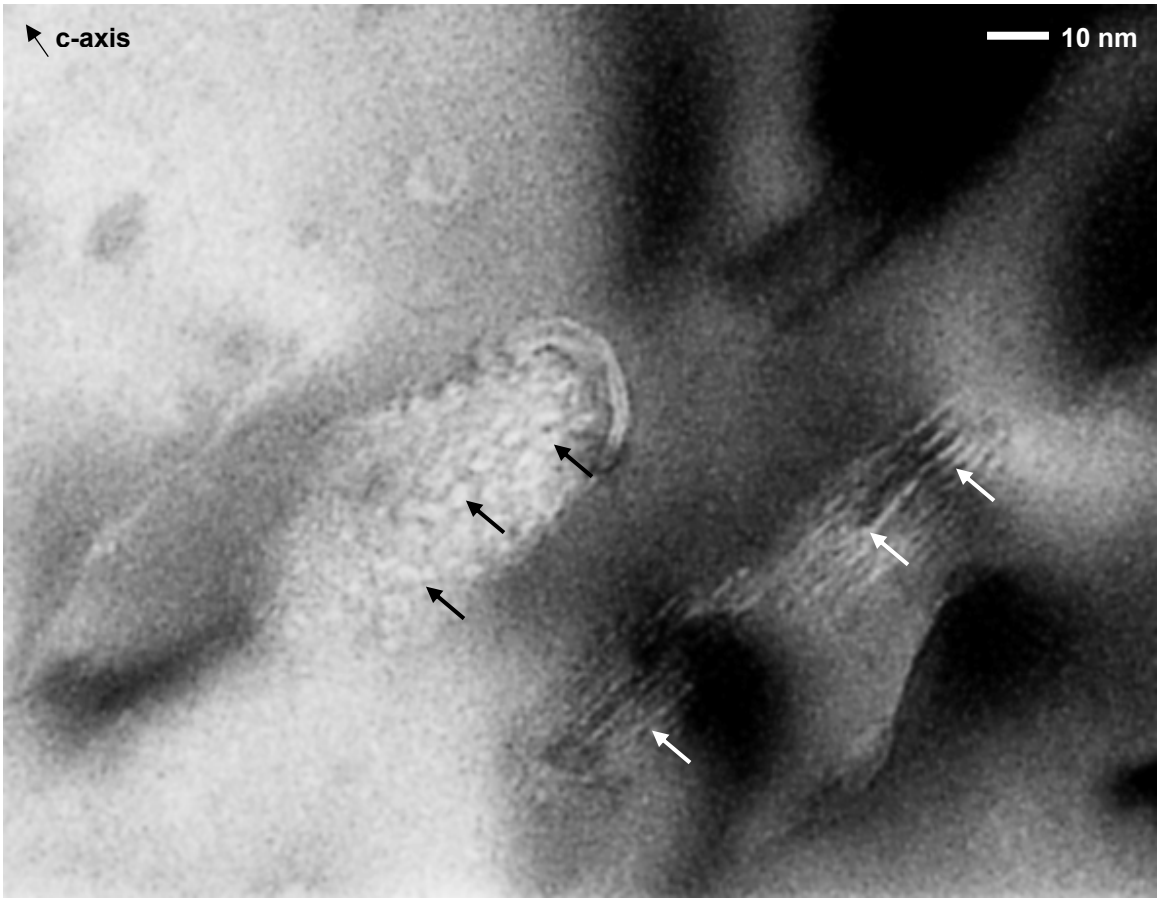

Fig. 3.25 TEM image of a detail of an ion-thinned cross-section of a single *T. niloticus* tablet, showing vacuoles filled with a fibrous substance (arrows). *Image by A. Baronnet*.
arising from polishing and ion thinning. Here again one can observe numerous pores with

Fig. 3.25 provides more evidence for these tubular pores in an ion-thinned sample from *T. niloticus*. Here a bundle of fibers can be seen running through pores within the tablets of *T. niloticus*. Their slightly wavy appearance is not compatible with the morphology of crystals at this length scale. Black arrows point to fibers oriented perpendicularly to the observation plane (apparent diameter ranging from 1 to 4 nm) and white arrows to fibers contained in the plane. As in Fig. 3.23, they tend to run parallel to the tablet basal plane. The slight change

3.3.9 INTERTABLET BRIDGE CROSS-SECTION

AFM imaging provided no evidence of mineral bridges between tablets. This could be due to the fact that these might be difficult to distinguish from nanoasperities. TEM on the other hand is a method of choice to explore the presence of true mineral bridges. In Fig. 3-26, a mineral bridge is shown at a resolution sufficient to distinguish

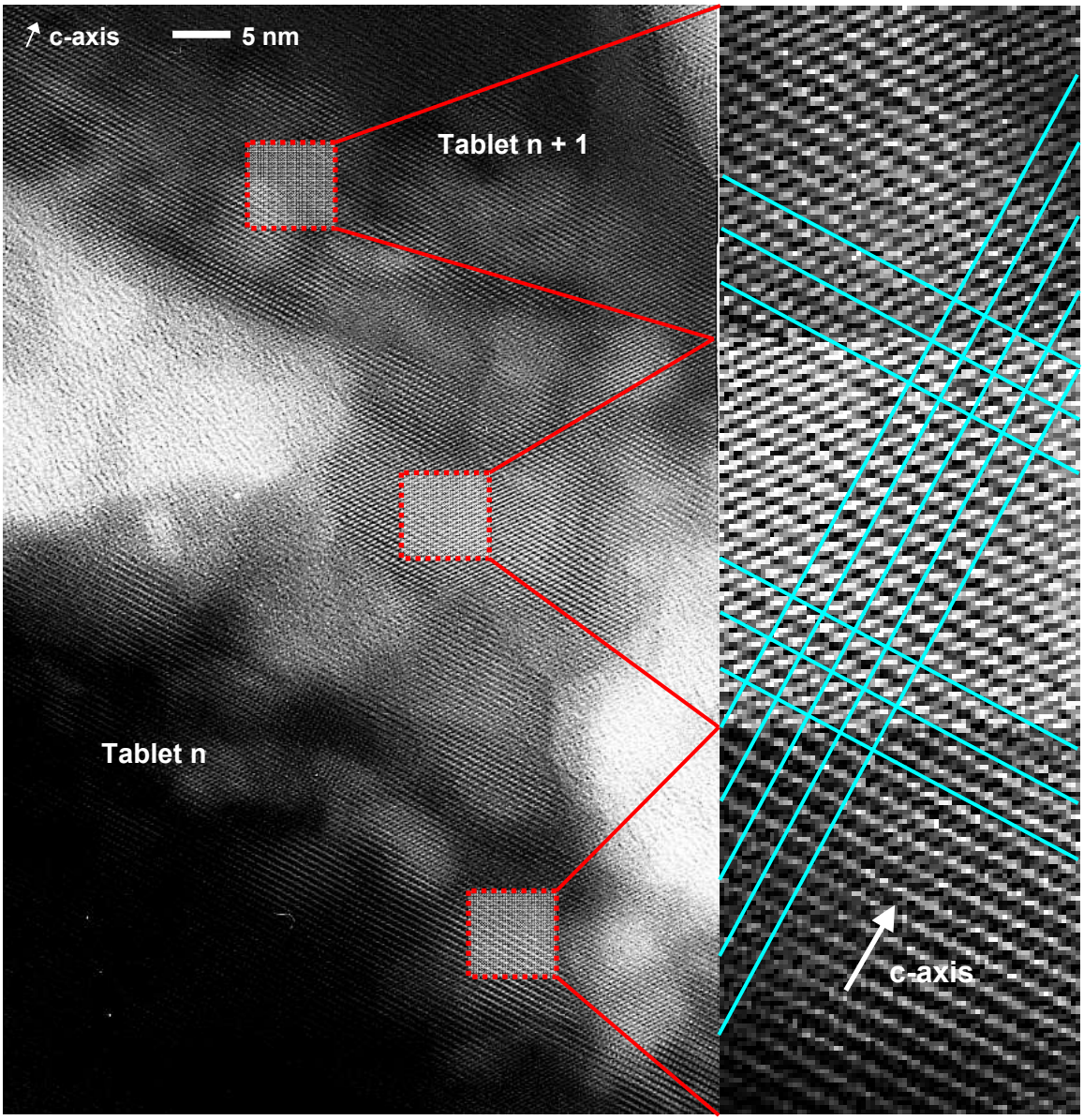

Fig. 3.26 TEM image of an ion-thinned cross-section of *T. niloticus*, showing a mineral bridge between two tablets. *Image by A. Baronnet*.

the lattice arrangement of aragonite. It can be seen that the crystalline orientation is perfectly conserved in both three regions analyzed, in the lower tablet, the bridge itself and the upper tablet. The ratio of the sides of the small blue unit rectangles delimited by the perpendicular lines is 1.35 in average, in very good agreement with the 1.36 value expected for the 2D projected aragonite unit cell in this orientation. Another fact worth noting is that despite contrast effects that seem to delimit rounded shapes, no grain boundaries can be detected, as in Fig. 3-19. On Fig. 3-27, one can see a close-up of the mineral bridge region with the position of the atoms overlaid. Only the heavier Ca atoms are apparent on the TEM image, and match perfectly with the schematic.

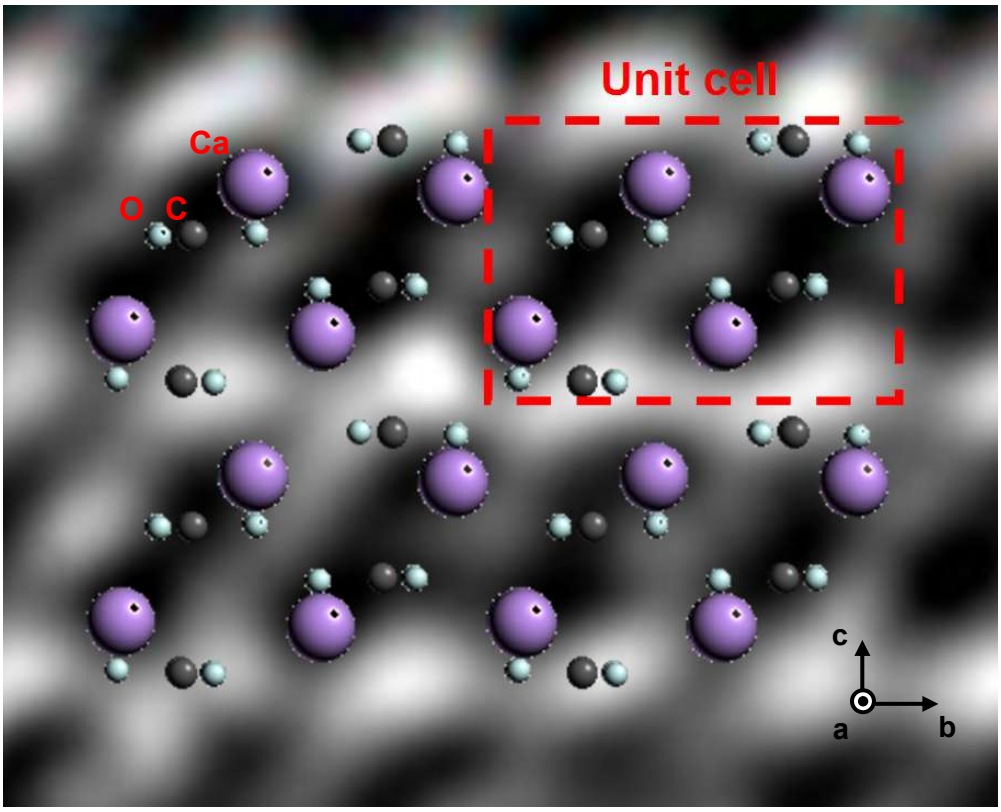

Fig. 3.27 Close-up of the aragonite crystalline lattice in the mineral bridge from the previous TEM image. The position of the larger Ca atoms appears clearly after overlaying a representation of the aragonite atomic structure with c vertical and a perpendicular to the page plane (taken from [104]).

3.4 DISCUSSION

3.4.1 PRISMATIC LAYER

Optical and SEM imaging of the prismatic layer in gastropod mollusk Trochus niloticus and Haliotis rufescens reveal highly oriented large prisms. At the scale of a few tens of microns, the prismatic layer exhibit faceted fracture surfaces, but high resolution scanning electron microscopy shows that the picture is more complex at lower scale. Though not as jagged as nacre, its surface does show a micron and sub-micron roughness typical of crystals with occluded organic component. The prisms appear to be composed of aggregated nanocrystallites assembled in a needle fashion and with size ranging from less than 30 nm to 100 nm. This nanostructure is reminiscent of the one of ganoine, which exhibits hydroxyapatite nanorods of similar dimensions (see chapter 5). Compared with pure crystalline calcite which cleaves very easily along its (104) plane, such nanoscale organizations seem to be common in the most outer hard layers of mineralized biocomposites and are likely to enhance the friction resistance of these protective layers.

3.4.2 NACREOUS LAYER

3.4.2.1 Tablet surface

High resolution AFM images of surface morphology elucidate new details of a very complex hierarchical structure at length scales below that of an individual nacre tablet sector including nanoscale resolution of the nacre tablet cross-section, the conformation of the organic matrix, and assemblies of nanoasperities. Identification the organic component (versus mineral-based nanoasperities) was made by a comparison of

topographic and phase images; topographic images showed a typical tortuous appearance characteristic of macromolecules at surfaces[99] and phase images showed that these regions had greater energy dissipative character. Overall, the AFM and SEM results are consistent with suggestions of an intratablet sector structure[31] and nanometer-sized asperities composing larger assemblies within individual nacre tablets.[23] The mean nanoasperity size reported here for the nacre of *T. niloticus* (28 ± 12 nm) is similar to that reported for *H. rufescens* nacre (~ 32 nm).[23] AFM imaging of the organic matrix yields low heights of ~ 1 nm which corresponds approximately to the thickness of an individual polymer chain and an irregular conformation, most likely due to collapse and denaturation during dehydration and / or partial removal during cleavage leaving only the most strongly bound macromolecules, presumably the polyanionic layer in closest proximity to the mineral tablets.[47] The spatial conformation and heterogeneities observed in the organic component are also likely highly dependent on the sample preparation procedures. Another study[105] on samples of *Haliotis laevigata* nacre that was cleaved, abrasively ground, processed with acryl polishing paste, and partially demineralized with 0.5M EDTA showed via contact mode AFM imaging in fluid larger filaments ~ 50 nm in diameter localized around the borders of the individual tablets and identified them as collagen fibers; no such features were observed in this study.

3.4.2.2 Tablet internal structure

A consistent trend in many SEM and AFM images presented in this chapter is that nacre tablets exhibit a nanoscale roughness, whether the sample preparation involved surface etching, fracturing or no treatment at all. Though for etched samples local

recrystallization of the aragonite upon removal of the sample from the solution is likely to play a role, it is tempting to conclude that nacre tablets are composed of nanograins, the average dimension of which would be about a few tens of nanometers. However, TEM images fail to show the existence of grain boundaries within the tablet thin sections. A more prudent conclusion from the observation of images obtained from surface microscopy thus seems to be that the nanoscale texture of tablets suggests a nanocomposite organization, where biomacromolecules are likely occluded in the crystalline aragonite. While our AFM images and other[106] show rounded nanoasperities potentially surrounded by an organic matrix coating, one should bear in mind that results from surface imaging techniques are inherently difficult to transpose to the bulk material. Our results do show the presence of organic matrix atop cleaved tablets, but it is unclear whether it is also present in-between the crystallites. Indeed, the extended TEM study of many aspects of the tablet presented here tends to show that the aragonite lattice is continuous throughout individual tablets. This clearly contradicts the view of tablets as an aggregation of nanocrystals surrounded by an organic coating. While it has been suggested that tablet mineralization occurs through the crystallization of amorphous calcium carbonate (ACC) delivered by small vesicles,[20, 107] nothing proves that the crystallites remain somehow separated from neighboring grains upon crystallization. On the contrary, from a mere biomineralization point of view, it is necessary that they be released from the vesicle in order to nucleate. And the perfect lattice arrangement of the aragonite crystal over length greater than 100 nm supports the idea that all ACC grains fuse together and share the same crystalline orientation upon crystallization, effectively becoming one large single crystal.

Rather than uniformly coating putative nanograins, the organic component of the tablets seems to run through excessively small tubular pores, with average diameter of about a few nanometers at most. A more likely inner structure for the tablets would then be a sponge-like organization, with pores containing the organic material and running through a continuous crystalline structure. The origin of this porosity could well be the fact that ACC contracts during crystallization, due to a greater order of its crystalline form. The difference of morphology between the core of the tablets and the more outer regions could be due to a higher concentration of occluded macromolecules as the crystallization front pushes them ahead and against the chitinous structural template. Some of the organic molecules present in nacre, namely, the silk fibroin proteins, are known to be rather hydrophobic and to impede calcium carbonate crystallization. This possible higher density of organic phase along the boundaries of the tablets could thus also partially prevent a complete crystallization of the ACC. This would likely result in a decreasing porosity away from the core, as well as a more globular aspect of the surface, such the observed nanoasperities (Fig. 3-28).

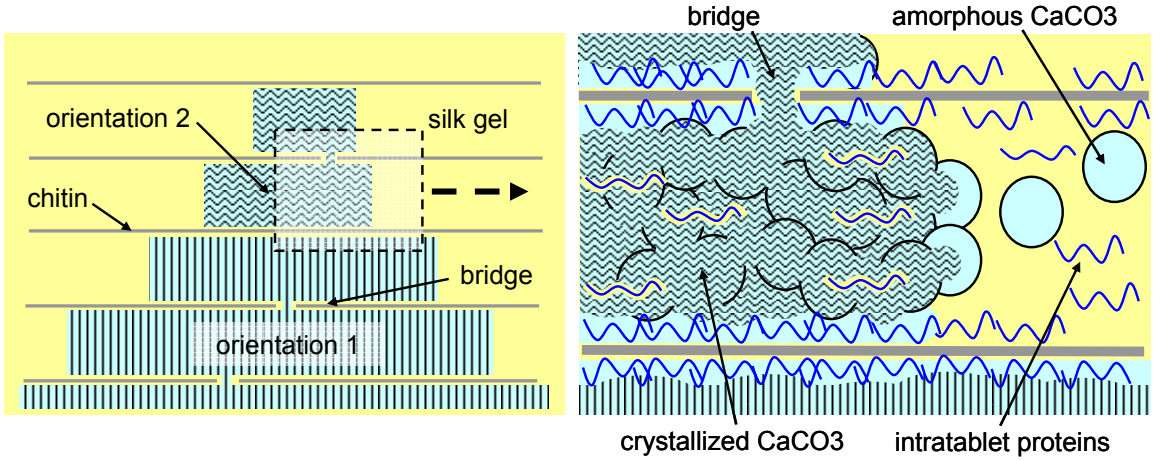

Fig. 3-28. Suggested model for the biomineralization of gastropod mollusk nacreous tablets.

Finally, the presence of what we consider mineral bridges between superimposed tablets lends credence to the hypothesis that crystalline domains of several tablets are made possible by the passing of the orientation information through crystalline mineral bridges rather than organic epitaxy. Indeed, it seems difficult to imagine that an organic template, less organized than the mineral,[44] could promote the growth of a perfectly crystalline mineral phase from one tablet to another. Still, as Addadi, et al.[48] have suggested, both crystalline and epitaxial growth types could actually play a role in nacre formation. The former could be responsible for the excessively high crystalline order at the scale of a few tablets, and the latter for the disorder that arises over larger distances.

CHAPTER 4 NANOSCALE MECHANICAL PROPERTIES OF GASTROPOD NACRE

4.1 INTRODUCTION

It has become increasingly evident that knowledge of the fine details of the nanoscale mechanical properties and deformation mechanisms will be critical to the success of such theoretical efforts in their attempt to understand macroscopic mechanical function and performance. Research in this area is just beginning with a few studies recently reported as follows. Nanoindentation experiments up to 200 μN of force on individual thermally etched nacre tablets from *California red abalone* were found to be minimally hysteretic and exhibited two distinct deformation regimes which were attributed to initial plastic flattening of surface nanoasperities followed by elastic deformation of the tablet body.[108] The secondary elastic regime data was well described by an analytical solution to a transversely isotropic elastic contact mechanical model[109] using the known elastic constants for aragonite.[93] Another nanoindentation study[23] up to larger forces of ~ 800 μN on diamond-cut, mechanically ground, polished, and hydrated nacre from *California red abalone* showed marked hysteresis and fits of these data to an elastic contact mechanical model[110] yielded moduli between ~ 60 - 80 GPa. Atomic force microscopy (AFM) imaging of the indented regions showed plastic deformation, a pile-up height of a few nm spanning lateral distances of ~ 100 nm, and no indication of

microcracks.[23] These studies however lend to some criticism: they all use sample preparation protocols somewhat destructive (polishing, chemical etching, thermal treatment, embedding), lack careful prior- and post-deformation characterization and present only basic interpretations of the experimental data. Furthermore, the capabilities of novel techniques such as AFM have yet to be fully exploited.

In this study, we report the nanoscale elastic and plastic indentation properties of individual nacre tablets from the gastropod mollusk *Trochus Niloticus* using a sample preparation methodology which involved uniaxial compression with the externally applied load oriented perpendicular to the nacre tablet *c*-axis, producing intertablet cleavage with minimal damage to the individual nacre tablets and an exceedingly clean and flat surface. This unique sample preparation protocol (which avoided polishing, chemical etching, thermal treatment, and embedding) combined with high resolution AFM imaging enabled the surface morphology to be studied before and after nanoindentation and, for the first time, shows nanoscale resolution of fractured tablet cross-sections, the conformation of the organic component, and deformation of individual nanoasperities. Another objective of this work was to study the effect of hydration and hence, freshly cleaved samples were compared to ones that had been soaked for 30 days in artificial seawater (0.4221 mol/L NaCl, 0.011 mol/L KCl). The range of applied forces was ~50-1000 μN, corresponding to indentation depths of ~10-100 nm and a maximum contact area of ~ 0.1 μm^2 at a maximum load of 1000 μN. Lastly, a bilayered continuum mechanical elastic-plastic FEA model was developed and refined to capture the observed deformation behavior.

4.2 MATERIALS AND METHODS

4.2.1 SAMPLE PREPARATION

Trochus Niloticus shell specimens (~ 10 cm in size) were purchased from Shell Horizons (Clearwater, FL). The least destructive, minimum sample preparation procedures possible were employed including no alcohol dehydration, thermal or chemical treatment, embedding, or polishing. First, nacre from the inner layers of *Trochus Niloticus* shells were sectioned into parallelepipedal samples using a diamond impregnated annular wafering saw (Buehler, Isomet 5000) running at 800-900 rpm. After cutting, the samples were cleaned in reverse osmosis filtrated water for 15 minutes using an Ultramet ultrasonic cleaner. Samples for nanoindentation were produced by uniaxial compression using a *Zwick* mechanical tester (Model BTC-FR010TH.A50, 10 kN maximum load cell, 0.01 mm/min, ambient conditions). The externally applied load was oriented perpendicular to the aragonite *c*-axis, producing a clean intertablet cleavage. For nanoindentation tests, two types of samples were employed. "Freshly cleaved" samples were tested within less than one hour after cleaving via uniaxial compression. "Artificial seawater soaked" samples were immersed for 10 weeks in reverse osmosis filtrated water with 0.4221 mol/L NaCl, 0.011 mol/L KCl, pH = 7.1 in a hermetically sealed container at 20ºC, uniaxially compressed, and then tested within less than one hour after cleaving.

4.2.2 AFM IMAGING

Contact and tapping mode atomic force microscope (CMAFM and TMAFM, respectively) imaging in ambient conditions were employed to produce surface topographical images of freshly cleaved nacre samples. In ambient humidity, a thin layer of water (2 –10 Å thick) exists on the surface[99] yielding closer to physiological images than completely dried samples. A *Digital Instruments* (*DI*, Santa Barbara, CA) Multimode SPM IIIA was used with AS-130 "JV" or "EV" piezoelectric scanners. Contact mode scans were conducted with *Veeco* Si_3N_4 cantilevers (V-shaped with approximately square pyramidal probe tip geometry, tip half angle of ~35^o, cantilever length, l ~ 200 μm, nominal spring constant, k ~ 0.32 N/m, and nominal probe tip radius of curvature, R_{TIP} ~ 40 nm) and tapping mode scans with *Veeco* Si cantilevers (V-shaped with approximately square pyramidal probe tip geometry, tip half angle of ~17.5^o, l ~ 125 μm, k ~ 0.40 N/m, and R_{TIP} ~ 10 nm). A scan rate of 0.25-2 Hz using a maximum sample size of 512 x 512 pixels was employed at gains between 0.1-0.3. The drive amplitude and amplitude set-point were optimized upon tuning. The x- and y- scan directions were calibrated with a 10 x 10 μm^2 grid and the z-direction was calibrated with 5 nm diameter beads on a cleaved mica surface. The images to be shown report amplitude (i.e. cantilever oscillation amplitude) and phase (i.e. cantilever phase lag) for tapping mode or deflection for contact mode (i.e. cantilever deflection). Amplitude and deflection both reflect of surface topography while phase mode is sensitive to many properties such as friction, adhesion, (visco)elasticity, and composition.

For *in-situ* imaging of residual indents, a *Quesant* Q-Scope 350 (attached to a *Hysitron, Inc.* nanoindenter*)* was used in tapping mode with a piezoelectric tube scanning

element (X-Y scan range ~40 μm, vertical Z limit ~4.5 μm) and Si_3N_4 Wavemode NSC16 cantilevers (rectangular shaped with conical probe tip geometry, l ~ 230 μm, width ~ 40 μm, cone angle < 20°, probe tip height ~ 15-20 μm, resonance frequency, ω ~170 kHz, k ~ 40 N/m, and R_{TIP} ~10 nm). A scan rate of 2 Hz using a maximum sample size of 512 x 512 pixels was employed. The drive amplitude and amplitude set-point (~0.25 V) were optimized prior to imaging and gains between 350 and 550 were employed.

4.2.3 NANOINDENTATION

Nanoindentation experiments (Fig. 2-1) were conducted in ambient conditions using a *Hysitron, Inc*. (Minneapolis, MN) Triboindenter equipped with tapping mode atomic force microscope (TMAFM, Quesant Q-Scope) for topographic imaging of residual impressions. The instrument is housed in a granite frame environmental isolation chamber so as to minimize instabilities due to the ambient background noise, active piezoelectric vibration control stages (Hysitron, Inc.), and a thermal drift calibration step. Load-controlled nanoindentation was performed using a Berkovich (trigonal pyramid) diamond probe tip with the loading axis parallel to the aragonite *c*-axis. The piezoelectric transducer was allowed to equilibrate for 660 seconds (the last 60 seconds with digital feedback) prior to each indent. The drift rate of the transducer was automatically monitored by the software before indentation was initiated. The applied load function was divided into five segments as follows. The first segment consisted of a 3 second hold at zero force allowing for tip-sample equilibration. Segment

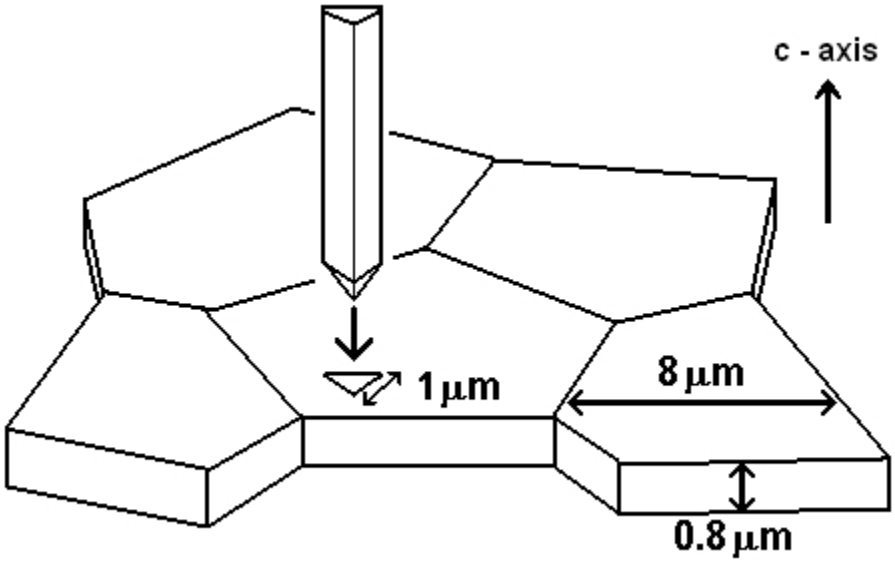

Fig. 4-1. Schematic of the nanoindentation of an individual nacre tablet.

two was a constant loading rate of 10 μN/sec. Once the maximum set peak load was reached, a third segment which was a hold period of 10 seconds would ensue. The fourth segment decreases the load until reaching zero force with an unloading rate equivalent to that of segment two. The fifth segment would conclude the experiment with a 50 second hold at zero force, in order to calculate the final drift rate of the piezo. Maximum loads of 50, 100, 250, 500, 750 and 1000 μN were selected. ~ 15 experiments per maximum load were performed in a square grid arrangement with each indent spaced 15 μm apart (i.e. thus probing 15 different individual nacre tablets). Load versus indentation distance curves from multiple experiments using the same maximum load and from different sample locations were averaged and standard deviations calculated and reported. The probe tip area function ($^{A(}h_c$ which is $^{\text{the projected area of the Berkovich}}$ probe $^{\text{tip}}$ under load calculated from a 6th order polynomial fit accounting for non-ideal tip geometry as a

function of the contact depth, h_c) and frame compliance were calibrated prior to each set of experiments using a fused quartz sample.

4.2.4 Mechanical Property Approximation from Nanoindentation Data

The elastic, plastic, and total work of indentations (W_e, W_p, and W_T, respectively) were calculated from the nanoindentation data as follows; W_e was defined as the area under the unloading curve, W_p was defined as the area between the loading and unloading curves (mechanical hysteresis energy), and W_T was defined as the area under the loading curve.

Two different approaches were used to approximate the mechanical properties from nanoindentation data. First, the Oliver-Pharr (O-P) methodology[110] where the initial (95% to 20%) unloading curve was compared to continuum mechanical theory for an isotropic, elastic half-space where the elastic modulus, E, was the only fitting parameter. The hardness was calculated as $H = P_{max}/A_{max}$ where P_{max} is the maximum load and A_{max} is the projected area of contact at the maximum contact depth and represents the load-bearing capacity of the material. Unpaired student t-tests[111] were carried out to evaluate whether various datasets were statistically different from each other using $p<0.05$ as the minimum criterion.

Second, elastic-perfectly plastic finite element analysis (FEA) simulations were used where the loading and unloading curves were fit using two material parameters for

the nacre tablet, the elastic modulus and the yield stress, σ_Y.[1] The FEA model was constructed as a two layer material (i.e. the mineral and the organic matrix components) with a stiffer layer representing the nacre tablet that was 870 nm thick and an organic matrix layer that was 40 nm thick. The thickness values were chosen based on SEM measurements. The organic matrix was assumed to behave similar to an elastomer and modeled by the Arruda-Boyce 8-chain model,[112] which has been shown to adeduately capture the stress-strain behavior of rubbers and soft tissues.[113, 114] The stress-strain law for the Arruda-Boyce 8-chain model is:[112]

$$\mathbf{T} = \frac{1}{J}\mu\frac{\sqrt{N}}{\lambda}\mathcal{L}^{-1}\left(\frac{\lambda}{\sqrt{N}}\right)\overline{\mathbf{B}} + K_B\left[J-1\right]\mathbf{I} \qquad (1)$$

where : $\mathbf{T}$ is the Cauchy stress tensor, $\overline{\mathbf{B}}$ is the Cauchy-Green tensor from which strain is calculated. μ, N, and K_B are material parameters in which μ is the shear modulus (set equal to 100 MPa), N is the number of the rigid links between crosslink sites in the macromolecule and characterizes molecular chain extensibility (set equal to 10), and K_B is the bulk modulus (set equal to 2 GPa). Among these parameters, μ has the strongest influence on the material shear stress-strain response at small strains whereas N more heavily influences the large strain behavior. The organic matrix is 870

[1] Aragonite is known to be orthotropic.[35] Within an individual nacre tablet, random in-plane (perpendicular to the *c*-axis) orientation due to the sector structure is expected, yielding a transversely isotropic solid at these length scales (Fig. 1c). Simulations were performed taking into account both elastic and plastic anisotropy; this anisotropy was found to have minimal influence (<5%) on the resulting values of the modulus and yield stress.

nm below the indenting surface and laterally confined due to the high stiffness of the mineral tablet: the lateral confinement will make the stress state in the organic layers predominantly (negatively) hydrostatic during these indentation loading conditions, thus the choice of μ was expected to have small effect on the overall indentation force versus depth predictions. This was demonstrated by comparing the results from three simulations, where μ was chosen as 1 GPa, 100 MPa, and 10 MPa, respectively. The resulting difference in indentation force vs. penetration responses was < 4% (data not shown). E and $\int_Y$ of nacre tablet were best fit to capture the experimental data. 40 nm was employed for the thickness of the organic layer (as measured by SEM). The symmetry of the Berkovich indenter enabled simulations using 1/6 of the indenter and the material with appropriate symmetry boundary conditions. Since the elastic modulus of the diamond probe tip is approximately 10 × greater than that of nacre, the indenter was modeled as a rigid surface. Due to fabrication and wear, the Berkovich probe does not possess a precisely sharp tip geometry; instead it is rounded and can be characterized by a finite probe tip end radius and truncate height (which is defined to be the distance between the apex of the rounded tip and the apex of the imaginary ideally sharp tip). In order to approximate the probe tip end radius and truncate height, nanoindentation experiments were conducted on a standard fused quartz sample. Hertz contact solution provided an initial estimate and FEA simulations refined this estimate to give more accurate values. Hence, for all FEA simulations the indenter was modeled as a rigid surface with Berkovich geometry (ideal geometry possesses an inclined face angle, β, of 24.7° and an apex angle, γ, of 77.1°) having a probe tip radius of 300 nm and truncate

height of 7 nm. The nacre was modeled using 8-node trilinear hybrid tablet elements (C3D8H in ABAQUS element library). The mesh was refined in the vicinity of the contact region where large gradients in stress and strain prevail. Several mesh densities were analyzed and an optimal mesh was finally chosen for use in all simulations which contained 6195 nodes and 5491 elements. Large deformation theory and frictionless contact between the indenter and material were assumed throughout the analysis. A smaller number of individual experimental nanoindentation curves were fit (n=3, where the average, high, and low curves were fit for each dataset) and compared to the O-P method due to the longer time and computational cost required for the FEA simulations.

4.3 RESULTS

4.3.1 NANOINDENTATION

Fig. 4-2 a is a plot of multiple individual nanoindentation curves on loading and unloading (force versus depth) where each curve is on a different individual freshly cleaved *Trochus Niloticus* nacre tablet (from the same sample). A maximum load of 1000 μN resulted in an indentation depth of ~ 65 nm. Some curves exhibited small "kinks" at a variety of different forces and depths while others were relatively smooth (Fig. 4-2b). A marked and consistent change in slope was observed at ~ 73 μN force and ~ 7 - 15 nm depth (Fig. 4-2c), consistent with the peak-to-valley height of the nanoasperities. Plots of the averaged nanoindentation curves corresponding to different maximum loads are given in Fig. 4-3 comparing the freshly cleaved and artificial seawater soaked nacre. Increased hydration by soaking the nacre samples in artificial

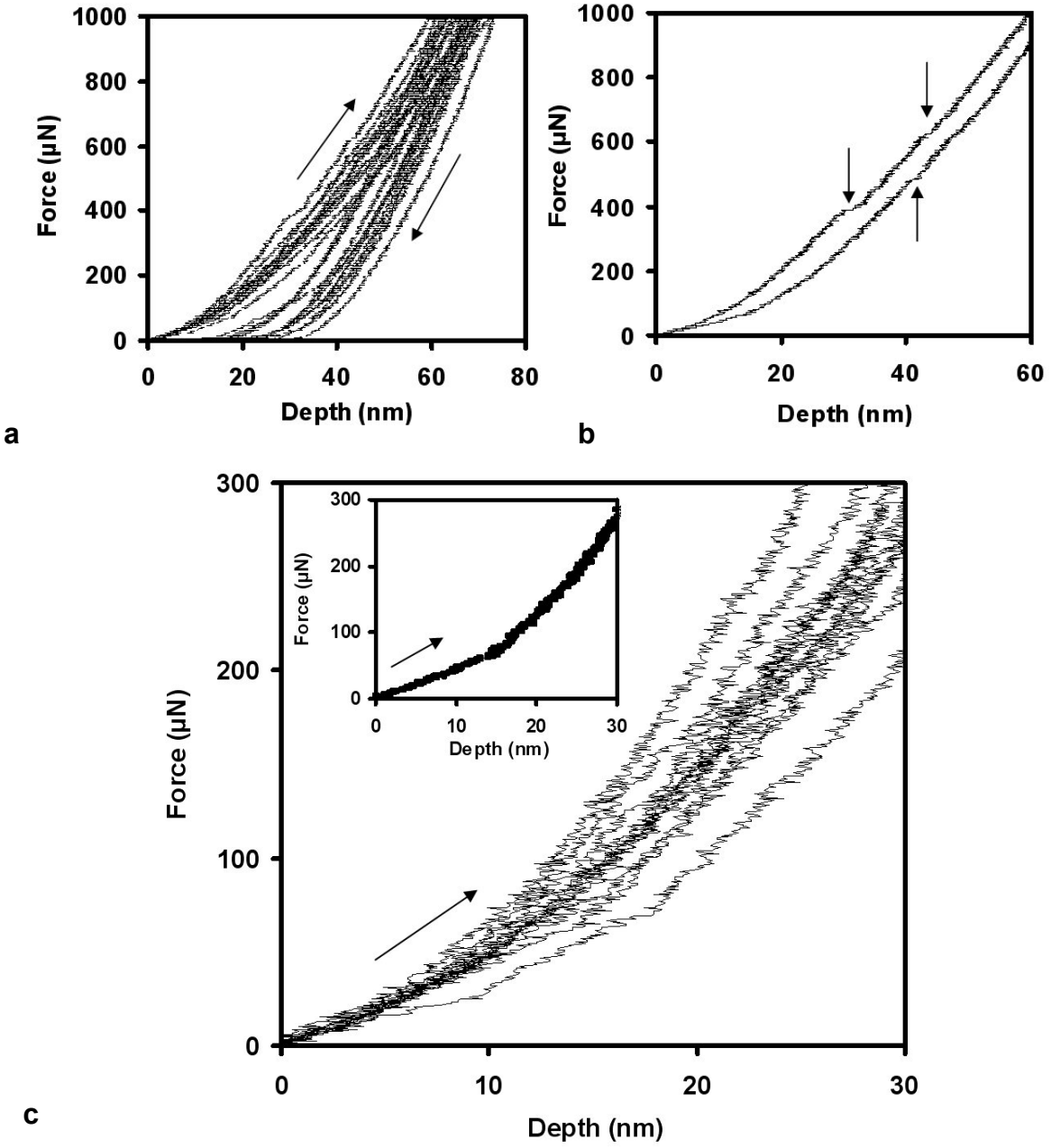

Fig. 4-2. Individual nanoindentation curves each on a single freshly cleaved *T. Niloticus* nacre tablet **(a)** multiple curves on loading and unloading up to a maximum load of 1000 μN, **(b)** two of the curves from the dataset shown in **(b)** on loading with arrows indicating minor inflections, and **(c)** multiple curves on loading and unloading up to a maximum load of 300 μN; inset is one individual curve from this dataset with a pronounced variation in slope at ~ 15 nm and ~73 μN.

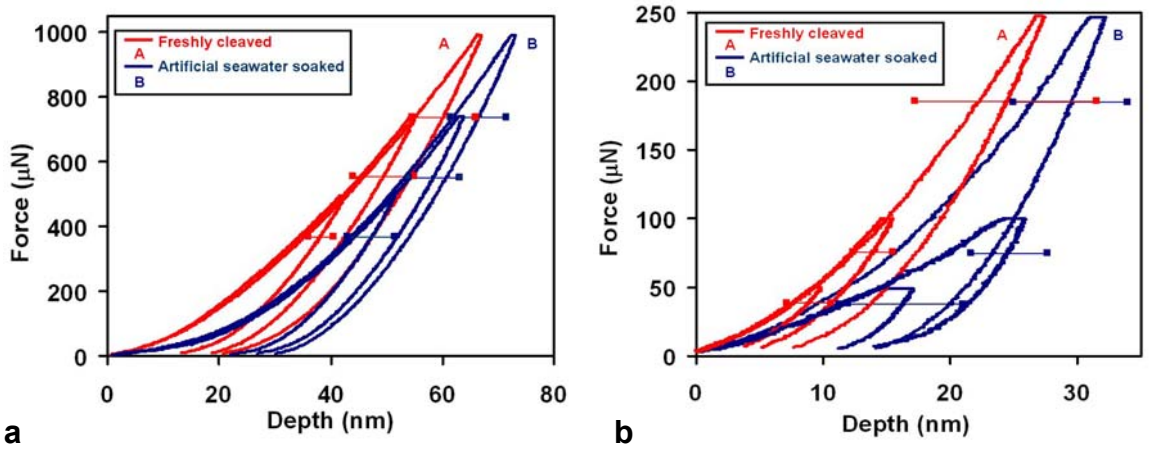

Fig. 4-3. Average nanoindentation curves on freshly cleaved and artificial seawater-soaked individual *Trochus Niloticus* nacre tablets on loading and unloading as a function of maximum load; **(a)** 500 μN, 750 μN, and 1000 μN maximum loads and **(b)** 50 μN, 100 μN, and 250 μN maximum loads. The horizontal error bars represent the standard deviation for that particular dataset.

seawater resulted in an increase in depth of indentation for a given force (e.g. from ~ 68 nm to ~ 74 nm for a 1000 μN maximum force) and an increased residual displacement upon unloading (e.g. from ~ 23 nm to ~ 27 nm for a 1000 μN maximum force) for all maximum loads tested. Nacre samples soaked in artificial seawater also sometimes exhibited kinks in the individual nanoindentation curves (data not shown). All samples exhibited mechanical hysteresis.

4.3.2 NANOSCALE DEFORMATION

Fig. 4-4a-c are tapping mode AFM images (*Q-scope*) of the indented region of freshly cleaved nacre samples (individual tablets shown in the plane perpendicular to the aragonite *c*-axis; the length scale corresponds to the schematic shown in Fig. 1c), upon removal of maximum loads of 1000, 5000, and 10,000 μN, respectively, and Fig. 4-4d is for artificial seawater soaked nacre upon removal of a

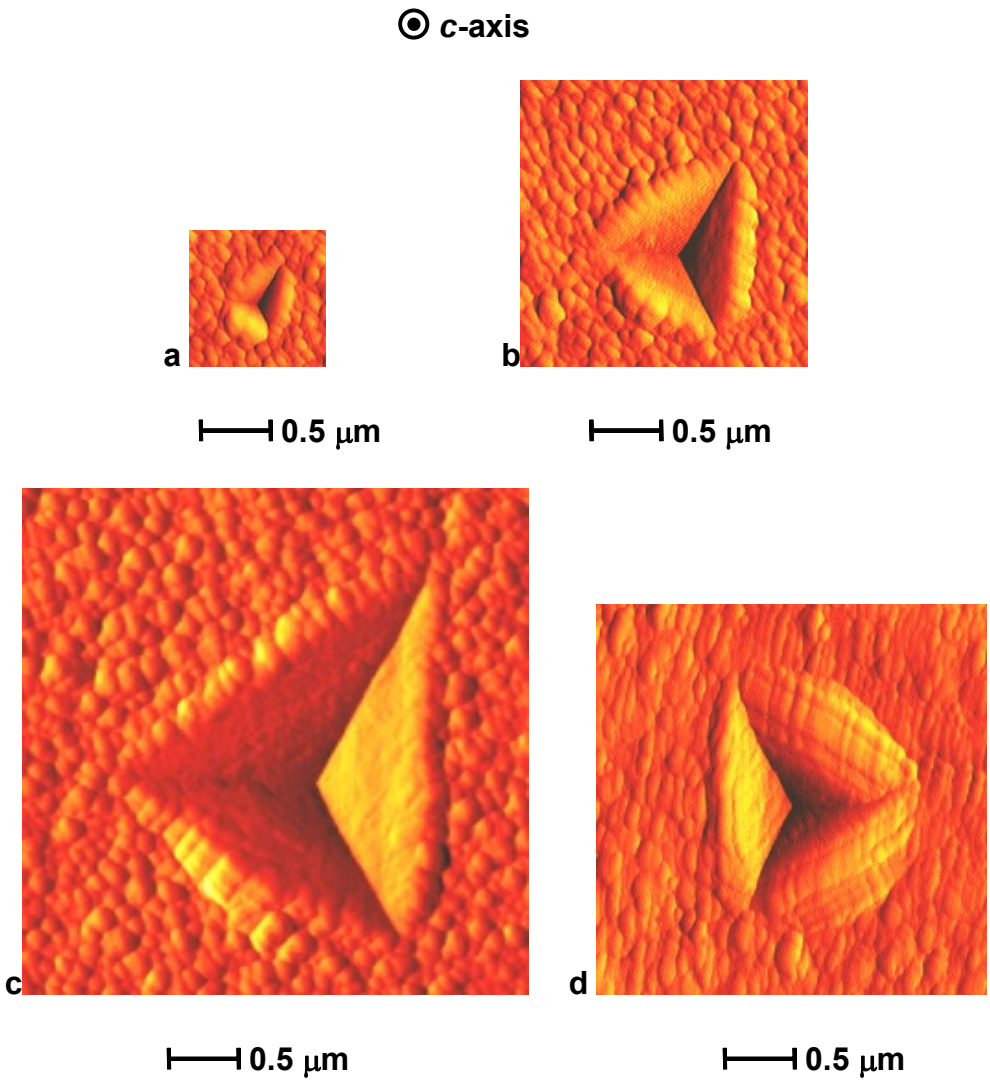

Fig. 4-4. Tapping mode atomic force microscopy (AFM) images of top down view of residual nanoindentation impression on individual freshly cleaved *Trochus Niloticus* nacre tablet; **(a)** maximum load = 1000 μN and 1.8 μm scan, **(b)** maximum load = 5000 μN and 3 μm scan, **(c)** maximum load = $1 \bullet 10^4$ μN and 3.7 μm scan, and nacre incubated in artificial seawater for 10 weeks **(d)** maximum load = 5000 μN, 3.0 μm scan. ⊙ indicates *c*-axis direction is out of the page.

maximum load of 5000 μN. The features observed away from the indent region in all four images are the larger nanoasperity assemblies. Residual deformation was clearly visible, exhibiting a residual central indent and a pileup zone indicating plastic flow of

the material from beneath the indenter. No microcracks were evident beneath the indenter, in the pileup zone, or in the region immediately outside the contact area. The nanoasperity assemblies were significantly flattened within the indent region.

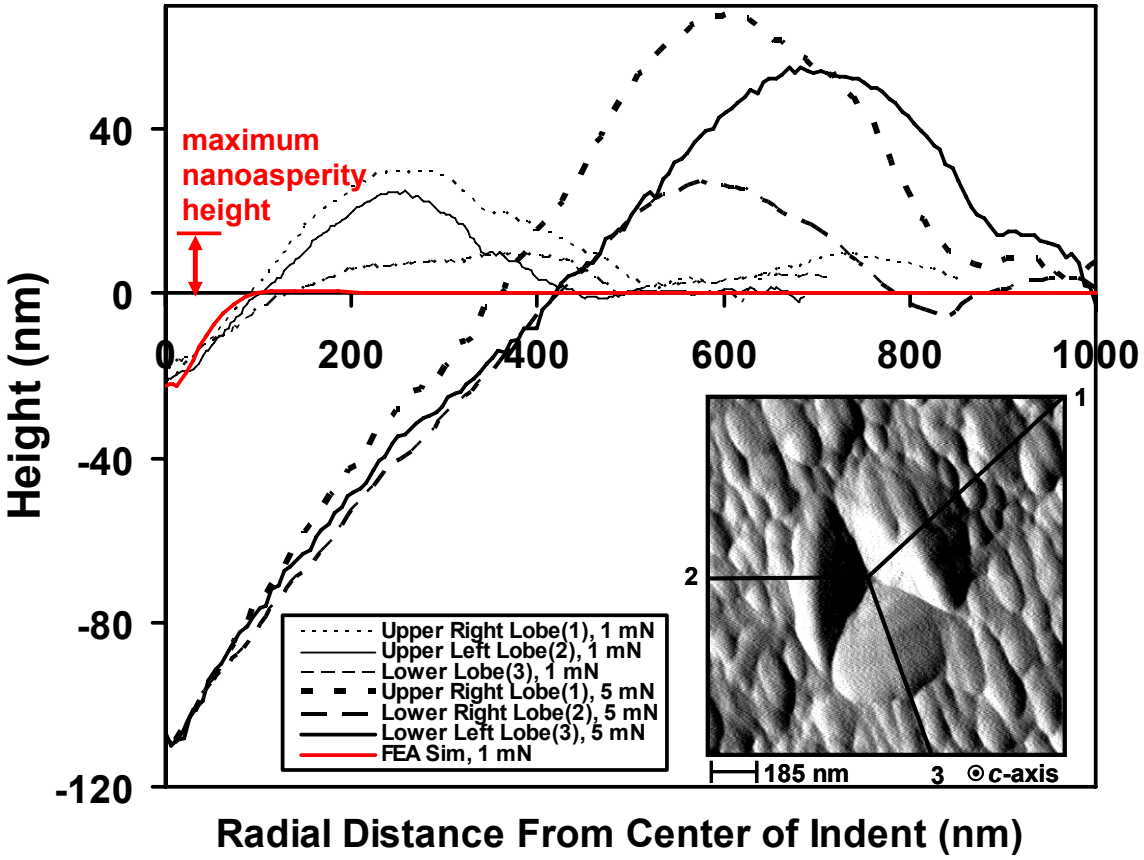

Fig. 4-5. Height profiles for 1000 μN and 5000 μN maximum load indents taken from tapping mode atomic force microscopy (AFM) images on freshly cleaved individual *Trochus Niloticus* nacre tablets. The inset is an AFM image of the residual indent for the 1000 μN maximum load.

Fig. 4-5 shows height profiles for indentations on freshly cleaved nacre showing pileup at maximum loads of 1000 μN and 5000 μN. For the 1000 μN maximum load, the average pileup height was ~ 21.1 ± 10.5 nm and spanned lateral distances from the edge of the indent of ~ 363 ± 49 nm (somewhat larger than that previously reported on *California red abalone*[23]).

4.3.3 ESTIMATION OF MATERIAL PROPERTIES

Work of Indentation. The plastic work or mechanical hysteresis energy, W_p, was found to be 10.1 ± 1.8 mN nm for the freshly cleaved nacre and 9.15 ± 1.76 mN nm for the artificial seawater soaked nacre at a 1000 μN maximum load. The elastic work, W_e yielded a value of 16.4 ± 1.0 mN nm for the freshly cleaved nacre and 16.0 ± .0.7 mN nm for the artificial seawater soaked nacre while the total work of deformation at a 1000 μN maximum load was 26.5 ± 1.6 mN nm and 25.2 ± 1.5 mN nm, respectively. All three mechanical works showed no statistically significant differences when comparing the two types of samples.

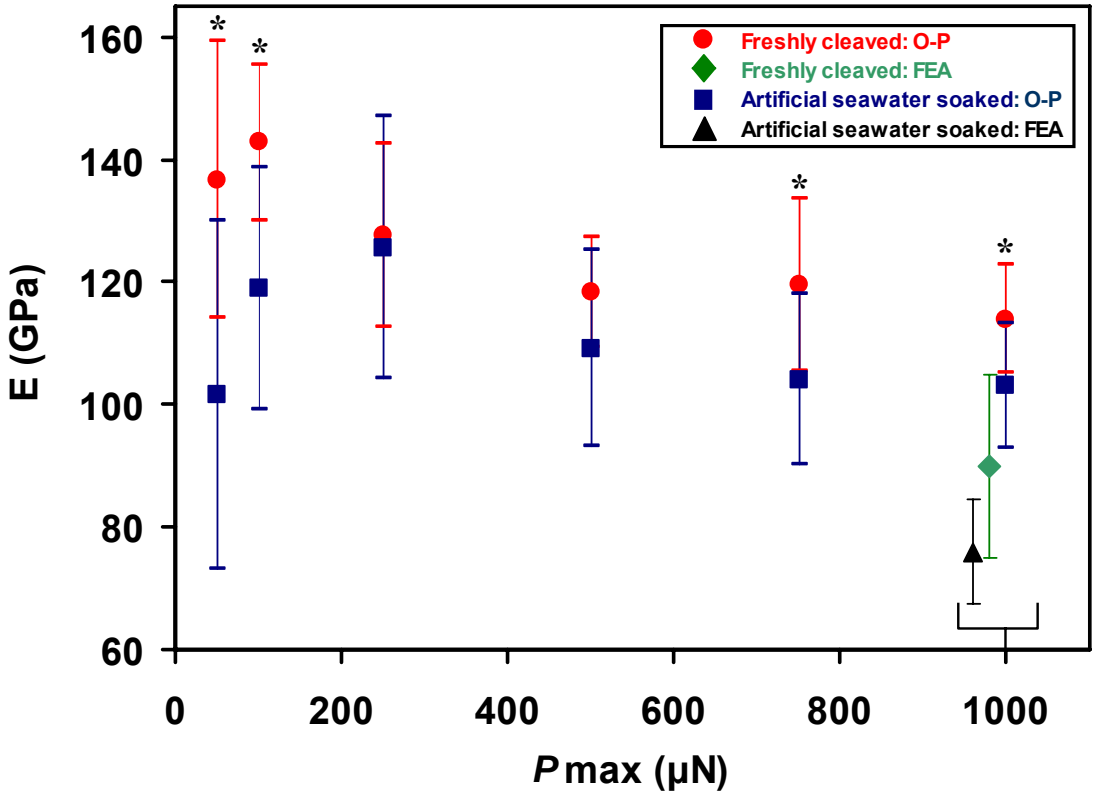

Fig. 4-6. Mechanical properties derived from nanoindentation curves on freshly cleaved and artificial seawater-soaked individual *Trochus Niloticus* nacre tablets as a function of maximum load; average elastic moduli, E, using both Oliver-Pharr analysis and FEA simulations

Oliver-Pharr (O-P) Estimations of Elastic Moduli. For freshly cleaved nacre, average values of the elastic moduli ranged between 114 and 143 GPa and for artificial seawater soaked nacre, average values ranged between 101 and 126 GPa (Fig. 4-6a). When comparing the data for freshly cleaved to artificial seawater soaked nacre at a given maximum load, all were found to be statistically different except for 250 and 500 μN maximum loads. For freshly cleaved nacre, elastic moduli compared at different loads were statistically different in 9/15 comparisons with 50-100, 100-250, 250-750, 500-750, 500-1000, and 750-1000 μN maximum loads being statistically similar. For artificial soaked nacre, elastic moduli compared at different loads were statistically different in 6/15 comparisons (50-250, 100-750, 100-1000, 250-500, 250-750, 250-1000

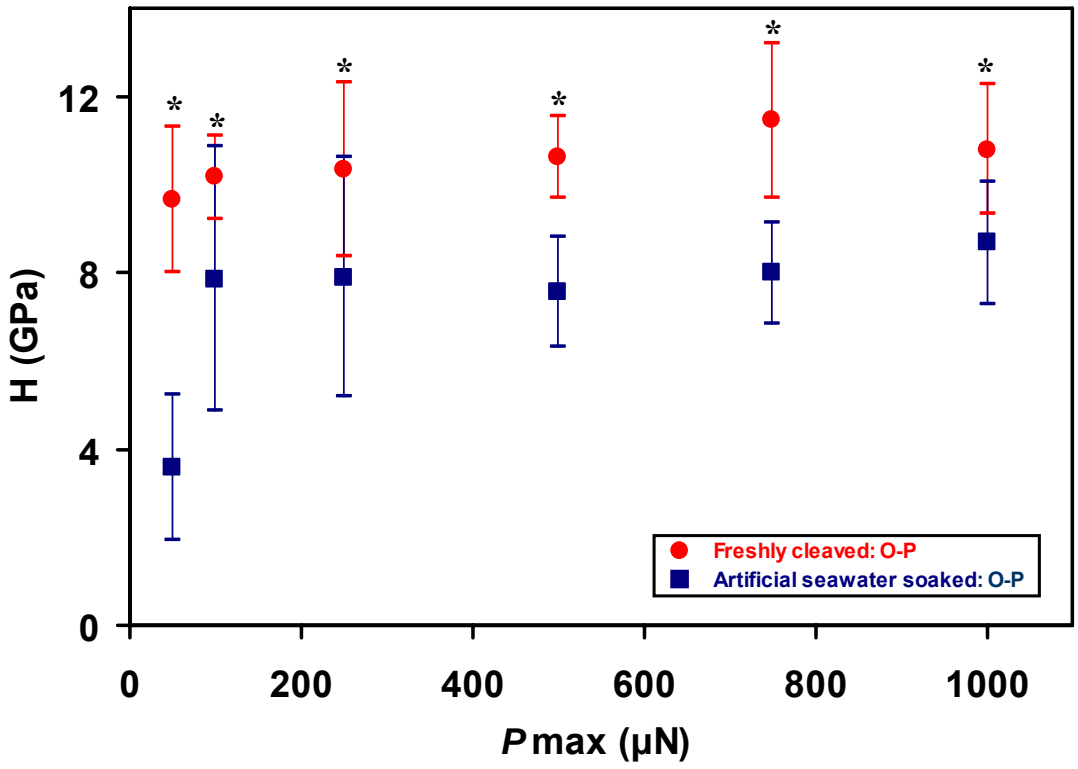

Fig. 4-7. Average hardness, H, derived using the Oliver-Pharr analysis.

μN).

Oliver-Pharr (O-P) Estimations of Hardness. Average hardness values ranged between 9.7 and 11.4 GPa for the freshly cleaved nacre and 3.6 and 8.7 GPa for the artificial seawater soaked samples (Fig. 4-7). When comparing the data for freshly cleaved to artificial seawater soaked nacre at a given maximum load, all were found to be statistically different. For freshly cleaved nacre almost no statistically significant differences were found as a function of maximum load (except for the 50-750 and 100-750 μN datasets). For artificial seawater soaked nacre, hardness compared at different

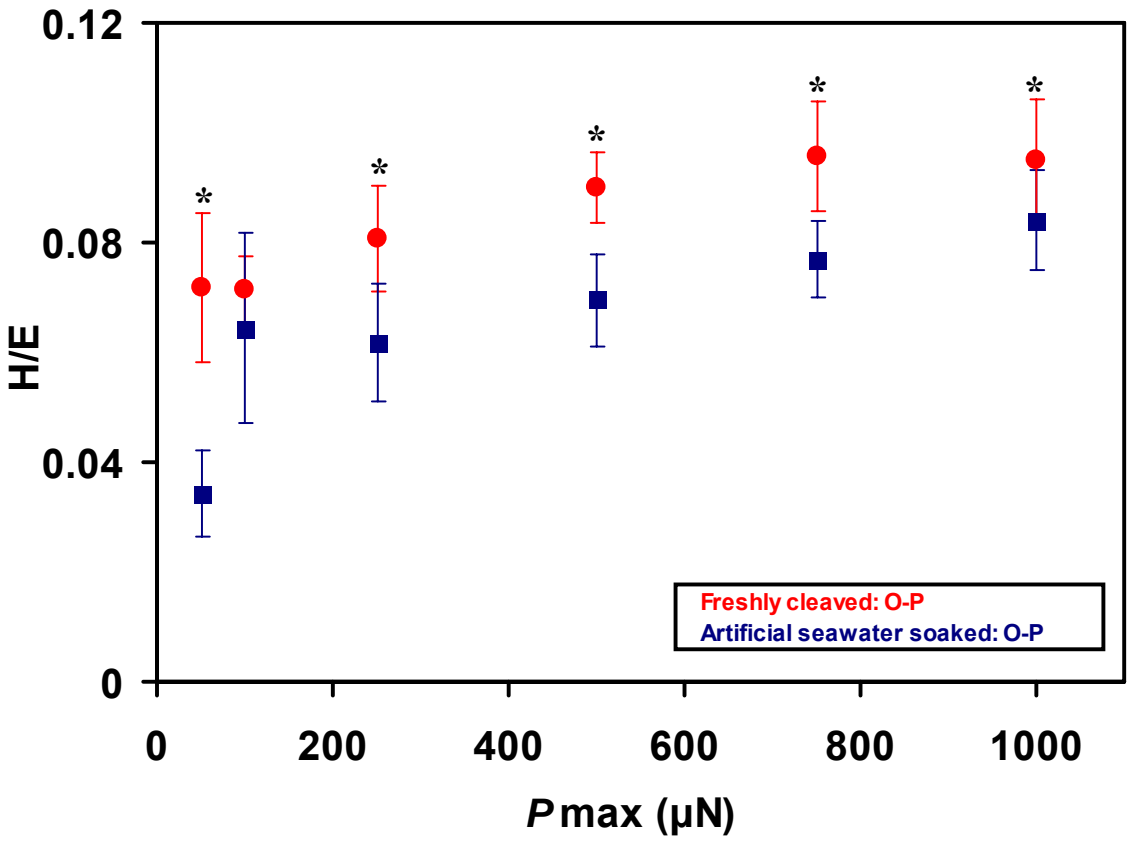

Fig. 4-8. H/E plot. The vertical error bars represent the standard deviation for that particular dataset and the * datasets indicate statistically significant differences ($p<0.05$) between the freshly cleaved and artificial seawater-soaked samples.

loads were statistically different in 6/15 comparisons where the 50 μN data compared to all the other loads was significantly different, as well as the 500–1000 μN comparison.

Oliver-Pharr Estimations of H/E Ratio. H/E values (Fig. 4-8) ranged between 0.072 and 0.096 for the freshly cleaved samples and between 0.034 and 0.084 for the artificial seawater soaked nacre. When comparing the data for freshly cleaved to artificial seawater soaked nacre at a given maximum load, all were found to be statistically different except for the 100 μN data. For the freshly cleaved samples, H/E values compared at different loads were statistically different in 10/15 comparisons (50-100, 50-250, 500-750, 500-1000, and 750-1000 μN were statistically similar). For the artificial seawater soaked samples, H/E values compared at different loads were statistically different in 12/15 comparisons (100-250, 100-500, and 250-500 μN were statistically similar).

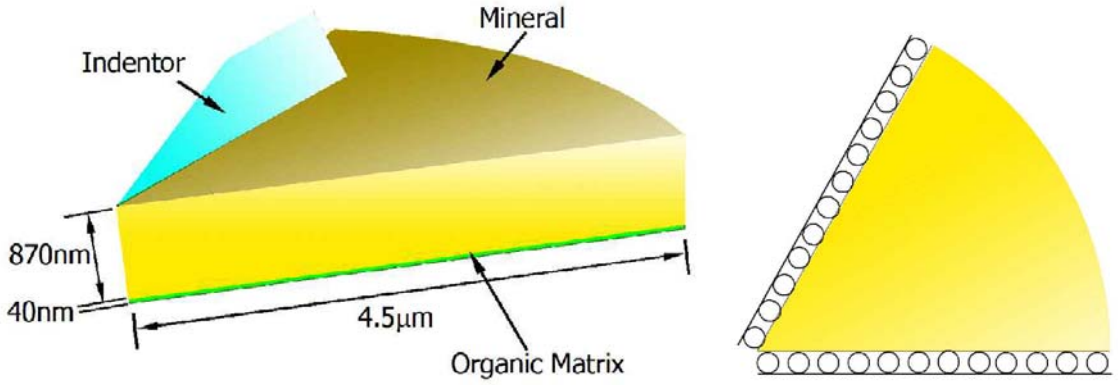

a **b**

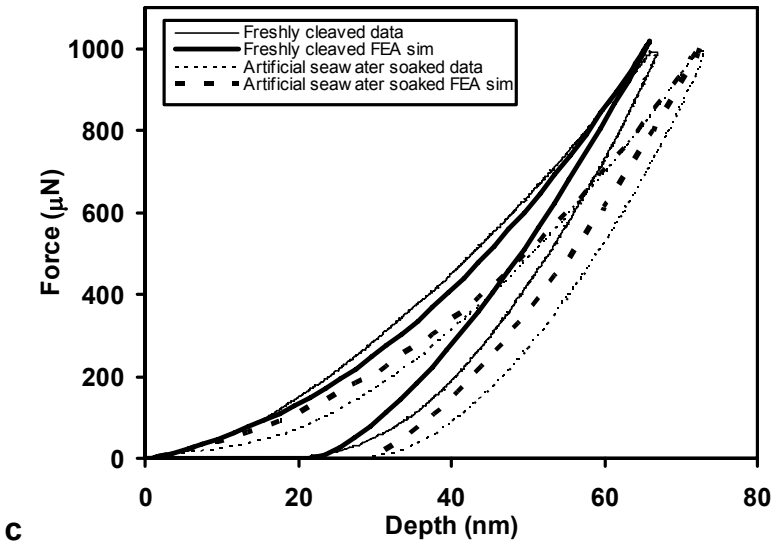

c

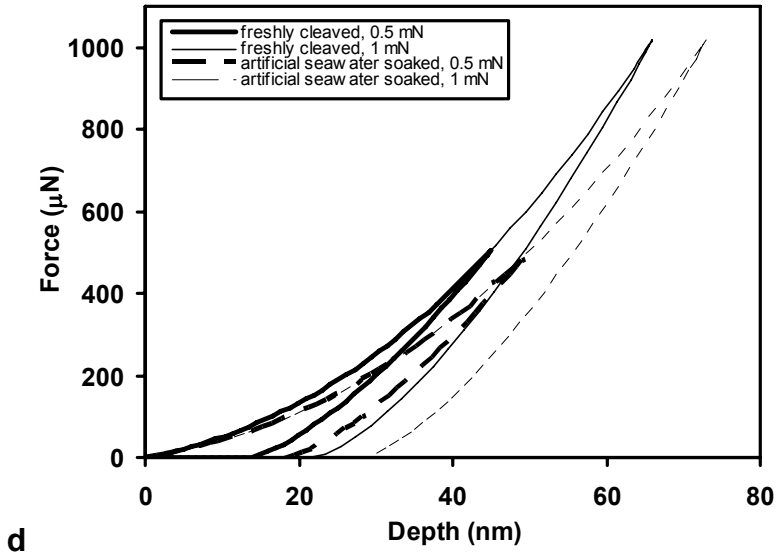

d

Fig. 4-9. Isotropic elastic-plastic finite element analysis (FEA) nanoindentation simulations; **(a)** schematic of model, **(b)** boundary conditions to ensure one sixth symmetry (top view), **(c)** simulations fit to average nanoindentation data on loading and unloading for 1000 μN maximum load. Input parameters were as follows; freshly cleaved nacre (E = 90 GPa, σ_Y = 11GPa) and artificial seawater soaked nacre (E = 76 GPa, σ_Y = 8.4 GPa) and **(d)** simulations for both nacre samples for maximum loads of 500 μN and 1000 μN.

Finite Element Analysis. FEA simulations (Fig. 4-9a,b) were used to fit values for the elastic modulus and yield stress to nanoindentation data. Three experimental

nanoindentation curves (1000 μN maximum load) were fit on both loading and unloading: the averaged curve (Fig. 4-9c,d), the highest curve, and the lowest curve for each of the two types of nacre samples. The elastic modulus of freshly cleaved nacre was found to be 92 ± 13 GPa (the standard deviation being due to the range in fits from low-to-average-to-high curves), whereas the nacre soaked in artificial seawater was found to have an elastic modulus of 79 ± 15 GPa (data plotted in Fig. 4-6 with the O-P estimations, a statistically insignificant difference comparing freshly cleaved and artificial seawater soaked due to the small number of data points, n=3). The yield strength of fresh nacre was found to be 11.1 ± 3.0 GPa and that for nacre soaked in artificial seawater was found to be 9.0 ± 3.2 GPa (a statistically insignificant difference comparing freshly cleaved and artificial seawater soaked due to the small number of data points, n=3). Fig. 4-10a shows a contour of the maximum principal stress on the surface when indented to 1000 μN, revealing very large tensile stresses in the pileup region. Fig. 4-10b shows the corresponding contour after unloading also revealing very high tensile principal stresses in the pileup region (a characteristic stress state seen in the extruded pileup region of indented materials). Note that cracks were not observed in the experiments indicating an ability to withstand these high tensile stresses at small length scales. Fig. 4-10c and d show 2D height maps at the point of maximum load (1000 μN) and after unloading, respectively. Fig. 16d reveals the residual indent as well as the surrounding pileup resulting in plastic extrusion from under the probe tip. A 1D height profile corresponding to the same radial directions as shown in the inset of Fig. 4-5 is plotted in Fig. 4-5 along with the experimental profiles.

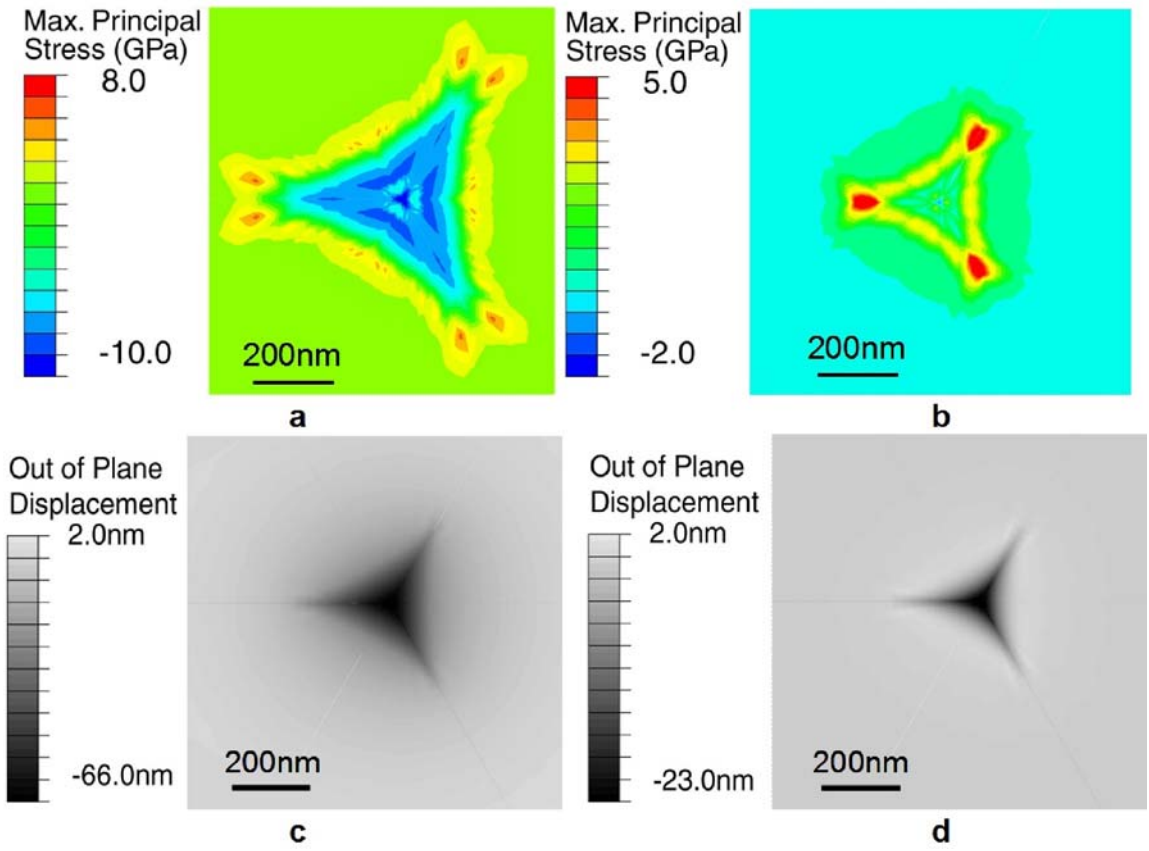

Fig. 4-10. The top view (plane perpendicular to nacre tablet *c*-axis) of the contour for the maximum principal stress **(a)** at a maximum load of 1000 μN, and **(b)** after unloading from 1000 μN and height contours **(c)** at a maximum load of 1000 μN and **(b)** after unloading from 1000 μN. Since only one sixth of the material is modeled, the plot here consists of six identical images from numerical simulations (E = 90 GPa, σ_Y = 11 GPa).

4.4 DISCUSSION

4.4.1 ULTRASTRUCTURE

Nanoindentation

The consistent change in slope observed in the nanoindentation curves for freshly cleaved *Trochus Niloticus* nacre at ~ 73 μN force and ~ 7-15 nm depth (Fig. 4-2c) is similar to a phenomenon previously reported for thermally etched *California red abalone*

nacre which takes place at ~25 μN and ~ 30 nm depth and has been suggested to be caused by a change in mechanism from plastic deformation and flattening of nanoasperities to deformation of the tablet over larger length scales.[108] The distance range over which the slope change was observed to take place in these experiments on *Trochus Niloticus* correlates well with the measured height of the nanoasperity assemblies and lends credence to this idea. Small kinks observed in the individual curves may be due to interfacial collapse, which is seen to take place over a small range of a few ~ nm. Table 2 summarizes all of the various nanomechanical properties measured in this study comparing the freshly cleaved and artificial seawater soaked nacre samples at a maximum load of 1000 μN.

Property	**n**	**Fresh**	**Hydrated**	**p<0.05**
maximal depth, h_{max} (nm)	14	67.0 ± 3.2	72.9 ± 4.6	Yes
O-P maximal contact area A_c (μm^2)	14	0.093 ± 0.012	0.117 ± 0.019	Yes
residual depth, h_p (nm)	14	20.8 ± 3.6	30.1 ± 5.3	Yes
plastic work, W_p (mN nm)	14	10.1 ± 1.8	9.2 ± 1.8	No
elastic work, W_e (mN nm)	14	16.4 ± 1.0	16.0 ± 0. 8	No
total work, W_T (mN nm)	14	26.5 ± 1.6	25.2 ± 1.5	No
O-P modulus, E (GPa)	14	114.0 ± 8.8	103.0 ± 10.1	Yes
O-P hardness, H (GPa)	14	10.8 ± 1.5	8.7 ± 1.4	Yes
O-P (H/E)	14	0.095 ± 0.011	0.084 ± 0.009	Yes
FEA modulus, E (GPa)	3	92 ± 13	79 ± 15	No
FEA yield stress, $\int_Y$ (GPa)	3	11.1 ± 3.0	9.0 ± 3.2	No
pileup height (AFM, nm)	3	21.1 ± 10.5	-	-
lateral pileup distance* (AFM, nm)	3	363.9 ± 49.3	-	-
residual indent area excluding pileup (AFM, μm^2)	3	0.072	-	-

Table 2. Nanoindentation properties (at a maximum load of 1000 μN) of nacre from *Trochus Niloticus* comparing freshly cleaved samples to hydrated samples incubated in artificial seawater for 10 weeks. Reported values are means ± one standard deviation.

Elastic Moduli

The elastic moduli obtained at a 1000 μN maximum load by the O-P method (114 ± 9 GPa and 103 ± 10 GPa for the freshly cleaved and artificial seawater soaked samples, respectively) were 21-26% higher than those estimated by the FEA simulations (92 ± 13 GPa and 79 ± 15 GPa for the freshly cleaved and artificial seawater soaked samples, respectively) which is statistically significant. The accuracy of the O-P predictions depend on the estimation of the contact area function and for the case of pileup (as observed via AFM), the O-P method underestimates this value, thus overestimating the moduli (since $E \sim 1/\sqrt{A}$). The FEA simulations more specifically account for the geometric details of the Berkovich geometry and also capture the details of the entire elastic-plastic loading/unloading process. Hence, FEA is expected to provide a more accurate estimation. However, the results indicate that a rather good approximation is obtained with the O-P fits. The FEA simulations predict the residual depth of the indent well but underestimate the experimentally observed pileup height (Fig. 4-5), most likely because it does not account for deformation of the nanoasperities.

Overall, values obtained from nanoindentation experiments were consistent with macroscopic measurements of aragonite.[93] The O-P moduli values for the nacre of *Trochus Niloticus* were found to be somewhat higher than that reported for diamond-cut, mechanically ground, polished, and hydrated nacre from *California red abalone* (60-80 GPa) at similar maximum loads (800 μN) calculated using the O-P method,[23] which could be due to a variations in sample preparation, species, age, *c*-axis orientation, location within in the shell, and/or degree of hydration. A decrease in modulus with increasing maximum load (-17 % from 50 μN to 1000 μN) was observed suggesting a length scale dependence. Hydration was found to generally result in a decrease in the

moduli (-1.5 to -26%). However, the elastic work for the freshly cleaved and seawater soaked nacre was found to be statistically similar; this result was due to the fact the unloading slopes were similar but the maximal depths were different (they varied only by ~6 nm) resulted in a statistically different contact areas calculated by the O-P method and thus, yielded statistically different values of moduli. This suggests that small variations in the surface nanoasperity structure can result in calculations of statistically different values of moduli not reflective of bulk tablet nanomechanical properties.

O-P Hardness and H/E

Hydration was observed to conclusively decrease the O-P hardness (-20 to -63%). Once again, this is not consistent with the statistically similar differences in plastic or total work due to the statistically different contact areas calculated by the O-P method. The hardness of the freshly cleaved samples was found to have minimal dependence on maximum load and the seawater soaked samples had a slight increase with maximum load. Due to pileup, an underestimation in contact area is expected to lead to an overestimation in the absolute values of hardness (H~1/A).

Nanoscale Deformation. AFM inspection of the indented region showed the existence of nanoasperity flattening within the indent region, plastic deformation, and no microcracks in the pileup region (as might be expected in a larger scale indentation process). This suggests that the length scale of the material and the indent process reveals a ductility that is not expected to be present at larger length scales (where a ceramic would be expected to exhibit microcracking under the tensile stresses observed in the pileup region and fail in a brittle manner). The observed ductility may be due to the small length scale ruling out defect initiated microcracking (i.e. the Griffith flaw

argument) and/or may indicate that occluded biomacromolecules within the tablet further mitigate any defects and add ductility to the deformation process. The configuration of the pile-up zones on the border of the indents (Figs. 4-4,4-5) demonstrates that the nanoasperities have the ability to undergo plastic deformation to accommodate the strain imposed by the indenter tip. Imaging of the indents (Fig. 4-4) is consistent with these results, as the region indented in hydrated nacre exhibits a much greater plastic deformation than the one in fresh nacre for the same load, consistent with the fact that the hydrated nacre tablet indicates a lower yield stress than those of the fresh nacre tablets.

4.5 CONCLUSION

It has been suggested that the nacre tablets serve as the primary load-bearing elements where the load is transferred through the bridging organic matrix via a shear lag mechanism.[115] The unique combination of both high local stiffness and strength of the individual nacre tablets observed here likely facilitate energy dissipating mechanisms such as intertablet shear and pullout (which are experimentally observed[6]) rather than brittle intratablet failure. Intertablet shear and pullout also allow for additional energy dissipation via extension and progressive unfolding of protein modules in the organic matrix (i.e. rupture of "sacrificial" weaker bonds).[67, 97, 98] It has also been suggested that interacting nanoasperities and mechanical interlocking provide resistance to interfacial sliding, thus determining the level of stress needed to initiate inelastic strain.[3, 94] The existence of a finer nanoasperity structure arranged into assemblies of larger nanoasperities would provide additional lateral resistance at an even smaller length scales

than previously thought. At high enough stress values, our data suggests that plastic deformation of the nanoasperities can take place initially and may act as a "safety mechanism," prior to intertablet shear.

CHAPTER 5 3D VISUALIZATION OF THE NANOMECHANICAL HETEROGENEITY WITHIN INDIVIDUAL NACRE TABLETS

5.1 MOTIVATION

A ubiquitous characteristic feature of natural materials is structural *heterogeneity*. Biological materials are composed of nanosized building blocks with distributions in shape, size, composition, and mechanical properties, innumerate interfaces, and a multitude of different types of biomacromolecules. Heterogeneity in structure leads to local variations in mechanical properties, which is a critical determinant of macroscopic mechanical properties of nanostructured composite materials. At this point, virtually nothing is known about the two-dimensional spatial distribution of mechanical properties at very small length scales in natural materials. To study this area, we have employed new nanomechanics methodologies and our preliminary experiments in this area have started to yield fascinating data. Modulus and hardness maps obtained by nanoindentation can be overlaid with a outline of the intra- and intertablet interfaces measured using tapping mode AFM after completion of the nanoindentation experiments. This procedure allows for correlation of spatial nanomechanical properties directly with specific nanoscale structural features.

5.2 MATERIALS AND METHODS

5.2.1 SAMPLE PREPARATION

T. niloticus shell specimens were purchased from *Shell Horizons* (Clearwater, FL) and *H. rufescens* specimens from *The Abalone Farm* (Cayucos, CA)Nacre samples were cut from shells of mature *Trochus niloticus* (purchased from Shell Horizons, Clearwater, FL). The shells were cut using a diamond-impregnated circular saw (Buehler, Isomet 5000) at a blade speed of 975 rpm and cooled with a PBS-buffered water solution (pH 8.0). Slices of nacre were harvested from the inner nacreous chamber walls. These slices were then cleaned and sonicated in de-ionized water for 10 seconds with an Ultramet ultrasonic cleaner. All samples used for nanoindentation were cleaved in uniaxial compression in ambient conditions using a Zwick-Roell mechanical tester (Model BTC-FR010TH.A50, 10-kN maximum load cell, 0.01 mm/min), with axis of loading parallel to the tablet layers (i.e. perpendicular to the aragonite c-axis). This method of preparation produced cleavage between the tablet layers, leaving a flat surface for nanoindentation.

5.2.2 NANOINDENTATION

A *Hysitron, Inc.* ® Triboindenter nanoindenter was used to conduct nanoindentation experiments in ambient conditions. Two different probe tips were employed, a trigonal pyramidal Berkovich tip (mean conical angle of 70.3°) and a sharper cube corner tip (mean conical angle of 42.3°). Mapping nanoindentation experiments were carried out on freshly cleaved samples at maximum loads ranging from 30 to 500

μN maximum load with a loading rate of 50 μN/s. Square grids of 21 indents on each side were set as the indentation pattern for a total of 441 indents per grid respectively. Neighboring indents were separated by 1.5 μm on each side. The entire grids, therefore, covered an area of 900 μm^2 (30 μm x 30 μm) respectively. Eight large indents were also positioned at a maximum load of 10 mN along a circle of 50 μm diameter in order to facilitate locating of the indents upon optical and AFM imaging. Values for the elastic modulus were calculated by means of Oliver-Pharr (O-P) analysis of the nanoindentation curves[110].

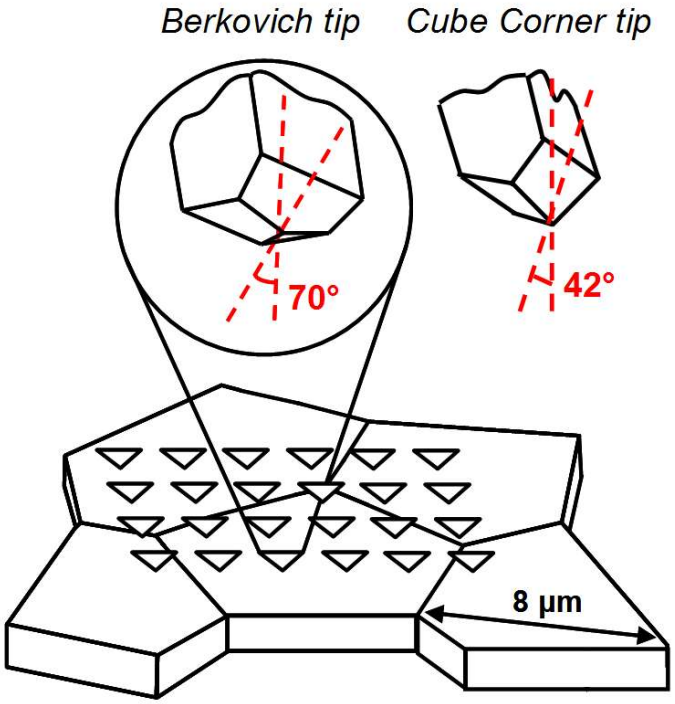

Fig. 5-0 Schematic of the mapping indentation experiments and relative shape of indenter probes.

5.2.3 ATOMIC FORCE MICROSCOPY

Tapping mode atomic force microscope (TMAFM) imaging in ambient conditions was employed to produce surface topographical images of freshly cleaved nacre samples. In ambient humidity, a thin layer of water (2 –10 Å thick) exists on the surface[99] yielding closer to physiological images than completely dried samples. A *Digital Instruments* (*DI*, Santa Barbara, CA) Multimode SPM IIIA was used with AS-130 "JV" or "EV" piezoelectric scanners. Tapping mode scans with *Veeco* Si cantilevers (V-shaped with approximately square pyramidal probe tip geometry, tip half angle of ~17.5°, l ~ 125 μm, k ~ 0.40 N/m, and R_{TIP} ~ 10 nm). A scan rate of 0.25-2 Hz using a maximum sample size of 512 x 512 pixels was employed at gains between 0.1-0.3. The drive amplitude and amplitude set-point were optimized upon tuning. The x- and y- scan directions were calibrated with a 10 x 10 μm^2 grid and the z-direction was calibrated with 5 nm diameter beads on a cleaved mica surface. The images to be shown report amplitude (i.e. cantilever oscillation amplitude) and phase (i.e. cantilever phase lag). Amplitude reflects of surface topography while phase mode is sensitive to many properties such as friction, adhesion, (visco)elasticity, and composition.

For *in-situ* imaging of residual indents, a *Quesant* Q-Scope 350 (attached to a *Hysitron, Inc.* nanoindenter*)* was used in tapping mode with a piezoelectric tube scanning element (X-Y scan range ~40 μm, vertical Z limit ~4.5 μm) and Si_3N_4 Wavemode NSC16 cantilevers (rectangular shaped with conical probe tip geometry, l ~ 230 μm, width ~ 40 μm, cone angle < 20°, probe tip height ~ 15-20 μm, resonance frequency, ω ~170 kHz, k ~ 40 N/m, and R_{TIP} ~10 nm). A scan rate of 2 Hz using a maximum sample size of 512 x 512 pixels was employed. The drive amplitude and amplitude set-point

(~0.25 V) were optimized prior to imaging and gains between 350 and 550 were employed.

5.3 RESULTS

Fig. 5-1 a shows an AFM image of the cleaved surface of T. niloticus after indentation. The outlines of the tablets have been overlaid with dark lines. Fig. 5-1 b and

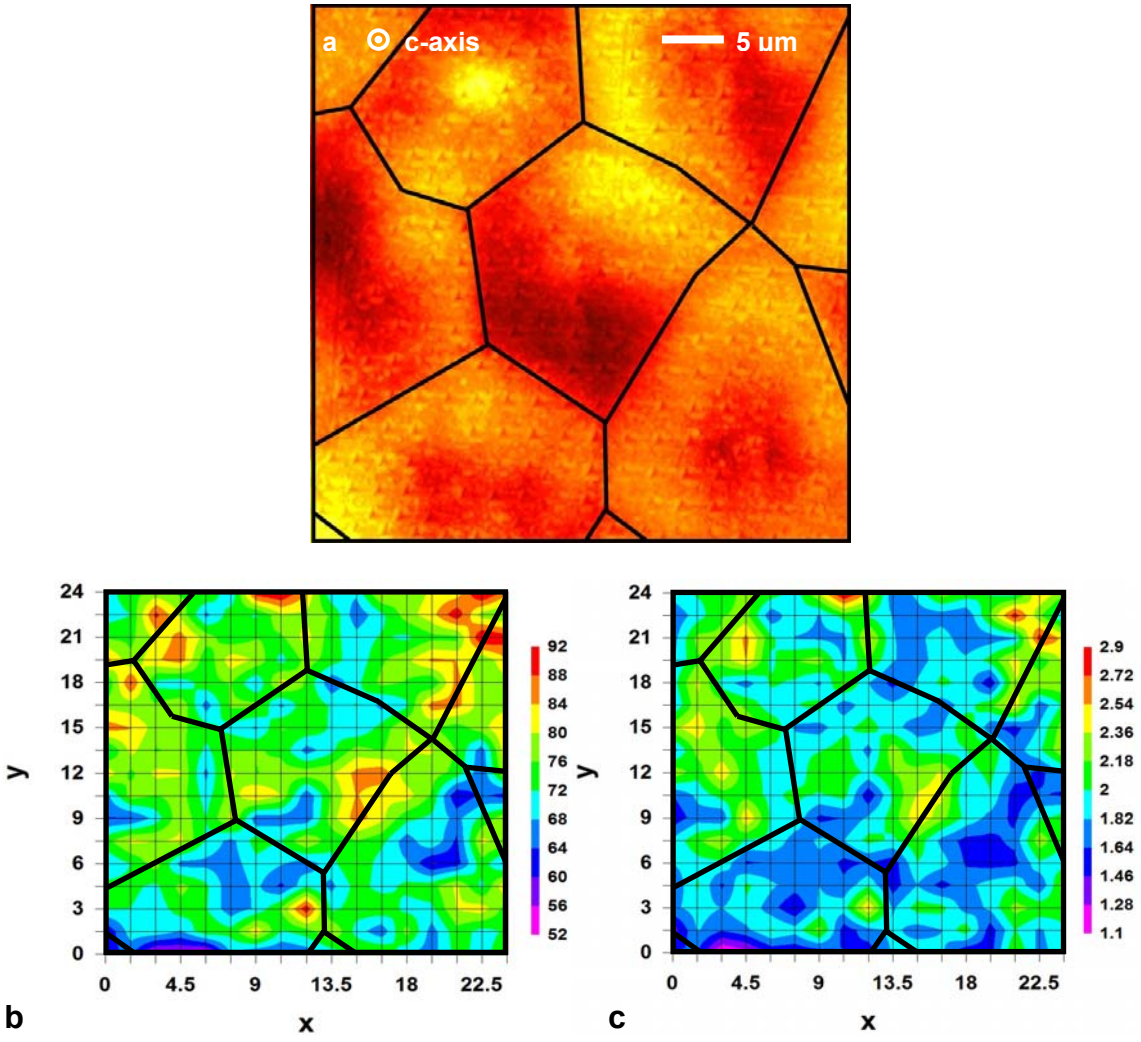

Fig. 5-1 100 μN indentation mapping of the polished surface of T. niloticus **(a)** TMAFM height image of the indented region. **(b)** corresponding Indentation modulus map and **(c)** hardness map.

c show the 2-D maps for Indentation modulus and hardness respectively, measured by nanoindentation of the surface at a maximum load of 100 µm. The lines delimiting the tablets have been overlaid in order to be able to correlate the mechanical properties to the tablets features. No obvious correlation between topography and mechanical properties can be observed from the maps, and this is further verified by a statistical analysis presented in Fig. 5-2. The Indentation modulus and hardness values are plotted versus the indent distance to the closest tablet border in Fig. 5-2 a and b. A linear regression of the

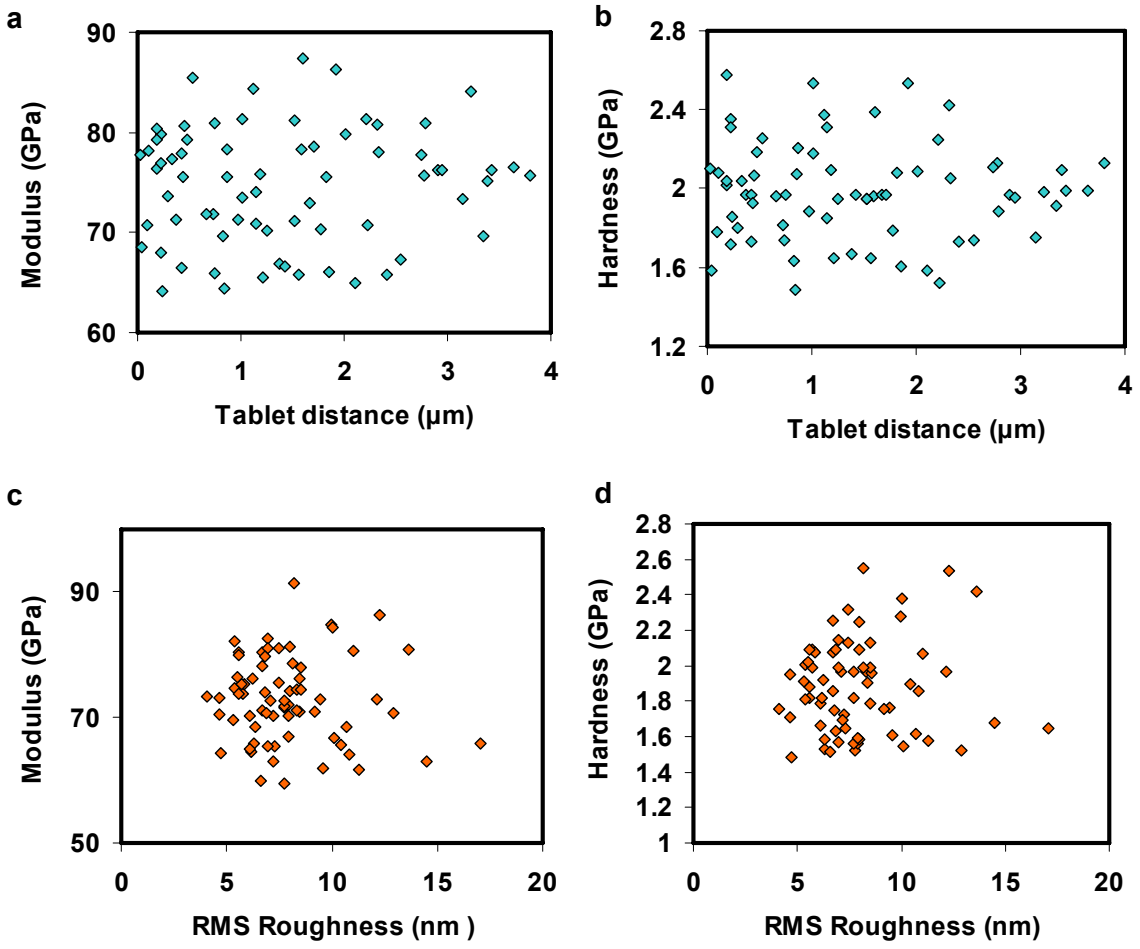

Fig. 5-2 Correlation between mechanical properties and probed location **(a)** Indentation modulus versus distance to tablet boundary **(b)** hardness versus distance to tablet boundary **(c)** modulus versus RMS roughness and **(d)** hardness versus RMS roughness.

distribution yielded a regression coefficient R^2 of 0.0044 and 0.0011 respectively, indicating that there is no correlation between the indents and their location on a tablet. In Fig. 5-2 c and d, Indentation modulus and hardness were plotted versus the local RMS roughness and again did not show any correlation (R^2 = 0.0047 and 0.0031 respectively). Coefficients of variations were found to range from 10 to 20% for the modulus, and from 10 to 25% for the hardness.

The next series of experiments was conducted on the polished tablet surface of H. rufescens. Measurement of the local RMS roughness by AFM yielded values consistently lower than 1 nm. Mapping indentation across several layers resulted in intriguing periodic patterns for both Indentation modulus and hardness. The use of different loads (30, 100 and 500 μN) and different probe tips (Berkovich and Cube corner) resulted in the same trends. Fig. 5-3 a is the TMAFM height image of the indented region (Cube corner, maximum load of 30 μN) where one can distinguish the array of indent residual footprints covering the surface. Several superimposed tablet layers can be observed due to the fact that the polishing was conducted at a slight angle with regard to the local plane of the tablet layers. In most locations (white arrows) the surface is extremely smooth (RMS roughness < 1 nm) however the transition from one layer to another occurs as a relatively more abrupt step, as can be seen by the sudden change of contrast (black arrows). AFM measurement of the steps shows that they span a height of 30 to 60 nm, and have a slope approximately 3 times steeper than the rest of the surface.

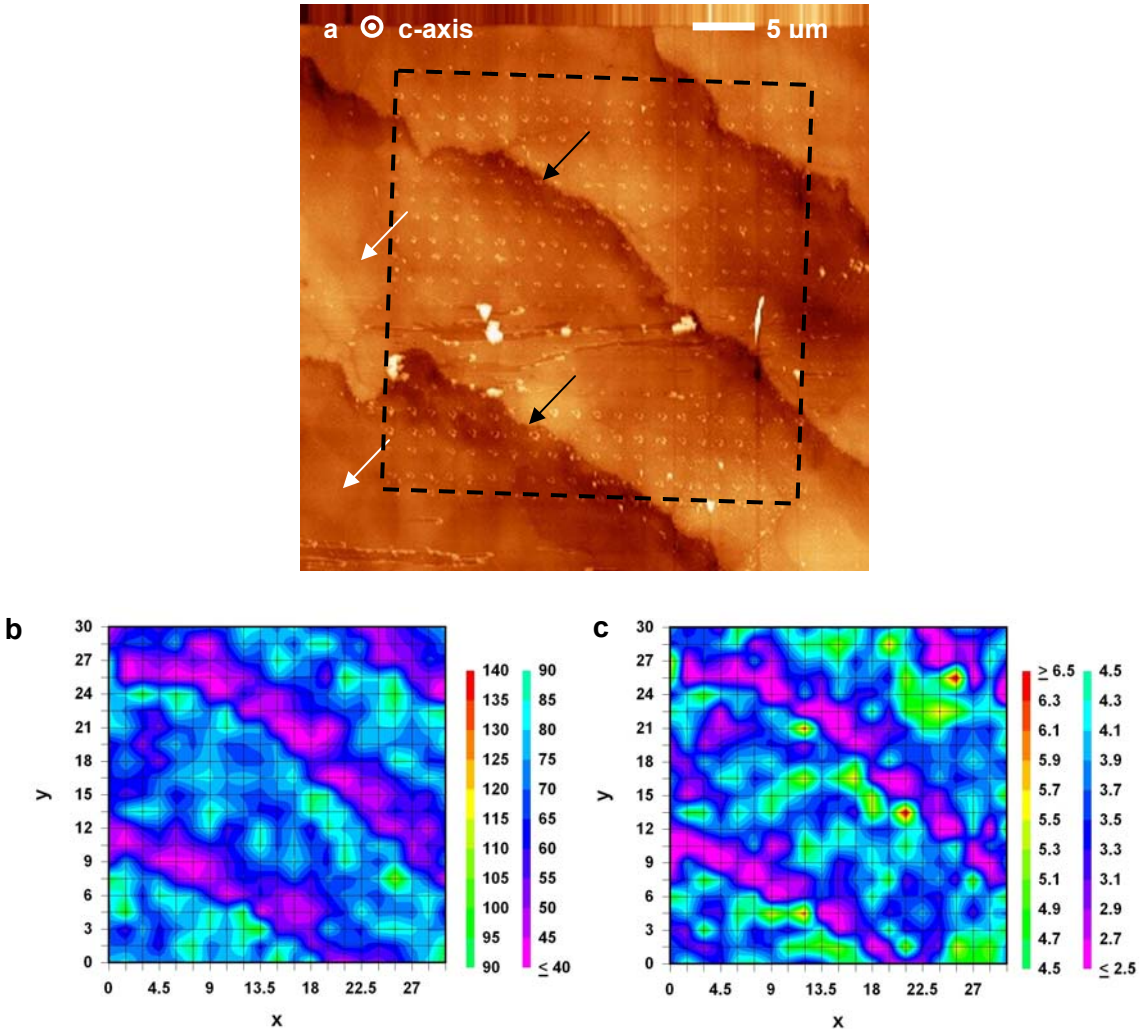

Fig. 5-3 30 μN indentation mapping of the polished surface of H. rufescens **(a)** TMAFM height image of the indented region. **(b)** corresponding Indentation modulus map and **(c)** hardness map.

In Fig. 5.3 b (Indentation modulus) and c (hardness) one can see that areas close to the layer ledges seem to have lower values than away from it. Closer examination reveals that it actually is the region just above the ledge that exhibits these low values. On the contrary, the region just below the ledge tends to exhibit slightly higher values than other parts of the surface. For this 30 μN experiments, the values for E and H in the softer

region are about 50 GPa and 2.7 GPa respectively, and in the hard region about 80 GPa and 4.5 GPa, which are significantly different values.

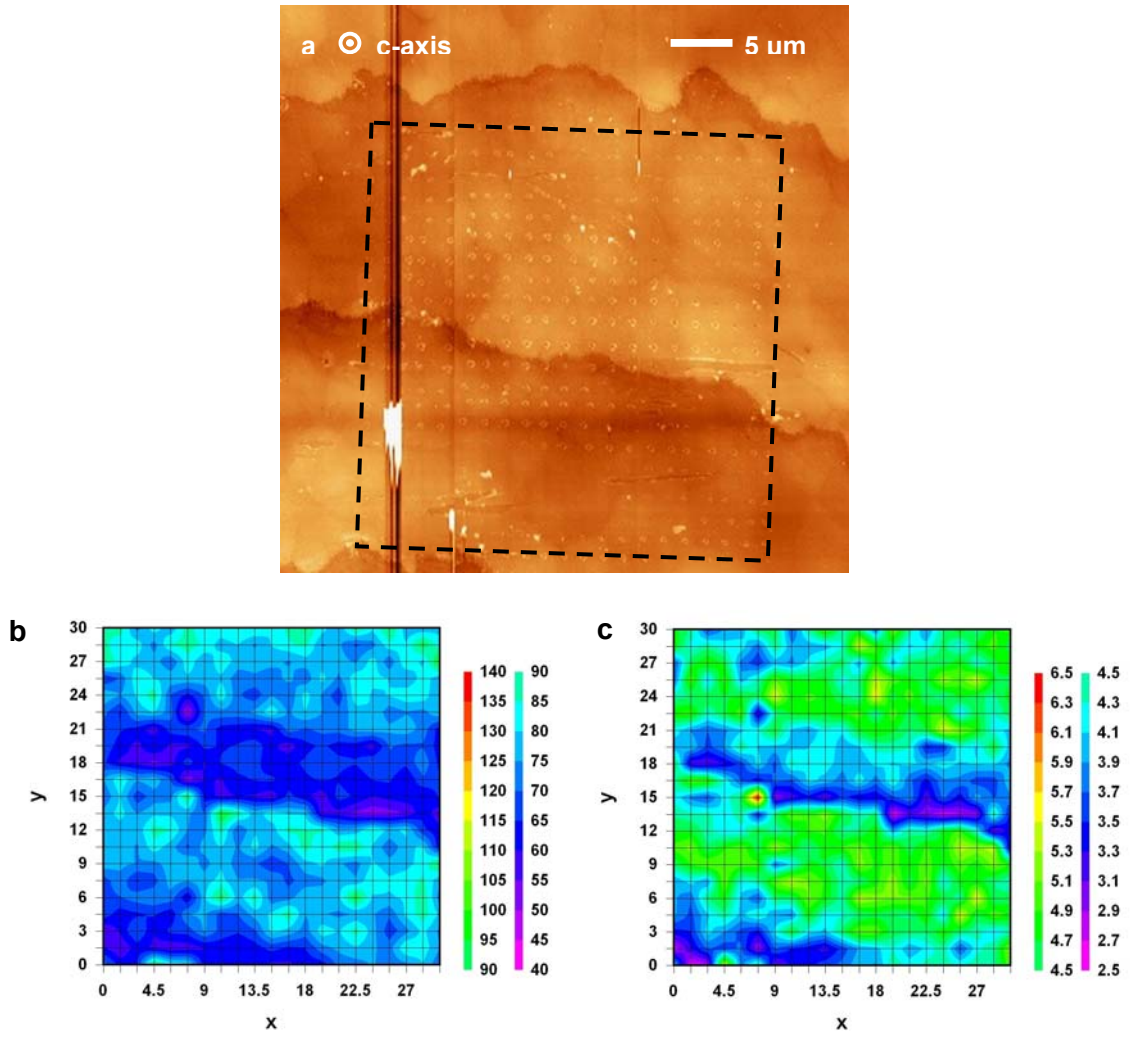

Fig. 5-4 100 µN indentation mapping of the polished surface of H. rufescens **(a)** TMAFM height image of the indented region. **(b)** corresponding Indentation modulus map and **(c)** hardness map.

Fig. 5-4 and 5-5 present similar data for maximum loads of 100 and 500 µN respectively. The color scales are conserved from one figure to another to allow easier comparison. For these higher loads, the trends observed in Fig. 5-3 are also apparent, even though the absolute values are somewhat different. For the 100 and 500 µN

experiments respectively, the values for the soft surface are E ~ 55 and 50 GPa, H ~ 3.3 and 2.7 GPa, and for the harder surface E ~ 80 and 65 GPa, H ~ 5.1 and 3.8 GPa.

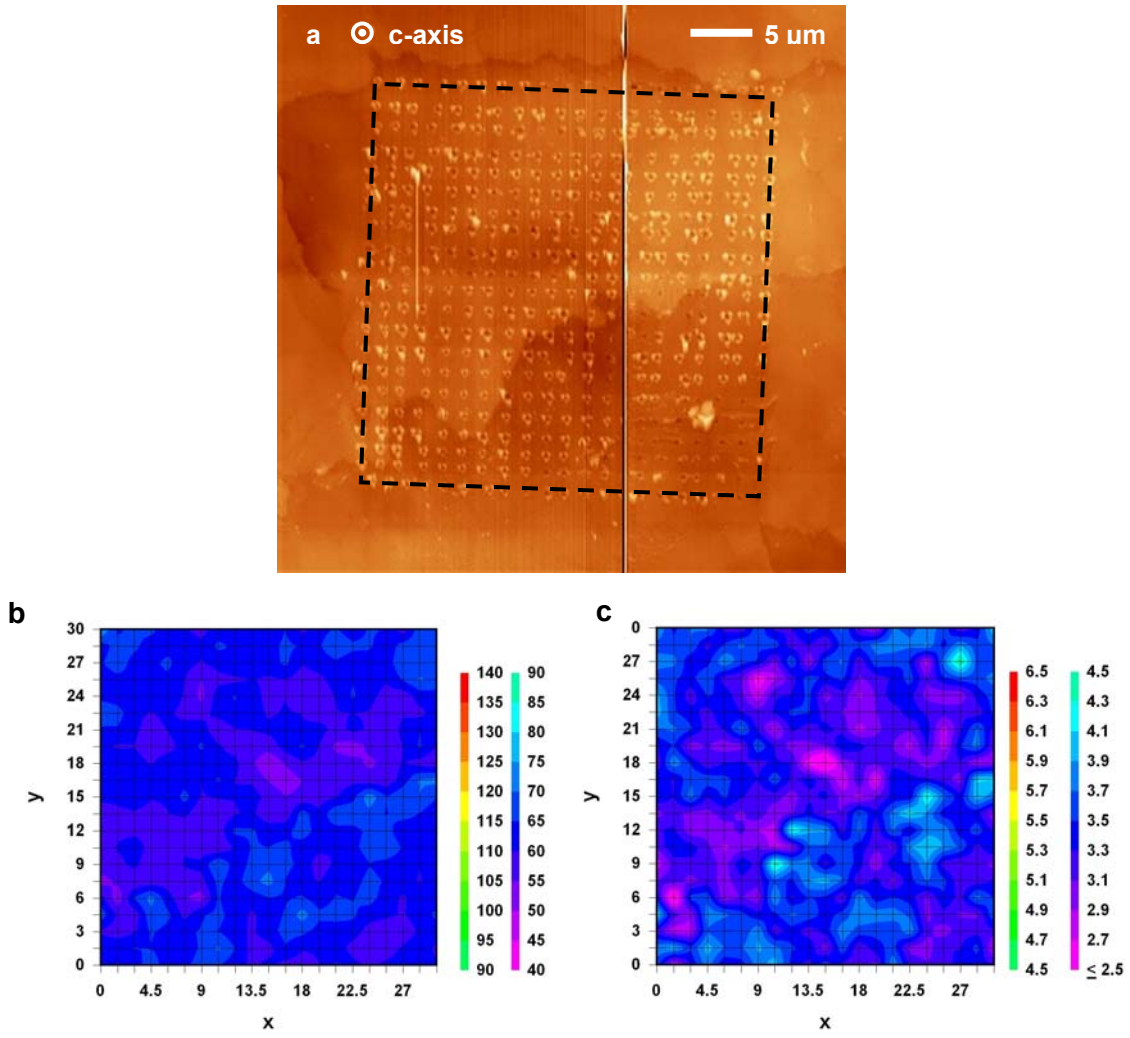

Fig. 5-5 500 μN indentation mapping of the polished surface of H. rufescens **(a)** TMAFM height image of the indented region. **(b)** corresponding Indentation modulus map and **(c)** hardness map.

Fig. 5.6 is a summary of the measured Indentation modulus and hardness for about 30 nanoindentation experiments on either cleaved or polished H rufescens tablet surface. A few experiments conducted on polished single crystal aragonite (with the c-axis parallel to the load) are also reported. Both Berkovich and Cube corner probe tips

were used. The maximum load was 100 µN for all experiments, and resulted in maximum depth of indentation ranging from 20 to 50 nm (Berkovich tip) and 40 to 105 nm (Cube corner tip) in nacre. In nacre, some samples were polished (yellow symbols) and other were simply cleaved along the tablet layers (green symbols). The red symbols are for aragonite. It clearly appears that single crystal aragonite is both stiffer and less

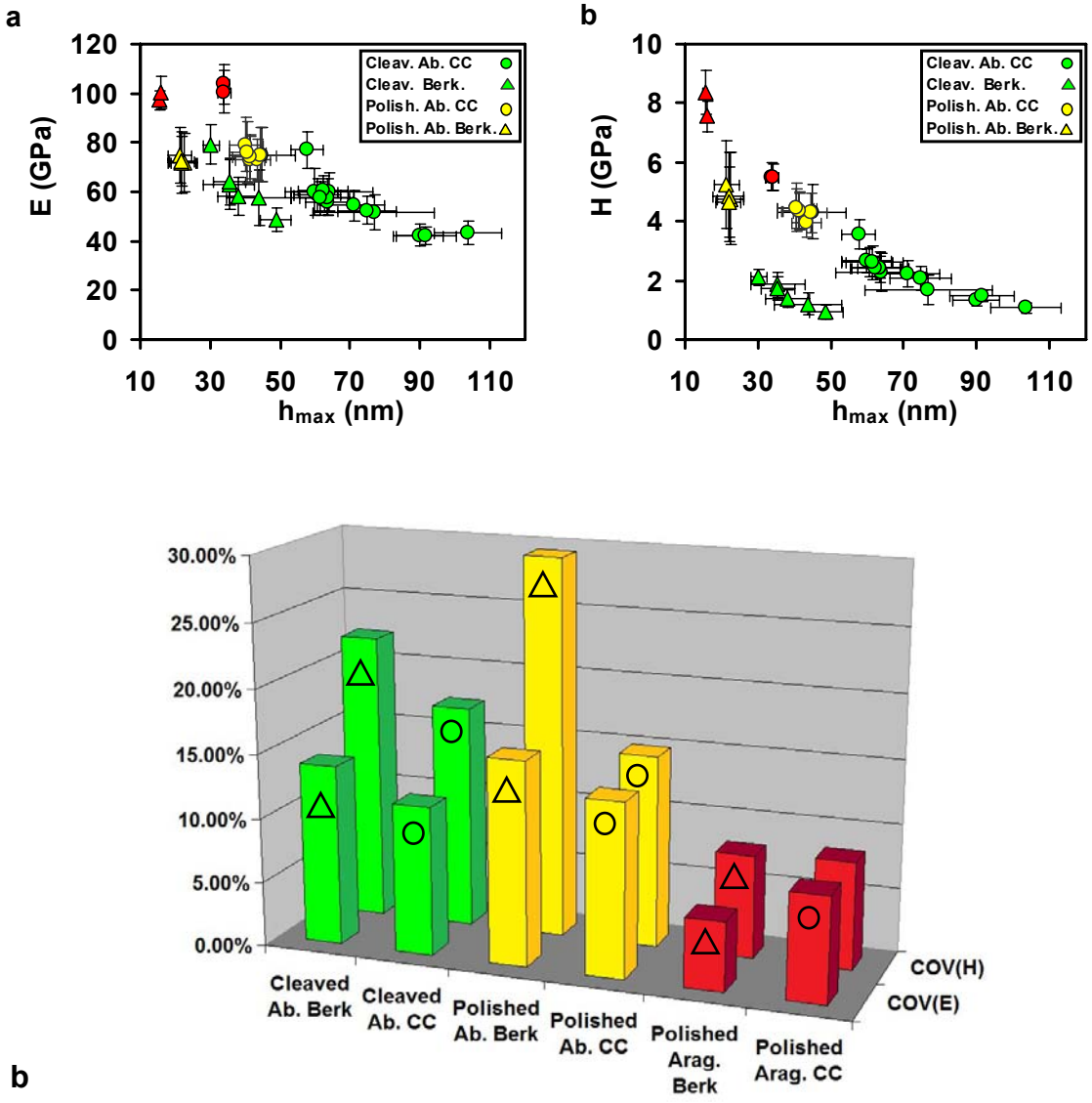

Fig. 5-6 Summary of thirty 100 µN indentation mapping on single crystal aragonite and H. rufescens samples **(a)** indentation modulus versus max. depth of indentation, **(b)** hardness versus max. depth of indentation, **(c)** coefficient of variation for modulus and hardness of each group

ductile than nacre. Cleaved nacre has a surface that is almost always more compliant and always more ductile than polished nacre. The distribution of the values is larger for cleaved nacre than for polished nacre (Fig 5-6 c). Compared to crystalline aragonite, both polished and cleaved nacre exhibit a significantly higher COV (about 2 times greater). Experiments were conducted on the surface of tablets facing the outside of the fish as well as tablets facing the inside of the fish, but no significant difference could be found.

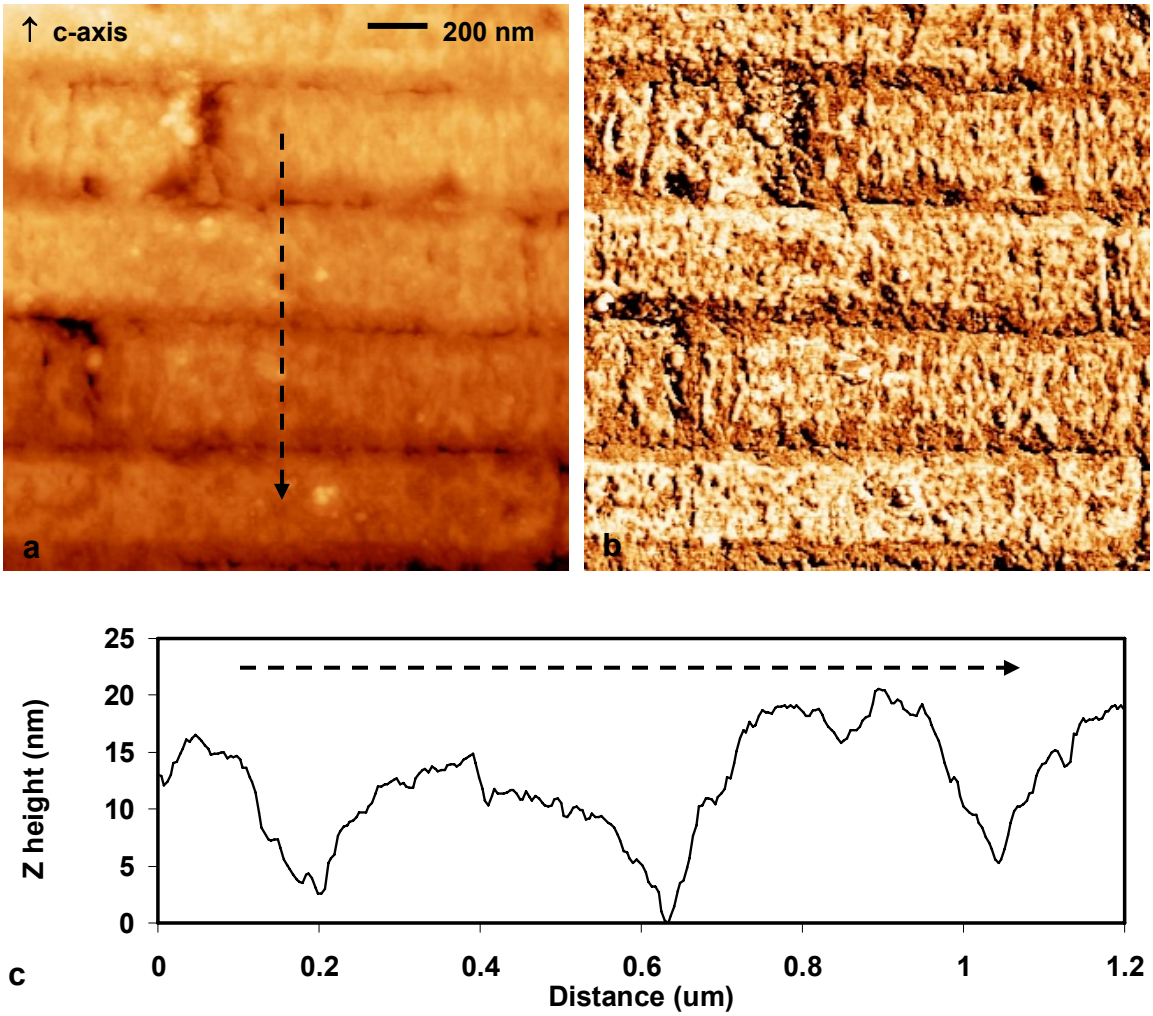

Fig. 5-7 100 μN indentation mapping of the polished surface of H. rufescens **(a)** TMAFM height image of the indented region. **(b)** corresponding Indentation modulus map and **(c)** hardness map. **(c)** variation of the polished surface topography (z-height profile) along the cross-section.

AFM imaging of the polished cross-section of the nacreous layer of H. rufescens provides some very interesting results with regard to potential heterogeneity in the tablet mechanical properties and nanostructure. Fig. 5-7 shows the TMAFM height and phase images of the cross-sectional surface of the tablets after polishing. It can be seen that more material is being grinded away near the interlamellar region than at the core of the tablets. This is further confirmed by the alternation of darker (softer) and lighter (harder) zones on the phase imaging and by the appearance of profiles drawn across several tablets.

5.4 DISCUSSION

In this chapter, we report several results on the distribution of mechanical properties within single nacre tablets. No correlation could be found with either the location of the indents on the tablet surface with regard to its boundaries or the local topography. This suggests that the mechanical heterogeneity observed for individual tablets (COVs ranging from 10 to 25 %) finds its origin at smaller length scale rather than by a continuous variation across one or several tablets. It is very likely that the local organic and water content plays a defining role, as was found in Chapter 4.

Another important result lays in the discovery of layers of different mechanical properties within a tablet. One could object that this phenomenon might be an artifact from the sample preparation, since the samples have to undergo polishing. However, the rate of dissolution of calcium carbonate in water is much lower than the mechanical grinding that occurs during polishing. Samples let to soak for one hour in DI water where found to exhibit a very slight surface etching, probably of the order of a few nanometers

since the appearance was still very smooth. Polishing using colloidal suspension removes several tens of microns per hour, which is 4 orders of magnitude faster. Furthermore, polished samples were probed at depths ranging from 20 to 50 nm and consistently showed the reported trends. Since water affects at most the first nanometers, it is unlikely that the contact with water during polishing has much impact on the properties measured here. Other common artifacts in the measurement such as roughness can be ruled out since the tablet surface was measured by AFM to have a RMS roughness below 1 nm.

Experiments conducted with different tips, at different loads, in several specimens from two distinct gastropod mollusk species consistently show an alternation of hard and soft layers with the same periodicity as the tablet layer thickness. TMAFM imaging provides further evidence that the outer surfaces of each tablet (lining the interlamellar region) have a more compliant and ductile behavior than the core of the tablets.

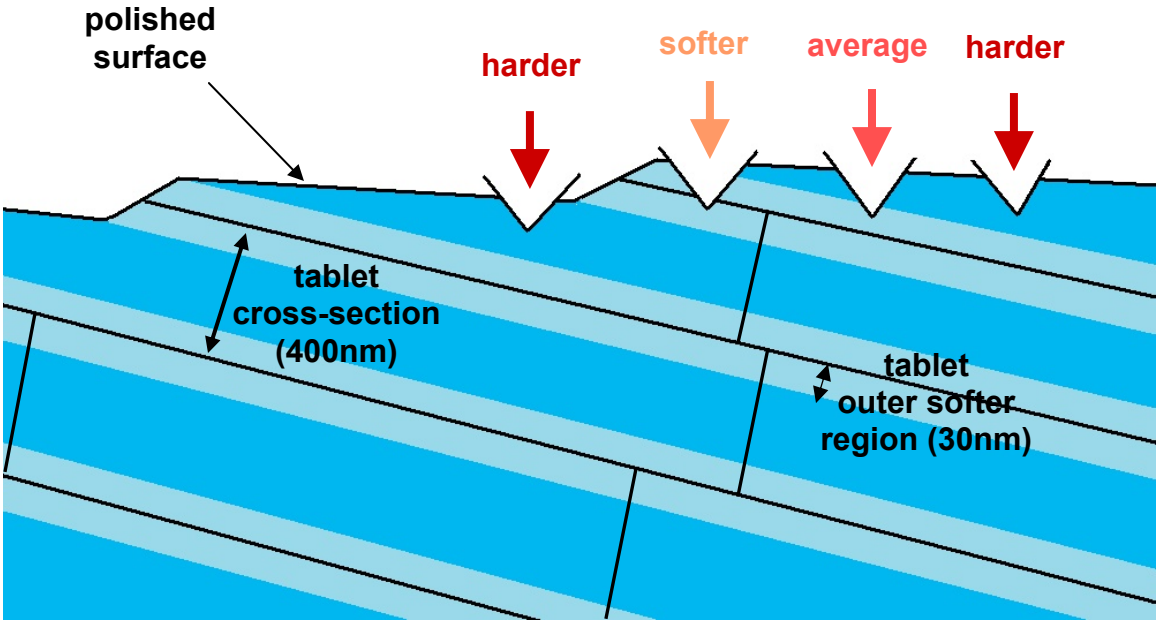

Fig. 5-8 Dual-layer model for the inner nanoscale structure of single nacre tablets in gastropod mollusks.

The model described in Fig. 5-8 can account for the different findings. The increased slope at the ledge of tablet layers can be accounted for by the presence of this doubled soft layer, which polished away faster than the harder core layer and hence produces steeper slopes on the surface. This also explains the abrupt change of measured mechanical properties that occurs when switching layers on the polished surface.

CHAPTER 6 ULTRASTRUCTURAL STUDY OF THE ARMORED SCALES OF *POLYPTERUS SENEGALUS*

Part of this chapter is submitted for publication.

6.1 INTRODUCTION

Dermal armor in fish first appeared during the beginning of the Paleozoic period during the Ordovician with the rise of the Ostracoderms ~ 500 million years ago[116] and was common among these earliest fishes.[117] In 1857, the geologist Hugh Miller speculated on the mechanical design of ganoid scales by drawing analogies with "the principle of the two tables and *diploe* of the human skull, the principle of the variously arranged coats of the human stomach, and the principle of Oliver Cromwell's fluted pot."[118] Romer in 1933 hypothesized that dermal armor served as a protection from predators,[119] and subsequently a number of additional mechanical and non-mechanical functions have been proposed.[120-122] As ancient fish became more predaceous,[123] their armor evolved in terms of their multilayered material structures and overall geometries, e.g. larger plates broke up into many smaller ones, the thickness of various layers decreased, and the number of layers decreased; all of which would have decreased weight, improved flexibility and maneuverability, and increased speed.[117] Interestingly,

many parallels can be found between the evolution of armor in the animal world and human-designed engineered body armor, both of which appear to be controlled by a balance between protection and mobility, in order to maximize survivability.[124] The design strategies utilized by mineralized biological tissues, in general, is an area of great interest and much progress has been made in the understanding of concepts such as crystalline nucleation, growth, and morphology, biomacromolecular intercalation and reinforcement, modulation of crystal texture, stabilization of amorphous phases, small length scale effects, etc.[125-129] Little is known about the mechanical properties of dermal armor and scales, as well as the specific *mechanical roles* of the mathematical form of material property variations (e.g. gradients) both within and between various layers, the number of layers, the layer and junction thicknesses, structures, and geometries, the constitutive laws of each layer, etc. and more importantly, the relationship of these parameters to larger scale biomechanical performance and environmental stresses (e.g. predatory attacks, etc.). Here, we employ a multiscale experimental and computational approach to elucidate such design principles, in particular with regards multilayering and grading. The general methodologies presented here are applicable to a broad range of multilayered structural biological materials (e.g., crustacean[130] and insect exoskeletons,[131] gastropod mollusk shells,[125] teeth,[132] etc.) and are able to yield a mechanistic understanding of how different organisms were designed, and possibly evolved, to sustain the loads they experience in their environment. Such fundamental knowledge, in particular threat-design relationships, holds great potential for the development of improved biologically-inspired structural materials,[133] for example; soldier, first responder, and military vehicle protective applications.[124] The present chapter reports the

investigation of the multiscale structure of the scales, while Chapter 7 is devoted to their mechanical study.

6.2 SCALE AND TOOTH FORMATION: A QUICK REVIEW

The elements composing the skeleton of vertebrates are quite diverse, in particular in fish: teeth, cranial bones, dermal plates, scutes, spines, fin rays etc. They find their origin in the mineralized plates that covered early vertebrates, 500 million of years ago.[134] These primitive dermal units had either a "dental" or bony nature, the former being called odontodes and the later bony plates.[135] The modifications they have undergone over millions of years lead to the large variety of skeletal elements present in extant vertebrates. Hence the formation mode and the structure of the scales of *Polypterus senegalus* bear some similarities with the ones of mammal teeth for instance, and yet they also have striking differences.[136] This section quickly reviews some of the related literature.

6.2.1 TOOTH FORMATION

Tooth formation is governed by the action of two main types of cells, namely the odontoblasts (which control the formation of dentin) and ameloblasts (which have a similar role for enamel).[137] Fig. 6-1 schematically presents this process. Odontoblasts lay down a loose network of collagen fibers roughly parallel to tooth axis (enamel matrix). They then start depositing a network of thicker longitudinal fibers that will mineralize into dentin, leaving their processes behind inside the tubules. Meanwhile, ameloblasts start mineralizing the collagen template that will become enamel. Mineralization

continues, with the ameloblasts removing the organic matrix to leave room for crystallites, and the dentin growing downward and inward. Bone starts forming and ligaments anchor the tooth dentin into the bone socket. It is known that for small tooth or denticles, the odontoblasts do not leave any extensions of their cytoplasms, which results in a tubule-less dentin.

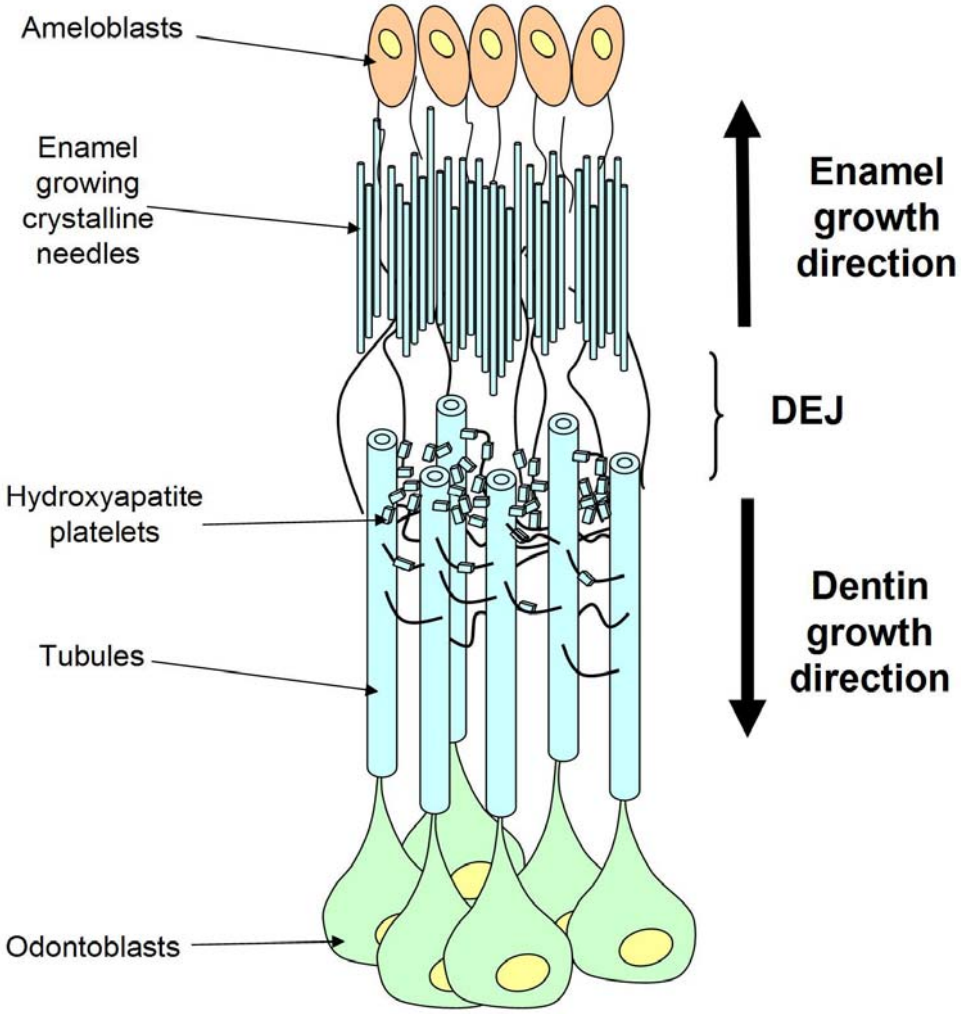

Fig. 6-1: Formation of human tooth dentin and enamel layers.

Human tooth enamel consists of micron-sized vertical rods with a "key-hole" shaped cross-section.[138] The rods are made of elongated nanocrystals of hydroxyapatite[139], while the inter-rod region is more protein rich[140] (Fig. 6-2). The nanocrystals are approximately oriented along the vertical rod axis in the "head" of the key hole, but tend to have a more transverse orientation in the tail. They have a width of about 70nm and a thickness of about 30 nm.

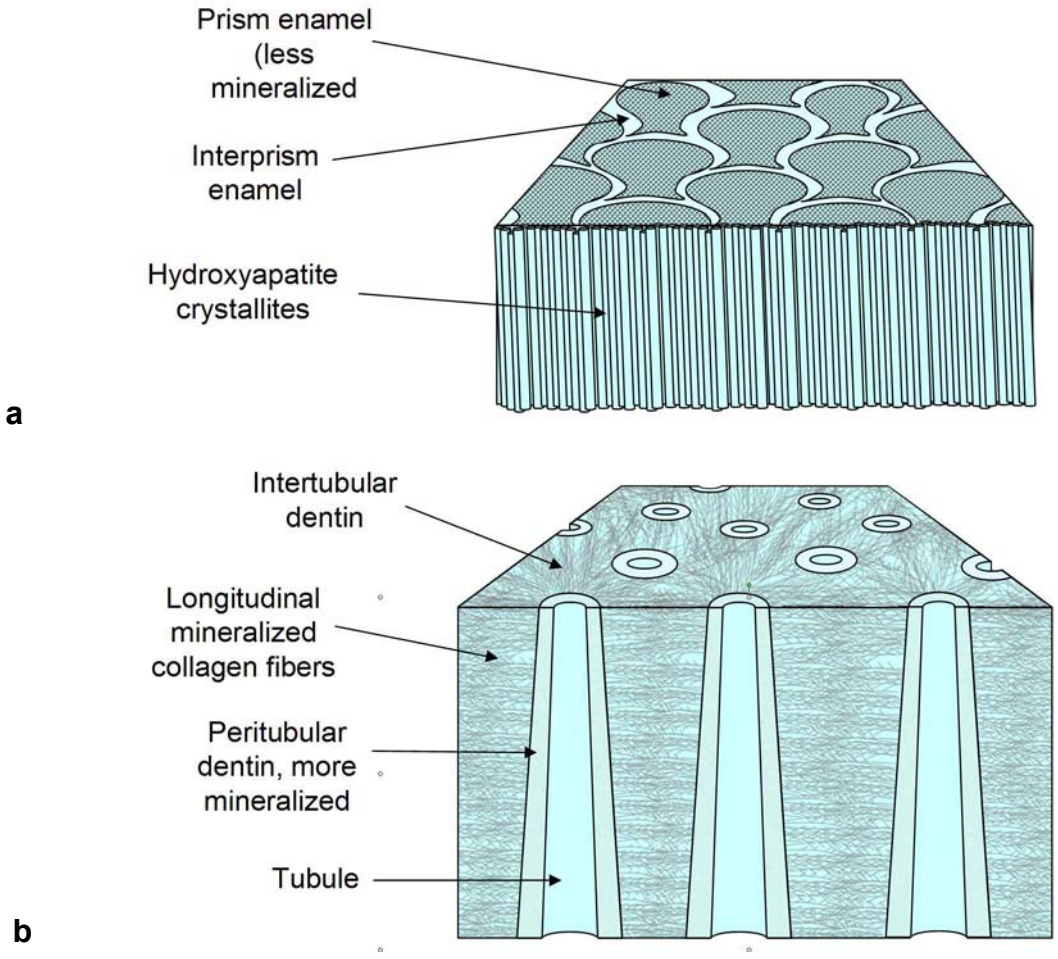

Fig. 6-2: Mature human **(a)** enamel and **(b)** dentin microstructure.

Dentin is less mineralized than enamel, with hydroxyapatite accounting for about 70 %wt compared to more than 95% for enamel.[141] The nanocrystallites were measured

to be of the order of 30 nm in width between 10 and 40 nm.[142, 143] The dentino-enamel junction has a three-level scalloped structure, with collagen fibrils that emerge from the dentin and are inserted into the enamel.[144] The size of the main scallops varies between 25 and 100 µm.

6.2.2 GANOID SCALE FORMATION

The formation of ganoid scale has been studied in particular through the regeneration of such scales after surgical removal of the original scale.[136, 145-148] The first steps of this process are described in Fig. 6-3 a: Elasmoblasts lay down a plywood structure of collagen fibers long before any other layer. Odontoblasts start depositing a woven fiber matrix around the upper blood vessels. They contribute to centripetal closing of the vascular canals, turning them into mineralized denteons. The mineralization of the dentin continues until it reaches the epithelial covering. Meanwhile the elasmoblasts have

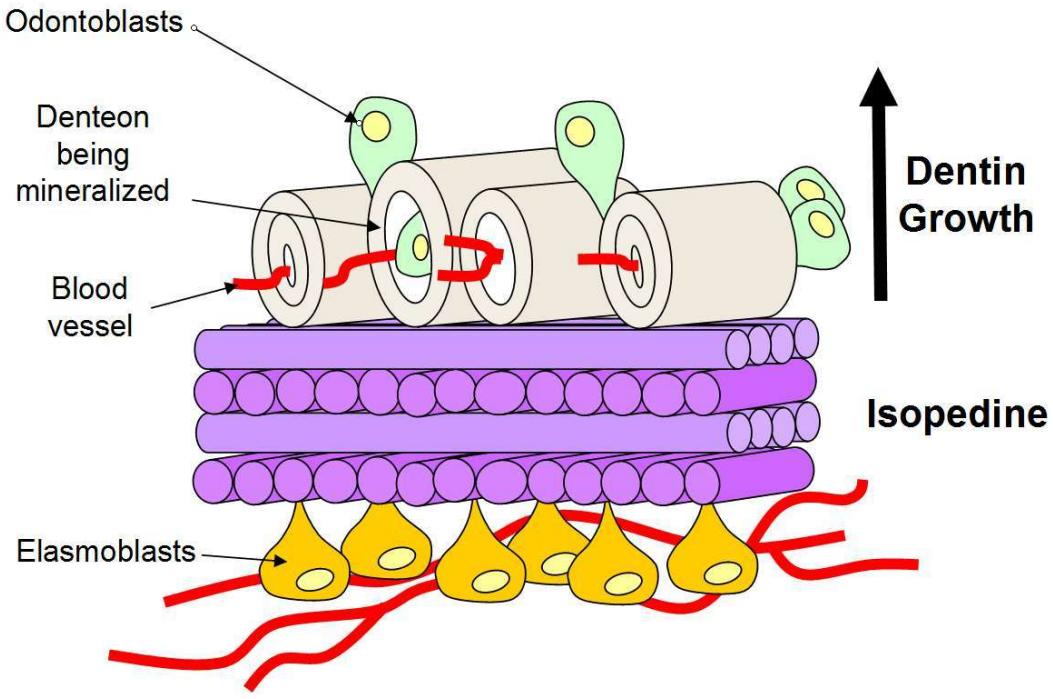

a

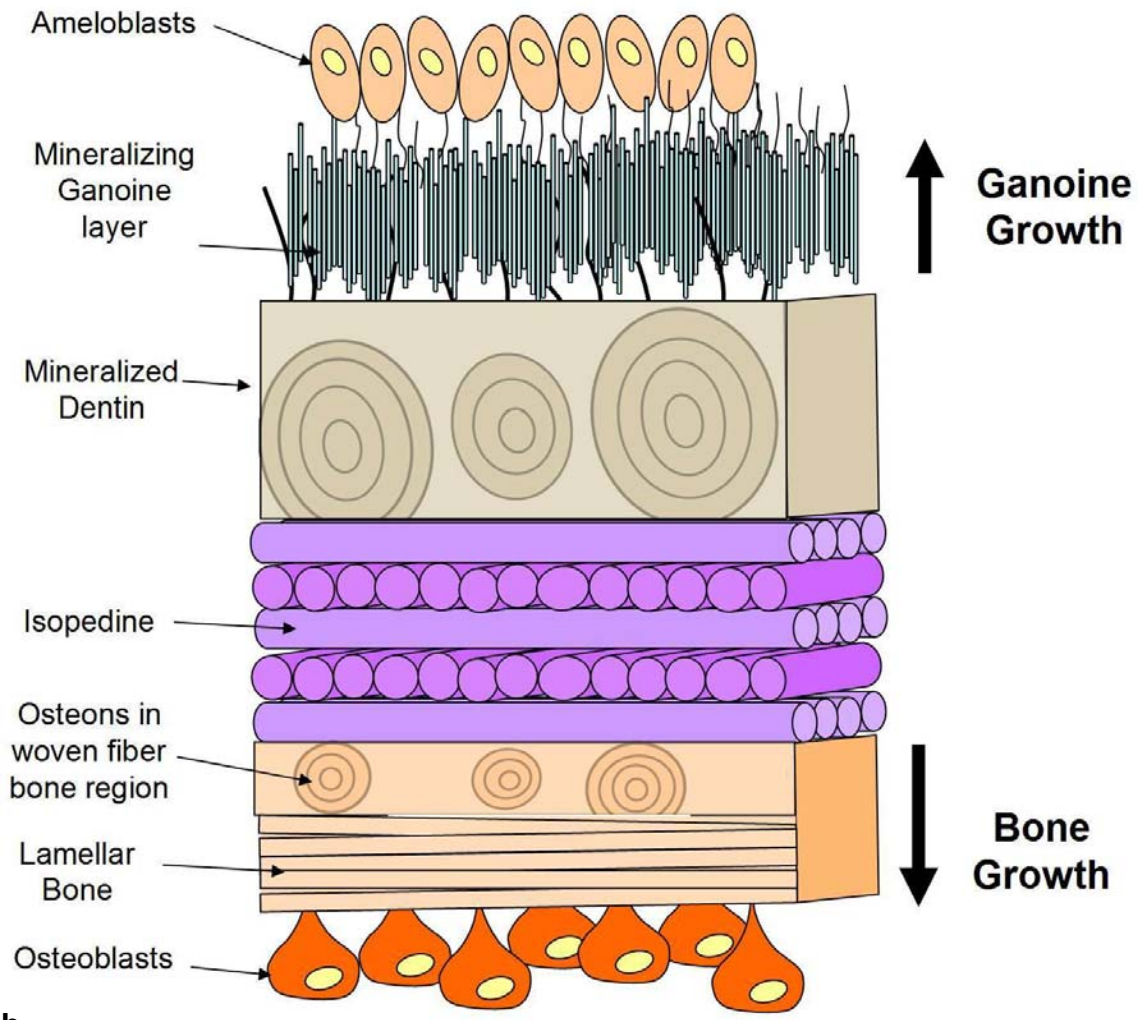

Fig. 6-3 Formation and structure of a typical ganoid scale. **(a)** isopedine and dentin formation, **(b)** ganoine and bone formation.

reached the bottom blood vessels.

Fig. 6-3 b shows the next stage: the bottom blood vessels are been turned into partially closed osteons by the osteoblasts. Then osteoblasts start laying down pseudo lamellar bone. On the upper front, the dentin layer is completed and the ameloblasts finish mineralizing the ganoine.

6.3 MATERIALS AND METHODS

6.3.1 SCALE REMOVAL

A living *Polypterus senegalus* (length ~ 210 mm) was anesthetized in order to surgically dissect rows of scales (for example, one row was taken from the 49th left flank (posterior region) (Fig. 1a). Tricanemethanesulfonate (MS-222) was used; 1.6 g/500 mL HOH/ 3 pellets of KOH for neutralization. This mixture was poured into 5L water to initially anesthetize the fish for about 10 minutes. The fish was periodically moved to a mixture of 50/50 MS-222 and water to keep anesthetized. Surgery was done under an optical microscope and the fish was treated with Tetracycline afterwards. The scales were stored in phosphate buffered saline solution (PBS, pH 8.0) until experimentation.

6.3.2 SAMPLE PREPARATION

The least destructive, minimum sample preparation procedures possible were used, which involved no alcohol dehydration or thermal treatment. Samples designated for external surface imaging/testing were sonicated in distilled water for 15 minutes. Samples designated for cross-sectional imaging/testing were embedded in a room-temperature curing epoxy (Loctite Fixmaster Poxy-Pak 81120, Henkel KGaA, Düsseldorf, Germany) and let to cure for 16 hours, then sectioned using a diamond impregnated annular wafering saw (Buehler Isomet 5000, Lake Bluff, IL) running at 800–900 rpm. The samples were polished on a polishing wheel (South Bay Technology Inc., Model 920, Lapping & Polishing wheel, San Clemente, CA) with 15 μm, 6 μm and 1 μm silica nanoparticles on a soft pad and again with 50 nm silica nanoparticles on cloth pad in distilled water. The samples were then sonicated for 10 seconds in distilled water.

6.3.3 SCANNING ELECTRON MICROSCOPY (SEM)

Prior to imaging, the samples were stuck on a steel support by means of conductive tape and coated with conductive paint and all scales were sputter coated with gold to a depth of 5 nm in a Denton Vacuum Desk II or with gold-palladium to a depth of 3 nm. Samples were imaged in a JEOL JSM-6060 (Peabody, MA) SEM or a JEOL JSM-6700F field emission SEM with chamber pressure on the order of 10-5-10-6 Torr and working distances of 6-9 mm. Images were sampled at 15kV acceleration voltage with a spot size of 35. Backscattered electron microscope (BSE) images of freshly cleaved samples were taken with the JEOL JSM-6700F. BSE imaging can be used to assess the mineral content at the surface of a sample by correlating the local mean atomic number with the image gray levels.[149-153] Based on prior calibration with substances of known mean atomic number, one can extrapolates the values for samples of unknown composition based on their BSEM image gray levels. The mean atomic number can then be approximated as a mineral content percent weight. For the experiment described in this chapter, the calibration samples were chosen to be Al_2O_3 HA, MgO and Na_2CO_3.

6.3.4 OPTICAL MICROSCOPY

Samples were observed using a Nikon Eclipse L150 (Tokyo, Japan).

6.3.5 ATOMIC FORCE MICROSCOPY IMAGING (AFM)

Tapping mode atomic force microscope (TMAFM) imaging in ambient conditions was used to produce surface images of the sample surface upon nanoindentation. A Digital Instruments Multimode SPM IV (Veeco, Santa Barbara, CA) was used with AS-130 “JV” or “EV” piezoelectric scanners. Tapping mode scans were conducted with Veeco Si cantilevers (V-shaped with approximately square pyramidal probe tip geometry,

tip half angle of <17.5°; l =125 μm; k < 0.40 N/m; and R_{tip} < 10 nm). A scan rate of 0.25–1 Hz using a maximum sample size of 512 × 512 pixels was used at gains between 0.1 and 1. The drive amplitude and amplitude set-point were optimized upon tuning. The x and y scan directions were calibrated with a 10 × 10 μm^2 grid and the z direction was calibrated with a 20 nm step silicon grating.

6.4 RESULTS

The skeleton of *P. senegalus* (Fig. 6-4) possesses millimeter-sized, mineralized scales (Fig. 6-5 a and b) that use a peg-and-socket interlocking mechanism (Fig. 6-5 c and d) to form a tough, yet flexible, armor directly below the epidermis.

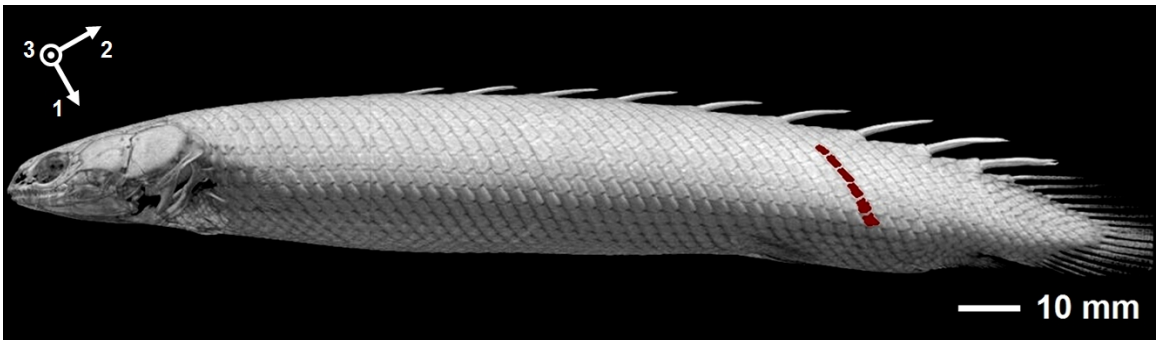

Fig. 6-4 Three-dimensional visualization of *P. senegalus* skeleton obtained via High Resolution X-Ray Computed Tomography;[154] scales removed for nanomechanical testing are colored and correspond to the middle scales of the 40th row posterior region.

Fig. 6-5 a shows the hard outer ganoine layer of the scale, which is the side in contact with the skin of the animal. It possesses an anterior process (ap), an articulating peg (p), and pores due to vascular channels (po). The maximum length of the entire scale including anterior process is about 4.5 mm, the maximum width about 2.4 mm, and the maximum thickness about 0.4-0.5 mm. Fig. 6-5 b of shows the inner bony surface of an

individual scale, which is the side in contact with the inner body of the fish. It has an axial ridge (axr) which measures 2.1 mm × 0.6 mm in dimension, an anterior process (ap), an articulating peg (p) and a socket (s). Sharpey's fibers originate from the ridge and create a strong but flexible connection between adjacent scales.

Fig. 6-5 c shows the perfect match between two adjacent scale curvatures (outer layer). On the inner side, in addition to a complex network of fibers spanning the entire scale armor, the peg and socket mechanism links each scale with its neighbors within a row. Again, strong Sharpey's fibers tighten the junction.

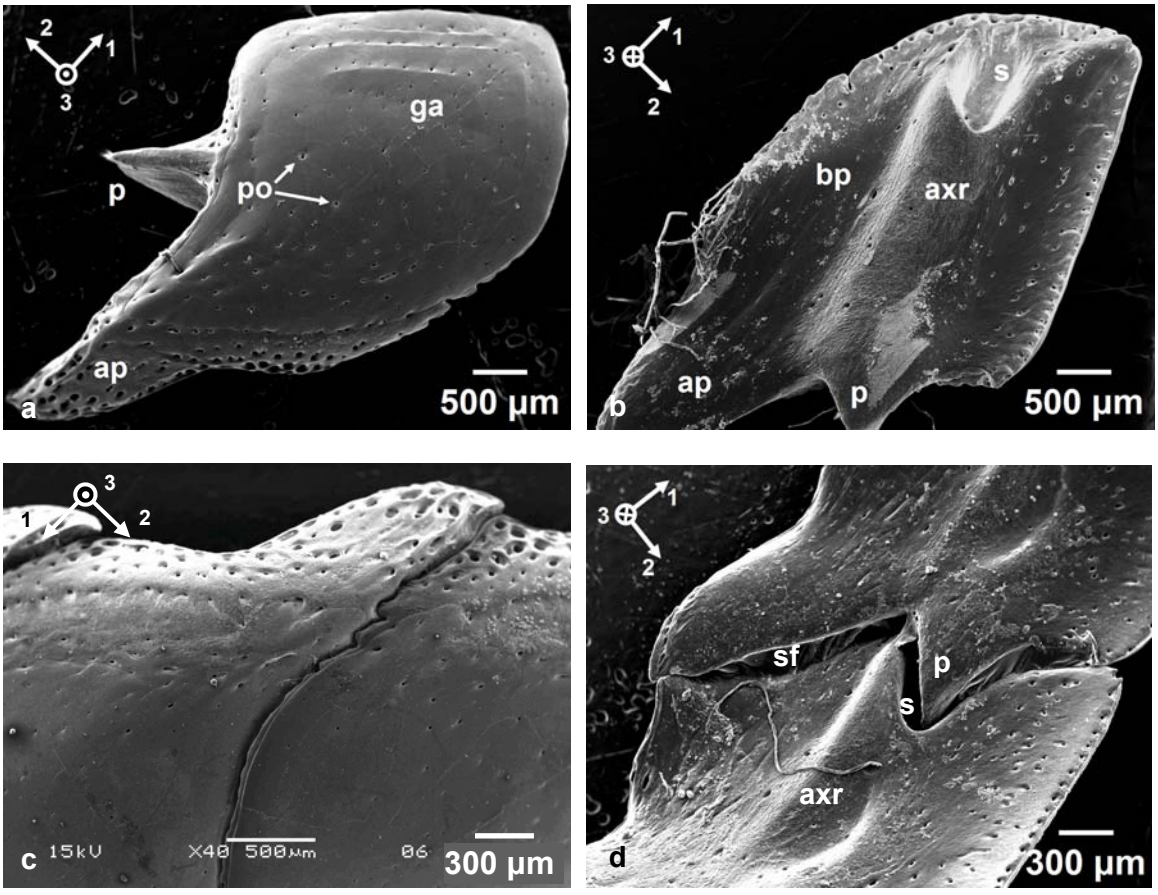

Fig. 6-5 (a) Scanning electron microscope (SEM) image of the outer ganoine surface (facing the epidermis) of an individual scale **(b)** SEM image of the inner bony plate surface. **(c)** Detail of the joint between two adjacent scales within a same row (top surface). **(d)** Interlocking mechanism between two scales.

Fig. 6-6 shows the details of the anterior process region. One can distinguish pores with sizes ranging from 10 to 50 μm as well as a multitude of small prominences called tubercles[155] and that span the entire ganoine surface with great regularity.

In Fig. 6-7, the polished cross section of a scale is observed at different magnifications using an optical microscope in polarized light. Fig. 6-7 a reveals the overall microstructure and dimensions of four different material layers (from outer to inner); ganoine (thickness ~ 10 μm), dentine (thickness ~ 50 μm), isopedine (thickness ~ 40 μm, though not continuous throughout the whole width of the scale), and a bone basal plate (thickness ~ 300 μm). One can find the presence of denteon cross-sections in the

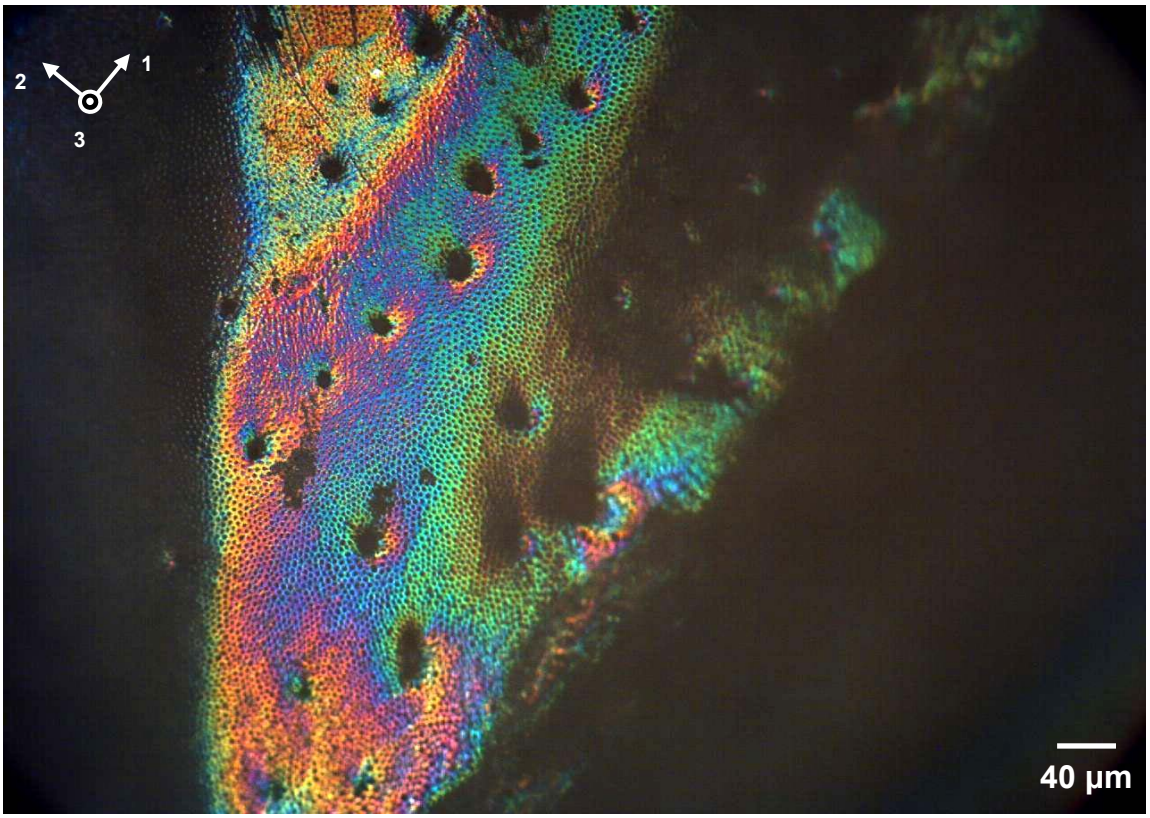

Fig. 6-6 Optical microscope image of the scale peg top surface. The regular arrangement of tubercles is distinguishable

dentin layer (pink-orange) as well as not completely mineralized osteons just under the isopedine layer. The isopedine is easily recognizable by the succession of a few well-defined lamellae, each a few microns in thickness, in the center region of the scales. The bony plate seems to exhibit two distinct microstructures, one where the bone lamellae are parallel to the inner side of the scale, and another one where some fibers are radiating perpendicularly to the inner surface, in the central region of the scale. This location corresponds to the axial ridge where the Sharpey's fibers connecting adjacent scales together are emitted. Fig. 6-7 b and c show more details of the microstructure. In

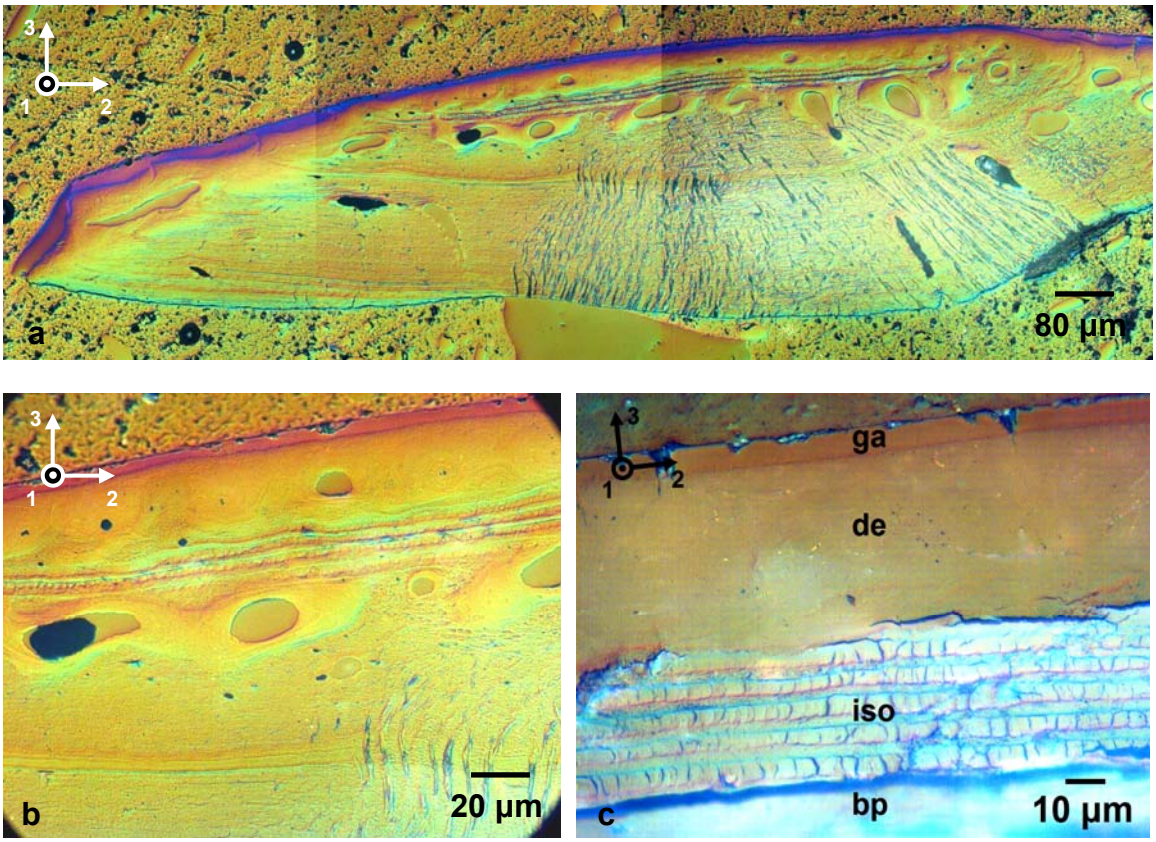

Fig. 6-7 Cross-polarized optical micrograph of the polished cross-section of an individual scale showing **(a)** four distinct layers including (from top to bottom); ganoine (ga), dentin *t* ~ 410 µm) **(b)** Higher magnification of the central region. **(c)** Details of the different layers.

particular, one can observe that denteons are not spanning the entire dentin layer, but (de), isopedine (iso), and the bony basal plate (bp) (only a fraction visible, total thickness instead have a more homogeneous looking phase in-between them. In isopedine, every other sub-layer seem to be constituted of large fibrils running perpendicular to the plane of the cross-section, with diameter approximately between 5 and 10 µm. The other sub-

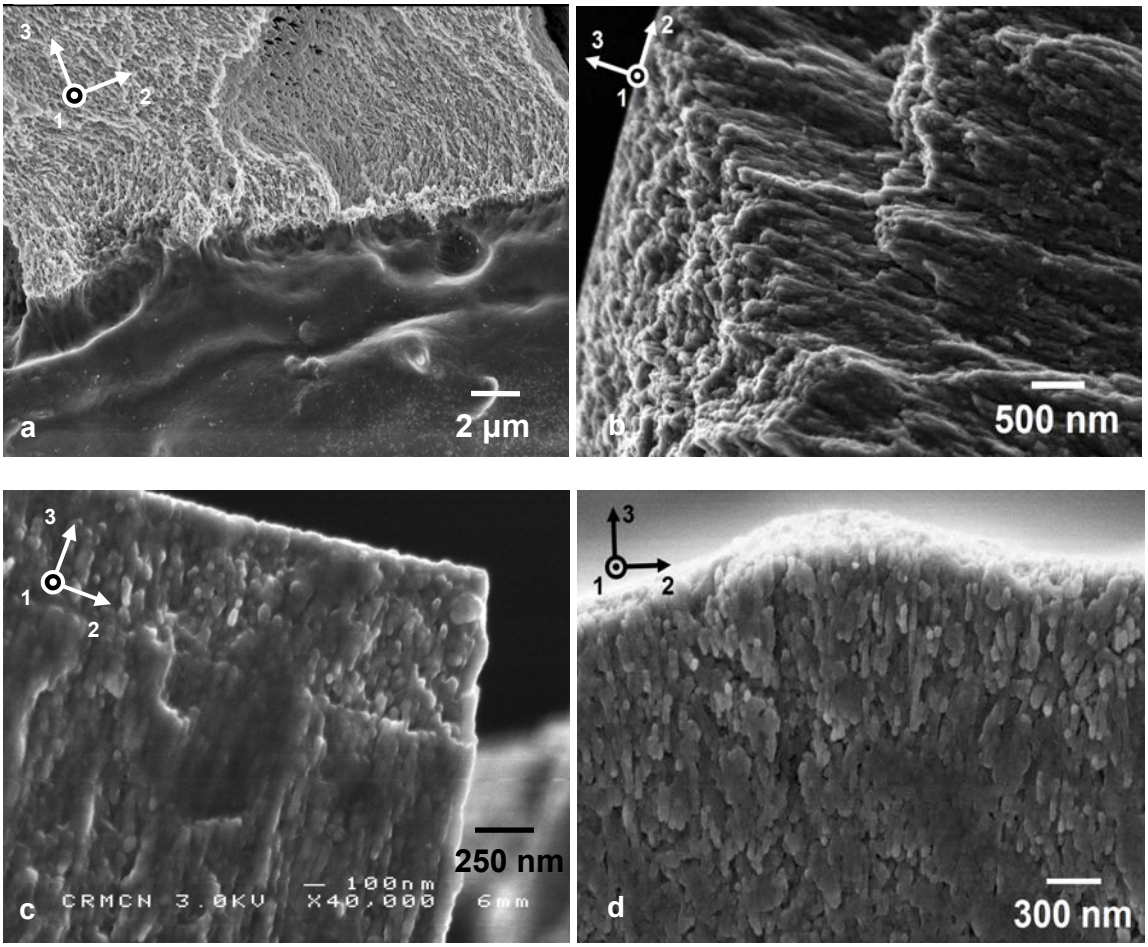

Fig. 6-8 (a) SEM image of the ganoin and dentin underneath after 20 seconds etching with H_3PO_4 **(b)** High resolution SEM image of the thin elongated nanocrystals (in a fractured area) constituting the ganoine layer after 5 minutes of etching with NaOCl **(c)** High resolution SEM image of the nanocrystals after 2 minutes of etching with EDTA 0.5M. **(d)** High resolution SEM image of ganoine surface cross-section after 5 minutes of etching with NaOCl. Axis 1 is parallel to the long axis of a scale, axis 2 is parallel to short axis of a scale, and axis 3 is perpendicular to the ganoine layer surface. The raised topographical feature observed of one of the array of surface "tubercules."[156]

layers have a smoother appearance and look somewhat thinner.

In Fig. 6-8, the etching of the ganoine cross-section reveals an overall twisting of the orientation of the crystalline needles (in particular close to the dentin-ganoine junction), although their average direction remains parallel to the outer surface of the scale.. It is composed of long, pseudoprismatic crystallites (Fig. 6-8 b) and is stratified (Fig. 6-9 c). Nanocrystallites composing the tubercles do not seem to differ in shape or size from nanocrystallites of other regions.

Fig. 6-9 reveals the unique corrugated microstructure of the dentin-ganoine junction. Back Scattered Electron (BSE) microscopy allows one to distinguish area of greater mineral content from areas more organic rich, the former appearing brighter than the later. The back scattered electrons also penetrate deeper in the material (from a few tens to a few hundreds of nanometers) and thus can yield information about the local 3-D structure to some extent. We can see on both Fig. 6-9 a (simple polishing) and 6-9 b (polishing followed by a 10-minute etching in EDTA 0.5M) that the end of the crystallite bundles have a corrugated morphology. Fig. 6-9 c also shows that organic ligaments emanating from the dentin layer (bottom) are anchored within the crystallite bases. The dentin layer develops on top of the isopedine and is organized around denteons (analog to osteons in bone, i.e. concentric lamellae of dentin) surrounding the vascular canals. In Fig. 6-9 c, one can observe two partially demineralized large denteons and the possible presence of demineralized tubules (micron-sized holes) throughout the dentin layer.

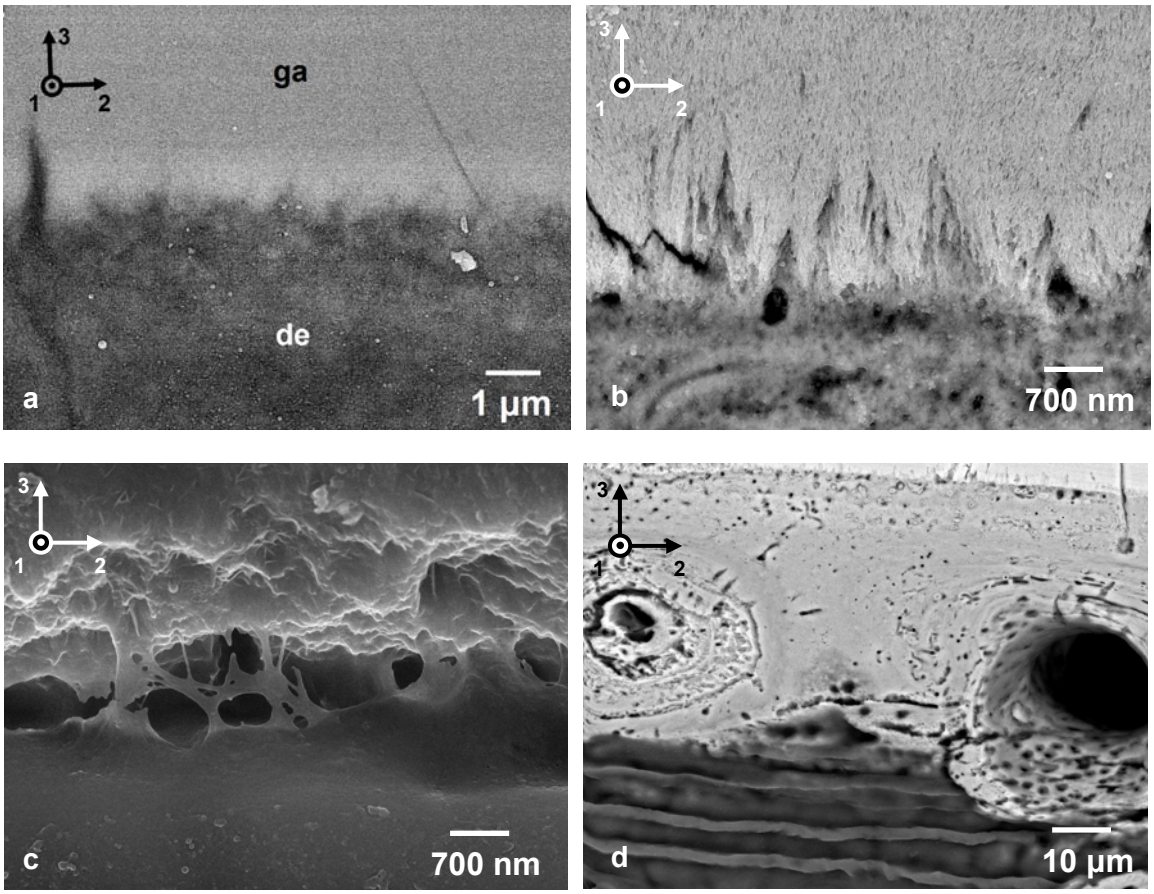

Fig. 6-9 (a) BSEM image of the polished dentin-ganoin junction **(b)** BSEM image of the dentin-ganoin junction after 10 minutes etching with EDTA 0.5M **(c)** SEM image of the dentin-ganoin junction after 10 seconds etching with H_3PO_4 **(d)** BSEM image of the cross-section of dentin and underlying isopedine after 10 minutes EDTA 0.5M etching.

Fig. 6-10 a and b present the morphology of an inter-denteon region etched for 10 seconds in H_3PO_4. In these zones, dentin is not organized in concentric layers, but has a seemingly less organized, grainier structure, with possible alternation of micron-sized regions more or less mineralized (variation of contrast in the BSE image).

When prepared with the same treatment, isopedine offers a very different appearance. (Fig. 6-11 a and b). Alternating thin (~ 3 µm) and thick (~ 6 µm) sublayers can be observed with, the thinner sub layers possibly having slightly more mineralized surface. Cross-section of collagen fibrils cannot be readily observed.

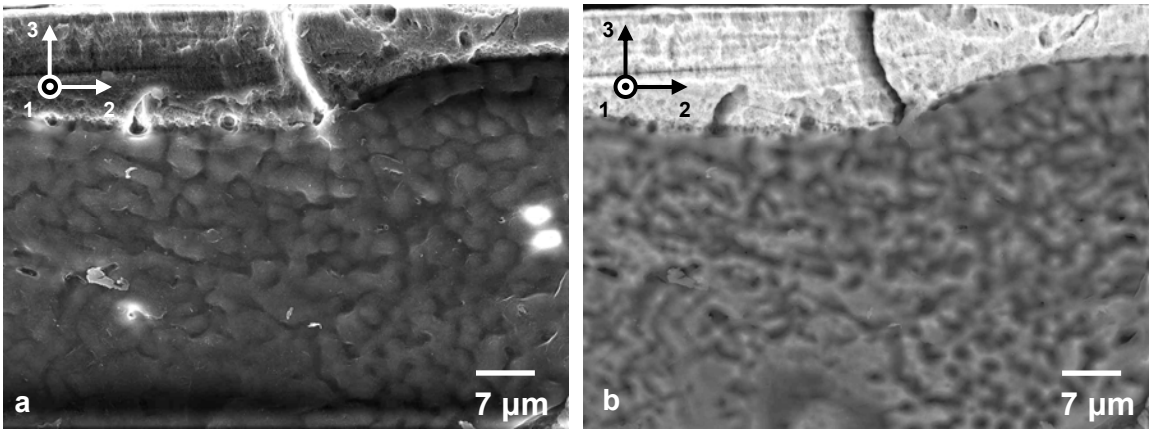

Fig. 6-10 (a) SEM image of the ganoine and dentin layers after 10 seconds etching with H_3PO_4 **(b)** BSEM image of the same area.

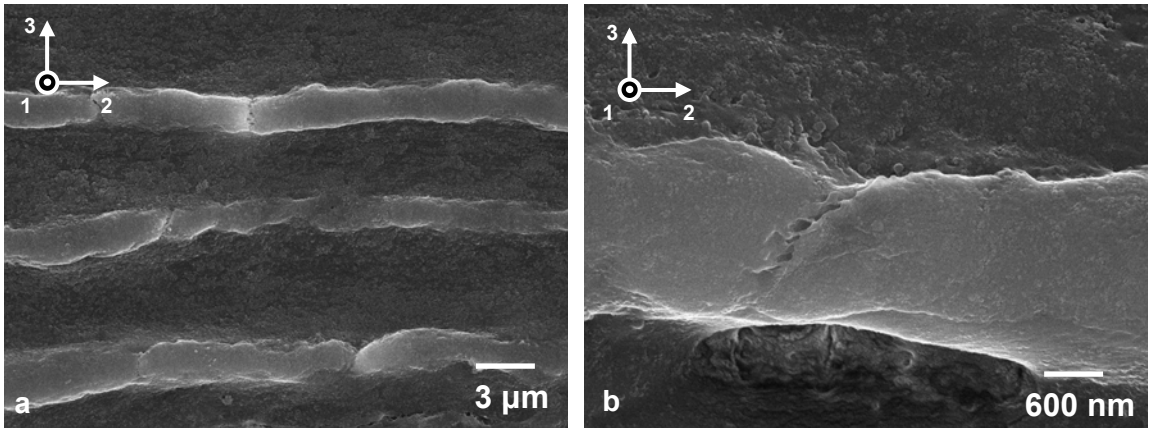

Fig. 6-11 (a) SEM image of the isopedine layer cross-section after 10 seconds etching with H_3PO_4 **(b)** High resolution SEM image of one of the isopedine sub-layers.

The basal osseous plate is the thickest layer in a scale and is composed of a succession of bone lamellae, with the major axis of the collagen fibrils approximately parallel to the scale border (Fig. 6-12 a and b). One can distinguish an additional level of organization within the lamellae, which seem to be further subdivided in smaller cells with a ~ 1 µm diameter.

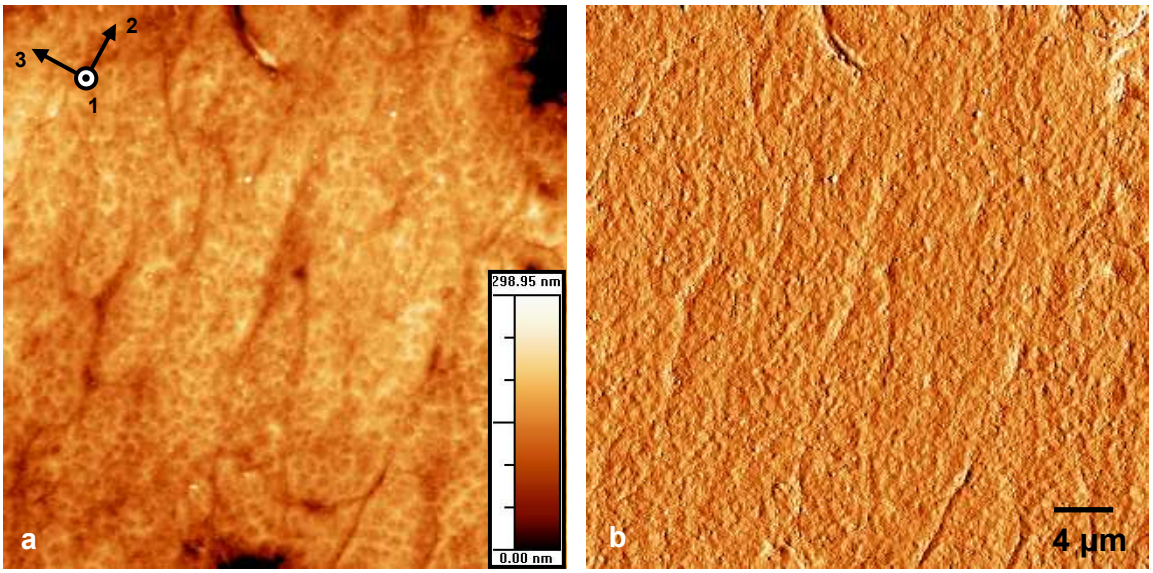

Fig. 6-12 (a) Tapping Mode Atomic Force Microscope (TM-AFM) height image of the polished cross-section of the bony plate. **(b)** TMAFM amplitude image of the same area.

Fig. 6-13 gives an overview of the nanoscale morphology for the cross-section of each of the material layers when TMAFM imaged after simple polishing. Each material layer is a complex organic-inorganic nanocomposite. Ganoine (Fig. 6-13 a, b and c) has the smoothest surface upon polishing, and little can be distinguished. At this length scale, the phase image does not reveal localized coils of organic material on the ganoine cross-sectional surface.

Contrary to their microstructure, the nanostructure for dentin, isopedine and bone looks rather similar. Dentin (Fig. 6-13 d, e and f) has a strikingly different morphology. We can see densely packed nanocrystallites possibly lined with an organic phase (see Fig. 6-13 f). While in the image presented here the crystallites have a diameter above 100 nm in average, the size of the crystallites varies greatly from location to location. The range for the crystallite diameters measured over several samples is 30 to 200 nm. The polished cross-section of isopedine (Fig. 6-13 g, h and i) shows slightly smaller crystallites than

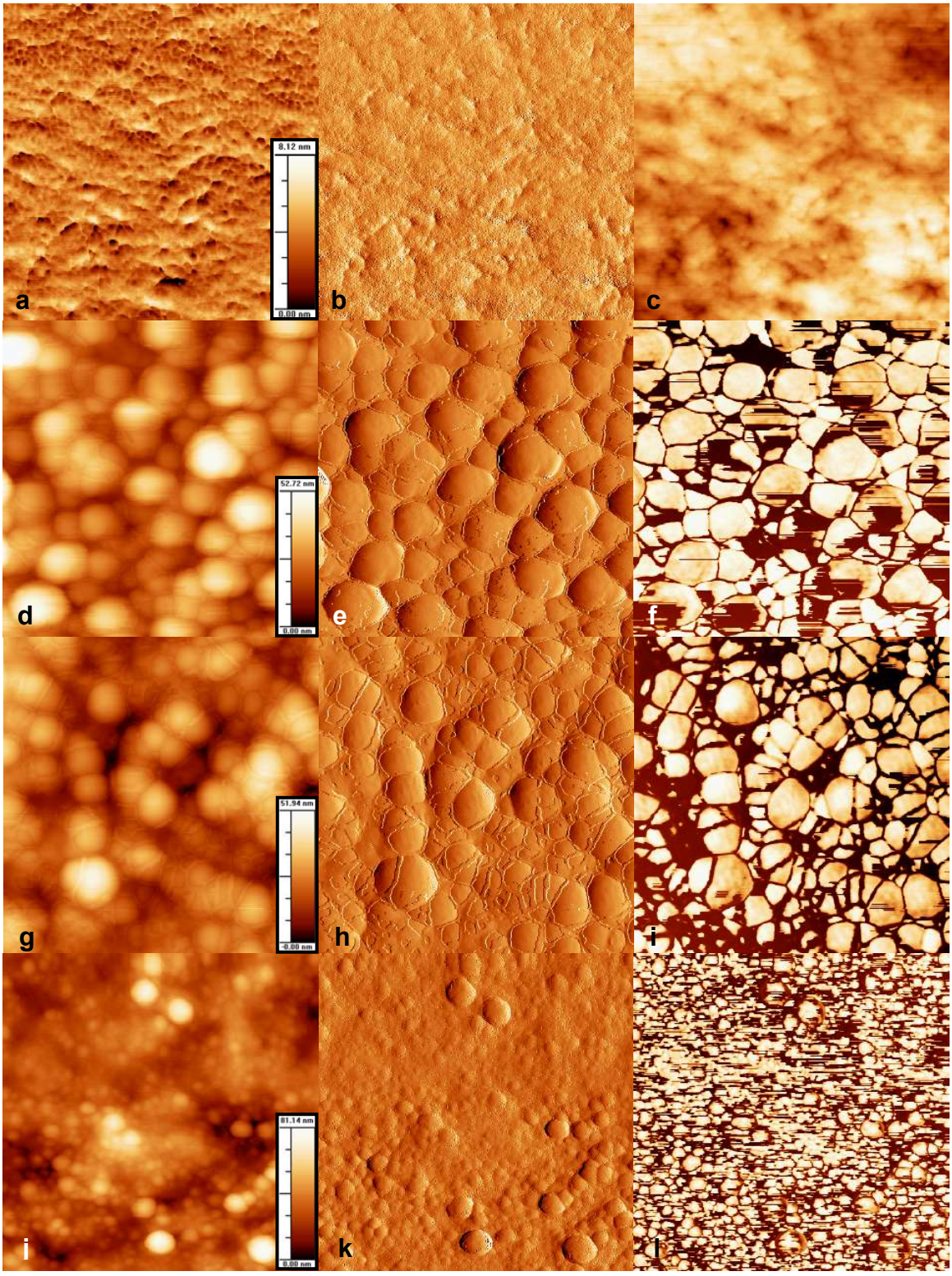

Fig. 6-13 1 μm scan size Tapping Mode Atomic Force Microscope (TM-AFM) images of the polished cross-section of an individual scale. Leftmost are height images, middle are

amplitude images and rightmost are phase images. From top row to bottom, images were taken in ganoine, dentin, isopedine and bone.

dentin in average, but again their average diameter varies greatly from one imaging location to another. The measured range is 40 to 150 nm. The dark regions in the phase image (related to greater quantity of organic content) are in general more spread out than for dentin. Compared to dentin and isopedine, bone (Fig. 6-13, j, k and l) almost always has a smoother, more homogeneous appearance, with both smaller and more uniform crystallites (20 – 100 nm diameter).

Based on BSE images, the mineral content was found to decrease from the outer ganoine layer toward the inner bony plate. The approximate mineral content percent weight was found to be ~100% for ganoine, ~80% for dentin, 60-75% for isopedine and 60-70% for bone.

6.5 DISCUSSION

Certain aspects of the microstructure of *P. senegalus* scales have been studied extensively (see review by Daget, et al.[156]) and will be compared to the results presented in this chapter.

The images shown in Fig. 6-8 are consistent with the outer ganoine layer being a stratified, enamel-like, acellular, highly mineralized (< 5% organic[157]), noncollageneous tissue composed of rod-like pseudoprismatic crystallites of apatite (average diameter ~ 50 nm) twisting in a bundle toward the outer scale surface.[158] The twisting of the hydroxyapatite crystalline nanoneedles in Fig. 6-8 a is reminiscent of that of microprisms in mammal enamel, albeit at a smaller lengthscale.[159] This is consistent with the fact that

the ganoine layer is true enamel[146, 160] (i.e. being deposited by epidermis cells) although it is one or two orders of magnitude thinner than human tooth enamel for instance. Similarities between these materials are not limited to their structure, since an immunocytochemical study showed that the organic matrix contains proteins similar to the amelogenins found in mammalian tooth enamel.[161]

The dentin-ganoin junction is the region where ganoin nanorods penetrate the dentin in a corrugated fashion. This configuration maximizes the contact surface between both layers and likely impedes the propagation of lateral cracks along the interface. Furthermore, organic ligaments originating from the dentin layer are anchored inside the ganoin structure, providing a natural reinforcement of the junction, increasing its toughness and its cohesion.

The structure of dentin, has been studied extensively in teeth, and is known to be composed primarily of type I collagen fibrils reinforced with nanocrystalline apatite mineral that forms called dentinal tubules, i.e. cylindrical channels 1-2 μm in diameter with a thin, highly mineralized cuff of peritubular dentin surrounding each tubule.[162] Such tubules could not be detected on fractured surface for *P. senegalus* dentin. known to be less mineralized than ganoine, but more so than the osseous basal plate.[156] Here, the dentin layer to develops on top of the isopedine and is organized around denteons (analog to osteons in bone, i.e. concentric lamellae of dentin) surrounding the vascular canals[163].

The third layer, isopedine (also called elasmodine), consists of a uniform superimposition of orthogonal collagenous layers that form a plywood-like structure, but we could not see an obvious decrease in mineralization with distance towards the inner surface of the scale, as have been noted by other researchers.[164] It consists in a very

regular superimposition of orthogonal collagenous layers that form a plywood-like structure and slowly mineralizes from it surface toward the bottom of the scale[165].

The innermost thick basal osseous plate is composed of a succession of bone lamellae. It has been reported that besides the spatial organization of their fibers, isopedine and bone also differ by the larger diameter of the isopedine collagen fibrils (~100 nm versus ~20 nm respectively) and by the thickness of its sublayers (~5 μm versus < 1 μm).[166] Here the isopedine and bone sublayers dimensions were found to match these values quite well. However, with the etching techniques and microscopy instruments employed here, it was never possible to directly visualize the collagen fibers, in particular their banding.

The appearance of the nanostructure of the polished cross-section of ganoine was the smoothest (RMS roughness of ~1 nm) and no clear morphology could be outlined, suggesting that the mineral content is very high (as confirmed by BSEM). No organic coils could be detected between the grains. Dentin (RMS roughness ~ 8 nm) and isopedine (RMS roughness ~8 nm) had more similar appearance, with a large distribution of rounded nanocrystallites. The bone layer exhibited consistently smaller crystallites and had a higher RMS roughness (~11 nm).

In conclusion, the scales of *Polypterus senegalus* all have a multiscale structure, with distinct microstructures and nanostructures. Each layer is thus likely to undergo its own unique deformation mechanisms. The interface between ganoine and dentin was reinforced in at least two ways, through corrugation of the interface and anchoring of organic ligaments.

CHAPTER 7 MULTISCALE MECHANICAL STUDY OF *POLYPTERUS SENEGALUS* ARMORED SCALES

This chapter is submitted for publication.

7.1 INTRODUCTION

In this chapter, we focus on a fascinating model system, the interlocking, quad-layered, mineralized scales from *Polypterus senegalus*, which belongs to the fish family *Polypteridae (*appearing ~ 60 million years ago in the Cretaceous period[156]), and still lives today primarily at the bottoms of freshwater, swampy, muddy shallow floodplains and estuaries in Africa.[167] *P. senegalus* scales have conserved many characters of the ancestral type of dermal skeletal element resembling that of ancient palaeoniscoids[168] and its structure has been studied in detail (see review by Daget, et al.[156] and Fig. 1), consisting of four different organic-inorganic nanocomposite material layers (from outer to inner); ganoine, which is a type of enamel (thickness ~ 10 μm), dentin (thickness ~ 46 μm), isopedine (thickness ~ 45 μm, located in the center of the scale), and a bone basal plate (thickness ~ 300 μm). Here, we use high resolution nanomechanical methods to probe, for the first time, the elastic and plastic mechanical properties spatially through the four layers that compose the cross-section of an individual scale from *P. senegalus*.

7.2 MATERIALS AND METHODS

7.2.1 SCALE REMOVAL

A living *Polypterus senegalus* (length ~ 210 mm) was anesthetized in order to surgically dissect rows of scales (for example, one row was taken from the 49th left flank (posterior region) (Fig. 1a). Tricanemethanesulfonate (MS-222) was used; 1.6 g/500 mL HOH/ 3 pellets of KOH for neutralization. This mixture was poured into 5L water to initially anesthetize the fish for about 10 minutes. The fish was periodically moved to a mixture of 50 /50 MS-222 and water to keep anesthetized. Surgery was done under an optical microscope and the fish was treated with Tetracycline afterwards. The scales were stored in phosphate buffered saline solution (PBS, pH 8.0) until experimentation.

7.2.2 SAMPLE PREPARATION

The least destructive, minimum sample preparation procedures possible were used, which involved no alcohol dehydration or thermal treatment.. Samples designated for external surface imaging or testing and testing were sonicated in distilled water for 15 minutes. Samples designated for cross-sectional imaging or testing were embedded in a room-temperature curing epoxy (Loctite Fixmaster Poxy-Pak 81120, Henkel KGaA, Düsseldorf, Germany) and let to cure for 16 hours, then sectioned using a diamond impregnated annular wafering saw (Buehler Isomet 5000, Lake Bluff, IL) running at 800–900 rpm. The samples were polished on a polishing wheel (South Bay Technology Inc., Model 920, Lapping & Polishing wheel, San Clemente, CA) with 15 μm, 6 μm and 1 μm silica nanoparticles on a soft pad and again with 50 nm silica nanoparticles on cloth pad in distilled water. The samples were then sonicated for 10 seconds in distilled water.

7.2.3 NANOINDENTATION

Prior to testing, the samples were stuck on a steel puck by means of cyanoacrylate glue (Loctite 495, Henkel KGaA, Düsseldorf, Germany). Nanoindentation experiments were conducted in ambient conditions using a Hysitron, Inc. Triboindenter (Minneapolis, MN) mounted with a Berkovich (trigonal pyramid) diamond probe tip. The drift rate of the transducer was automatically monitored by the software before indentation was initiated. The applied load function was divided into five segments as follows. The first segment consisted of a 3 second hold at zero force allowing for tip–sample equilibration. Segment two was a constant loading rate of 50 μN/s. Once the maximum set peak load was reached, a third segment, a hold period of 3 seconds, would follow. The fourth segment decreases the load until reaching zero force with an unloading rate equivalent to that of segment 2. The fifth segment would conclude the experiment with a 3 second hold at zero force to calculate the final drift rate of the piezo. The samples were indented across their cross section (following the direction of axis 3 as in Fig. 7-1) with the load parallel to axis 1. The interindent spacing was 1 and 3 μm for 100 and 500 μN maximum load indents, respectively. Load versus indentation depth curves from multiple experiments using the same maximum load and from different sample locations were averaged and standard deviations calculated and reported. The probe tip area function [$A(hc)$, which is the projected area of the Berkovich probe tip under load calculated from a 6th order polynomial fit accounting for non-ideal tip geometry as a function of the contact depth hc] and frame compliance were calibrated prior to each set of experiments using a fused quartz sample.

7.2.4 MICROINDENTATION

Prior to testing, the samples were stuck on a steel puck by means of a cyanoacrylate glue (Loctite 495, Henkel KGaA, Düsseldorf, Germany). Microindentation experiments were conducted in ambient conditions. Loads ranged from 0.25 to 2 N, and the inter-indent spacing was always at least 5 ×greater than the indent residual size to prevent any interaction between the indents. The probe tip end radius was measured using atomic force microscopy and found to be ~ 3.7 μm.

7.2.5 ATOMIC FORCE MICROSCOPY IMAGING

Tapping mode atomic force microscope (TMAFM) imaging in ambient conditions was used to produce surface images of the sample surface upon nanoindentation. A Digital Instruments Multimode SPM IV (Veeco, Santa Barbara, CA) was used with AS-130 "JV" or "EV" piezoelectric scanners. Tapping mode scans were conducted with Veeco Si cantilevers (V-shaped with approximately square pyramidal probe tip geometry, tip half angle of <17.5°; l =125 μm; k < 0.40 N/m; and R_{tip} < 10 nm). A scan rate of 0.25–1 Hz using a maximum sample size of 512 × 512 pixels was used at gains between 0.1 and 1. The drive amplitude and amplitude set-point were optimized upon tuning. The x and y scan directions were calibrated with a 10 × 10 μm^2 grid and the z direction was calibrated with a 20 nm step silicon grating.

7.2.6 FINITE ELEMENT ANALYSIS (FEA)

A nonlinear FEA nanoindentation model was employed which approximated the three-dimensional Berkovich nanoindentation experiments using a two-dimensional,

conical-like axisymmetric indenter. The accuracy of the 2D axisymmetric approximation was assessed by comparison with fully 3D simulation results; the modulus and yield stress values obtained in the 2D simulations differed from those from 3D by less than 2-3% (a range within any experimental comparison significance). The indenter geometry was chosen to correspond to the experimentally determined indenter cross-sectional tip area function, The indenter tip was modeled as rigid since the elastic modulus of the diamond probe tip is at least 20 × greater than that for the indented samples. The indented samples were modeled as isotropic elastic perfectly plastic using 4-node bilinear axisymmetric quadrilateral elements (CAX4R in ABAQUS element library, Providence, RI). Mesh convergence simulations were carried out and an optimal mesh (in terms of accuracy and calculation costs) was chosen for use in all simulations. Large deformation theory and frictionless contact between the indenter and material were assumed. Fully 3D nanoindentation simulations were also conducted on samples with two layers oriented normal to the surface, simulating several indentations with each indentation progressively closer to the layer/layer interface in order to assess the role of any constraint of a neighboring layer on the indentation load-depth behavior. FEA models of Microindentation followed a similar methodology to the axisymmetric nanoindentation simulations. The indenter was taken to be rigid with a conical tip geometry emulating a Vickers microhardness tip with a tip radius of 3.7 μm (found from AFM measurement of the tip geometry). Mesh convergence studies were used to assess the needed mesh for accurate solutions to the load-depth and stress contours; additional refinement was used as needed to capture the gradients within layers and junction regions.

7.3 RESULTS

7.3.1 EVALUATION OF THE LOCAL MECHANICAL PROPERTIES OF THE CONSTITUTIVE LAYERS OF *P. SENEGALUS* SCALES

The technique of instrumented nanoindentation was employed which involved the controlled compression (loading) and decompression (unloading) of a diamond Berkovich probe (end radius ~ 220 nm) into a freshly extracted scale while simultaneously recording the force or load versus penetration or indentation depth over nanometer length scales. The interindent spacing was chosen to avoid overlap of neighboring inelastic strain/residual stress zones estimated by appropriate finite element analysis (FEA) simulations at the appropriate maximum load.[169] The maximum depth normalized by the root-mean-square roughness (quantified by atomic force microscopy imaging) was always ensured to be >10 to avoid surface topographical effects.[169] Two methods were employed to reduce mechanical properties from the load-depth data. First, the unloading slope was used to calculate an indentation modulus, $E_{O\text{-}P}$, on the basis of the widely used Oliver-Pharr (O-P) isotropic, elastic contact mechanics model.[170] Owing to the assumptions of this model and the hierarchical structure of scale layers, the extracted $E_{O\text{-}P}$ values reflect relative mechanical stiffness and are not absolute quantitative values. However, relative spatial differences in stiffness can be accurately compared.[169] Hardness, $H_{O\text{-}P}$, values were calculated as the maximum load divided by the projected contact area at maximum load which was also estimated by the Oliver-Pharr analysis[170] (see Methods). A representative dataset is presented in Fig. 7-1; $E_{O\text{-}P}$ and $H_{O\text{-}P}$ are plotted as a function of distance across the cross-section of an individual *P. senegalus*

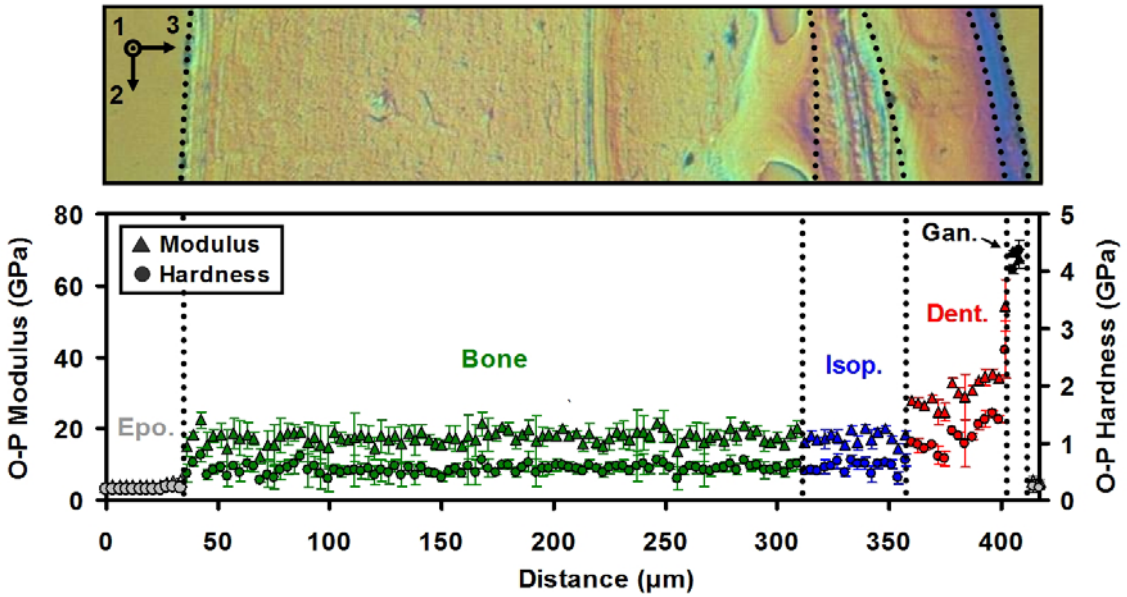

Figure 7-1 Mechanical properties derived from nanoindentation experiments across the cross-section of the different material layers of an individual *Polypterus senegalus* scale. Indentations were conducted across the scale cross-section with the loading axis parallel to axis 1. All data represents an average of three parallel columns of 125 indents each. 500 μN maximum load; average indentation moduli, $E_{O\text{-}P}$, and hardness, $H_{O\text{-}P}$, both reduced from Oliver–Pharr analysis[170] as a function of distance across the scale cross-section. The vertical error bars represent one standard deviation. "Epo." is the epoxy used for embedding.

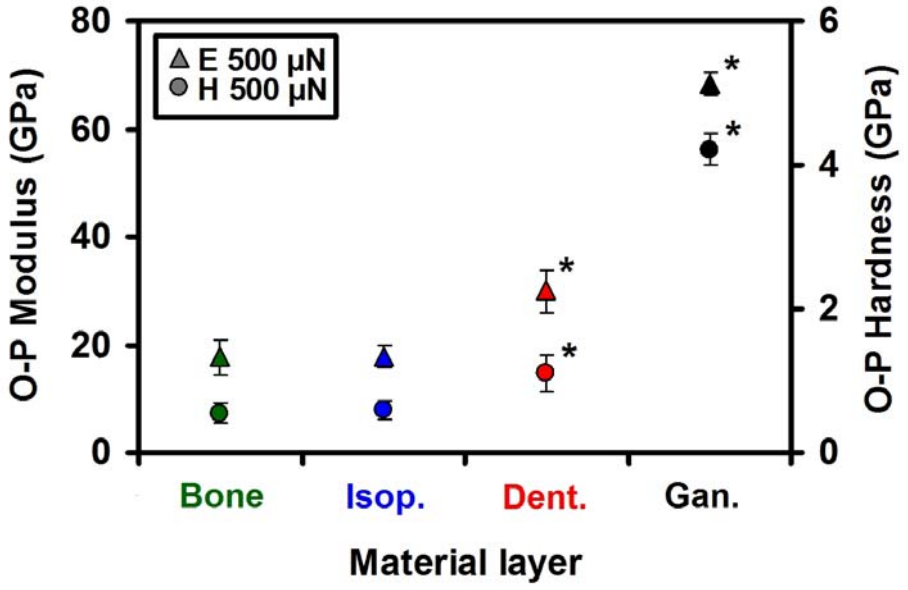

Figure 7-2 Average $E_{O\text{-}P}$ and $H_{O\text{-}P}$ for each of the different layers derived from 500 μN maximum load nanoindentation curves using Oliver–Pharr analysis.[170] The vertical error bars represent one standard deviation for that particular dataset (n = number of individual nanoindentation experiments: ganoine, n=6; dentin, n=24, isopedine, n=32, bone, n=336).

scale (each data point represents an average of three parallel columns of indents of 125 indents each) at a maximum load of 500 μN and an interindent spacing of 3 μm. These data show that both $E_{O\text{-}P}$ and $H_{O\text{-}P}$ decrease with distance from the outer to the inner surfaces of the scale (from ~62 to ~17 GPa and ~4.5 to ~0.54 GPa, respectively, see also Fig. 7-2).

Each material layer was found to have significantly different mechanical properties compared to the others ($p<0.05$), except for bone compared to isopedine. The highest average indentation modulus (~62 GPa) and hardness (4.5 GPa) of the outer ganoine layer is consistent with its known highly mineralized (<5% organic[157]) noncollageneous structure consisting rod-like, pseudoprismatic crystallites of apatite (Chapter 6).[171] The collagenous dentin layer has a reduced mineral content compared to ganoine, but is more mineralized than the osseous basal plate,[156] consistent with the mechanical property trends observed in Fig. 7-1 and 7-2 ($E_{O\text{-}P}$ and $H_{O\text{-}P}$ ~29 and 1.2 GPa, respectively). The third layer, isopedine (also called elasmodine), consists of a uniform superimposition of orthogonal collagenous layers (alternating thin, ~ 3-5 μm, and thick, ~ 4-10 μm, Chapter 6) that form a plywood-like structure and decrease in mineralization with distance towards the inner surface of the scale.[172] At the resolution of these nanomechanical experiments, no conclusive variations in mechanical properties could be observed within the isopedine layer due to its sublayers. The innermost thick basal osseous plate is composed of a succession of vascularized bone lamellae, with the major axis of the collagen fibrils approximately parallel to the scale surface.[156] Besides the spatial organization of their fibers, isopedine and bone also differ by the larger

diameter of the isopedine collagen fibrils (~100 nm versus ~20 nm, respectively) and by the thickness of its sublayers (~3-10 μm versus < 1 μm, respectively).[173] Surprisingly, there were no statistically significant differences detectable for the average $E_{O\text{-}P}$ and $H_{O\text{-}P}$ of the bone and isopedine layers ($p>0.05$). Multiple cross-sectional indents were taken on an individual scale, on different scales from the same animal, and on scales from a number of different animals and the trends presented in Fig. 2 and described above were consistently obtained (*data not shown*).

A negative approximately linear gradation (going from the outer to inner surface) in both $E_{O\text{-}P}$ and $H_{O\text{-}P}$ exists within the outer ganoine (-1.16 and -0.2 GPa/μm, respectively) and underlying dentin (-0.23 and -0.015 GPa/μm, respectively) layers, while isopedine and bone were found to exhibit relatively constant mechanical properties with cross-sectional distance (no gradation), as calculated from the slope of $E_{O\text{-}P}$ and $H_{O\text{-}P}$ with cross-sectional distance taken at load of 100 μN and a 1 μm interindent spacing for increased spatial resolution. The ganoine-dentin and dentin-isopedine junctions exhibited a steeper gradation relative to their neighboring layers; -5.9 and -0.44 GPa/μm for $E_{O\text{-}P}$ and $H_{O\text{-}P}$, respectively for the ganoine-dentin junction and -3.2 and -0.1 GPa/μm for $E_{O\text{-}P}$ and $H_{O\text{-}P}$, respectively for the dentin-isopedine junction. The thicknesses of the ganoine-dentin and dentin-isopedine junctions were found to be ~5 μm and ~3 μm, respectively (as indicated by the nanomechanical measurements). Nanoindentation FEA simulations (see Methods) approaching and across a discrete ganoine-dentin interface were employed to determine the width of the apparent gradient due the mechanical influence of a neighboring layer constraining or easing an indentation; for a maximum load of 100 μN,

the apparent width for $E_{O\text{-}P}$ was found to be ~ 1 μm and ~ 600 nm for $H_{O\text{-}P}$, less than the experimentally measured gradient widths. The ganoine-dentin junction is shown at high resolutions via back-scattered electron microscopy (contrast reflective of mineral content)

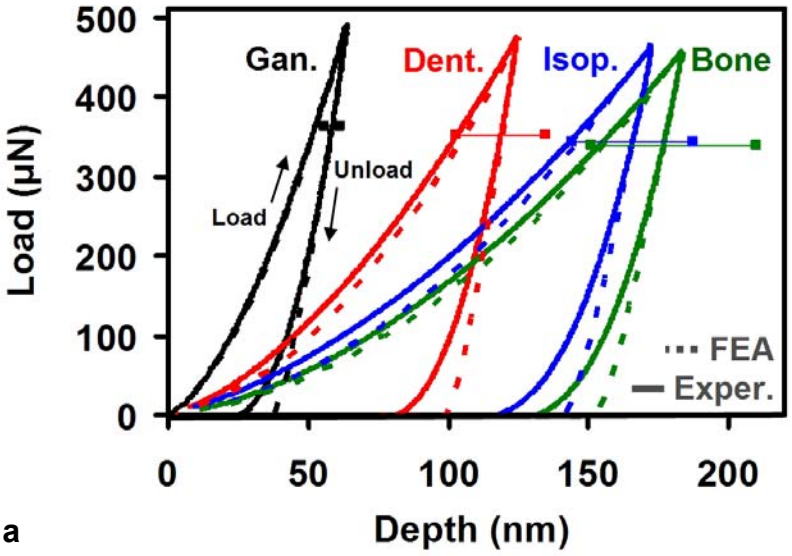

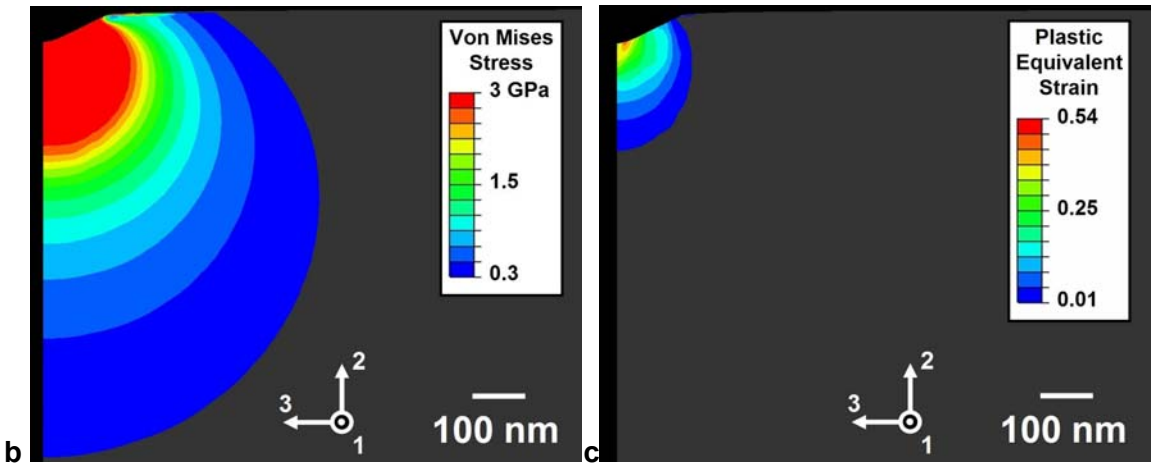

Fig. 7-3 **(a)** Average nanoindentation load-depth curves for all four layers. Solid lines are the experimental data averages, dashed lines are elastic-perfectly plastic finite element analysis (FEA) predictions. Horizontal error bars represent one experimental standard deviation. **(b)** FEA predictions of von Mises stress field for the indentation of the cross-section of ganoine at a maximum depth of 62 nm correspondingly to a maximum load of 500 μN. **(c)** FEA predictions of plastic equivalent strain (PEEQ) for indentation of the cross-section of ganoine at a maximum depth of 62 nm corresponding to a maximum load of 500 μN.

in Fig. 1e and shows an exceedingly sharp (<500 nm) and corrugated transition between the layers, which is expected to lead to spatially heterogeneous stresses and a higher net interfacial compression which could serve to prevent delamination.[174] Hence, the larger measured functional mechanical widths in *P. senegalus*, compared to the microstructurally apparent width (Chapter 6), are likely due to structural, rather than compositional, variations.

The second method used for evaluating mechanical properties involved fitting the entire averaged experimental load-depth data curve for each layer to an isotropic, elastic-perfectly plastic finite element analysis (FEA) computational model (Fig. 7-3) which approximates the three-dimensional Berkovich indenter geometry as two-dimensional, axisymmetric, conical-like, and rigid (see Methods). Plasticity is known to occur since

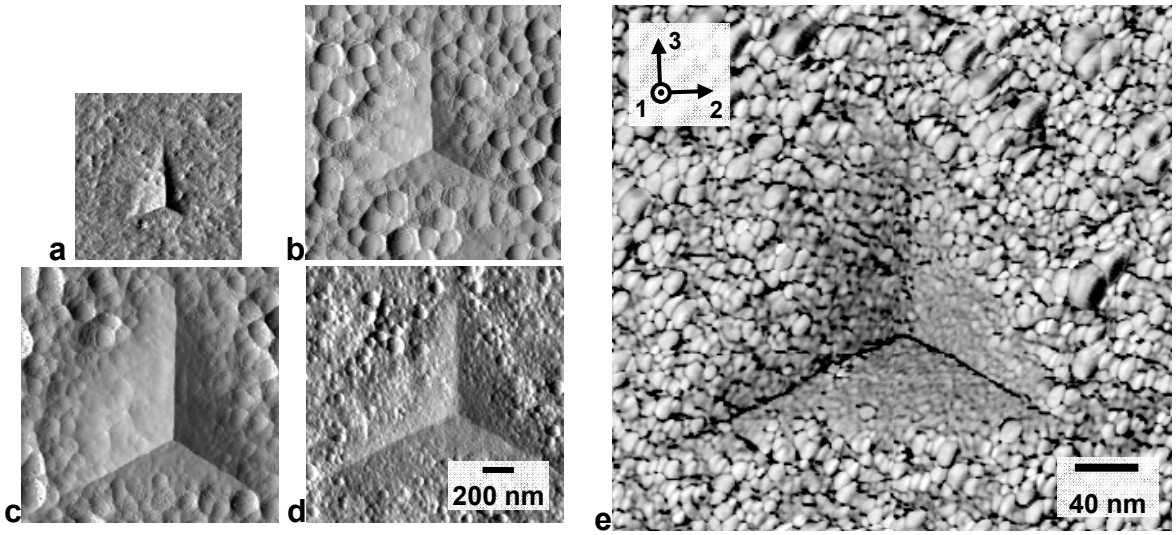

Fig. 7-4. Tapping mode atomic force microscopy (TMAFM) amplitude images of the residual indents (500 μN maximum load) on the cross-section of each of the four material layers. From top left to bottom right: **(a)** ganoine, **(b)** dentin, **(c)** isopedine, and **(d)** bone. **(e)** TMAFM phase image of the residual indentation (500 μN maximum load) on the cross-section of isopedine.

there is a finite residual depth observed experimentally after unloading (Fig. 7-3) and residual impressions after unloading are directly imaged by atomic force microscopy (Fig. 7-4).

In the FEA simulations, the indentation modulus, *E,* and the yield stress, σ_Y, were determined by a best fit to the averaged loading and unloading experimental data (Fig. 7-3), with the indentation modulus calculated from the FEA-predicted unloading slope matched to the experimentally calculated average $E_{O\text{-}P}$ (Fig. 7-2). Best fits were quantitatively assessed by calculating the percent error, ξ, per a given load value at 25 μN increments, where $\xi=|F_{FEA}- F_{EXP}|/F_{EXP}$, F_{FEA} is the indentation load as predicted from the FEA simulations at a particular depth, and F_{EXP} is the corresponding experimental load. Fig. 7-3 shows good agreement between the FEA theoretical predictions and the experimental data and produced average σ_Y values of 2000, 400, 215, and 180 MPa for the ganoine, dentin, isopedine, and bone, respectively. An extensive parametric study showed that the inclusion of post-yield strain hardening (linear isotropic hardening, linear kinematic hardening, and Ramberg-Osgood isotropic[175]) in the FEA simulations had a minimal effect in providing an improved prediction of the nanoindentation load-depth data and on the estimated σ_Y value (*data not shown*). All material layers were observed to undergo mechanical hysteresis (Fig. 7-3) and energy dissipation (calculated as the area between the average indentation loading-unloading cycle) and increased with distance from the outer surface of the scale inward from ganoine ~ 5.98 μJ to bone ~ 23.79 μJ.

7.3.2 MULTILAYERING OF THE P. SENEGALUS SCALE PROVIDES AN EFFECTIVE LENGTH-SCALE DEPENDENT "MACROSCOPIC" LOAD-DEPTH RESISTANCE

In order to explore the role of the local multilayered and graded micromechanical properties on the larger length scale biomechanical deformation of the entire *P. senegalus* scale, two axisymmetric, two-dimensional finite element analysis (FEA) models were constructed (Fig. 7-5, see Methods).

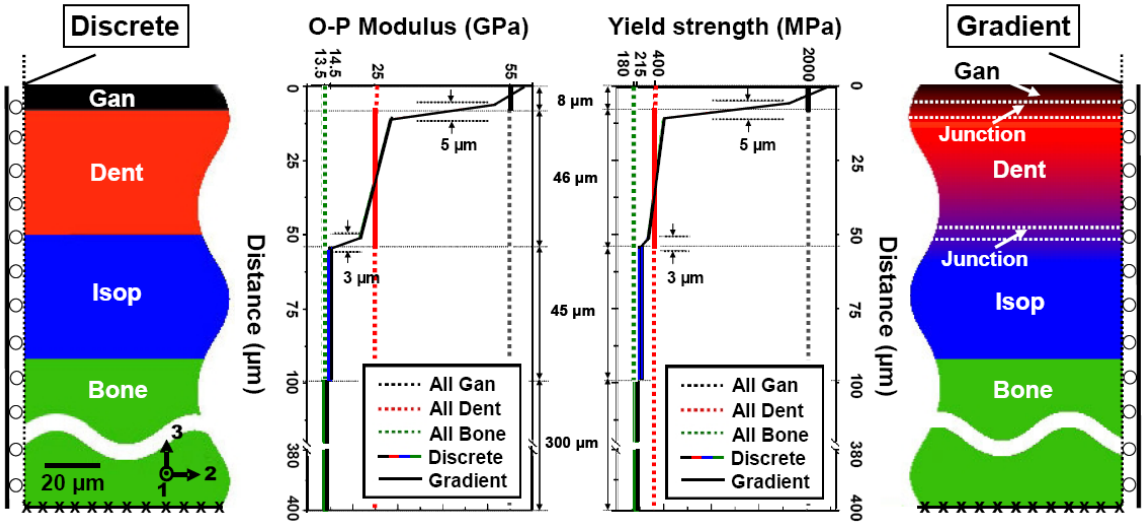

Fig. 7-5 Predictions of effective microindentation mechanical properties of *P. senegalus* scale via multilayered finite element analysis (FEA) simulations. a, Multilayered structures of discrete layers (left) and gradient layer and junctions (right) with their corresponding elastic modulus and yield stress distributions (center). *Figure by J. Song.*

The first "discrete" model (Fig. 7-5, left schematic) was composed of the four material layers with thicknesses corresponding to their experimentally measured values (Chapter 6) where each layer was assumed to possess isotropic, elastic-perfectly plastic constitutive behavior with E and σ_Y taken as that reduced from FEA predictions of the averaged load-depth data in Fig. 7-3 as described above. E and σ_Y of each layer were assumed to be constant through the thickness of each layer with a discontinuous jump at

each interface, i.e. the interfaces were abrupt and perfectly bonded. The second "gradient" model (Fig. 7-5 right schematic) also was composed of the four material layers with thicknesses corresponding to their experimentally measured values (Chapter 6) and assumed isotropic elastic-perfectly plastic material behavior, but rather incorporated linear gradients in E (scaled by the experimentally measured $E_{O\text{-}P}$ gradient values of Fig. 7-1) and σ_Y (scaled with the experimentally measured $H_{O\text{-}P}$ gradient values of Fig. 7-1) within the ganoine and dentin layers, as well as the ganoine-dentin and dentin-isopedine interphases (which were assumed to be 5 μm and 3 μm in thickness, respectively based on the experimental data of Fig. 7-1). The predictions of these two multilayered models were compared to three simulations of a single homogeneous layer of material with a thickness equivalent that of the entire scale (~ 400 μm) including; all ganoine ("All Gan"), all dentin ("All Dent"), and all bone ("All Bone"). The material properties of the three single layer simulations were again assumed to be elastic-perfectly plastic with E

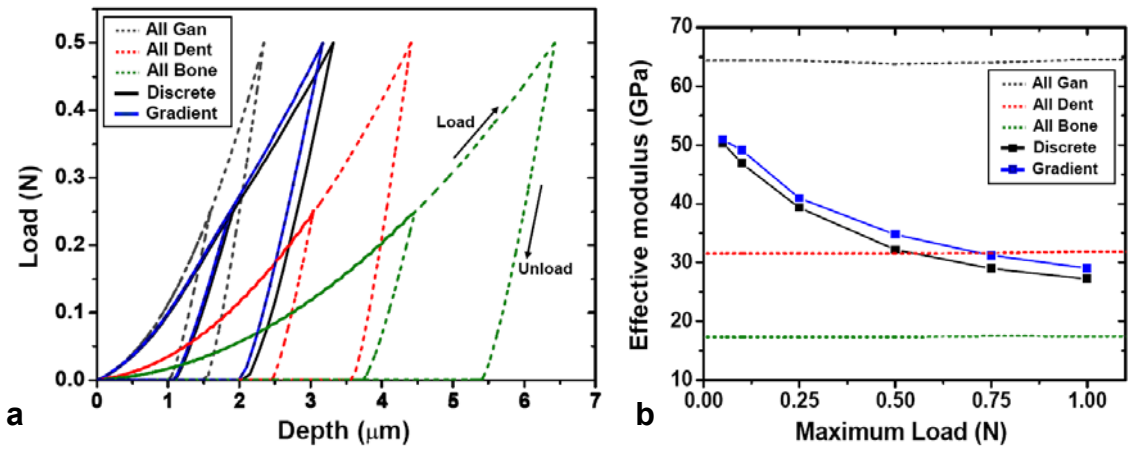

Fig. 7-6 **(a)**, Simulated microindentation load versus depth curves showing loading and unloading maximum loads of 0.25 and 0.5 N comparing the discrete and gradient multilayer systems to all-ganoine, all-dentin, and all-bone. **(b)**, Simulated effective indentation modulus as a function of maximum indentation load for the five material systems revealing the load-dependent effective modulus of the multilayered structures. *Figure by J. Song.*

and σ_Y taken as that reduced from FEA predictions of the averaged load-depth data in Fig. 7-3) and constant through the thickness of the entire scale.

Virtual microindentation experiments on loading and unloading were then performed using an axisymmetric, conical-like, rigid indenter (emulating an axisymmetric equivalent Vicker's microhardness tip using end radius ~ 3.7 μm, conical angle ~ 70.3°) up to maximum loads of 0.25 and 0.5 N (Fig. 7-6a). The two multilayered model predictions both tracked the ganoine load-depth curve up to a load of ~0.10 N and then at increasing penetrations, the multilayered load-depth profiles were found to fall in between the all ganoine and all dentin simulations (Fig. 7-6a). For the multilayered simulations, at a maximum load of 0.5 N, the indenter had penetrated ~45% of the way into the ganoine layer (Fig. 7-6a). There was minimal difference observed in the load-depth behavior for the discrete and gradient models, indicating the overall microlayering (and not the gradients) provides the effective "macroscopic" effective mechanical load-depth resistance (which is not to suggest that gradients do not play a role in penetration resistance, as will be discussed later on).

The "effective" behavior of the microlayered structures was further examined by reducing each load-depth behavior (for each material system taken to several maximum indentation loads) to an effective O-P modulus, effective microhardness (where microhardness is defined as the maximum indentation load divided by the residual indentation area after unloading), and energy dissipation. Interestingly, a load-dependent effective modulus and microhardness are predicted for the multilayered models, which is not the case for the homogeneous single-layered systems (Fig. 7-6b). The effective

modulus for these two models is seen to decrease nonlinearly from close to that of all ganoine at small maximum loads to values *below* that of all dentin by a maximum load of 1N (corresponding to a penetration depth of~ 5.5-5.7 μm, Fig. 7-6b).

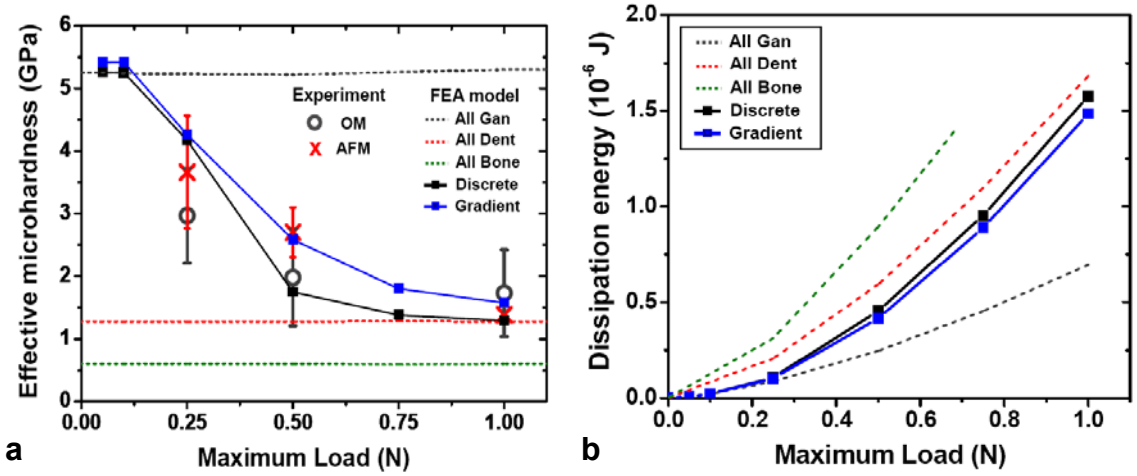

Fig. 7-7 Predictions of effective microindentation mechanical properties of *P. senegalus* scale via multilayered finite element analysis (FEA) simulations. **(a)** Simulated effective microhardness as a function of the maximum indentation load for the five material systems and the experimentally measured values. **(b)** Simulated effective energy dissipation as a function of the maximum indentation load for the five material systems. *Figure by J. Song.*

Hence, the underlying micromechanics of the multilayered structure directly govern the effective "macroscopic" indentation modulus, where the indenter increasingly "feels" the more compliant dentin layer as the indentation load is increased. The dentin layer is deforming while under the constraint of the stiffer, harder ganoine layer – which leads to elevated hydrostatic pressures in the dentin layer (Fig. 7=8); at the highest loads, these elevated hydrostatic pressures lead to more recovery upon unloading and the effective modulus is seen to drop below the dentin modulus (Fig. 7-7). For the multilayered simulations, the effective microhardness is also predicted to decrease nonlinearly and sigmoidally between values corresponding to all ganoine (at small

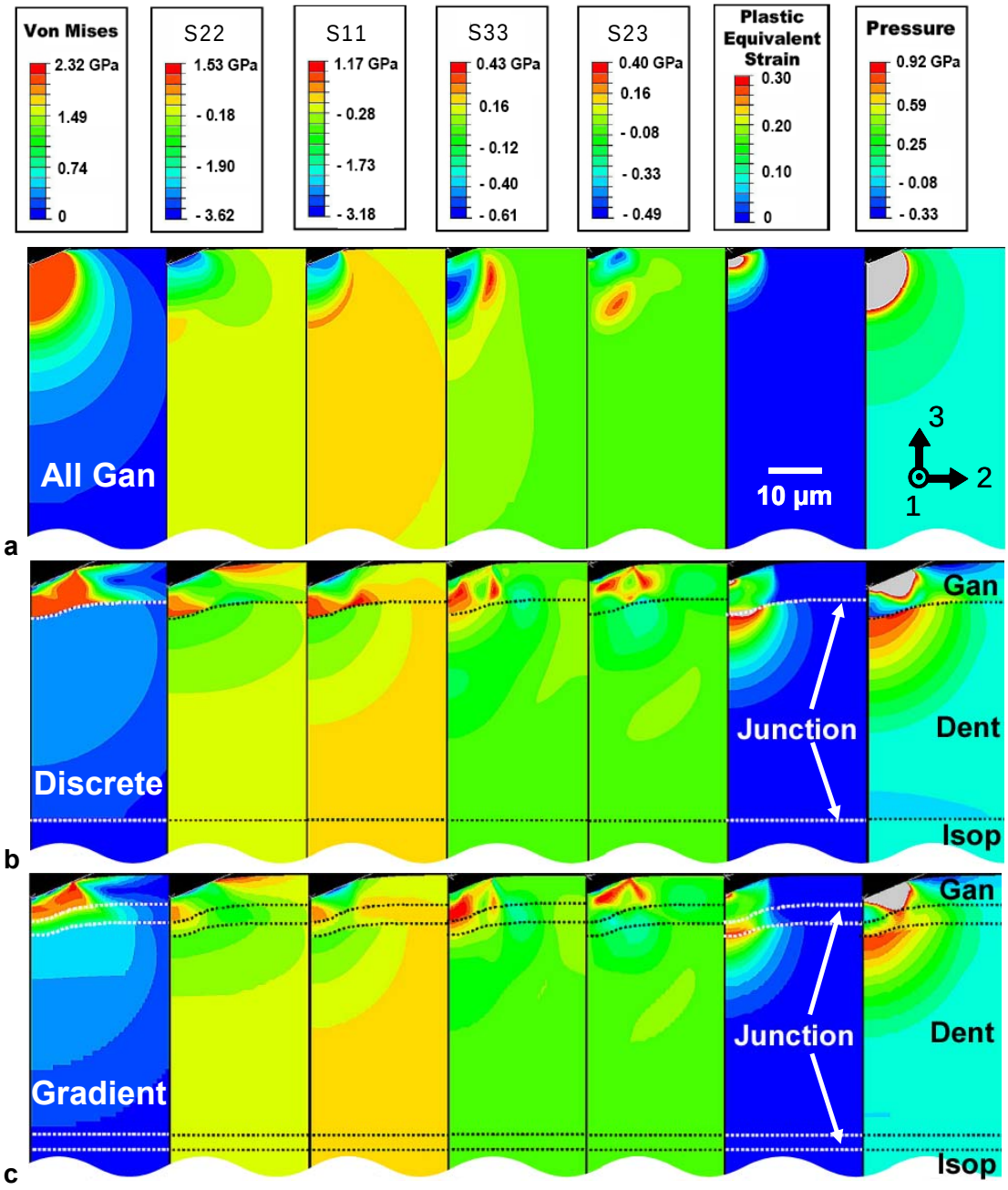

Fig. 7-8 Simulation contours of stress, plastic strain, and pressure fields of *P. senegalus* scale via multilayered finite element analysis (FEA) simulations. FEA predictions of von Mises stress field, S11 (normal stress on the plane perpendicular to the 1 axis), S33 (normal stress on the plane perpendicular to the 3 axis), and pressure at a maximum depth when fully loaded, and S12 (shear stress on the plane perpendicular to 2 axis acting in the 1 direction), S22 (normal stress on the plane perpendicular to the 2 axis) and plastic equivalent strain after fully unloaded for three models: **(a)** all ganoine, **(b)** discrete and **(c)** gradient FEA models for 1 N maximum load indentation. *Figure by J. Song.*

maximum loads <0.1 N) and all dentin (by a 1 N maximum load corresponding to a penetration depth of ~5.5-5.7 μm, Fig. 7-7). The gradient model was found to have a consistently higher effective modulus and microhardness compared to the discrete model, a direct result of the ganoine-dentin junction and dentin layer of the gradient case having higher modulus and yield stress values in the regions that undergo deformation during indentation compared to the discrete model. The multilayer microhardness predictions were compared to experimentally measured Vickers hardness values (measuring residual area using both tapping mode atomic force microscopy and optical microscopy) on an individual *P. senegalus* scale and both the magnitude and load dependence were accurately captured (Fig. 7-7), experimentally verifying the load-dependent aspect of the effective material properties of the microlayer. The effective energy dissipation of the microlayered models were found to increase nonlinearly with maximum load (Fig. 3e) and fall in between the all ganoine and all dentin curves.

7.3.3 GRADATION AND PLASTICITY OF THE *P. SENEGALUS* SCALE PROVIDES FURTHER PENETRATION RESISTANCE

Fig. 4 shows the stress contours and plastic equivalent strain (defined as a scalar measurement of the accumulated plastic strain work conjugate to the scale equivalent Mises stress) after unloading for the simulated microindentation multilayer models as compared to that of the all ganoine material for a maximum load of 1 N. The gradient junction is observed to provide a transitional region for stress redistribution between layers of differing materials (Fig. 7-8a), as opposed to the more abrupt changes observed in the discrete model (Fig. 7-8b). Such smoother stress gradients are expected to mitigate interface failure and increase interfacial toughness, thereby providing increased

penetration resistance. Hence, while the discrete and gradient multilayered systems case achieve similar macroscopic effective indentation modulus and microhardness, the gradient case micromechanically achieves more gradual stress redistribution providing robustness to interfacial failures. The plastic equivalent strain contours reveal the greater depths and greater area of plastic straining for the multilayer system compared to the all ganoine model, due to the increased plastic strain of the underlying dentin which possesses a lower σ_Y compared to ganoine; this correlates with the greater dissipation seen in the load-depth curves (Figs. 7-2). The simulations also show that the magnitude of the plastic strain in the ganoine layer of the multilayered system are lower than that experienced in the all ganoine system even though the overall depth of penetration in the multilayer (5.46-5.72 μm) is more than twice that of the all ganoine system (3.63 μm); this is a direct result of the dentin deformation accommodating the imposed penetration depth.

The 1 N maximum load is appropriate to estimate a brittle failure condition for the ganoine layer since 1 N microhardness experiments were found to exhibit circumferential cracks in some cases and only plastic strain in other cases (Fig. 7-9) – indicating the 1 N case is at the border of meeting crack initiation conditions. Contours of the radial stress, S22 (Fig. 7-8, column 2) reveal elevated tensile surface values of 1.66 GPa at the perimeter of the contact area (in the same region where the circumferential cracks are found), suggesting a maximum normal brittle stress failure condition of 1.66 GPa. We note that the values are a little lower and the regions of elevated stress are smaller in the gradient case than the discrete case indicating the smoothing role of the gradient in reducing the surface stresses. A second prominent surface failure condition is

often radial cracks which were not observed in the microhardness experiments; this is consistent with the simulation results which show the surface circumferential stress

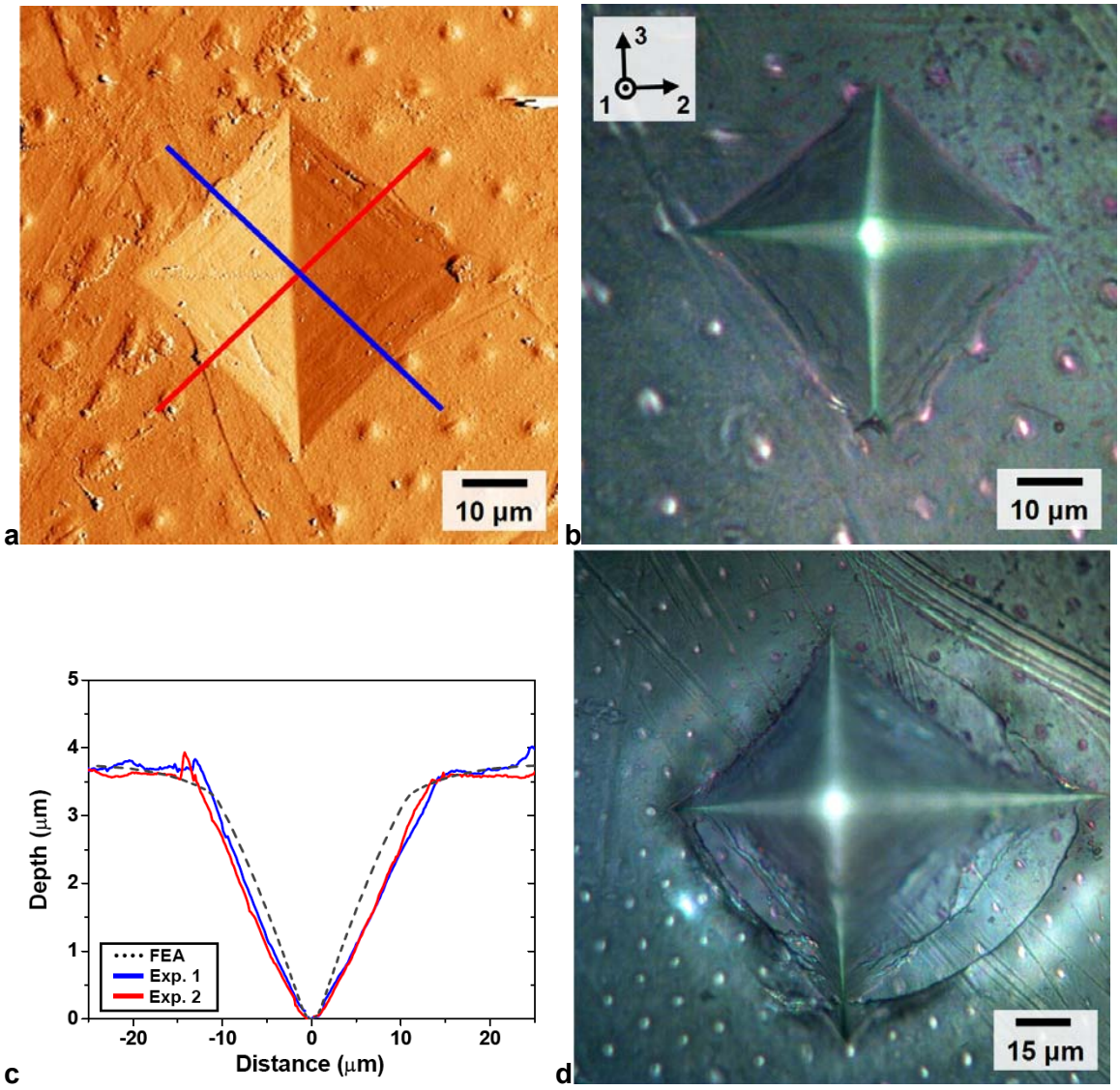

Fig. 7-9 Topographic profiles, residual impressions of microindentation, and fracture of the outer ganoine surface of an individual *P. senegalus* scale. **(a)**, Tapping mode atomic force microscopy (TMAFM) amplitude image of a 1 N maximum load microindentation. **(b)** Optical micrograph of a 1 N maximum load microindentation **(c)** Finite element analysis prediction of the residual depth topography obtained from the gradient multilayer simulation and experimental height profiles from TMAFM images (from Fig. 7-9 a) for 1 N maximum load microindentation **(d)** Optical micrograph of a 2 N maximum load microindentation

values, S11, which would be needed to initiate radial cracks, to be dramatically lower than the S22 surface values. As seen in other multilayer systems [176], the interfacial normal and shear stresses were found to be more severe upon unloading; hence the S33 and S23 contours are depicted in the unloaded state in Figure 7-8 (columns 4 and 5). The stress levels and distributions are found to be similar for the discrete and gradient systems with the exception of a peak shear stress present on the interface of the discrete system and which is absent in the gradient system.

Excellent agreement between simulation and experiment was also demonstrated in comparison of the measured residual topography after unloading (Fig. 7-9); where we note that the 0.5 N cases deformed in an elastic-plastic manner with no cracks in most cases (~ 9 out of 10 indents, Fig. 7-9a,b), for the 1 N ~50% of the samples exhibited circumferential cracking, and circumferential cracks were observed in all of the 2.0 N cases (Fig. 7-9d, plasticity, i.e. residual deformation, was always visible at all loads tested)

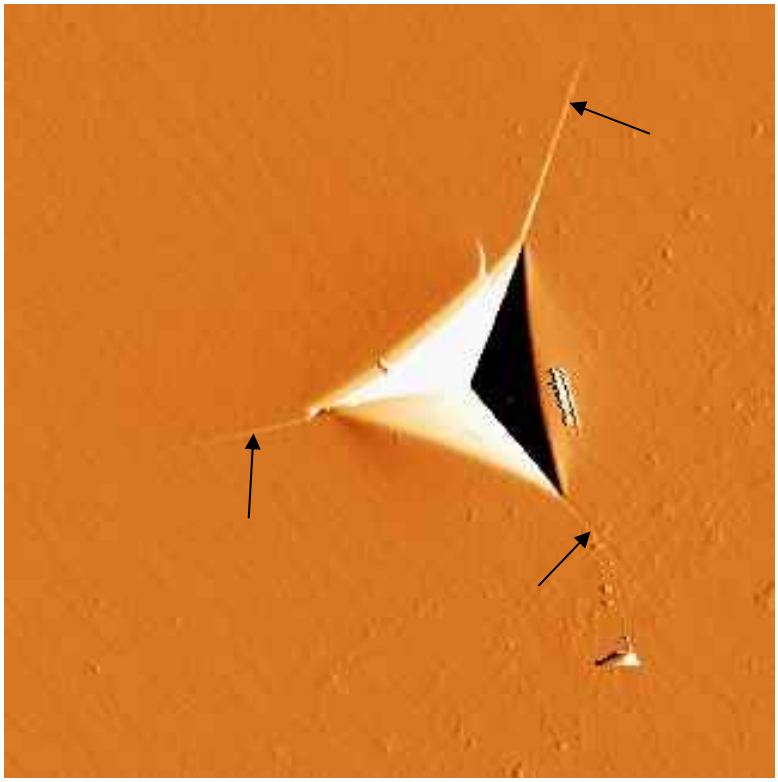

Fig. 7-10 TMAFM amplitude image of the residual imprint of a 10 mN Berkovich indent in fused silica. The black arrows indicate radial cracks emanating from the indent apexes.

As noted earlier, all simulations assumed each constituent material to exhibit an isotropic elastic-plastic mechanical behavior; the microstructure of these materials (Chapter 6) suggests an anisotropic mechanical behavior which is an avenue of ongoing investigation. The excellent agreement between the simulation and experimental results regarding hardness and residual topographies (Fig. 7-7, 7-9c) suggests that the simulations do capture the basic design principles of the layered structure and the role of the strong contrast in properties from layer to layer being a governing feature for indentation behavior (as opposed to a smaller contrast in direction-dependent properties within a layer). Anisotropy has been found to play a role in fine details of the underlying stress distributions within and between layers and how these engage failure mechanisms

(which will be clearly direction dependent). For example, the surface radial stresses in the ganoine clearly correlate with the observed circumferential cracks which likely penetrate into the interior directly to the interface given the needle-like structure of the ganoine (more is discussed on this below). Multilayered simulations which take into account both elastic and plastic mechanical anisotropy reveal minimal variation in the predictions of effective modulus and microhardness and also little difference in the radial and circumferential stress magnitudes and distributions - therefore, further supporting the conclusions based on the isotropic simulations. However, interestingly anisotropy is found to have a significant advantageous effect on reducing the interfacial normal and shear stresses (a result of the directional and reduced shear modulus of the needle-like structure of the ganoine); this reduction in interface stress is consistent with the crack arrest at the interface (described in more detail below), as well as increasing plasticity within the isopedine layer.[177]

7.4 DISCUSSION

While mineralized dermal fish scales serve many functional roles simultaneously,[120-122] we limit our discussion here to biomechanical aspects, in particular protection from predators.[119] *P. senegalus* living today are territorial and in prone to in-fighting with its own species (via biting[167] and body-thrashing) or their own carnivorous vertebrate relatives.[119] In ancient times, many large invertebrate predators existed such as the carnivorous Eurypterid (thought to be a predator of the armored Ostracoderms) which was a giant arthropod that possessed biting mouth parts, grasping jaws, claws, spines, and

a spiked tail,[119] and it has been suggested that the Placoderm *Dukleosteus terelli* possessed a bite force large enough to puncture through the mineralized exoskeletal materials of its prey, in order to consume the flesh underneath.[123] Mechanically, such predatory attacks would represent a penetrating load (approximated by the multilayered indentation FEA simulations), which involves a multiaxial and largely compressive stress field. We note that *P. senegalus* exhibits a multilayered scale design over a micrometer-sized length scale, suggesting that the purpose of this design is for resistance to mechanical loads and deformations existing over these small length scales as well, for example the teeth of a similar-sized *P. senegalus* were measured to possess an end-radius of 14.7 ± 8.8 μm ranging from ~ 3.0 μm to ~ 44.0 μm.

Mineralized dermal scales of fish have certain histological similarities to mammalian teeth, including an external highly mineralized enamel layer capping a softer underlying dentin layer,[178] and a brief comparison is instructive. Teeth and scales are considered to originate from "a single modifiable morphogenetic system"[179]; the odontodes ("fundamental dermal skeletal units" [180, 181]) present in the first vertebrates ~500 million years ago.[182] The magnitude of the ganoine and dentin average indentation modulus and hardness, as well as the ganoine-dentin interfacial gradient, measured here are, in fact, similar to the properties reported for mammalian tooth enamel and dentin.[183-186] The magnitude of the ganoine and dentin layer gradients in the *P. senegalus* scale, however, are much larger (three to four orders of magnitude) than those reported for mammalian tooth enamel and dentin.[187] The loads and deformations experienced by the mineralized scales of *P. senegalus* under a penetrating impact are expected to be quite different compared to those in teeth during masticatory crushing and grinding, in

particular more localized spatially in the plane of the surface but with increased deformation normal to the surface (relative to length scale of the interacting object causing the deformation). These differing functional requirements are expected to be reflected in the internal layer properties, interfacial gradients, and multilayered design, as well as the larger length scale geometry of the entire structure. Even though the measured averaged mechanical properties of ganoine are found to be similar to those reported for enamel in mammalian teeth,[183-186] differences in structure are known to exist (e.g. ganoine is frequently observed to be stratified[156]) and also, a wide diversity of crystallite orientation is observed for ganoine of distinct genera.[188] Additionally, regular arrays of micrometer-sized dentinal tubules were not observed in the *P. senegalus* scale, as exists for mammalian teeth.[189] These structural differences will affect smaller lengths scale local stresses and modes of deformation, such as spatial distributions of plasticity and crack propagation, rather than the averaged values of the layer and effective multilayer mechanical properties. As ganoine transfers load through the ganoine-dentin junction, the underlying softer, more compliant dentin layer dissipates energy via plasticity (at high enough loads). Then, the presence of the additional isopedine stratified layer with its plywood-like structure can serve as a second line of defense for deeper penetrations, preventing catastrophic crack propagation and increasing energy dissipation and fracture toughness. We have observed microcracking confined within the sublayers of the isopedine (Fig. 70), where each layer has cracks running in approximately orthogonal directions (consistent with the known structure) but arrested at the edge of each sublayer, i.e. not running continuously through the entire isopedine layer. Isopedine in the Sarcoptrygian families can be more complex; rather than having just two collagen fibril

perpendicular orientations (as it is for Actinopterygians / Polypteridae), it can have with double twisted plywood structures with up to seven orientations.[190] The underlying bone acts as the base skeletal physical support structure for normal physiological loading conditions, where plastic deformation (if forced beyond the elastic limit via a traumatic event) takes place via mechanisms such as nanogranular friction,[191] collagen fibril shear[192] and denaturation,[193] crack initiation / propagation[194] and intraorganic extensibility and sacrificial bond rupture.[195] Older dermal armor, from Cephalaspidomorphi (Agnathans), Placodermi, fossil Sarcopterygii during the Ordovician possessed an additional spongy bone layer above the lamellar bone layer,[196] which would be beneficial for additional energy absorption during mechanical impacts. It appears that the one overarching mechanical design strategy is the juxtaposition of multiple distinct reinforcing layers, each of which has its own *unique* deformation and energy dissipation mechanisms, and that additional layers exist for increased protection, at the expense of added weight and reduced mobility/speed. Additionally, anisotropy within these layers appears to have an advantageous effect on mitigating the build-up of interfacial stresses and promoting energy dissipation and plasticity within deeper layers.

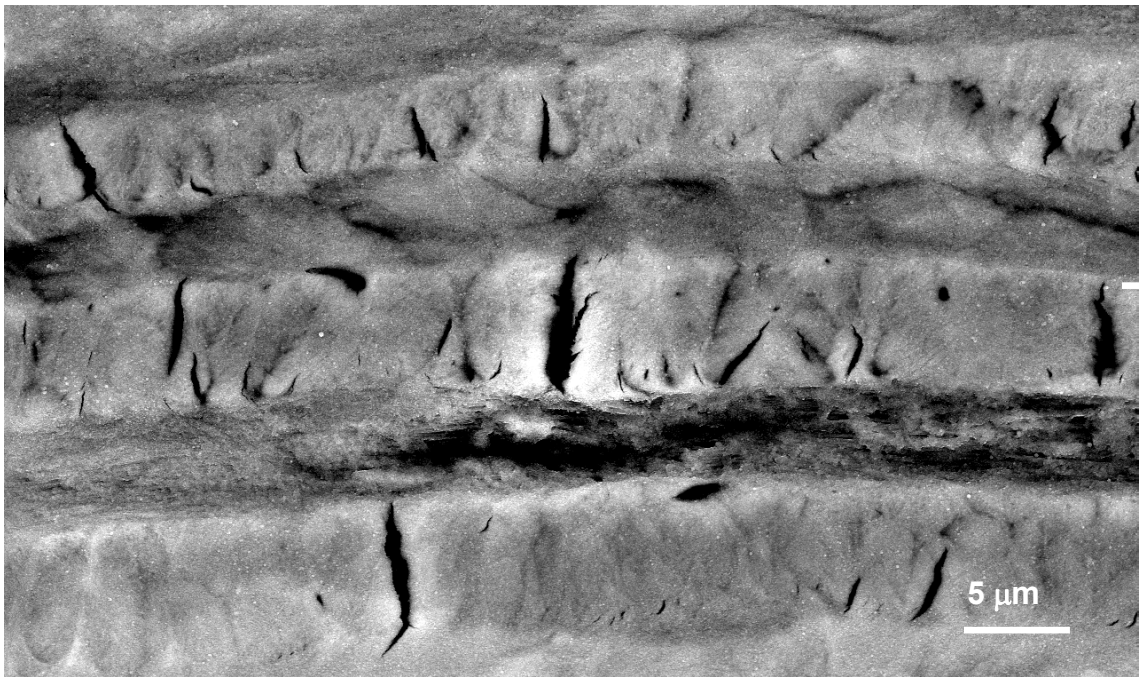

Fig. 7-11 Scanning electron micrograph (SEM) of cross-section of isopedine layers showing orthogonal cracks in sublayers.

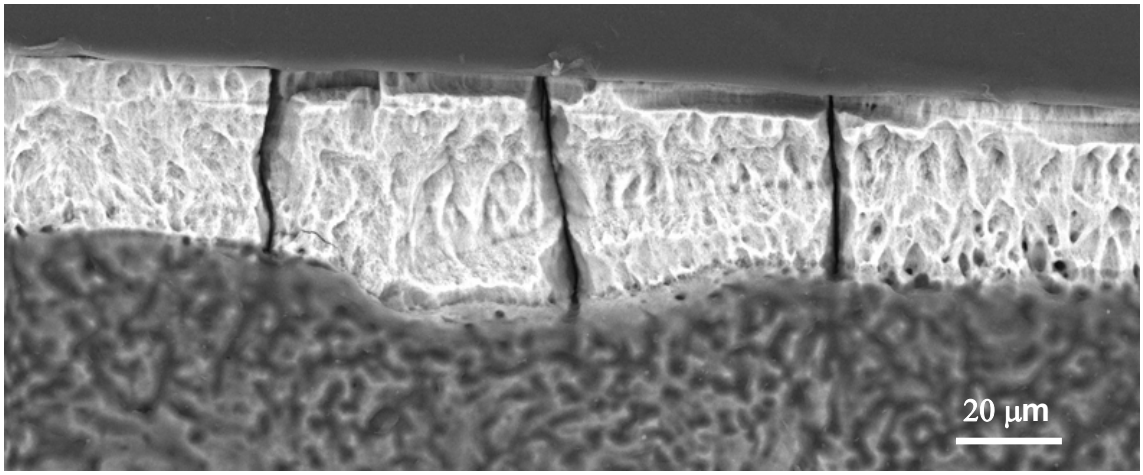

Fig. 7-12 Back-scattered SEM of cross-section of ganoine and dentin layers (etched with phosphoric acid for 20 seconds) showing cracks arrested at ganoine-dentin interface as well as pieces of ganoine cracked off from outer surface.

We have observed the interfaces between layers in *P. senegalus* scales to be exceedingly strong and tough, e.g. the ganoine-dentin junction is able to arrest cracks

(Fig. 7-12) as in mammalian teeth.[132] Localized fractures within the brittle ganoine layer and detachment of pieces of the ganoine layer off the scale is seen, while the ganoine-dentin junction remains wholly in-tact (Fig. 7-12), which may be a sacrificial mechanism. The junctions between material layers are clearly "functionally graded," i.e. they possess a gradual spatial change in properties motivated by the functional performance requirements which also varies with location and are able to promote load transfer and stress redistribution thereby suppressing plasticity, crack arresting, improving adhesion and preventing delamination between dissimilar material layers.[197] As mentioned previously, the corrugated junction between the layers is expected to lead to spatially heterogeneous stresses and a higher net interfacial compression which could serve to prevent delamination.[174]

Another possible mechanical function of dermal armor is abrasion and wear-resistance against rocky surfaces in fast-flowing streams or the abrasive action of mud and/or sand particles,[122, 198] although modern fishes seem to survive fine in such environments with this additional protection.[119] Indeed, placoid scales have been reported to "show extensive wear (scrapes and scratches) particularly on those demersal species frequently hard substrates (i.e. coral reefs, rocky outcrops)."[122] Polypterids have an additional respiratory organ, a lung-like "swim bladder" which allows them to come to the surface and breathe air and limblike fins and powerful tails that enables them to dig into the mud, and even crawl over land for short distances to reach alternate water sources;[167] ganoid scales could also serve as protection for these purposes.

In addition to the nanoscale to microscale mechanical design principles described here for localized penetrations, the higher level scale-to-scale peg-and-socket articulation

reinforced with extensible fibrillar collagenous layers allows *Polypteridae* to undergo extreme body curvatures during sharp turns and prey strikes.[199] Dermal scales clearly represent an intermediate tradeoff between body protection and maximum mobility,[124] when comparing the larger, heavier dermal armor of the Ostracoderms and bare skin (e.g. canines, felines use speed, strength, and intelligence to survive without armoring[124]). Modern human body armors generally employ helmets and plate-like inserts to protect the head and vital organs, respectively with extremities left free for mobility, fighting capabilities, and basic bodily functions. The multiscale mechanical design principles found in natural armor, such as those described here, may facilitate new ideas both on material design of individual plates, as well as the larger length scale geometry of the armor as a whole. [153]

APPENDIX A NACRE PHYSICAL CHARACTERIZATION

Ash Weight (Deorganified Nacre) Samples masses were measured after desiccation in a vacuum chamber at room temperature for 24 hours and then again after a subsequent 2 days at 250◦C in vacuum, which presumable removes the majority of the organic component. The difference was found to be 2.4 ± 0.3% wt.

Demineralized Nacre Weight. Samples masses were measured after 24 hours of desiccation in a vacuum chamber at room temperature, immersion in a disodium salt ethylenediaminetetraacetic acid aqueous solution (0.5M EDTA) for 10 days (the solution was refreshed every day), and an additional 24 hours of desiccation in a vacuum chamber at room temperature. After this last step, the mass was found to be 6.4 ± 1.4% wt. of the original sample mass.

Raman Spectroscopy. A *Kaiser Hololab* 5000R Raman spectrometer was used at 785 nm utilizing coherent continuous wave Argon/Ion and Ti/S Lasers. Fresh nacre showed 4 sharp bands due to the vibration of the carbonate ions at 1085 (symmetric stretching, ν_1), 852 (out of plane bending, ν_2), 705 (in-plane bending, ν_4), 207, and 154 cm^{-1} characteristic of the aragonite structure.[200]

X-Ray Diffraction (XRD). Samples were crushed using mortar and pestle to a fine powder which was then analyzed with a Rigaku RU300 18kW Rotating Anode X-Ray

generator coupled with a 250 mm High Resolution Bragg-Brettano Diffractometer. The generating voltage was set to 60kV, the current to 300 mA, the scan speed to 0.014◦ per second, and an angular range of 8-55◦**.** For fresh nacre, the spectrum showed peaks characteristic of aragonite.[201] Another series of X-Ray powder diffraction spectra for *Trochus niloticus, Haliotis rufescens* and geological aragonite was obtained using a PANalytical X'Pert Pro. Results showed that the geological aragonite is shifted at higher angle, which is usually due to a smaller d-spacing or a higher content of impurities. The values for the unit cell parameters for the two different seashells was extremely close: 5.751 Å (*Trochus*) and 5.753 Å (*Haliotis*) for c, 4.965 Å both for a and 7.962 Å both for b, compared with 5.740 Å (c of geological aragonite), 4.960 Å (a) and 7.964 (b). The X-Ray spectra for seashells all had peaks slightly broader than for single crystal aragonite, but the mean crystallite size obtained by the whole pattern fitting method was above 150 nm for all seashell samples. This value is a the limit of resolution of the instrument, thus the true crystallite diameter mean value could very well be significantly higher.

Fourier Transform Infrared Spectroscopy (FTIR).[40, 202] A *Perkin Elmer* 2000 FTIR Spectrometer was scanned at a resolution of 4 cm^{-1} with steps of 1 cm^{-1} and the results are shown in Fig. A1.

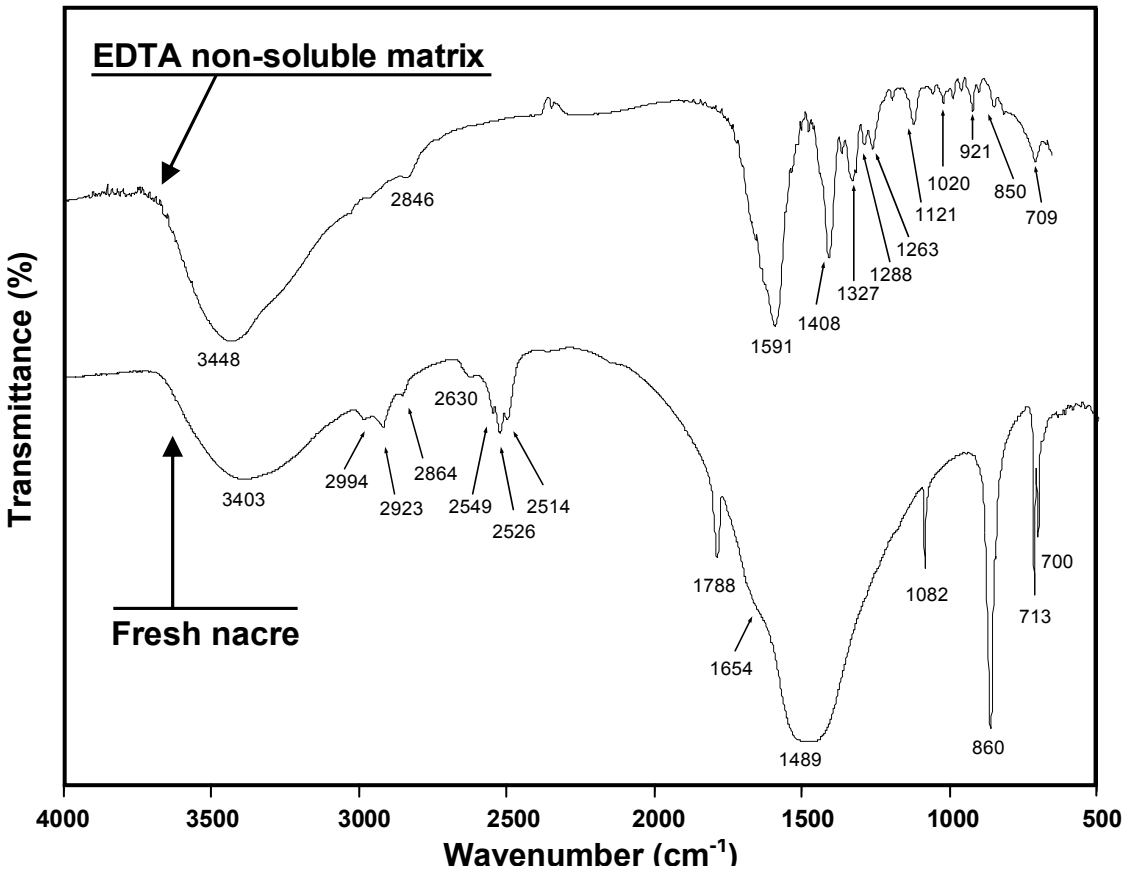

Fig A1. FTIR spectra of fresh and EDTA-demineralized nacre from *Trochus Niloticus*.

EDTA-demineralized nacre. The broadest band on the FTIR spectrum (Fig. A1, upper spectrum) is located at 3448 cm^{-1} (OH and/or NH stretching modes of the organic matrix components). The 2800–3000 cm^{-1} range is characteristic of the C-H stretching modes, and exhibits a small band at 2846 cm^{-1}. The material is found to be mainly composed of EDTA-protein complexes as demonstrated by the presence of intense bands at 1591 cm^{-1} (carboxylate groups coordinated asymmetric stretching band) and 1409 cm^{-1} (carboxylate symmetric stretching band). Smaller peaks detected at 1288, 1263, 921 and 850 cm^{-1} are characteristic of sulfate groups, while the 1000–1150 cm^{-1} peaks correspond to the major polysaccharide absorption region. The presence of bands at 1327 cm^{-1} and

709 cm^{-1} indicates amide group absorption (amide III C-N stretching vibration and amide V/VII respectively).

Fresh nacre. Bands are observed in the 3200-3500 cm^{-1} and 2800-3000 cm^{-1} range, as in the spectrum of EDTA-demineralized nacre, and thus attributed to the insoluble organic matrix. Peaks in the 2500-2650 cm^{-1} range (2630, 2549, 2526 and 2514 cm^{-1}) correspond to the EDTA soluble organic matrix (OH groups of carboxylic amino acids) and/or carbonate groups (HCO_2^{3-}) present in the mineral component, as they do not appear on the EDTA demineralized nacre spectrum. The following wavenumbers peaks were observed that are characteristic of the carbonate ions in aragonite: 713 and 700 (ν_4), 860 (ν_2), 1082 (ν_1) and 1489 cm^{-1}. The peak located at 1788 cm^{-1} is related to the C=O groups of the carbonate ions.

APPENDIX B FINITE ELEMENT ANALYSIS (FEA) MODEL USING TWO-DIMENSIONAL AXISYMMETRIC INDENTER

A FEA nanoindentation model was employed which approximated the three-dimensional Berkovich nanoindentation experiments using a two-dimensional conical-like axisymmetric indenter (Fig. B-1). The indenter geometry was chosen in order to correspond to the experimentally determined indenter cross-sectional tip area function, $A(h_c)$, where h_c is the maximum contact depth. $A(h_c)$ was determined by carrying out a series of nanoindentations into a fused quartz sample (Micro Materials, Ltd. Wrexham, U.K) of known elastic modulus (72 GPa[203]) at depths up to 200 nm. A at each h_c was estimated via the Oliver-Pharr analysis[203] from the unloading stiffness, S, and the effective modulus, E_r, ($A=\pi/4\times(S/E_r)^2$) and h_c was determined from the maximum load, P_{max}, the maximum depth, h_{max}, and S (using $h_c=h_{max}-0.75\times P_{max}/S$). These data were fit to a polynomial function, yielding; $A(h_c) = 26.88h_c^2 - 2094.49h_c + 172363.99h_c^{1/2} - 1457791.58h_c^{1/4} + 3286246.01h_c^{1/8} - 1995783.19h_c^{1/16}$. The indenter tip was designed as a rigid analytical profile since the elastic modulus of the diamond probe tip is at least 20× greater than that for the indented samples. The indented sample was modeled as elastic perfectly plastic using 4-node bilinear axisymmetric quadrilateral elements (CAX4R in ABAQUS element library, Providence, RI). Mesh convergence simulations were carried out and an optimal mesh (in terms of accuracy and calculation costs) was chosen for use in all simulations, which contained 1378 nodes and 1251 elements. Large deformation

theory and frictionless contact between the indenter and material were assumed. The deformation mode was chosen as quasistatic.

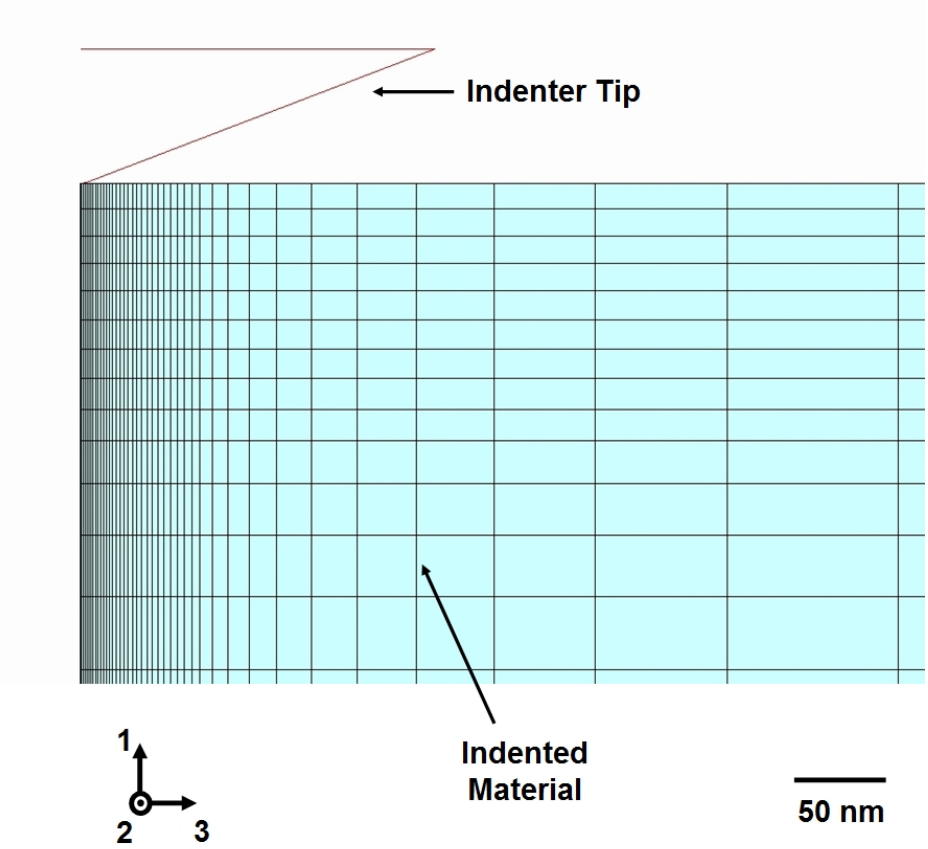

Fig. B-1 Finite element analysis model using two-dimensional axisymmetric indenter. Sample mesh and indenter tip surface profile.

In order to validate the two-dimensional axisymmetric approximation described. above, this model was compared to an ideal three-dimensional FEA Berkovich indenter tip with a rounded end model (Fig. B-2 a) with an identical tip area function. For the three-dimensional indenter tip, the angles were assumed to be that of an ideal Berkovich geometry (i.e. a total included angle of 142.3° and half angle of 65.35°) with a rounding

of the tip end. This translated into a half angle of 70.3° for the two-dimensional axisymmetric indenter tip for an equivalent tip area function as the three-dimensional

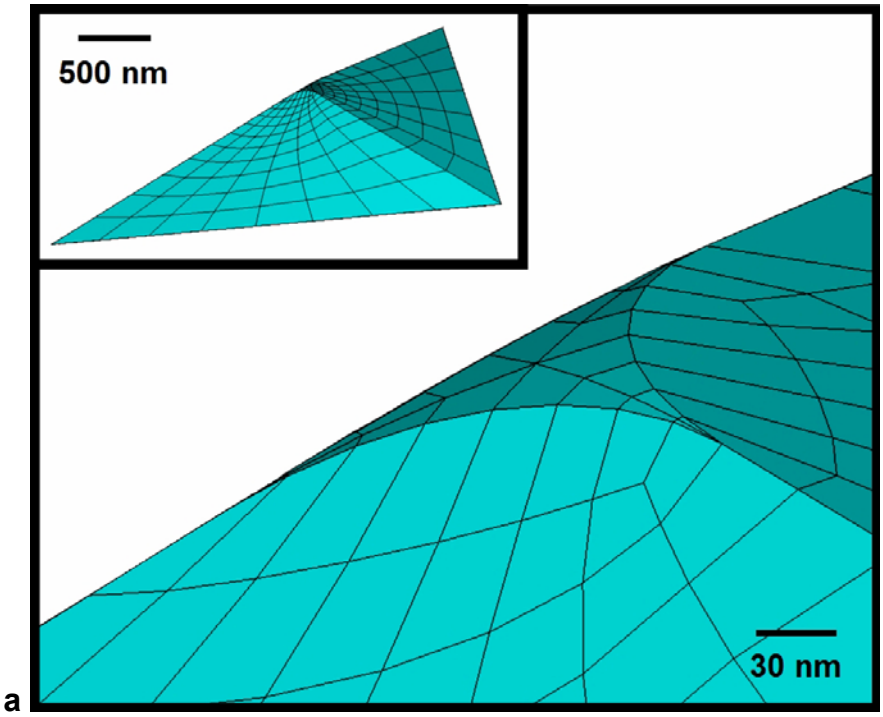

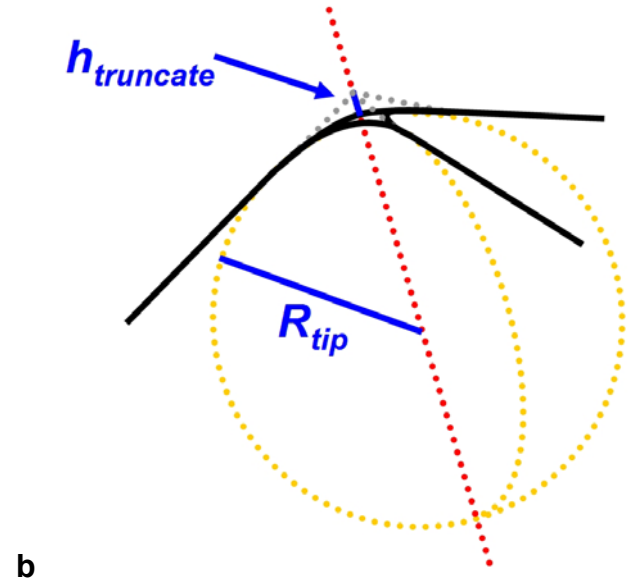

Fig. B-2. Three-dimensional Berkovich indenter FEA model. **(a),** Rounded Berkovich indenter tip mesh. The entire tip is shown in the inset. **(b)**, Schematic of the indenter tip end showing how the end radius, R_{tip}, and truncate height, *h,* are defined.

model. The rounding of the three-dimensional indenter tip was defined by a revolving cut of the ideal tip end along a sphere tangent to each of the three edges of the tip and with an end radius, R_{tip} (Fig. B-2 b). The truncate height, h, was defined to be the distance between the apex of the rounded tip and the apex of the imaginary ideally sharp tip as shown in

Fig. B-2 b and is a function of R_{tip}. For the two-dimensional tip, this translated into having the tip end cut by a circle of radius R_{tip} so that the truncated height was equivalent to the three-dimensional case. In order to chose realistic geometric values, R_{tip} and h were estimated using FEA simulations to best predict nanoindentation experimental load versus depth data conducted on a fused quartz sample (Micro Materials, Ltd. Wrexham, U.K) and modeled as a perfectly elastic solid. The best fits were obtained corresponding to an indenter tip end radius R_{tip} = 275 nm (corresponding to h = 7 nm). The symmetry of the three-dimensional indenter tip enabled simulations using 1/6 of the indenter and the indented material with appropriate boundary conditions. The indenter tip was modeled as rigid using 4-node bilinear rigid quadrilateral elements (R3D4 in ABAQUS element library, Providence, RI) for the three-dimensional model and a rigid analytical profile for the two-dimensional case. The indented sample was modeled as elastic perfectly plastic using 8-node linear brick element (C3D8R in ABAQUS element library, Providence, RI) for the three-dimensional case and 4-node bilinear axisymmetric quadrilateral elements (CAX4R in ABAQUS element library, Providence, RI) for the two-dimensional case. Mesh convergence simulations were carried out and an optimal mesh (in terms of accuracy and calculation costs) was chosen for use in all simulations, which contained 11737 nodes and 9672 elements (three-dimensional case), and 1378

nodes and 1251 elements (two-dimensional case). Large deformation theory and frictionless contact between the indenter and material were assumed. The deformation mode was chosen as quasi-static.

The three-dimensional and two-dimensional FEA indenter tip models were then compared by best fitting the loading curve and the initial unloading slope for the average nanoindentation curves. The fitting parameters were the elastic modulus E and the yield stress, σ_Y. E and σ_Y were found to be respectively 2.6 and 1.9% higher in average for the three-dimensional model than for the 2D one. These small differences show that for the experiment considered in this article, the use of a two-dimensional axisymmetric approximation for the Berkovich geometry is appropriate.

APPENDIX C CHOICE OF INTERINDENT SPACING VIA FEA SIMULATIONS

The spacing between neighboring indents or the interindent spacing was chosen in order to avoid overlap of inelastic strain and residual stress zones. A three-dimensional FEA model was constructed of nine indents on a square grid with the same interindent spacing as chosen for the experiments reported in Chapter 7, i.e. 3 μm. The 3D Berkovich indenter tip geometry described in Appendix B was used. The indented material was

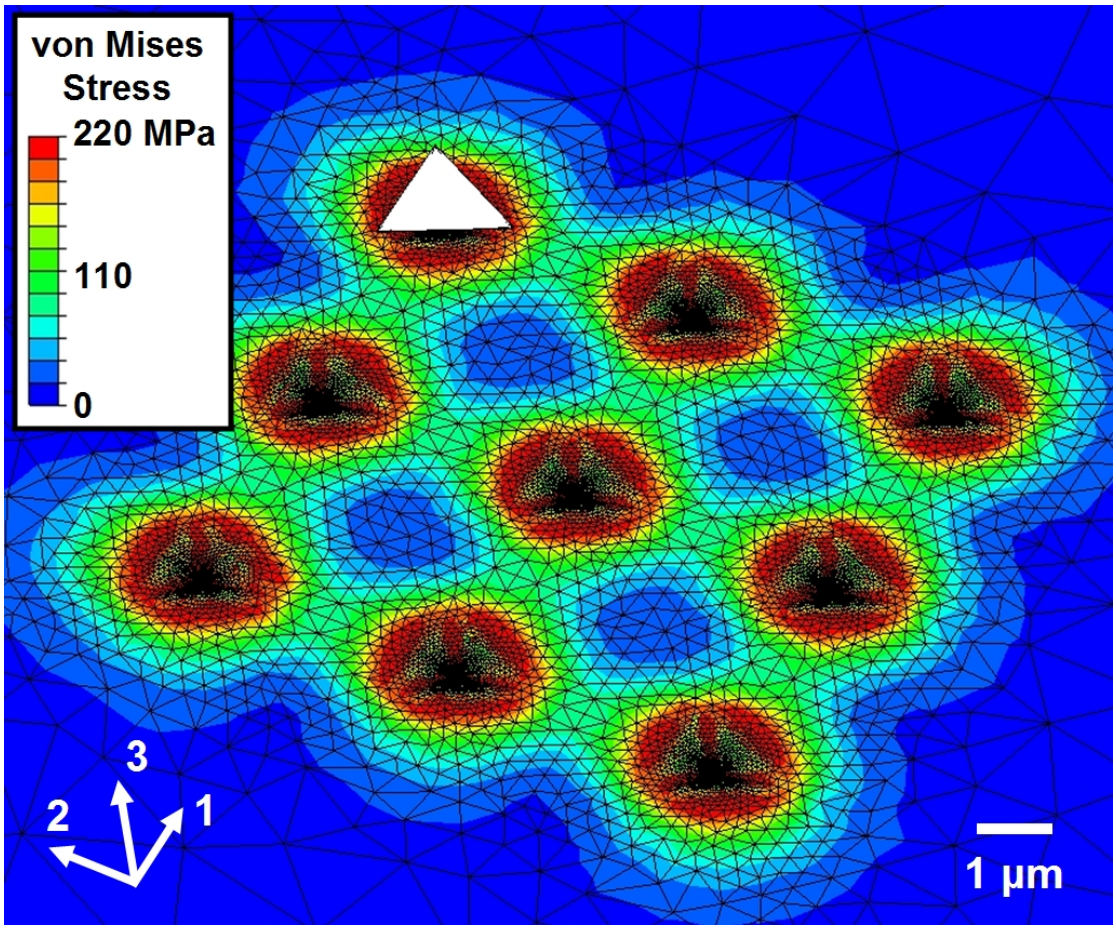

a

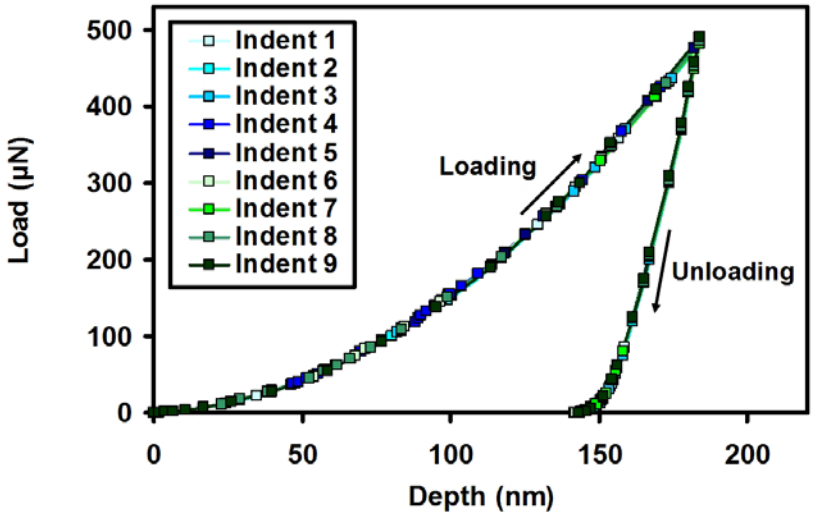

b

Fig. C-1. FEA simulation of a series of nine nanoindentations in a bone sample positioned on a 3 × 3 square grid spaced 3 um apart. **(a)**, The residual von Mises stress field. For illustration, the uppermost residual indentation is covered by the Berkovich indenter tip. **(b)**, Simulated load-depth nanoindentation curves corresponding to all nine grid indentation virtual experiments from a.

modeled as an elastic-perfectly plastic square parallelepiped with a width of 30 μm and a thickness of 10 μm, using 4-node linear tetrahedral elements (C3D4 in ABAQUS element library, Providence, RI). Mesh convergence tests were carried out and an optimal mesh (in terms of accuracy and calculation costs) was chosen for use in all simulations, which contained 169742 nodes and 261312 elements. Large deformation theory and frictionless contact between the indenter and material were assumed. Material properties were assigned for bone that were obtained through elastic-perfectly plastic FEA simulations compared to averaged nanoindentation load-depth data; i.e. E = 13.5 GPa and $\int_Y$ = 220 MPa. Bone was chosen for this simulation because it corresponded to the most unfavorable situation, where the maximal depth of indentation (~180 nm) was observed to be the greatest out of all four materials in the fish scale (i.e. ganoine, dentin, isopedine, and bone) leading to the largest residual indents. Fig. C-1 shows the residual von Mises

stress field, as well as the simulated load-depth curves corresponding to all nine virtual indents. E was calculated from the FEA load-depth curves using the Oliver-Pharr or O-P method[203] for the data in Fig. C-1 and < 1% difference was found between all nine indentation simulations. These results confirm that the chosen interindent spacing enabled accurate reproducible data for each indentation that was independent of each neighboring pre-existing indentation.

APPENDIX D GANOINE OUTER SURFACE

NANOMECHANICAL TESTING

Indentation experiments were also carried out on the ganoine outer surface (which is facing towards the epidermis), with the load parallel to the 1 axis (see Chapter 7). Prior to testing, the scales sonicated in distilled water for 15 minutes and gently dried with a stream of nitrogen. They were then directly stuck on steel pucks using a cyanoacrylate glue (Loctite 495) rather than embedded in epoxy. To ensure that the glue layer underneath the scales did not cause the scale to bend during nanoindentation an FEA simulation of the nanoindentation was conducted, using a perfectly elastic axisymmetric model of the scale (with the scale and epoxy moduli chosen as 15 and 1 GPa respectively). The maximum vertical displacement of the epoxy layer was found to be < 0.1% (at a depth of indentation into the scale of 400 nm). Lower depths of indentations resulted in errors < 0.1%. 25 experiments per maximum load were performed in a square grid arrangement with each indent spaced 5 μm (for loads of 1000 μN and below) and 10 μm (for loads above 1000 μN) apart. Plots of the averaged nanoindentation curves corresponding to different maximum loads for indents conducted perpendicular to the outer ganoine surface are given in Fig. D-1 (a) and (b). The purple curves are for indents located on the center of the scale surface, while orange curves are for indents located on the anterior process surface. The depth of indentation at maximum load was significantly greater ($p<0.05$) for the tail location for all loads except for the 10 mN. The slope of the

force-depth curves changes markedly after a depth of 40-50 nm, and the distribution

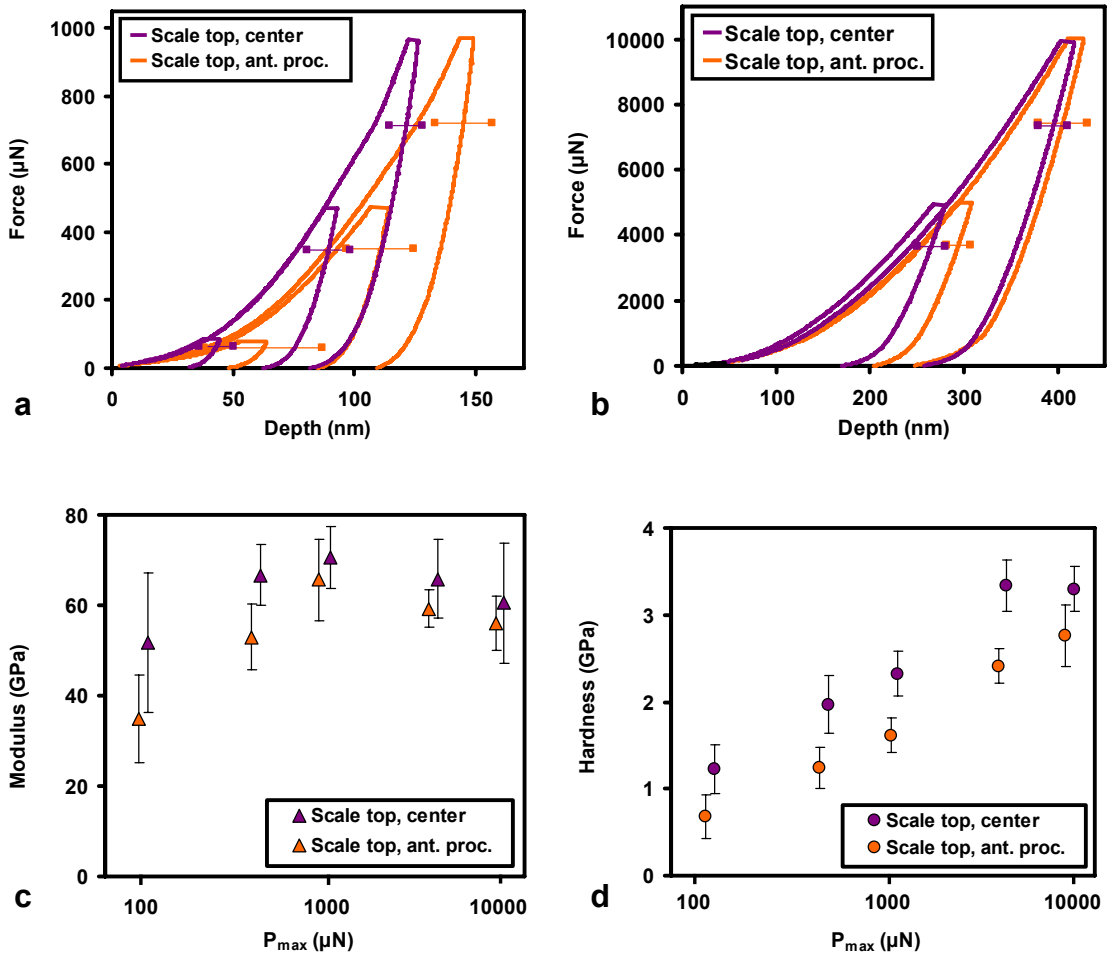

Fig. D-1. Nanoindentation data for loading axis normal to the outer *Polypterus senegalus* ganoine scale surface at two different locations (center of scale and anterior process) on loading and unloading for different maximum loads. Average force versus depth data for **(a)** 100, 500 and 1000 μN maximum loads and **(b)** 5000 and 10,000 μN maximum loads. The horizontal error bars represent the standard deviation for that particular dataset (n=25). Mechanical properties reduced from the data shown in parts **(a)** and **(b)**; **(c)** average indentation moduli, E, calculated via the Oliver–Pharr analysis[203] **(d)** average hardness, H, derived using Oliver–Pharr analysis.[203] The vertical error bars represent the standard deviation for that particular dataset (n=25)

(standard deviation) of the curves increases. All samples exhibited mechanical hysteresis. Oliver-Pharr analysis[110] of the indentation curves indicated average values of the indentation moduli ranging between 34.9 and 65.6 GPa for the anterior process indents

(depending on the maximum load) and between 51.7 and 70.5 GPa for the indents close to the outer surface center (Fig. D-1**(c)**). Average hardness values ranged between 0.68 and 2.75 GPa (depending on the maximum load) for the anterior process indents and between 1.22 and 3.33 GPa for the center indents [Fig. D-1**(d)**]. Indentation modulus and hardnesses at each maximum load showed a significant statistical difference ($p<0.05$) between the two indentation locations on the scale, except for the 10 mN experiments. AFM inspection of the indented region showed extensive plastic deformation of the surface, including pile-up around the residual impression and flattening of the nanoasperities (Fig D-2).

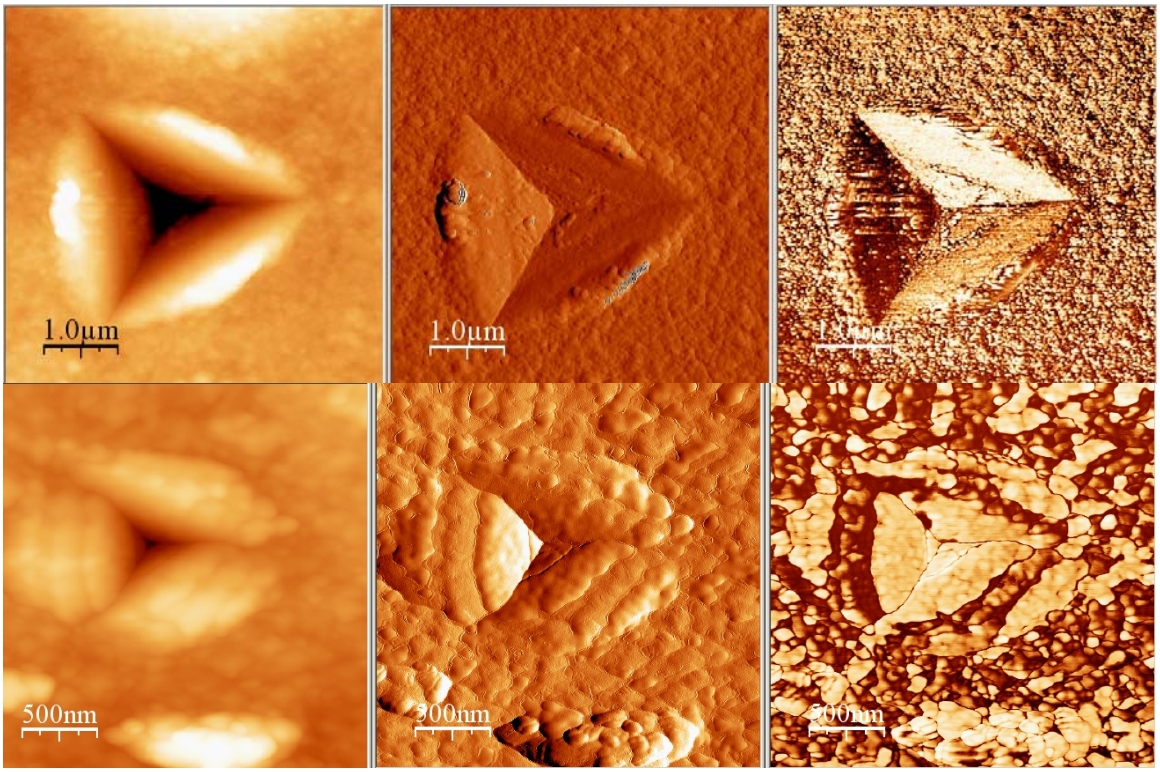

Fig. D-2. TMAFM images of the residual indentation at the ganoine surface (height, amplitude and phase) **(a)** 10 mN indent **(b)** 1mN indent.

REFERENCES

1. McMenamin, M. A. & McMenamin, D. L. S. The Emergence of Animals: The Cambrian Breakthrough (Columbia University Press, 1990).
2. Boggild, O. B. The shell structure of the Mollusks. K. Danske Vidensk. Selsk. Skr., Nat. Mat. Afd 9, 230-326 (1930).
3. Wang, R. Z., Suo, Z., Evans, A. G., Yao, N. & Aksay, I. A. Deformation mechanisms in nacre. J. Mater. Res. 16, 2485-2493 (2001).
4. Menig, R., Meyers, M. H., Meyers, M. A. & Vecchio, K. S. Quasi-static and dynamic mechanical response of Haliotis Rufescens (abalone) shells. Acta Mater. 48, 2383-2398 (2000).
5. Jackson, A. P., Vincent, J. F. V. & Turner, R. M. Comparison of Nacre with other ceramic composites. J. Mater. Sci., 3173-3178 (1990).
6. Jackson, A. P., Vincent, J. F. V. & Turner, R. M. The mechanical design of nacre. Proc. Roy. Soc. London, Series B 234, 415-440 (1988).
7. Currey, J. D. Mechanical properties of mother pearl in tension. Proc. Roy.Soc. Lond. Series B 196, 443-463 (1977).
8. Wada, K. & National Pearl Research, L. Crystal Growth of Molluscan Shells (National Pearl Research Laboratory, 1961).
9. Erban, H. K. On the structure and growth of the nacreous tablets in gastropods. Biomineralisation 4, 14-27 (1972).
10. Taylor, J. D., Kennedy, W. J. & Hall, A. Shell structure and minerology of the bivalvia: Introduction Nuculacea-Trigonacea. Bull. Br. Mus. nat. Hist. Zool. Suppl. 3, 1-125 (1969).
11. Lowenstam, H. A. & Weiner, S. On biomineralization (Oxford University Press New York, 1989).
12. Carter, J. G. & Clark II, G. R. C. Classification and phylogenetic significance of molluscan shell microstructure. Mollusks, Notes for a Short Course, organized by DJ Bottjer, CS Hickman, and PD Ward. University of Tennessee, Department of Geological Sciences, Studies in Geology 13, 50–71 (1985).
13. Runnegar, B. Crystallography of the foliated calcite shell layers of bivalve molluscs. Alcheringa(Sydney) 8, 273-290 (1984).
14. Lutts, A., Grandjean, J. & Grégoire, C. X-ray diffraction patterns from the prisms of mollusk shells. Archives Of Physiology And Biochemistry 68, 829-831 (1960).
15. Bevan, D. J. M. et al. On the structure of aragonite – Lawrence Bragg revisited. Acta Cryst.Section B: Structural Science B58, 448–456 (2002).
16. Wilmot, N. V., Barber, D. J., Taylor, J. D. & Graham, A. L. Electron Microscopy of Molluscan Crossed-Lamellar Microstructure. Philosophical Transactions: Biological Sciences 337, 21-35 (1992).

17. Hedegaard, C. & Wenk, H. R. in Journal of Molluscan Studies 133-136 (Malacological Soc London, 1998).
18. Chateigner, D., Hedegaard, C. & Wenk, H.-R. Mollusk shell microstructures and crystallographic textures. J. Struct. Geo. 22, 1723-1735 (2000).
19. Wheeler, A. P. & Sikes, C. S. Regulation of Carbonate Calcification by Organic Matrix. American Zoologist 24, 933-944 (1984).
20. Weiss, I. M., Tuross, N., Addadi, L. & Weiner, S. Mollusc larval shell formation: amorphous calcium carbonate is a precursor phase for aragonite. Journal of Experimental Zoology 293, 478-491 (2002).
21. Nassif, N. et al. Amorphous layer around aragonite platelets in nacre. Proceedings of the National Academy of Sciences 102, 12653-12655 (2005).
22. Wise, S. W. Microarchitecture and mode of formation of nacre (mother-of-pearl) in pelecypods, gastropods, and cephalopods. Eclogae Geologicae Helveticae 63, 775-797 (1970).
23. Li, X., Chang, W.-C., Chao, Y. J., Wang, R. & Chang, M. Nanoscale Structural and mechanical characterization of a natural nanocomposite material: The shell of red abalone. Nano Lett. 4, 613-617 (2004).
24. Bevelander, G. & Nakahara, H. An electron microscope study of the formation of the nacreous layer in the shell of certain bivalve molluscs. Calc. Tissue Res. 3, 84 (1969).
25. Wada, K. Nucleation and growth of aragonite crystals in the nacre of some bivalve molluscs. Biomineralisation-Biomineralization. Biomineralisation 6, 141 (1972).
26. Mutvei, H. On the internal structures of the nacreous tablets in molluscan shells. Scanning Electron Micro. 2, 457 (1979).
27. Schäffer, T. E. et al. Does Abalone nacre form by heteroepitaxial growth or by growth through mineral bridges? Chem. Mater. 9, 1731-1740 (1997).
28. Manne, S. et al. Atomic Force Microscopy of the Nacreous Layer in Mollusc Shells. Proc. of the Royal Soc.: Bio. Sci. 256, 17-23 (1994).
29. Mutvei, H. Ultrastructural studies on cephalopod shell part 1: The septa and siphonal tube in Nautilus. Bull. Geol. Inst. Univer. Upsala (N.S.) 3, 237-261 (1972).
30. Dauphin, Y., Cuif, J. P., Mutvei, H. & Denis, A. Mineralogy, chemistry and ultrastructure of the external shell-layer in ten species of Haliotis with reference to Haliotis tuberculata (Mollusca: Archaeogastropoda). Bull. Geol. Inst. Univ. Upps. NS 15, 7–38 (1989).
31. Mutvei, H. Ultrastructural Characteristics of the Nacre in some Gastropods. Zool. Scr. 7, 287-296 (1978).
32. Mutvei, H. The nacreous layer in Mytilus, Nucula, and Unio (Bivalvia). Calcif. Tissue Res 24, 11–18 (1977).
33. Nakahara, H., Bevelander, G. & Kakei, M. Electron microscopic and amino acid studies on the outer and inner shell layers of Haliotis rufescens. Venus 41, 33 (1982).
34. Song, F., Zhang, X. H. & Bai, Y. L. Microstructure and characteristics in the organic matrix layers of nacre. J. Mater. Res. 17, 1567-1570 (2002).

35. Bruet, B. J. F. et al. Nanoscale morphology and indentation of individual nacre tablets from the gastropod mollusc Trochus niloticus. Journal of Materials Research 20, 2400-2419 (2005).
36. Levi-Kalisman, Y., Falini, G., Addadi, L. & Weiner, S. Structure of the Nacreous Organic Matrix of a Bivalve Mollusk Shell Examined in the Hydrated State Using Cryo-TEM. Journal of Structural Biology 135, 8-17 (2001).
37. Sarikaya, M. & Aksay, I. A. Nacre of abalone shell: a natural multifunctional nanolaminated ceramic-polymer composite material. Results Probl Cell Differ 19, 1-26 (1992).
38. Sarikaya, M. & Aksay, I. A. Biomimetics: design and processing of materials (American Institute of Physics, 1995).
39. Lowenstam, H. A. Minerals formed by organisms. Science 211, 1126-1131 (1981).
40. Pereira-Mouries, L. et al. Soluble silk-like organic matrix in the nacreous later of the bivalve Pinctada maxims. Eur. J. Biochem. 269, 4994-5003 (2002).
41. Clark, G. R. Organic matrix taphonomy in some molluscan shell microstructures. Palaeogeography, Palaeoclimatology, Palaeoecology 149, 305–312 (1999).
42. Jeuniaux, C. Chitine et chitinolyse: un chapitre de la biologie moléculaire (Masson, 1963).
43. Weiner, S. & Traub, W. X-ray Diffraction study of the insoluble organic matrix of mollusk shells. FEBS Lett. 111, 311-316 (1980).
44. Weiner, S., Talmon, Y. & Traub, W. Electron diffraction of mollusc shell organic matrices and their relationship to the mineral phase. Int. J. Biol. Macromol. 5, 325-328 (1983).
45. Weiss, I. M., Renner, C., Strigl, M. G. & Fritz, M. A Simple and reliable method for the determination and localization of chitin in abalone nacre. Chem. Mater. 14, 3252-3259 (2002).
46. Grégoire, C. Structure of the molluscan shell. Chemical Zoology 7, 45–102 (1972).
47. Weiner, S. & Traub, W. Macromolecules in Mollusc Shells and their functions in biomineralization. Philosoph. Trans. Roy. Soc. London Series B Bio. Sci. 302, 425-433 (1984).
48. Addadi, L., Joester, D., Nudelman, F. & Weiner, S. Mollusk shell formation: A source of new concepts for understanding biomineralization processes. Chemistry(Weinheim) 12, 980-987 (2006).
49. Grégoire, C., Duchâteau, G. & Florkin, M. La trame protidique des nacres et des perles (impr. de Soulisse et Cassegrain), 1955).
50. Grégoire, C. On submicroscopic structure of the Nautilus shell. Bull. Inst. R. Sci. Nat. Belg. 38, 1–71 (1962).
51. Levi, Y., Albeck, S., Brack, A., Weiner, S. & Addadi, L. Control Over Aragonite Crystal Nucleation and Growth: An In Vitro Study of Biomineralization. Chemistry- A European Journal 4, 389-396 (1998).
52. Belcher, A. M. et al. Control of crystal phase switching and orientation by soluble mollusc-shell proteins. Nature 381, 56-58 (1996).

53. Heinemann, F., Treccani, L. & Fritz, M. Abalone nacre insoluble matrix induces growth of flat and oriented aragonite crystals. Biochemical and Biophysical Research Communications 344, 45-49 (2006).
54. Crenshaw, M. A. The inorganic composition of molluscan extrapallial fluid. The Biological Bulletin 143, 506 (1972).
55. Weiner, S. Aspartic acid-rich proteins: Major components of the soluble organic matrix of mollusk shells. Calcified Tissue International 29, 163-167 (1979).
56. Watabe, N. & Wilbur, K. M. Influence of the organic matrix on crystal type in molluscs. Nature 188, 334 (1960).
57. Falini, G., Albeck, S., Weiner, S. & Addad, L. Control of Aragonite or Cacite polymorphism by mollusk shell macromolecules. Science 271, 67-69 (1996).
58. Thompson, J. B. et al. Direct Observation of the Transition from Calcite to Aragonite Growth as Induced by Abalone Shell Proteins. Biophysical Journal 79, 3307-3312 (2000).
59. Nakahara, H., Kakei, M. & Bevelander, G. Fine structure and amino acid composition of the organic "envelope" in the prismatic layer of some bivalve shells. Jpn. J. Malacol. 39, 167 (1980).
60. Dauphin, Y. The organic matrix of coleoid cephalopod shells: molecular weights and isoelectric properties of the soluble matrix in relation to biomineralization processes. Marine Biology 125, 525-529 (1996).
61. Crenshaw, M. A. The soluble matrix from Mercenaria mercenaria shell. Biomineralization 6, 6-11 (1972).
62. Worms, D. & Weiner, S. Mollusk shell organic matrix: fourier transform infrared study of the acidic macromolecules. J Exp Zool 237, 11-20 (1986).
63. Mann, S. et al. Problems in the understanding of biominerals. Biomineralization and Biological Metal Accumulation (1983).
64. Fu, G., Qiu, S. R., Orme, C. A., Morse, D. E. & De Yoreo, J. J. Acceleration of calcite kinetics by abalone nacre proteins. Advanced Materials 17 (2005).
65. Kim, I. W., Collino, S., Morse, D. E. & Evans, J. S. A Crystal Modulating Protein from Molluscan Nacre That Limits the Growth of Calcite in Vitro. Crystal Growth & Design 6, 1078-1082 (2006).
66. Michenfelder, M. et al. Characterization of two molluscan crystal-modulating biomineralization proteins and identification of putative mineral binding domains. Biopolymers 70, 522-533 (2003).
67. Smith, B. L. et al. Molecular mechanistic origin of the toughness of natural adhesives, fibres and composites. Nature 399, 761-763 (1999).
68. Wustman, B. A., Morse, D. E. & Evans, J. S. Structural analyses of polyelectrolyte sequence domains within the adhesive elastomeric biomineralization protein lustrin A. Langmuir 18, 9901-9906 (2002).
69. Fricke, M. & Volkmer, D. Crystallization of Calcium Carbonate Beneath Insoluble Monolayers: Suitable Models of Mineral–Matrix Interactions in Biomineralization? Top Curr Chem 270, 1-41 (2007).
70. Addadi, L. & Weiner, S. Control and Design Principles in Biological Mineralization. Angewandte Chemie. International edition in English 31, 153-169 (1992).

71. Crenshaw, M. A. & Ristedt, H. The histochemical localization of reactive groups in septal nacre from Nautilus pompilius L. The mechanisms of mineralization in the invertebrates and plants. University of South Carolina Press, Columbia, SC, 355–367 (1976).
72. Nudelman, F., Gotliv, B. A., Addadi, L. & Weiner, S. Mollusk shell formation: Mapping the distribution of organic matrix components underlying a single aragonitic tablet in nacre. Journal of Structural Biology 153, 176-187 (2006).
73. Addadi, L., Moradian, J., Shay, E., Maroudas, N. G. & Weiner, S. A Chemical Model for the Cooperation of Sulfates and Carboxylates in Calcite Crystal Nucleation: Relevance to Biomineralization. Proceedings of the National Academy of Sciences of the United States of America 84, 2732-2736 (1987).
74. Blakemore, R. Magnetotactic bacteria. Science 190, 377-379 (1975).
75. Aizenberg, J., Tkachenko, A., Weiner, S., Addadi, L. & Hendler, G. Calcitic microlenses as part of the photoreceptor system in brittlestars. Nature 412, 819-22 (2001).
76. Watabe, N. & Wilbur, K. M. The Mechanisms of Biomineralization in Invertebrates and Plants (Univ. South Carolina Press, Columbia, SC, 1976).
77. Mann, S. Molecular Recognition in Biomineralization. Nature 332, 119-124 (1988).
78. Meldrum, F. C. Calcium carbonate in biomineralisation and biomimetic chemistry. International Materials Reviews 48, 187-224 (2003).
79. Weiner, S. & Dove, P. M. An Overview of Biomineralization Processes and the Problem of the Vital Effect. Reviews in Mineralogy and Geochemistry 54, 1-29 (2003).
80. Xu, A. W., Ma, Y. & Cölfen, H. Biomimetic mineralization. Journal of Materials Chemistry 17, 415-449 (2007).
81. Wilbur, K. M. Shell formation in mollusks. Chemical Zoology 7, 103-145 (1972).
82. Nakahara, H. & Bevelander, G. The formation and growth of the prismatic layer ofPinctada radiata. Calcified Tissue International 7, 31-45 (1971).
83. Nakahara, H. An electron microscope study of the growing surface of nacre in two gastropode species Turbo cornutus and Tegula pfeifferi. Venus 38, 205-211 (1979).
84. Erben, H. K. & Watabe, N. Crystal formation and growth in bivalve nacre. Nature 248, 128-130 (1974).
85. Nakahara, H. Calcification of gastropod nacre. In Biomineralization and Biological Metal Accumulation. Reidel, Dordrecht, 225-230 (1983).
86. Volkmer, D., Fricke, M., Huber, T. & Sewald, N. Acidic peptides acting as growth modifiers of calcite crystals. Chemical Communications 2004, 1872-1873 (2004).
87. Greenfield, E. M., Wilson, D. C. & Crenshaw, M. A. Ionotropic Nucleation of Calcium Carbonate by Molluscan Matrix. American Zoologist 24, 925-932 (1984).
88. Katz, A. The interaction of magnesium with calcite during crystal growth at 25-90 C and one atmosphere. Geochimica et Cosmochimica Acta 37, 1563-1578 (1973).

89. Berner, R. A. The role of magnesium in the crystal growth of calcite and aragonite from sea water. Geochimica et Cosmochimica Acta 39, 489-494 (1975).
90. Giles, R. et al. Imaging single nacreous tablets with the atomic force microscope. Materials Research Society Symposium Proceedings 332, 413-22 (1994).
91. Giles, R. (1995).
92. Wang, R. Z., Wen, H. B., Cui, F. Z., Zhang, H. B. & H.D., L. Observations of damage morphologies in nacre during deformation and fracture. J. Mater. Sci. Lett. 30, 2299 (1995).
93. (eds. Levy, M., Bass, H., Stern, R., Every, A. G. & Sachse, W.) (2001).
94. Evans, A. G. et al. Model for the Robust Mechanical Behavior of Nacre. J. Mater. Res. 16, 2475-84 (2001).
95. Katti, D. R., Pradhan, S. M. & Katti, K. S. MODELING THE ORGANIC-INORGANIC INTERFACIAL NANOASPERITIES IN A MODEL BIONANOCOMPOSITE, NACRE. Rev. Adv. Mater. Sci. 6, 162-168 (2004).
96. Ji, B. & Gao, H. A study of fracture mechanisms in biological nano-composites via the virtual internal bond model. Mater. Sci. Eng. C A366, 96-103 (2004).
97. Qi, H. J., Bruet, B. F. J., Palmer, J. S., Ortiz, C. & Boyce, M. C. in Mechanics of Biological Tissues, Proceeding of IUTAM (eds. Holzapfel, G. & Ogden, R. W.) (Springer Verlag, Graz, Austria, 2005).
98. Qi, H. J., Ortiz, C. & Boyce, M. C. A Constitutive Model for the Stress-Strain Behavior of Biomacromolecular Networks Containing Folded Domains. submitted for publication (2005).
99. Sheiko, S. S. & Moller, M. Visualization of macromolecules:a first step to manipulation and controlled response. Chem.Rev. 101, 4099-4123 (2001).
100. Tan, T., Wong, D. & Lee, P. Iridescence of a shell of mollusk Haliotis Glabra. Optics Express 12, 4847-4854 (2004).
101. Snow, M. R., Pring, A., Self, P., Losic, D. & Shapter, J. The origin of the color of pearls in iridescence from nano-composite structures of the nacre. American Mineralogist 89, 1353-1358 (2004).
102. Sturges, H. The choice of a class interval. J. Amer. Statist. Assoc. 21, 65-66 (1926).
103. Scott, D. W. On optimal and data-based histograms. Biometrika 66, 605-610 (1979).
104. Barthelmy, D. Aragonite Mineral Data. http://webmineral.com/data/Aragonite.shtml.
105. Blank, S. et al. The nacre protein perlucin nucleates growth of calcium carbonate crystals. J. Micro. 212, 280-291 (2003).
106. Rousseau, M. et al. Multiscale structure of sheet nacre. Biomaterials (2005).
107. Amos, F. F. et al. Formation of Single-Crystalline Aragonite Tablets/Films via an Amorphous Precursor. Langmuir 23, 1988-1994 (2007).
108. Barthelat, F. & Espinosa, H. D. in SEM Annual Conference and Exposition on Experimental and Applied Mechanics, Session 68, Paper 187 (Charlotte, North Carolina, 2003).
109. Hanson, M. T. The elastic field for sperical Hertzian contact including sliding friction for transverse isotropy. J. Tribology 114, 606 (1992).

110. Oliver, W. C. & Pharr, G. M. An improved technique for determining hardness and elastic modulus using load and displacement sensing indentation experiments. J. Mater. Res. 7, 1564 (1992).
111. Harris, D. C. Quantitative Chemical Analysis (W. H. Freeman and Company, New York, 1995.).
112. Arruda, E. M. & Boyce, M. C. A Three-dimensional constitutive model for the large stretch behavior of elastomers. J. Mech. Phys. Solids 41, 389-412 (1993).
113. Bischoff, J., Arruda, E. M. & K., G. Orthotropic hyperelasticity in terms of an arbitrary molecular chain model. J. Appl. Mech. 69, 198-201 (2002).
114. Bischoff, J., Arruda, E. M. & Grosh, K. A microstructurally based orthotropic hyperelastic constitutive law. J. Appl. Mech. 69, 570-579 (2002).
115. Kotha, S. P., Li, Y. & Guzelsu, N. Micromechanical model of nacre tested in tension. J. Mater. Sci. 36, 2001-2007 (2001).
116. Hoedeman, J. J. Naturalists Guide to Fresh Water Aquarium Fish (Sterling Publishing Co., Oak Tree press Co. Ltd, New York, London, and Sydney, 1975).
117. Colbert, E. H. Evolution of the vertebrates (John Wiley and Sons, Inc, New York, London, Sydney, Toronto, 1955).
118. Miller, H. The Cruise of the Betsy or summer holiday in the Hebrides with Rambles of a Geologist or Ten Thousand Miles of Fossiliferous Deposits of Scotland (Gould and Lincoln, Boston, 1857).
119. Romer, A. S. Eurypterid Influence on Vertebrate History. 78, 114-117 (1933).
120. Ørvig, T. in Current Problems of Lower Vertebrate Phylogeny. Proceedings of the 4th Nobel Symposium. (ed. Ørvig, T.) 373-397 (Almqvist and Wiskell, Stockholm, 1968).
121. Long, J. H. & Nipper, K. S. The importance of body stiffness in undulatory propulsion. Am Zool 36, 678–694 (1996).
122. Raschi, W. & Tabit, C. Functional aspects of Placoid Scales: A review and update. Australian Journal of Marine and Freshwater Research 43, 123 - 147 (1992).
123. Anderson, P. S. L. & Westneat, M. W. Feeding mechanics and bite force modelling of the skull of Dunkleosteus terrelli, an ancient apex predator. Biology Letters 22, 76-9 (2006).
124. Arciszewski, T. & Cornell, J. Bio-inspiration: Learning creative design principles (ed. Smith, I. F. C.) (Springer-Verlag, Berlin, Heidelberg, 2006).
125. Weiner, S. & Addadi, L. Design strategies in mineralized biological materials. Journal of Materials Chemistry 7, 689-702 (1997).
126. Gao, H., Baohua, J., Jager, I. L., Arzt, E. & Fratzl, P. Materials become insensitive to flaws at nanoscale: Lessons from nature. Proceedings of the National Academies of Science 100, 5597-5600 (2003).
127. Buehler, M. J. Molecular nanomechanics of nascent bone: fibrillar toughening by mineralization. Nanotechnology 18, 1-9 (2007).
128. Currey, J. D. The design of mineralised hard tissues for their mechanical functions. Journal of Experimental Biology 202, 3285-3294 (1999).

129. Fantner, G. E. et al. Sacrificial bonds and hidden length dissipate energy as mineralized fibrils separate during bone fracture. Nature Materials 4, 612-616 (2005).
130. Raabe, D., Sachs, C. & Romano, P. The crustacean exoskeleton as an example of a structurally and mechanically graded biological composite material. Acta Materialia 53, 4281-4292 (2005).
131. Barbakadze, N., Enders, S., Gorb, S. & Arzt, E. Local mechanical properties of the head articulation cuticle in the beetle Pachnoda marginata (Coleoptera, Scarabaeidae). Journal of Experimental Biology 209, 722-730 (2006).
132. Imbeni, V., Kruzic, J. J., Marshall, G. W. & Ritchie, R. O. The dentin-enamel junction and the fracture of human teeth. Nature Materials 4, 229-232 (2005).
133. Hierarchical Structures in Biology as a Guide for New Materials Technology (National Academy Press, National Materials Advisory Board (NMAB), Washington DC, 1994).
134. Janvier, P. Early Vertebrates (Oxford University Press, USA, 1996).
135. Ørvig, T. A survey of odontodes ('dermal teeth') from developmental, structural, functional, and phyletic points of view. Andrews et al, 53–75 (1977).
136. Sire, J. Y. & Huysseune, A. N. N. Formation of dermal skeletal and dental tissues in fish: a comparative and evolutionary approach. Biological Reviews 78, 219-249 (2003).
137. Smith, M., Ferguson, M. W. J. & Teaford, M. Development, Function and Evolution of Teeth (Cambridge University Press, 2000).
138. Meckel, A. H., Griebstein, W. J. & Neal, R. J. Structure of mature human dental enamel as observed by electron microscopy. Arch Oral Biol 10, 775-83 (1965).
139. Young, R. A. Implications of Atomic Substitutions and Other Structural Details in Apatites. Journal of Dental Research 53, 193-203 (1974).
140. Weber, D. F. Sheath configurations in human cuspal enamel. Journal of Morphology 141, 479-489 (1973).
141. Weiner, S. et al. Peritubular Dentin Formation: Crystal Organization and the Macromolecular Constituents in Human Teeth. Journal of Structural Biology 126, 27-41 (1999).
142. Daculsi, G. & Kerebel, B. High-resolution electron microscope study of human enamel crystallites: size, shape, and growth. J Ultrastruct Res 65, 163-72 (1978).
143. Voegel, J. C. & Frank, R. M. Ultrastructural study of apatite crystal dissolution in human dentine and bone. J Biol Buccale 5, 181-94 (1977).
144. Lin, C. P., Douglas, W. H. & Erlandsen, S. L. Scanning electron microscopy of type I collagen at the dentin-enamel junction of human teeth. J Histochem Cytochem 41, 381-8 (1993).
145. Sire, J. Y. Ganoine formation in the scales of primitive actinopterygian fishes, lepisosteids and polypterids. Connect Tissue Res 33, 213-22 (1995).
146. Sire, J. Y. Light and TEM study of nonregenerated and experimentally regenerated scales of Lepisosteus oculatus (Holostei) with particular attention to ganoine formation. Anatomical Record 240, 189–207 (1994).
147. Sire, J. Y. Scales in young Polypterus senegalus are elasmoid: new phylogenetic implications. Am J Anat 186, 315-23 (1989).

148. Sire, J. Y., Geraudie, J., Meunier, F. J. & Zylberberg, L. Participation des cellules épidermiques à la formation de la ganoïne au cours de la régénération expérimentale des écailles de Calamoichthys calabaricus(Smith, 1886)(Polypteridae, Osteichthyeus). Comptes rendus de l'Académie des sciences. Série 3, Sciences de la vie 303, 625-628 (1986).
149. Lloyd, G. E. Atomic number and crystallographic contrast images with the SEM: a review of backscattered electron techniques. Mineralogical Magazine 51, 3-19 (1987).
150. Skedros, J. G., Bloebaum, R. D. & Bachus, K. N. The meaning of graylevels in backscattered electron images of bone. Journal of Biomedical Materials Research 27, 47-56 (1993).
151. Skedros, J. G., Bloebaum, R. D., Bachus, K. N., Boyce, T. M. & Constantz, B. Influence of mineral content and composition on graylevels in backscattered electron images of bone. J Biomed Mater Res 1993, 57-64 (2001).
152. Boyce, T. M., Bloebaum, R. D., Bachus, K. N. & Skedros, J. G. Reproducible methods for calibrating the backscattered electron signal for quantitative assessment of mineral content in bone. Scanning Microsc 4, 591-600 (1990).
153. Boyde, A. & Jones, S. J. Back-scattered electron imaging of skeletal tissues.
154. Humphries, J. Polypterus senegalus, Online Digital Morphology. Accessed June 1, 2007 at http://digimorph.org/specimens/Polypterus_senegalus/whole/. (2003).
155. Schultze, H. P. Morphologische und histologische Untersuchungen an den Schuppen mesozoischer Actinopterygier (Übergang von Ganoid-zu Rundschuppen). Neues Jahrbuch für Geologie und Paläontologie, Abhandlungen 126, 232-314 (1966).
156. Daget, J., Gayet, M., Meunier, F. J. & Sire, J. Y. Major discoveries on the dermal skeleton of fossil and Recent polypteriforms: a review. Fish and Fisheries 2, 113–124 (2001).
157. Ørvig, T. Phylogeny of tooth tissues: evolution of some calcified tissues in early vertebrates. Structural and Chemical Organization of Teeth 1, 45–110 (1967).
158. Meunier, F. J. Recherches histologiques sur le squelette dermique des Polypteridae. Archives de Zoologie Expérimentale et Générale 121, 279–295 (1980).
159. Lyngstadaas, S. P., Moeinichen, C. B. & Risnes, S. Crown morphology, enamel distribution, and enamel structure in mouse molars. The Anatomical Record 250, 268-280 (1998).
160. Sire, J. Y., Quilhac, A., Bourguignon, J. & Allizard, F. Evidence for participation of the epidermis in the deposition of superficial layer of scales in zebrafish(Danio rerio): A SEM and TEM study. Journal of Morphology 231, 161-174 (1997).
161. Zylberberg, L., Sire, J. Y. & Nanci, A. Immunodetection of amelogenin-like proteins in the ganoine of experimentally regenerating scales of Calamoichthys calabaricus, a primitive actinopterygian fish. Anat Rec 249, 86-95 (1997).
162. Nalla, R. K. et al. Ultrastructural examination of dentin using focused ion-beam cross-sectioning and transmission electron microscopy. Micron 36, 672-280 (2005).

163. Meunier, F. J. Recherches histologiques sur le squelette dermique des Polypteridae. Archives de Zoologie Expérimentale et Générale 121, 279–295 (1980).
164. Meunier, F. J. Os cellulaire, os acellulaire et tissus dérivés chez les Ostéichthyens: les phénomènes de l'acellularisation et de la perte de minéralisation. L'Année biologique 26, 201–233 (1987).
165. Meunier, F. J. Os cellulaire, os acellulaire et tissus dérivés chez les Ostéichthyens: les phénomènes de l'acellularisation et de la perte de minéralisation. L'Année biologique 26, 201–233 (1987).
166. Sire, J. Y. From Ganoid to Elasmoid scales in the Actinopterygian fishes. Neth. J. Zool 40, 75-92 (1990).
167. Kodera, H. et al. Jurassic Fishes: Selection, Care, Behavior (T.F.H. Publications, Inc., New Jersey, 1994).
168. Carroll, R. L. Vertebrate Paleontology and Evolution (W.H. Freeman and Company, New York, 1987).
169. Tai, K. D., M.; Suresh, S.; Palazoglu, A.; Ortiz, C. Nanoscale heterogeneity promotes energy dissipation in bone. Nature Materials 6, 454-462 (2007).
170. Oliver, W. C. & Pharr, G. M. An improved technique for determining hardness and elastic modulus using load and displacement sensing indentation experiments. Journal of Materials Research 7, 1564 (1992).
171. Meunier, F. J. Recherches histologiques sur le squelette dermique des Polypteridae. Archives de Zoologie Expérimentale et Générale 121, 279-295 (1980).
172. Meunier, F. J. Os cellulaire, os acellulaire et tissus dérivés chez les Ostéichthyens: les phénomènes de l'acellularisation et de la perte de minéralisation. L'Année biologique 26, 201-233 (1987).
173. Sire, J. Y. From Ganoid to Elasmoid scales in the Actinopterygian fishes. Netherlands Journal of Zoology 40, 75-92 (1990).
174. Shimizu, D. & Macho, G. A. Functional significance of the microstructural detail of the primate dentino-enamel junction: A possible example of exaption. Journal of Human Evolution 52, 103-111 (2007).
175. Ramberg, W. & Osgood, W. R. Description of stress-strain curves by three parameters. Technical Note No. 902, National Advisory Committee For Aeronautics (1943).
176. Jayachandran, R., Boyce, M. C. & Argon, A. S. Design of multilayer polymeric coatings for indentation resistance. Journal of Computer-Aided Materials Design 2, 151-166 (1995).
177. Song, J., Wang, L., Bruet, B., Ortiz, C. & Boyce, M. C. Effect of Material Anisotropy on the Microindentation Properties of P. Senegalus Mineralized Ganoid Scales, in preparation. (2007).
178. Teaford, M. F., Smith, M. M. & Ferguson, M. W. J. Development, Function and Evolution of Teeth (Cambridge University Press, 2000).
179. Schaeffer, B. in Problems in Vertebrate Evolution; Linnean Society Symposium Series 4 (eds. Andrews, S. M., Miles, R. S. & Walker, A. D.) 25-52 (Academic Press, London, 1977).

180. Orvig, T. in Structural and chemical organization of teeth (ed. Miles, A. E. W.) 45-110 (Stockholm, 1967).
181. Orvig, T. in Problems in vertebrate evolution (eds. Andrews, S. M., Miles, R. S. & Walker, A. D.) 53-75 (Academic Press, London, 1977).
182. Zylberberg, L., Sire, J. Y. & Nanci, A. Immunodetection of amelogenin-like proteins in the ganoine of experimentally regenerating scales of Calamoichthys calabaricus, a primitive actinopterygian fish. Anatomical Record 249, 86-95 (1997).
183. Cuy, J. L., Mann, A. B., Livi, K. J., Teaford, M. F. & Weihs, T. P. Nanoindentation mapping of the mechanical properties of human molar tooth enamel. Archives of Oral Biology, 281-291 (2002).
184. Tesch, W. et al. Graded microstructure and mechanical properties of human crown dentin. Calcified Tissue International 69, 147-157 (2001).
185. Marshall, G. W., Balooch, M., Gallagher, R. R., Gansky, S. A. & Marshall, S. J. Mechanical properties of the dentinoenamel junction; AFM studies of nanohardness, elastic modulus, and fracture. Journal of Biomedical Materials Research 54, 87-95 (2001).
186. Fong, H., Sarikaya, M., White, S. N. & Snead, M. L. Nano-mechanical properties profiles across dentin-enamel junction of human incisor teeth. Materials Science and Engineeirng C 7, 119-128 (2000).
187. Wang, R. Z. & Weiner, S. Strain-structure relations in human teeth using Moire fringes. Journal of Biomechanics 31, 135-141 (1998).
188. Richter, M. & Smith, M. A microstructural study of the ganoine tissue of selected lower vertebrates. Zoological Journal of the Linnean Society 114, 173-212 (1995).
189. Weiner, S. et al. Peritubular Dentin Formation: Crystal Organization and the Macromolecular Constituents in Human Teeth. Journal of Structural Biology 126, 27-41 (1999).
190. Meunier, F. J. & Francois, Y. Organisation spatiale des fibres de collagène de la plaque basale des écailles des Téléostéens. Zoologica Scripta 11, 141-153 (1982).
191. Tai, K. U., F. J.; Ortiz, C. Nanogranular origins of the strength of bone. Nano Letters 6, 2520-2525 (2006).
192. Gupta, H. S. et al. Nanoscale deformation mechanisms in bone. Nano Letters 5, 2108-2111 (2005).
193. Tai, K. J. Q., H.; Ortiz, C. Effect of mineral content on the nanoindentation properties and nanoscale deformation mechanisms of bovine tibial cortical bone. Journal of Materials Science: Materials in Medicine 16, 947 - 959 (2005).
194. Nalla, R. K., Kinney, J. H. & Ritchie, R. O. Mechanistic fracture criteria for the failure of human cortical bone. Nature Materials 2, 164-168 (2003).
195. Fantner, G. E. et al. Sacrificial bonds and hidden length dissipate energy as mineralized fibrils separate during bone fracture. Nature Mater. 4, 612-616 (2005).
196. Kardong, K. K. & Zalisko, E. J. Comparative Vertebrate Anatomy: A Laboratory Dissection Guide (McGraw-Hill, Columbus, Ohio, 2005).

197. Suresh, S. Graded materials for resistance to contact deformation and damage. Science 292, 2447-2451 (2001).
198. Holten-Anderson. Nano-Mechanical Investigation of the Byssal Cuticle, a protective coating of a bioelastomer. Materials Research Society Symposium Proceedings 844, Y3.7.1/R3.7.1 (2005).
199. Gemballa, S. & Bartsch, P. Architecture of the integument in lower teleostomes: Functional morphology and evolutionary implications. Journal of Morphology 253, 290-309 (2002).
200. Kontoyannis, C. G. & Vagenas, N. V. Calcium Carbonate phase analysis using XRD and FT-Raman Spectroscopy. Analyst I25, 251 (2000).
201. Power Diffraction File (PDF) 00-041-1475 from the International Centre for Diffraction Data (ICDD).
202. Balmain, J., Hannoyer, B. & Lopez, E. Fourier transform infrared spectroscopy (FTIR) and X-ray diffraction analyses of mineral and organic matrix during heating of mother of pearl (nacre) from the shell of the mollusc Pinctada maxima. J. Biomed. Mater. Res. 48, 749-54 (1999).
203. Pharr, G. M. & Oliver, W. C. An improved technique for determining hardness and elastic modulus using load and displacement sensing indentation experiments. J. Mater. Res 7, 1564-1583 (1992).